Modelling and Upscaling of Shallow Compaction in Basins

Jingchen Zhang

Submitted for the degree of Doctor of Philosophy

Heriot-Watt University

Institute of Petroleum Engineering

April 2015

ABSTRACT

Heterogeneous fine-grained sediments at shallow burial (< 1000m) below the seafloor can often experience large strain of mechanical compaction and variable degrees of overpressure in their pore space as a result of disequilibrium dissipation of pore fluid. Shallow overpressure can pose significant risks to economics and safety of hydrocarbon production and may impact on hydrocarbon generation deep in a basin and hydrocarbon migration to traps during basin evolution.

However, when basin modelling ignores the heterogeneity of sediments, large strain deformation and fluid flow conditions at smaller length- and/or time-scales than those at basin scales, it can lead to incorrect prediction of sediment compaction, and hence the mass of the sediment column, the magnitude of pore pressure and its distribution at shallow burials, and consequently can impact on the simulation of basin evolution.

In this thesis, the necessity of considering large-strain consolidation in modelling shallow compaction is demonstrated, and a one-dimensional large-strain numerical simulator, based on one of Gibson's consolidation models and suitable for basin modelling, is developed and verified. An analytical upscaling technique is also developed for determining the effective compressible parameters and permeability for horizontally layered systems of certain compaction characteristics. They are used subsequently to analyse parametrically the compaction behaviours of the layered systems and to calculate effective coefficients for the systems, with results showing that fine-scale simulation is required when considering the effect of fluid-structure interaction. However, the large strain model over-predicts the pressure of the Ursa region, Gulf of Mexico, based on information from the Integrated Ocean Drilling Program (IODP). An analysis indicates that horizontal fluid flow, or lateral motion of mass transport processes, may explain the over prediction. The limitation of a 1D model is further discussed thereafter both in fluid flow and mechanical deformation.

With strong applicability and fundamentality, the Modified Cam Clay model is adopted in 2D research, and related verification is provided. Modified Cam Clay can show elastic and elastic-plastic properties in basin evolution. Heterogeneous Modified Cam Clay materials can be upscaled to a homogenous anisotropic elastic material in elastic deformation and a homogenous Modified Cam Clay material in elastic-plastic deformation, however, the upscaled parameters vary with the effective stress. The value

of the upscaling is demonstrated by modelling the evolution of a simplified North Africa basin model.

ACKNOWLEDGEMENTS

I would like to express my sincere gratitude to my supervisors, Gary Couples and Jingsheng Ma, for providing me with the opportunity to study as a PhD student in the Institute of Petroleum Engineering, Heriot-Watt University at Edinburgh, Scotland, and also for their guidance and constant support throughout my course of PhD study.

ACADEMIC REGISTRY

Research Thesis Submission

Name*:*	**JINGCHEN ZHANG**		
School/PGI:	**Institute of Petroleum Engineering (IPE)**		
Version: *(i.e. First, Resubmission, Final)*	**Final**	Degree Sought (Award **and** Subject area)	**PHD**

Declaration

In accordance with the appropriate regulations I hereby submit my thesis and I declare that:

1) the thesis embodies the results of my own work and has been composed by myself
2) where appropriate, I have made acknowledgement of the work of others and have made reference to work carried out in collaboration with other persons
3) the thesis is the correct version of the thesis for submission and is the same version as any electronic versions submitted*.
4) my thesis for the award referred to, deposited in the Heriot-Watt University Library, should be made available for loan or photocopying and be available via the Institutional Repository, subject to such conditions as the Librarian may require
5) I understand that as a student of the University I am required to abide by the Regulations of the University and to conform to its discipline.

* *Please note that it is the responsibility of the candidate to ensure that the correct version of the thesis is submitted.*

Signature of Candidate*:*		Date:	

Submission

Submitted By *(name in capitals):*	**JINGCHEN ZHANG**
Signature of Individual Submitting:	
Date Submitted:	

For Completion in the Student Service Centre (SSC)

Received in the SSC by *(name in capitals):*			
Method of Submission *(Handed in to SSC; posted through internal/external mail):*			
E-thesis Submitted (**mandatory for final theses)**			
Signature:		Date:	

TABLE OF CONTENTS

LISTS OF TABLES

LISTS OF FIGURES

NOMENCLATURE

Symbols:

A B C D E F J M N c_1 c_2 : constant parameters

β_{fl} : fluid compressibility, Pa^{-1}.

β_p : drained rock/soil compressibility, Pa^{-1}.

c : clay fraction, %.

C_v : coefficient of consolidation, m^2/d.

C_{vo} : initial coefficient of consolidation, m^2/d.

C_{eq} : equivalent consolidation coefficient, m^2/d.

CSL: Critical State Line

d : variation of parameter

E_s : modulus of compressibility, Pa.

e : void ratio

e_0 : initial void ratio

e_∞ : void ratio when effective stress is infinite

e_{100}: void ratio corresponding to 100 kPa

e_s : structural void ratio

e_m : maximum suspension void ratio

e^* : upscaled void ratio

e^d : total deformation in creep compression analysis

e_s : structural void ratio

e_m : maximum suspension void ratio

$\bar{e}$: mean void ratio

exp(x): exponential function, equals 2.71828^x

E : Young modulus, Pa.

f : on behalf of function relations

G : shear modulus, Pa.

g_{ra} : gravity， 9.8 $m \cdot s^{-2}$

H : sediment thickness, m.

h : thickness in material coordinate, m.

h_i^v : the void volumes of cell i , m.

h_i^s : the solid volumes of cell i , m.

i : Subscripts - Integer from 1 to n, for counting

k : hydraulic conductivity, m/d.

k_0 : initial hydraulic conductivity, m/d.

k^* : upscaled hydraulic conductivity, m/d.

K : bulk modulus, Pa.

κ' : unloading line slope

m : material constant for Modified Cam Clay

mbsf: meters below sea floor

m/d: meter per day

m/y: meter per year

m_{vl} : coefficient of volume compressibility, MPa^{-1}

OCR: Over Consolidation Ratio

o : Subscripts - Initial condition or value at reference condition

p' : mean effective stress in Modified Cam Clay model, Pa.

ρ_f : fluid density, kg/m^3.

ρ_{gr} : density of the grain material, kg/m^3.

ρ_s : soil density, kg/m^3.

p_{ex} : effective fluid pressure, Pa or kPa.

p_{fl} : actual fluid pressure, Pa or kPa.

PTIB: Permeable Top Impermeable Base

PTPB: Permeable Top Permeable Base

p : pore pressure, Pa or kPa.

q : surcharge (on the top surface) , Pa or kPa.

q' : deviator stress, Pa.

γ_w : unit weight of water, 9.8 kN/m^3.

γ_s : unit weight of soil, kN/m^3.

γ_c : parameter equals γ_s - γ_w , kN/m^3.

S_i : solids content, %.

s : Laplace transform of time t

t : time, day.

μ : viscosity, Pa·s

v_x : subsidence rate comprises contributions from basement subsidence, m/year.

v_{gr} : sedimentation rate of the grain material, m/year.

V : specific volume

$\overline{V}$: average specific volume

visual: Subscripts - Corresponding to parameter of the visual grid

υ : Poisson's ratio

υ_{xy} : Poisson's ratio characterizing the contraction in x when tension is applied in y

u : excess pore pressure (overpressure), Pa or kPa.

X : direction in two-dimensional

Y : direction in two-dimensional

z : vertical coordinate, material coordinate in Gibson model,

Lagrangian coordinate for Terzaghi model, m.

σ : total stress or stress tensor(in 2D modelling) , Pa or kPa.

σ' : effective stress, Pa or kPa.

σ'_0 : initial effective stress, Pa or kPa.

λ : function of void ratio, for nonlinear simplification $\lambda(e) = -\frac{d}{de}(\frac{de}{d\sigma'})$, kPa^{-1}.

g : function of void ratio, for nonlinear simplification $g(e) = -\frac{k}{\gamma_w(1+e)}\frac{\partial\sigma'}{\partial e}$, m^2/d.

δ^*: upscaling coefficient

δ : parameter to characterize 'effective stress-void ratio'

ψ : sedimentation - consolidation parameter

ϕ : porosity (e/(1+e)), %.

ϕ_0 : initial porosity, %.

ε : strain tensor

λ' : loading line slope

$\overline{\sigma}$: mean effective stress in 1D modelling, Pa.

ε_v : strain induced by dp'

ε_s : strain induced by dq'

η : equals q'/p'

[2 4 6 8 10 …]: variables change according to this array

Δ : take the difference of parameter

Chapter 1 Introduction

1.1 Background of sediment consolidation

Sedimentary basins are large regions where subsidence allows major thicknesses of sediments to accumulate over tens of millions of years. Sediment consolidation is the process that reduces sediment bulk volume, mainly by vertical shortening during the progressive burial that creates the main energy source for the consolidation processes. Thus, consolidation is a ubiquitous mechanism in basin evolution. Mechanical consolidation is usually considered to be controlled by the effective stress generated by the weight of the overburden minus the pore pressure, and starts immediately after deposition. If the pore fluid is unable to escape quickly enough from the sediments during the consolidation or due to the influx of fluids from source rocks, the pore pressure may increase to levels higher than hydrostatic pressure, thus defining overpressure conditions (Swarbrick and Osborne, 1998). This pore pressure increase reduces the effective stress, thus retarding the mechanical consolidation. The rate of fluid dissipation is related to the permeability of the sediments, and this property is proportional to the degree of consolidation. Thus, consolidation and fluid flow are intimately linked in the fashion of a coupled feedback.

Many sedimentary strata are characterized to have elevated pore fluid pressures that are much greater than the hydrostatic pressures and therefore said to be over-pressured. The presence of over-pressured fluids in strata may represent a major hazard for the safety of drilling and hydrocarbon production at the present time. It can also influence fluid flow in basins strongly, altering hydrocarbon generation conditions and their migration (Bethke, 1985). Several mechanisms have been proposed for generating overpressures in sedimentary basins, including disequilibrium compaction (Bethke, 1986; Shi and Wang, 1986), tectonic collision (Ge and Garven, 1992), aqua-thermal expansion (Sharp, 1983), clay dehydration (Burst, 1969), gravity flow (Lee and Bethke, 1994; Wolf and Lee, 2005), gas capillary seals and hydrocarbon generation (Lee and Williams, 2000; Luo and Vasseur, 1996). Many of these mechanisms can only be important in the deeper parts of basins.

In fine-grained sediments deformations related to mechanical processes are dominant in the very first kilometres of depth (Hedberg, 1936; Maltman, 1994). At greater depths and temperatures, chemically modified consolidation becomes an important porosity reducing process (Bjørlykke, 1998; Bjørlykke, 1999; Bjørlykke et al., 1989; Schmid and Mcdonald,

1979). Focusing on shallow compaction only (<1000m), this research deals solely with mechanical deformations and associated water flows, and disregards other effects because pure mechanical/hydraulic phenomena prevail in the uppermost layers of basins.

During the compaction of sediment, the vertical strain of a volume of sediments is often much more significant than the lateral strain, and is therefore mainly responsible for its volumetric and hence porosity reductions. Void ratio (e) or porosity ($\phi=e/(1+e)$) is often taken as a proxy indicator of the vertical/oedometric strains to define empirical compaction relationships/trends with the effective stress or depth, and many such trends have been published in the literature based on oedometric-types of experiments on natural deposits. Linear trends have been considered by some authors to be appropriate for deposits in restricted depth intervals (Galloway, 1984; Ramm and Bjørlykke, 1994). However, a linear trend does not conform to the actual and hence exponential consolidation trends are therefore frequently used to describe porosities in mudstones and sandstones (Sclater and Christie, 1980).

Both data from natural consolidation studies and experimental work show that many mudstones have initial porosities of about 70 - 80%, which are rapidly reduced during early burial, while sandstones have lower initial porosities of 45 - 50% and retain higher porosities during the initial stages of burial, as shown in **Figure 1.1** (Chuhan et al., 2002; Mondol et al., 2007; Potter et al., 2005).

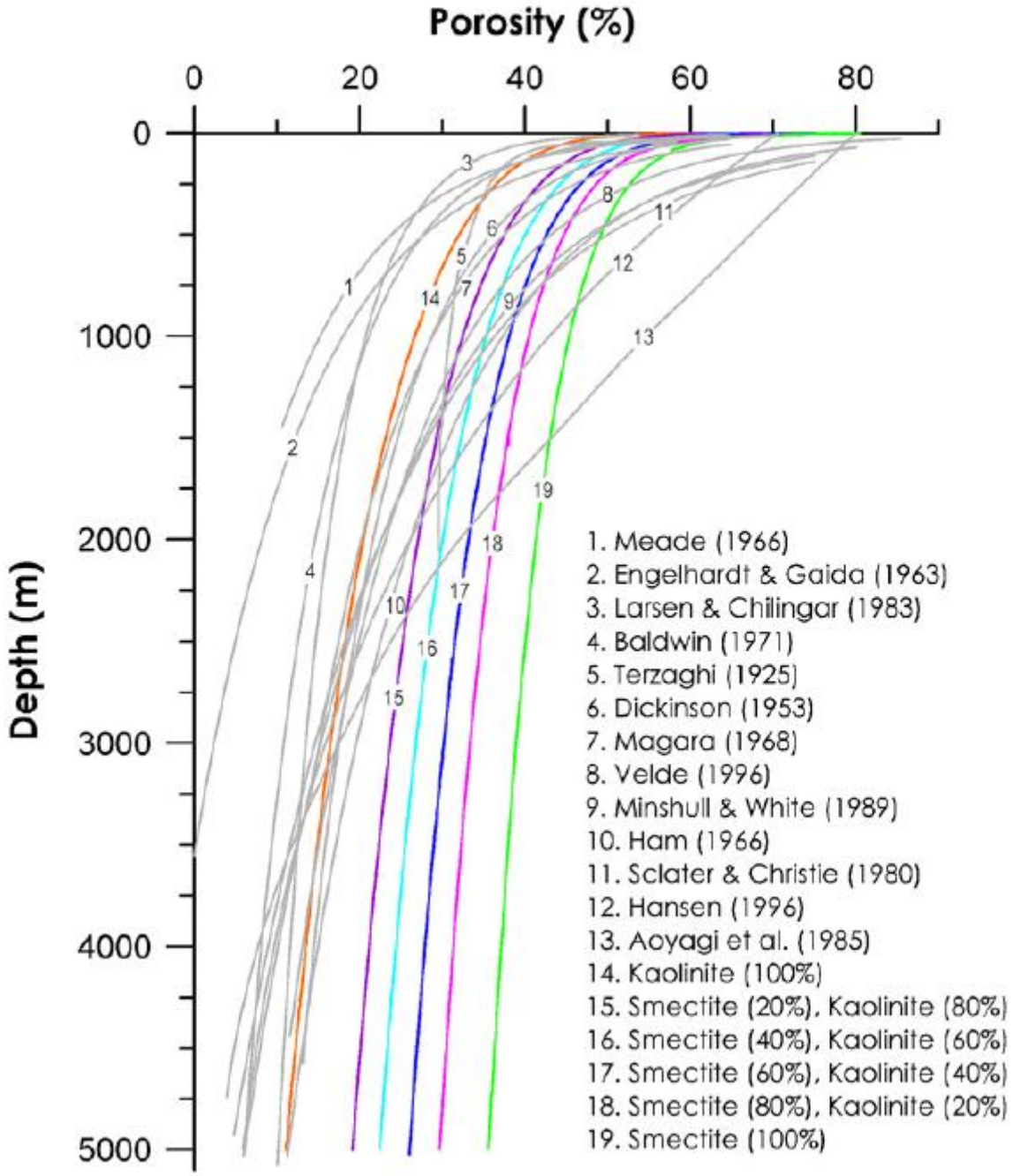

Figure 1.1 A comparison of published porosity–depth trends for shales and argillaceous sediments (gray curves) and experimentally compacted curves of brine-saturated smectite, kaolinite and their mixtures (colour curves), (Mondol et al., 2007)

A compilation of published porosity/depth curves for argillaceous sediments clearly demonstrates the wide range of possible porosities found for shales and mudstones at the same burial depth. Some of this variability can be explained as a lithological dependence (Yang et al., 1995). The rapid loss of porosity during shallow burial that is evident in many

of the published curves is due to an open sediment framework that consists mainly of clay mineral platelets, and the accumulated aggregates of platelets in newly-deposited mudstones. This open structure can relatively easily collapse during the initial stages of burial, causing a rapid early porosity reduction. This statement translates into mechanical terms as saying that high-porosity muddy sediments have low mechanical strength with plastic deformation occurring via a compactional volumetric-strain mode. Experimental consolidation studies of clay mineral aggregates have shown that they may lose more than 50% of their total porosity at effective stresses less than 1MPa or depths shallower than 100 metres (Marcussen, 2009; Mondol et al., 2007).

Despite the variations in consolidation trends, some curves have been adopted as standard consolidation curves for many basin analyses purposes. Giles (1997) analysed several of the published porosity/depth for sandstones and mudstones and came up with average consolidation curves for different lithologies. Such analysis may be used in areas with a small amount of data, but possible deviations of the true one from the standard consolidation curve need to be kept in mind. Yang and Aplin introduced a lithology parameter, the clay fraction, to account for much of the variability (Yang and Aplin, 2004; Yang and Aplin, 2007; Yang and Aplin, 2010).

In addition to 1D consolidation, there are other processes that happen during basin evolution, including slope-related deformations, such as mass transport processes, tectonic shortening or elongation, and the potential for lateral fluid flow etc. Under the otherwise-similar hydrodynamic and mechanical situations, consolidation will be affected by these geological processes, which are not convenient or appropriate for a 1D model to consider.

1.2 Consolidation theory

The consideration of soft soil consolidation can be traced to the work of Terzaghi in the early 1920's, who developed a linear soil consolidation theory and later an infinitesimal-strain consolidation theory (Terzaghi, 1943). The limitation placed by the assumption of small-strain theory was resolved by the development of a 1D nonlinear large-strain model by Gibson et al (1967), where primary consolidation of homogeneous layers was modelled with realistic finite strains. Further work by Gibson et al (1981) and Lee & Sills (1981) showed that a nonlinear model could be successfully applied to real mud samples (i.e. non-homogeneous layers) under self-weight loads.

The history of basin modelling development is characterized by a gradual progress from elastic to elastic-plastic, from one dimensional to multi-dimensional. Besides the Terzaghi and Gibson models, there are some similar models adopted in basin modelling. Athy proposed a phenomenological law describing the exponential decrease of porosity with increasing burial depth (Athy, 1930). Rubbey and Hubert, and Smith took into account the effect of overpressures on compaction, where porosity was a function of vertical effective stress (Rubey and Hubbert, 1959; Smith, 1971). The generalised Athy's law is now often used to study basin data (Hart et al., 1995; Luo and Vasseur, 1992; Ulisses et al., 1994; Wangen, 1992). Shi and Wang, and Schneider et al improved this law by taking into account an elastoplastic behaviour, they also pointed out that the soil consolidation equation and the generalised Athy's law provided similar compaction curves on a range of vertical effective stress up to 50 MPa (Schneider et al., 1996; Shi and Wang, 1986). For modelling compaction of sediments, Audet proposed to use a soil consolidation equation from the theory of soil mechanics (Audet, 1996). Jones and Addis claimed the interest of the critical state theory from the theory of soil mechanics for modelling compaction (Jones and Addis, 1985). However, these constitutive models apply only to vertical dimensional, without horizontal deformation and explicit stress tensor.

Although both small-strain and large-strain models are adopted for basin modelling of deep and shallow consolidation processes, respectively, when horizontal deformation is equally important, a 2/3D more general model is needed. A Modified Cam Clay model, which was proposed by Roscoe and Burland (Roscoe and Burland, 1968), and described and studied systematically by Muir Wood (Muir Wood, 1990), has found its way into basin modelling given its capability of capturing the stress-strain relationships for fine-grained sediments (Djeran Maigre and Gasc Barbier, 2000; Luo et al., 1998; Pouya et al., 1998).

Djeran Maigre and Gasc Barbier (2000) applied the modified Cam Clay model in numerical basin modelling with parameters obtained by experiments. The specially-designed oedometric cell permits the experiments of compacting samples with effective stresses ranging from 0.1 to 50MPa, representing the in-situ states of natural clays down to 2 or 3 kilometres in depth.

It is worth noting that the consolidation theories and models have been developed in the continuum framework without considering the movement of individual particles or its interaction with pore fluids explicitly. Particle scale studies might provide additional insights.

1.3 Motivation and objectives

Consolidation models used in basin modelling can be divided into two categories depending on whether deformation is approximated by small-strain or large-strain deformations. To date, small-strain consolidation models are adopted for basin modelling of sediment consolidation deep in a basin. Small-strain models can simulate deep consolidation where small-strain increments occur. However, it cannot represent large-strain shallow consolidation directly and may lead to big errors as shown in this thesis. Instead of using small-strain model directly, small-strain model can be extended to simulate some large-strain problems by meshes and property updating, that is finding an equivalent approach. Comprehensive comparisons among large-strain, small-strain and updating-small strain models can provide a basis for model selection in basin modelling. Confronted with the above-mentioned problems, a large-strain shallow basin compaction simulator is necessary for addressing the specific issues at shallow depth. It should not only represent the properties of shallow compaction, but also do so with high computational efficiency.

It is therefore not only desirable but also necessary to give a full account into the natures of large-strain, small-strain and modified small-strain models through an analysis and comparison of them and to provide a basis for model selection for basin modelling. To this end, in this thesis several 1D models have been developed and implemented, and from this a computationally efficient 1D large-strain consolidation simulator has been developed capable of addressing the specific compaction issues at the shallow depth for practical use.

However some processes challenge the validity of the 1D method and multi-dimensional methods are necessary. Besides sedimentation and consolidation, other geological processes exist and play significant roles in basin evolution, such as horizontal tectonic activity, lateral flow of fluid and mass transport deposition. Given that none of current commercial basin simulators sufficiently considers the situation where the stress is at non-equilibrium in horizontal directions, it is therefore imperative to introduce a 2D fluid-structure interaction model to assess the impacts of not considering it and to provide a set of evaluation criteria to judge whether a compaction model is sufficient or not under the situation.

A typical basin covers 100s kilometres square areally and several kilometres in depth and evolves over 10s to 100s Ma. A basin simulator models the evolution of a basin from its genesis and major events in a chronical order following physicochemical principles. The nature of major events is determined from supporting geological and geochemical data and

relevant models. Heterogeneous fine-grained sediments undergoing shallow burial below the seafloor experience large-strain mechanical compaction, and sometimes a medium or large degree of overpressure in their pore space as a result of disequilibrium dissipation of pore fluid. However, basin modelling ignores the small-scale heterogeneity of sediments, the large-strain deformation and fluid flow conditions that occur at smaller length- and/or time-scales than those at basin scales. These discrepancies can lead to incorrect prediction of shallow compaction and overpressure, and subsequently basin evolution.

In basin-scale modelling, the basin domain is discretised into blocks, and the evolutionary processes are divided into time steps. Regardless of what the numerical approach method is, high precision simulation results require small enough time steps and meshes sizes. These requirements add cost (computational time and facility request) and complexity, so the usual approach is to use coarse cells and large time steps, which introduces errors that may not be fully known or appreciated by all users.

Typically, the time steps are set to be thousands or millions of years in basin modelling. The properties are held constant during each time step, which is a relative long time. This may exert little effect on deep consolidation where the block properties have small changes over a long-time period. However, this may not be suitable for shallow consolidation where the block properties are strongly nonlinear and change substantially during each time step interval.

In the discretised blocks, whose sizes may be kilometres laterally and hundreds of meters vertically, each block is assumed to behave according to a single (homogeneous) consolidation and flow relationship, even though we know that the sediments are heterogeneous. Therefore, the effects of intra-block sediment heterogeneity must be taken into account by upscaling either formally or informally.

Consolidation may evolve along quite different paths with and without consideration of the two effects mentioned above. Errors occur because of large meshes size and time steps, and their effects need to be quantified.

In view of simulation cost, the effects of intra-block and time-interval heterogeneity must be taken into account by upscaling. If the upscaling methods can be adopted in the basin modelling workflow, equivalent consolation state at any time could be obtained without a need to explicitly model intra-block/time-interval changes.

Despite variations in consolidation trends, some curves have been adopted as standard consolidation curves in many basin analyses. However, the standard curves are not scrutinized through upscaling. Moreover, average or weighted-average upscaling might not be able to represent properties of the multi-layer systems under some circumstances. More research on upscaling properties of multi-layer systems is needed to derive guidance that is broadly applicable.

Consolidation characteristics of layered systems and subsequently upscaling should be analysed. Comparison between this analysis and standard curves or average upscaling can provide basis for selection of upscaling methods in basin modelling.

This research aims to fully consider these drawbacks, and derive an accurate picture of overpressure formation and basin evolution. In detail, the following research areas are addressed in chapters that examine simulation and upscaling first in 1D and then in 2D.

1.4 Concept of research

Firstly, several 1D consolidation models are compared for shallow compaction. A correct consolidation model is selected based on shallow compaction, which is verified with analytical solutions and experimental data. Upscaling and application are then carried out. Secondly, a similar research procedure is expanded into 2D, where an existing simulation tool is used here. The study workflow is shown as follows:

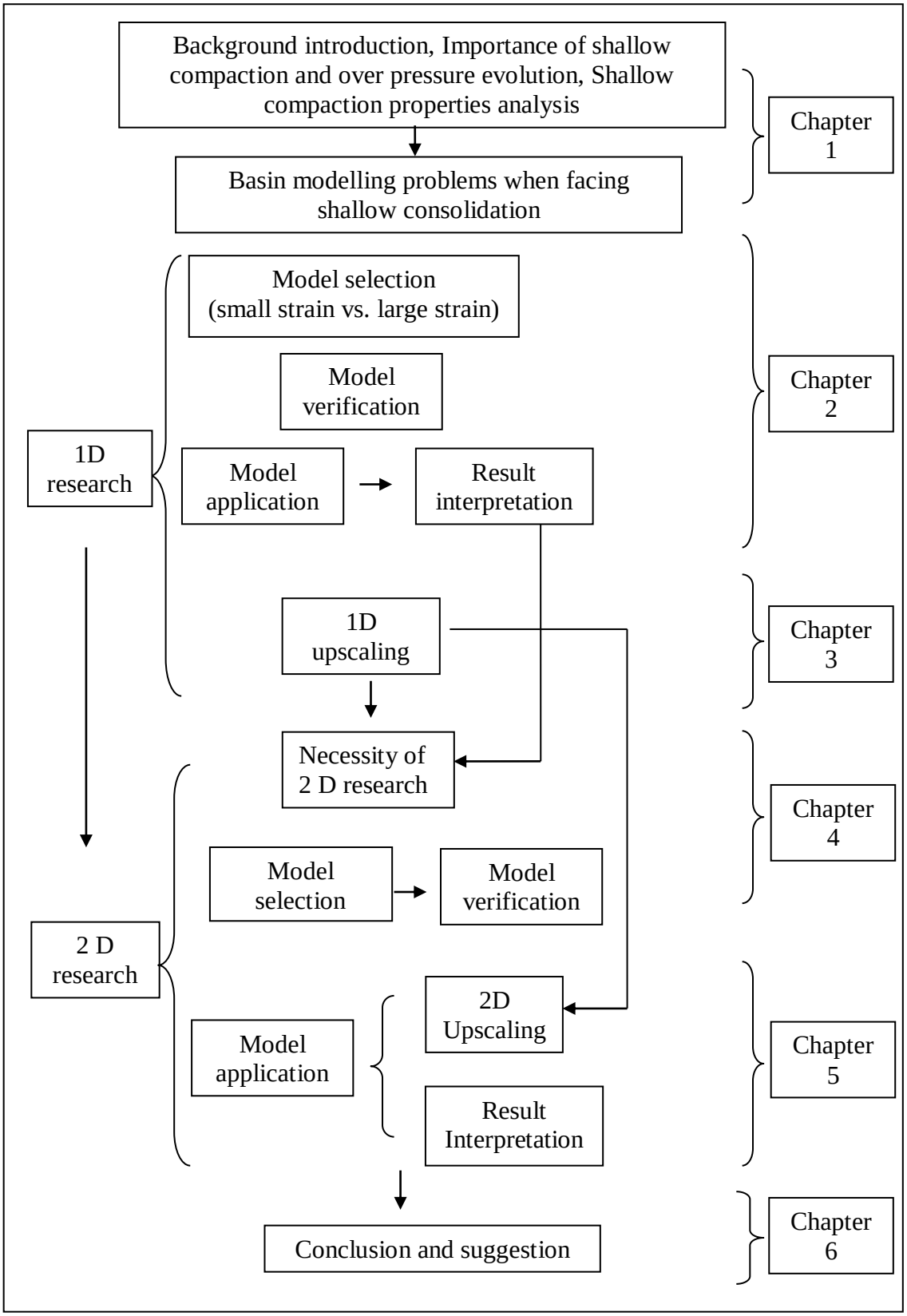

Figure 1.2 Research work flow

1.5 Outline of the thesis

This thesis is structured as follows:

Chapter 2 provides a brief comparison of consolidation theories. One of large-strain models is further developed into basin modelling simulator. The advantages of the large-strain model to small-strain model are also shown. The model is applied to the Ursa Region, Gulf of Mexico. However, overpressure is overestimated, hence the possible reasons and limitations of 1D model is further discussed thereafter.

Chapter 3 studies the upscaling methods and upscaled properties of multi-layer systems in 1D. Multi-layer upscaling consolidation properties are studied both analytically and numerically. Based on the 1D model, a back-stepping based the upscaling method is also developed for large-strain consolidation and applied in upscaling.

Chapter 4 shows a description of Modified Cam Clay model and its verification. The Modified Cam Clay model is adopted for modelling 2D compaction of clay-rich sediments and applied to basin modelling.

Chapter 5 proposes the upscaling method for Modified Cam Clay.

Chapter 6 concludes by summarizing the thesis, including its major findings and its possible contributions to industry. The outlines for the future work are also listed.

Chapter 2 One dimensional large-strain shallow compaction simulator development and verification

As previously mentioned, a large-strain basin simulator is necessary for shallow compaction. With this purpose, a brief comparison of three consolidation theories that are widely used in basin modelling is provided firstly in this chapter.

Several 1D small-strain and large-strain consolidation models are extended and implementated numerically. It is shown that the small-strain consolidation models can capture the compaction behaviour of sediments buried deeply in a basin where they generally undergo small-strain deformations vertically. However they cannot capture the behaviours of fine-grained sediments at shallow burials undergoing large-strain deformations without being modified. By using property updating, the small-strain models can simulate some large-strain problems with the added cost and complexity of undertaking the updating process. As to shallow compaction, there is no need to consider the fluid compressibility, and hence Gibson model is proved to be reasonable simple, as shown in section **2.4**.

Hence the large-strain Gibson model is further developed into a basin modelling simulator, and that simulator can be applied to complex geological processes in which the behaviours of the shallow compaction of fine-grained sediments, under complex loading and unloading conditions, are of concern. All related models are verified with published experimental data from section **2.1** to **2.3**. The advantages of the large-strain model compared with updating small-strain model are shown in section **2.4**. The limitation of 1D model is further discussed thereafter in section **2.5**, where the multi-dimensional simulation is encouraged.

In section **2.6**, the model is applied to an actual basin example. However, the 1D large-strain model is shown to over predict the pressure of the Ursa Region, Gulf of Mexico when using material properties estimated from the Integrated Ocean Drilling Program (IODP). The failure of the 1D approach may be due to horizontal fluid flow, loading from mass transport depositional processes, or non-oedometric horizontal strains.

2.1 Comparison of consolidation models

In order to describe the basin evolution and to solve the above-mentioned problems mathematically, a large-strain shallow basin compaction simulator is necessary. In this section, three consolidation theories that are widely used in basin modelling are compared.

As mentioned, the main mechanism involved is saturated soil consolidation. When saturated soil is loaded in an undrained condition, pore pressure increases. Then, the excess pore pressures dissipate and water leaves the soil, resulting in consolidation settlement and effective stress (borne by soil skeleton) increases. These processes do not happen instantly, but time-consuming processes subject to the seepage mechanism. The rate of settlement decreases over time because each new increment of settlement occurs under conditions where the fluid energy has already been decreased, and the flow rates are smaller due to that and to the decreased permeability. Different theories have been proposed for this consolidation process, among them the representative Terzaghi's (1929), Gibson et al's (1967) and Domenico & Schwartz's (1991) are compared. Moreover, these well known theories have all been utilized in basin modelling. Different theories do make certain assumptions about the responses of soils to a load, which will be discussed as follows.

The first one is Terzaghi's small-strain consolidation theory.

Terzaghi put forward a consolidation theory under the following assumptions (Terzaghi, 1929; Terzaghi, 1943).

(1) The soil is homogenous.
(2) The soil is fully saturated.
(3) The solid particles and water are incompressible.
(4) Soil compression and flow are one-dimensional
(5) Strains in the soil are relatively small.
(6) Darcy's Law is valid for all hydraulic gradients.
(7) The coefficient of permeability and the coefficient of volume compressibility remain constant throughout the process.
(8) There is a unique relationship, independent of time, between the void ratio and effective stress

Terzaghi's theory of one-dimensional consolidation states that all quantifiable changes in the stress of a soil (compression, deformation, shear resistance) are a direct result of changes in effective stress. The effective stress σ' is related to total stress σ and the pore pressure p by the following relationship:

$$\sigma = \sigma' + p \tag{2.1}$$

Overpressure dissipation is described by the following equation.

$$C_{\mathrm{v}} \frac{\partial^2 u}{\partial z^2} = \frac{\partial u}{\partial t} \tag{2.2}$$

$$C_{\mathrm{v}} = \frac{kE_s}{\gamma_w} \tag{2.3}$$

Where, C_{v} is coefficient of consolidation, E_s is modulus of compressibility, k is hydraulic conductivity, γ_w is unit weight of water, u is excess pore pressure.

Gibson et al. developed a large-strain consolidation theory (Gibson et al., 1967).

The basic assumptions of this theory are more general than small-strain theory in (3), (5) and (7) of Terzaghi's assumptions. The limitation of small strains has not been imposed. The soil compressibility and permeability are allowed to vary with void ratio during consolidation. These assumptions are closer to the actual behaviors of sediments. The Gibson's large-strain model is defined mathematically as follows:

$$-\frac{1}{1+e_0}\frac{\partial e}{\partial t} + (\frac{\gamma_{\mathrm{s}}}{\gamma_{\mathrm{w}}} - 1)\frac{d}{de}[\frac{k}{1+e}]\frac{\partial e}{\partial z} + \frac{\partial}{\partial z}[-\frac{k(1+e_0)}{\gamma_{\mathrm{w}}(1+e)}\frac{d\sigma'}{de}\frac{\partial e}{\partial z}] = 0 \tag{2.4}$$

Where, e is void ratio, e_0 is initial void ratio, k is hydraulic conductivity, γ_w and γ_s is unit weight of water and soil, z is solid coordinate, σ' is effective stress.

The third model, proposed by Domenico and Schwartz, is a large-strain consolidation theory on fluid pressures in deforming porous rocks (Domenico and Schwartz, 1991). The basic assumptions underlying the concept of compaction disequilibrium of Domenico and Schwartz's model are:

(1) Darcy flow in the porous sediment.
(2) Terzaghi's principle of effective stress.
(3) A constitutive law for the rock frame that provides a monotonic relationship between effective stress and strain, often in the form of a porosity - effective stress relationship.

In compaction disequilibrium models, the above three assumptions are combined with mass conservation of the solid and fluid phase. When the grain material is assumed incompressible, conservation of the fluid phase in a control volume of porous rock (Lagrangian reference frame attached to the grain material) can be expressed as follows (Domenico and Schwartz, 1991).

$$\phi\beta_{fl}\frac{\partial p_{fl}}{\partial t}-\beta_p\frac{\partial\sigma'}{\partial t}=\nabla(\frac{k}{\mu}\nabla p_{ex}) \tag{2.5}$$

Where, β_{fl} is fluid compressibility, β_p is drained rock/soil compressibility, p_{ex} is effective fluid pressure, p_{fl} is actual fluid pressure

The parameters of these models can be obtained through oedometric test. Comparison of these three models is shown in **Table 2.1**.

Model	Compressibility	Strain	Conductivity vs. void ratio	Void ratio vs. effective stress
Terzaghi	Fluid is incompressible soil skeleton is compressible	small	Conductivity is constant	linear relation
Gibson	fluid is incompressible soil skeleton is compressible	large	Conductivity varies with void ratio	nonlinear relation
Domenico and Schwartz	fluid is compressible soil skeleton is compressible	large	Conductivity varies with void ratio	nonlinear relation

Table 2.1 Comparison of different consolidation theories

In basin modelling the Terzaghi consolidation theory is normally used (Kauerauf and Hantschel, 2009; Wangen, 2010). It is simple, easy to use, and precise enough under certain conditions, such as deep basin modelling where small-strain deformation dominates. Gibson's equation is widely used in shallow rock-soil large-strain consolidation modelling. The Domenico and Schwartz theory take into account water compressibility, but it is a very small factor in shallow compaction.

By combining piecewise linear approximation, mesh updating, time- and space-step, the Terzaghi model has been successfully applied in large-strain consolidation problems (Fox and Berles, 1997). However, the large-strain model still has its own advantages, which will be illustrated in **Chapter 2.4**.

Domenico and Schwartz's model is also used in basin modelling. The main advance of Domenico and Schwartz's model to Gibson model is the consideration of fluid compressibility. This general geological model is often used in geological simulation processes from shallow to deep. As described, this research is constrained to shallow compaction (<1000m), hence fluid compressibility can be ignored, as shown in **Chapter 2.3.2.3.** In particular, the fluid is water in basin modelling of shallow compaction.

2.2 Model development for multi-layered soil

In consideration of the research object, i.e. shallow compaction, the Gibson consolidation model is adopted here, with the variable of void ratio in the calculation. There are no improvements on Gibson's constitutive equations in this research. Based on Gibson model, different phenomena that exist in the basin evolution can be simulated through numerical treatment. Such as basin is discretized into meshes, a continuous deposition process is divided into multi-segment processes, in which grids corresponding to the depth of new deposition are added. A numerical computation, using fully implicit finite difference discretization, with a Newton iterative solver, is performed to solve Gibson's equation for the void ratio distribution, and subsequently the stress distribution and pore pressure in sediment layers. The code is written in Matlab and described in Appendix A1 – A4 corresponding to four different situations commonly seen in basin modelling.

The real need is to pay special attention to the case of multi-layer calculation. When it comes to the multi-layer system, based on the continuity of effective stress, pore pressure and flow balance, the following method is taken.

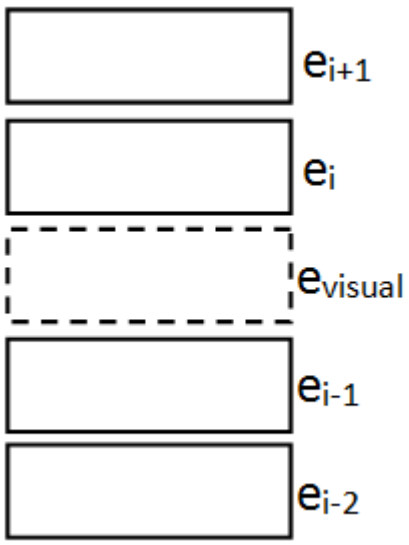

Figure 2.1 Computational elements of two different layers and a visual grid between them

As shown in **Figure 2.1**, a visual grid (nonexistent) is added between two different layers, that is e_{visual}. This will overcome the error of average induced by direct finite difference method.

According to Darcy flow in material coordinate system, flow balance equation is:

$$\frac{k_i(e)}{1+e_i}\frac{\partial u_i}{\partial z} = \frac{k_{i-1}(e)}{1+e_{i-1}}\frac{\partial u_{i-1}}{\partial z} \tag{2.6}$$

Where $k_i(e)$ means productivity is function of void ratio, u is overpressure, z is material coordinate. According to principle of effective stress in material coordinate system, the variation of pore pressure and effective stress follow **Equation 2.7**.

$$\frac{\partial u}{\partial z} + \frac{\partial \sigma'}{\partial z} = \gamma_w - \gamma_s = \gamma_c \tag{2.7}$$

Where γ_w and γ_s are unit weight of water and soil. After discretizing the partial differential terms using these two equations, one has:

$$\frac{k_{i-1}}{1+e_{i-1}}(\gamma_c - \frac{\sigma'_{visual} - \sigma'_{i-1}}{dz}) = \frac{k_i}{1+e_i}(r_c - \frac{\sigma'_i - \sigma'_{visual}}{dz}) \tag{2.8}$$

That means

$$\sigma'_{visual} = f(\sigma'_{i-1}, \sigma'_i) \tag{2.9}$$

With this visual effective stress, the void ratios of the interface can be determined with relationships of 'void ratio – effective stress'. Then equations with variable of void ratio only can be solved using the fully implicit finite Newton iteration method.

As for the sedimentation process, a continuous deposition process is divided into multi-segment processes, in which grids corresponding to the depth of new deposition are added.

In shallow compaction, there are self-consolidation, consolidation with surcharge (additional dead load at the top of the model domain), unloading or rebound, sudden loading, transition of sedimentation–consolidation. Moreover, there are different types of constitutive equations for 'void ratio - effective stress (e - σ')' and 'conductivity - void ratio (k - e)', such as creep deformation, layered effect of conductivity. This large-strain consolidation model is developed to fully consider these phenomena.

Based on the above mentioned setting, a large-strain shallow compaction simulator is developed.

2.3 Model verification

The developed simulator is verified with analytical solutions and experimental data in this section.

2.3.1 Verification with analytical results

The correctness of this implementation is proved by comparison with analytical results for self-consolidation, consolidation under surcharge and rebound. When it comes to the large-strain analysis, most of analytical models assume a simplified relationship between void ratio and effective stress and/or conductivity and void ratio.

In this research, a cross section map for all 1D consolidation models used are shown as illustrated generically in **Figure 2.2**. In **Figure 2.2** (a), a surcharge (additional dead load at the top of the model domain) may be applied on the top of the sediment with an initial thickness H. The horizontal width is infinite. The top(T) and bottom(B) boundaries may be permeable(P) or impermeable(I), and they may be marked, for example, as PTIB (permeable top and impermeable bottom) and PTPB (permeable top and permeable bottom). There may be a certain depth of water on the top of the sediment, corresponding to the sea water depth of the sedimentary basin. The sediment undergoes consolidation processes, in which water will flow out from the top and/or bottom boundaries only and sediment thickness will decrease. **Figure 2.2** (b) shows a typical consolidation curve – the consolidation degree versus the time. The consolidation degree can be defined as the ratio of the settlement at time t to the final settlement. A consolidation curve captures sediment consolidation characteristics.

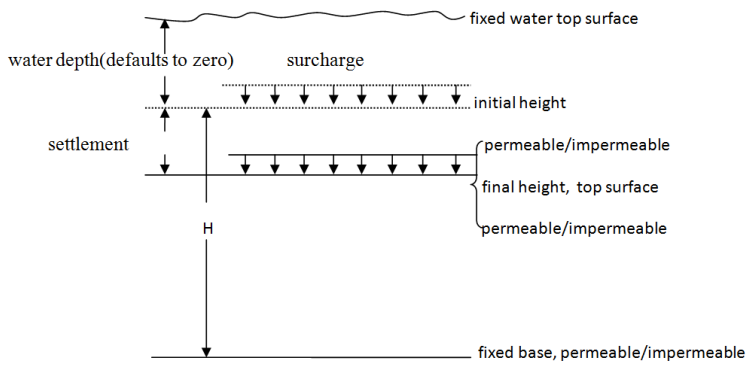

(a)

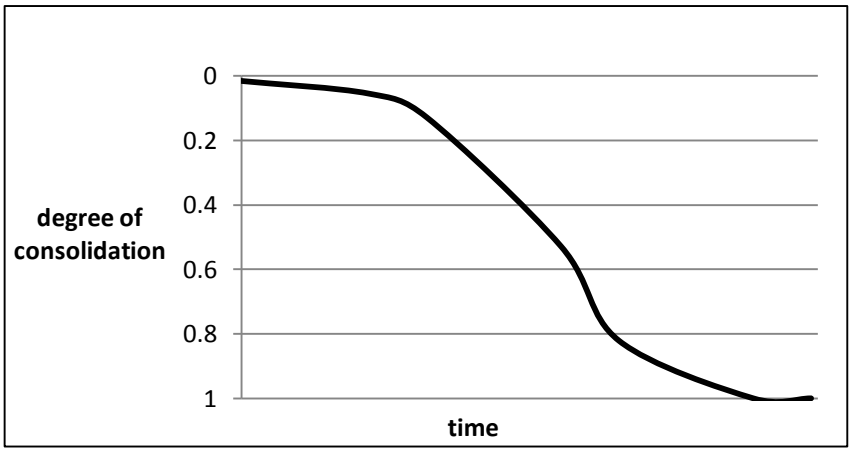

(b)

Figure 2.2 Consolidation model illustration, (a) consolidation boundary condition, (b) consolidation curve - consolidation degree changes with time.

Possible scenarios in basin evolution include self-consolidation, consolidation under surcharge and rebound under PTIB/PTPB. The developed model is verified against analytical result for all scenarios.

2.3.1.1 Verification against Morris's analytical solutions for self-consolidation

Morris obtained analytical solutions for Gibson's equation (**Equation 2.4**) for soil whose conductivity and compressibility obey certain relationships (Morris, 2002). Here the numerical results of the implemented 1D large-strain consolidation simulator are compared with the analytical solutions under both PTIB and PTPB conditions and they are found to be precise.

Gibson's equation can be re-written into a simpler form as shown in **Equation 2.12** by introducing two functions of **Equation 2.10** and **2.11** (Gibson et al., 1981)**.** In this simplified form, even constant λ and g can still preserve the essential nonlinearity of the 'conductivity - void ratio' and 'void ratio - effective stress'. The assumption that λ and g are constant is valid only over limited ranges of effective stress and void ratio.

$$g(e) = -\frac{k}{\gamma_w (1+e)} \frac{\partial \sigma'}{\partial e} \tag{2.10}$$

$$\lambda(e) = -\frac{d}{de}\left(\frac{de}{d\sigma'}\right) \tag{2.11}$$

$$\frac{\partial^2 e}{\partial z^2} + \lambda(\gamma_s - \gamma_w)\frac{\partial e}{\partial z} = \frac{1}{g}\frac{\partial e}{\partial t} \tag{2.12}$$

Combining equations above with the following assumption of **Equation 2.13**, Morris derived the analytical solution for self-weight large-strain consolidation.

$$e = (e_0 - e_\infty)\exp(-\lambda\sigma') + e_\infty \tag{2.13}$$

To make comparisons the following parameters and relationships are chosen as shown in **Table 2.2**, and the numerical results are plotted against Morris's analytical solutions with the PTIB and PTPB conditions in **Figure 2.3** and **Figure 2.4**, respectively. Note that the x-axis has been normalised into a dimensionless T defined as gt/h, where h is the sediment thickness in corresponding material coordinate.

Parameter	Value	Units
unit weight of water / γ_w	9.800	kN/m^3
unit weight of soil / γ_s	27.636	kN/m^3
initial thickness / H	0.4136	m
initial void ratio/ e_0	8.872	-
void ratio under Infinite stress / e_∞	6.334	-
λ	13.39	kPa^{-1}
g	1.6×10^{-5}	m^2/d
conductivity - void ratio/ $k-e$	$k = 0.0021(1+e)(e-6.334)$	m/d(k)
effective stress - void ratio/ $\sigma'-e$	$e = 2.538\exp(-13.39\sigma') + 6.334$	kPa(σ')
Gravity/ g_{ra}	9.800	$m\cdot s^{-2}$

Table 2.2 Parameters utilized in Morris' model

PTIB comparison:

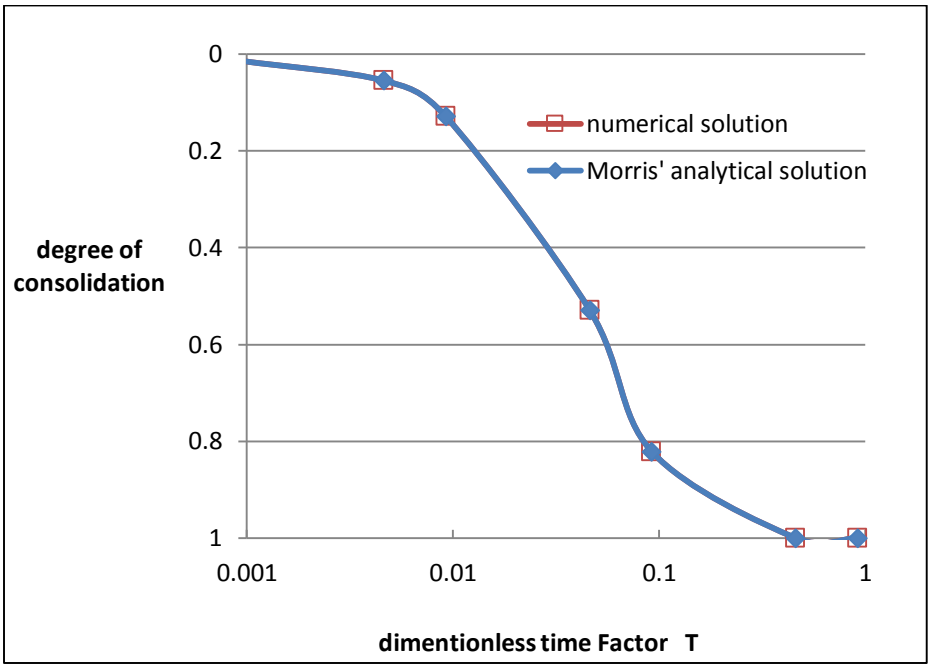

Figure 2.3 PTIB consolidation curve results for comparison with Morris' model

PTPB comparison:

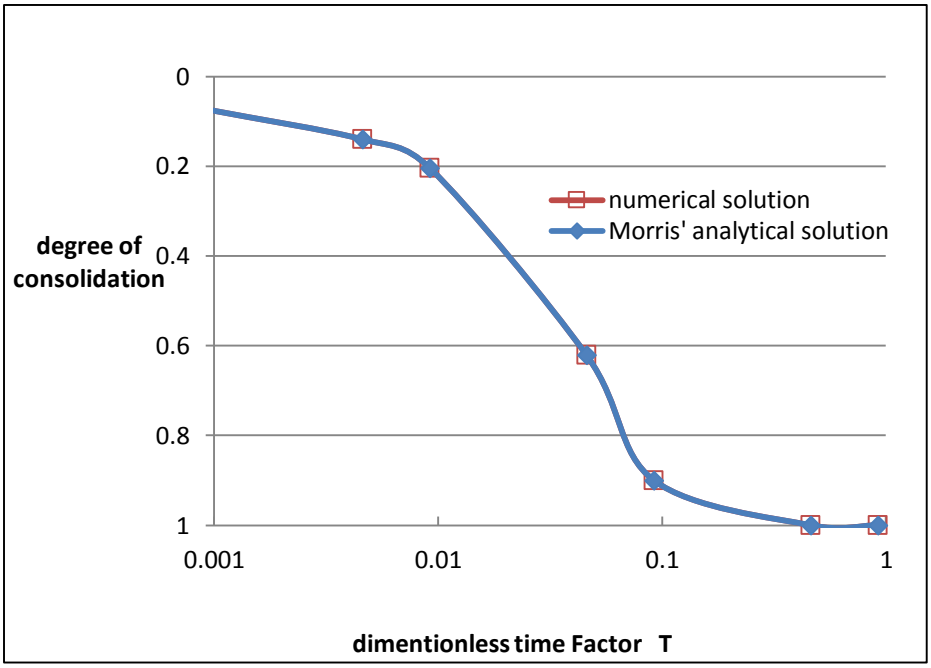

Figure 2.4 PTPB consolidation curve results for comparison with Morris' model

2.3.1.2 Verification against Xie and Leo's analytical solutions for consolidation with surcharge

Xie and Leo obtained analytical results for the large-strain consolidation with a surcharge on the top surface of sediment (Xie and Leo, 2004). The volume compressibility coefficient of the soil skeleton m_{vl} is constant during consolidation as shown in **Equation 2.14**. '$k-e$' relationship are defined in **Equation 2.15.**

$$-\frac{1}{1+e}\frac{de}{d\sigma'}=m_{vl} \tag{2.14}$$

$$(\frac{1+e}{1+e_0})^2=\frac{k}{k_0} \tag{2.15}$$

Under this condition the relationship between void ratio and the excess pore water pressure has been shown by the author as shown in **Equation 2.16**. Note that q_u is the surcharge load applied to the top of the soil at t = 0 and that same load is maintained thereafter.

$$\frac{1+e}{1+e_0}=\exp(-m_{vl}(q_u-u)) \tag{2.16}$$

Table 2.3 shows the parameters and values taken for making comparisons.

Parameter	Value	Units
unit weight of soil / γ_s	27.5	kN/m^3
initial thickness / H	10.0	m
e_0	3.0	-
m_{vl}	4.0	mPa^{-1}
k_0	10^{-9}	m/s
initial effective stress	10.0	kPa
load increment/ q_u	100.0	kPa
water level above the initial top surface of the layer	1.0	m

Table 2.3 Parameters utilized in Xie's model.

Numerical simulations are run with the parameter values given in the table under both PTIB and PTPB conditions, and their results are plotted against Xie and Leo's analytical solutions in **Figure 2.5** and **Figure 2.6**, respectively. It is clear that they agree each other well.

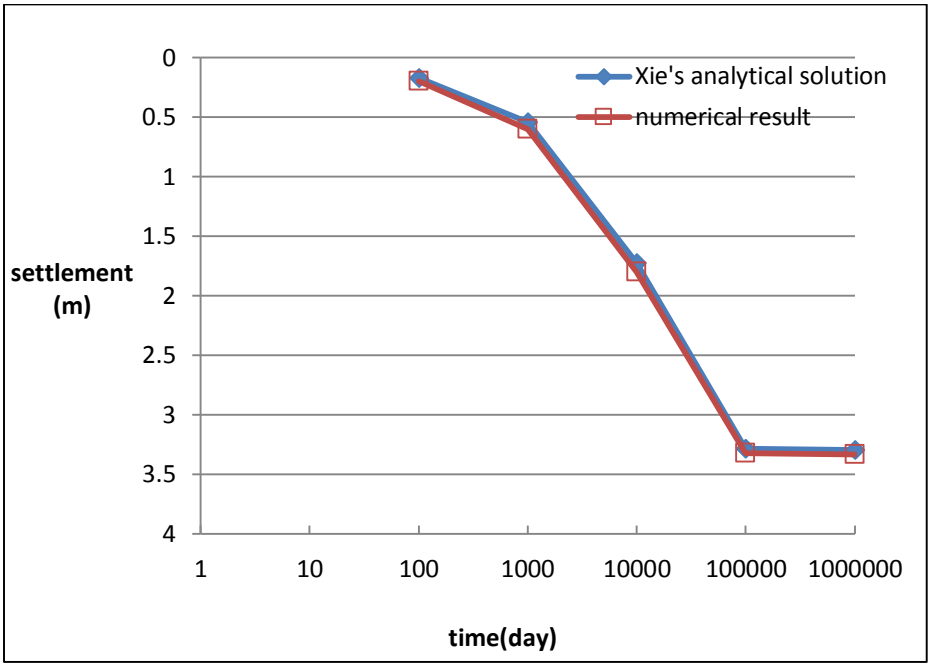

Figure 2.5 PTIB settlement results for comparison with Xie' model

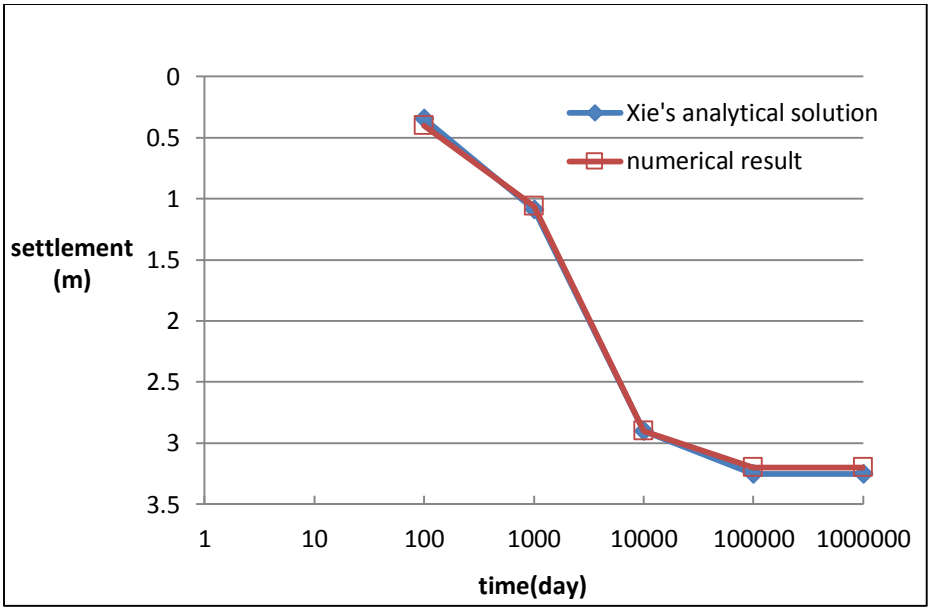

Figure 2.6 PTPB settlement results for comparison with Xie' model

2.3.1.3 Verification for cyclic stress loading

It is common to see loading, unloading and cyclic loading of stress in basin evolution. Under the same assumption with Morris, Cai et al obtained analytical solutions for cyclic loadings (Cai et al., 2007).

The soil is subjected to cyclic stress loading changes, which are illustrated in **Figure 2.7**. When saturated soil is loaded, the effective stress at every point increases and the soil is compressed, but this process is not completely reversible after the soil is unloaded as illustrated in **Figure 2.8**.

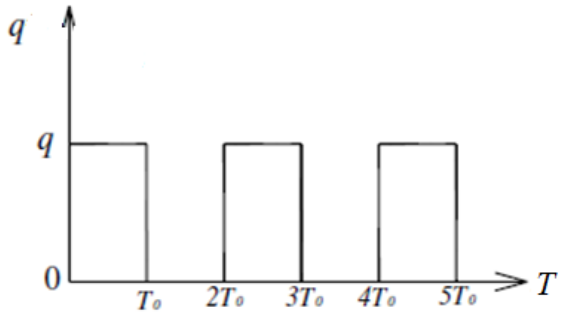

Figure 2.7 Surcharge vs. time relationships

As shown in **Figure 2.8**, when the soil is loaded to a certain effective stress point (C for example), the void ratio decreases with increase of the effective stress along a path from A to C (according to λ_1), λ_1 and λ_2 stand for the relationship between effective stress and void ratio as defined as **Equation 2.11**. When the load is removed the void ratio increases with decrease of the effective stress along a path from C to D (according to λ_2). **Table 2.4** lists the values of all model parameters used for calculations.

Parameter	Value	Units
unit weight of soil / γ_s	27.636	kN/m^3
initial thickness / H	0.540	m
initial effective stress	0.100	kPa
conductivity - void ratio/ $k-e$	$0.00158(1+e)(e-6.334)$	m/d(k)
loading/ $e-\sigma'$	$e=2.538\exp(-\sigma')+6.334$	kPa(σ')
Rebound/ $e-\sigma'$	$e=2.538\exp(-10\sigma')+6.334$	kPa(σ')
λ_1	1	-
λ_2	10	-
surcharge	10	kPa
Half time of load cycle	390	days

Table 2.4 Parameters utilized in cyclic loading verification.

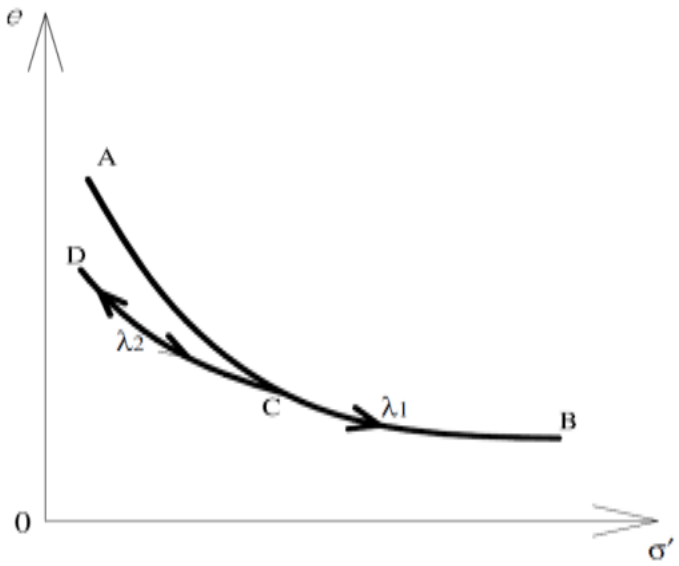

Figure 2.8 Void ratio - effective relationship for loading and unloading

Numerical simulations are run under PTIB conditions, and their results are plotted against the analytical solution of Cai et al. (2007) in **Figure 2.9**. There are small differences on the final settlements between these two solutions, the possible reason may be induced by the Laplace inversion utilized in the analytical solution. However, they agree with each other in change frequency and overall trend.

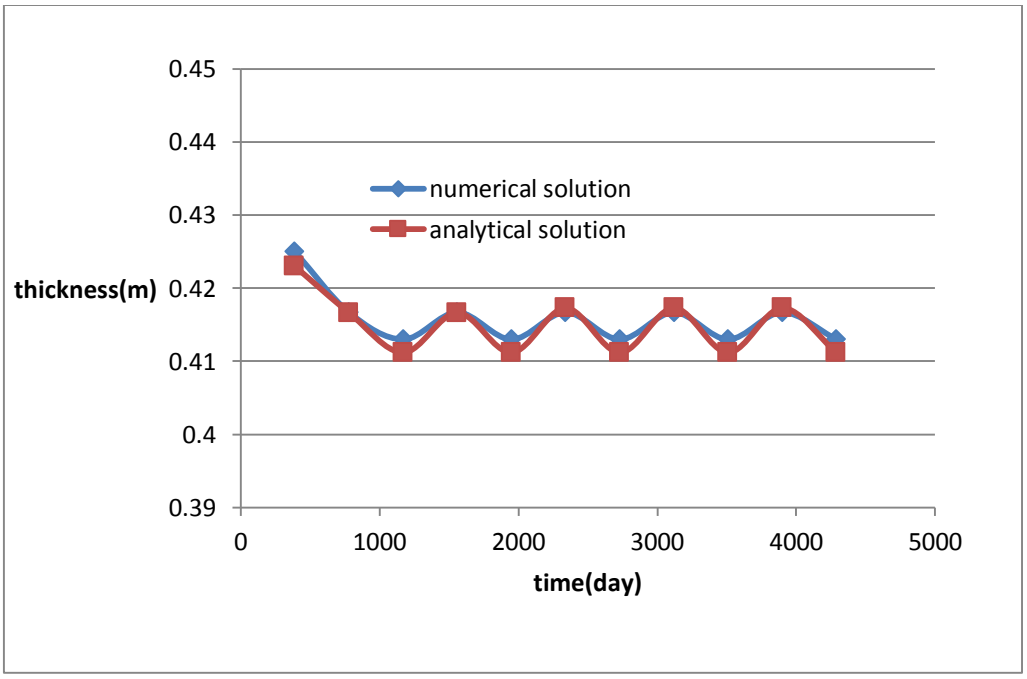

Figure 2.9 Comparison of thickness evolution with the analytical solution (thickness decreases – loading, such as $2T_0 - 3T_0$; thickness increases – rebound, such as $3T_0 - 4T_0$)

2.3.2 Verification with experimental results

Practical applicability is acquired by comparison with Twonsend's experiment.

2.3.2.1 Verification with classical Townsend's publication

Townsend's scenarios are intended to represent waste ponds that have recently received thickened clays (Townsend and Mcvay, 1991). These clays are allowed to consolidate under self-weight conditions. Close simulation results with experiments have been achieved, which means this numerical code is suitable for the scenarios of self-consolidation, sedimentation, oppressed consolidation and multi-layer consolidation. Experimental data and others validated modelling results are plotted with scatter plots, in which 'taga' and 'mcgill' are codes based on piecewise linear method, 'feldkamp' is based on the finite element method and 'b&ci' is Somogyi's equation-based (this equation can be seen in **Chapter 3.4**).

The numerical results of this thesis are shown as solid lines from **Figure 2.10** to **Figure 2.13**. It is worth noting that the numerical results of this thesis work for Scenario D of multi-layer self-consolidation is closer than results of others in faithful representation, void ratio distribution show clear boundary between two different layers.

Waste clay properties: $k = 0.8304 \times 10^{-6} e^{4.65}$, ($k$ - m/d); $e = 15.07\sigma'^{-0.22}$, (σ' - kPa).

6:1 sand/clay mix (scenario D): $k = 0.4235 \times 10^{-6} e^{4.15}$, ($k$ - m/d); $e = 32.5\sigma'^{-0.24}$, (σ' - kPa).

Scenario A - Quiescent consolidation, uniform initial void ratio. Scenario A is a quiescent consolidation prediction of a single drained waste clay pond instantaneously placed at a uniform void ratio, e_0 = 14.8 (initial solids content = 16%) having a thickness of 9.6 m. This case is intended to simulate waste ponds into which thickened clays have been recently pumped and that subsequently consolidate due to self-weight stresses. Overlying water thickness is 1 m, PTIB. The model cross section map and modelling results are shown in **Figure 2.10,** forecast results match each other well as can be seen.

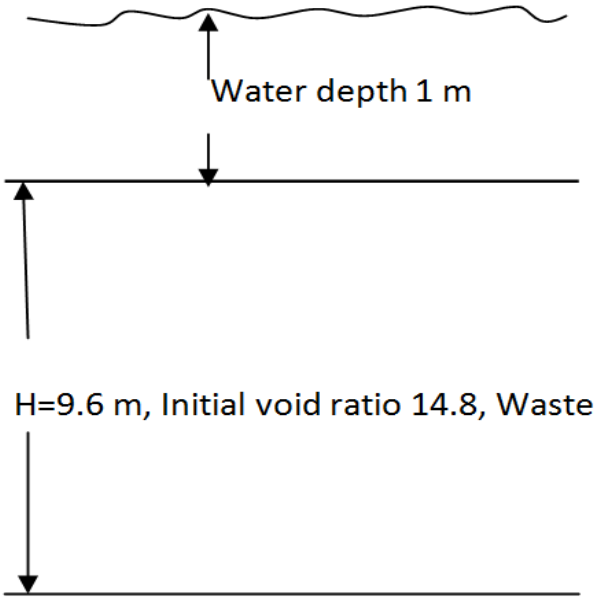

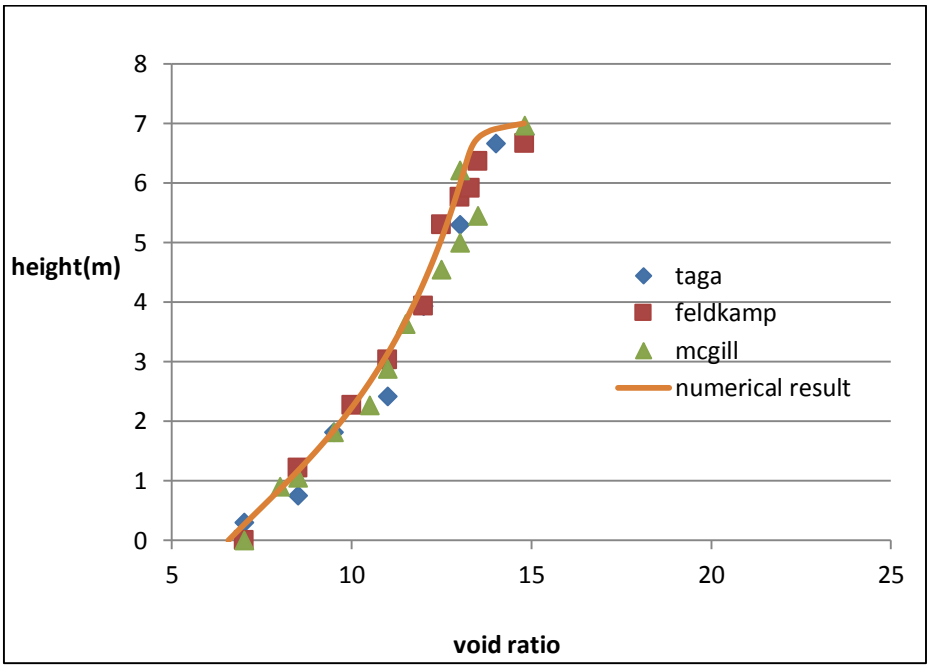

Figure 2.10 Scenario A and comparison results (Townsend and Mcvay, 1991), (Comparison of numerical result (line) of this research with other models(scatter plots) -self consolidation)

Scenario B - Stage filling, nonuniform initial void ratio. Scenario B is a prediction for a 7.2-m deep pond filled in two stages with two different initial void ratios. The pond will be filled in two six-month increments, separated by a six-month quiescent consolidation increment with the clay at an initial void ratio of 14.8 (initial solids content = 16%) for the first filling increment and at a void ratio of 22.82 (initial solids content = 11%) for the second filling

increment. The filling rate is 0.02 m/d. This case is intended to simulate final waste clay ponds that are filled intermittently with thickened clays pumped from an initial settling area. Overlying water thickness is 1 m, PTIB. The model cross section map and modelling results are shown in **Figure 2.11,** forecast results match each other well as can be seen.

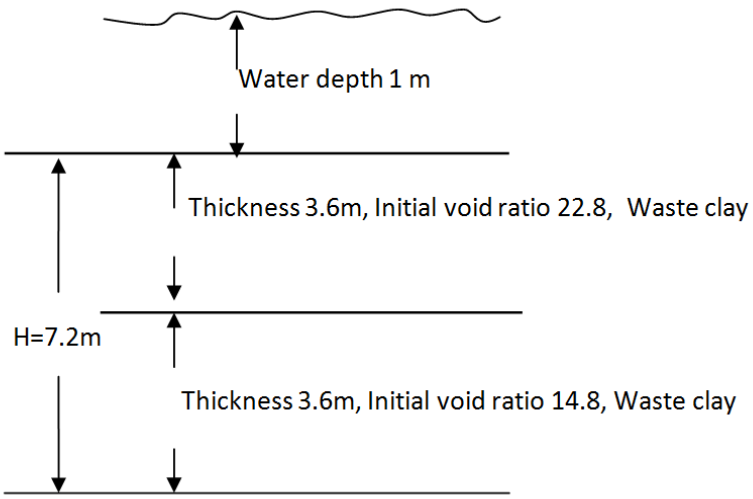

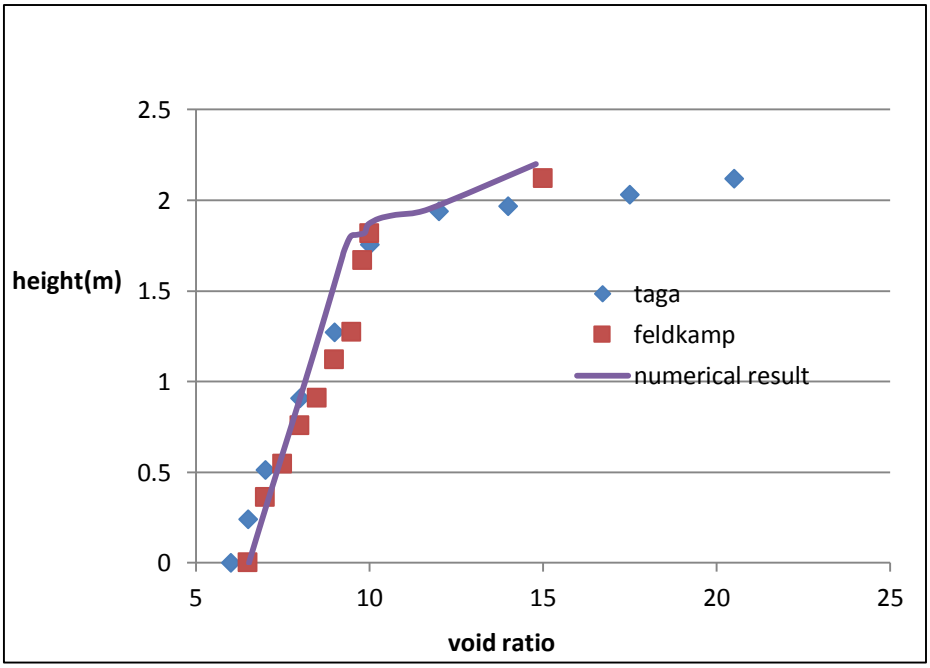

Figure 2.11 Scenario B and comparison results (Townsend and Mcvay, 1991), (Comparison of numerical result (line) of this research with other models(scatter plots) - sedimentation and self consolidation)

Scenario C - Quiescent consolidation under surcharge having a uniform initial void ratio. Scenario C predicts the consolidation of a 7.2-m deep waste pond with a uniform initial void

ratio of 14.8 (initial solids content =16%), subjected to surcharge of 967.5 kg/m^2. This scenario simulates a young waste pond, so the void ratio profile is uniform. It is to be capped with a 976.5 kg/m^2 surcharge, representing a 1.22-m thick sand layer with a buoyant unit weight of 800.9 kg/m^3. Overlying water thickness is 1 m, PTIB. The model cross section map and modelling results are shown in **Figure 2.12.** It worth noting that difference between predictions is induced by different boundary conditions on the top surface. There is no further information, such as time step or mesh size, for comparison However, the results obtained from the new developed numerical method are in a better agreement with those obtained from Svoffice, a recently developed commercial software (Murray and Robert, 2011).

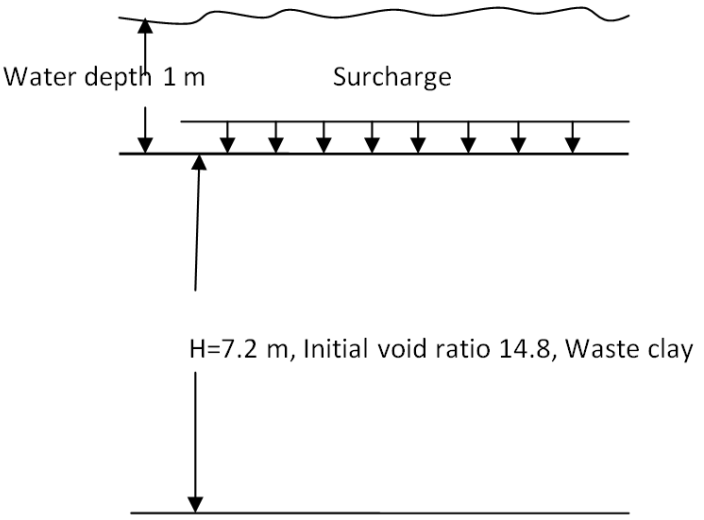

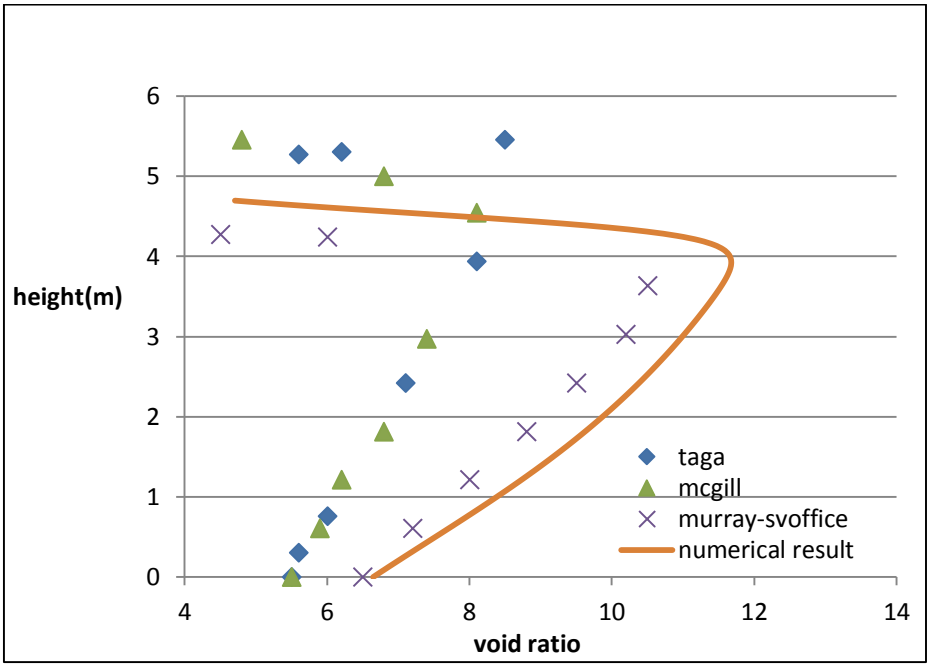

Figure 2.12 Scenario C and comparison results (Townsend and Mcvay, 1991), (Comparison of numerical result (line) of this research with other models(scatter plots) - consolidation with surcharge)

Scenario D - Two-layer quiescent consolidation, sand/clay (S/C) surcharge and nonuniform initial void ratio. Scenario D is the prediction of a 7.2-m deep waste pond with a nonuniform initial void ratio profile varying from 14.8 to 6.28 (initial solids content = 16 - 31%) that is subjected to a 6.8-kPa surcharge load by a 6:1 S/C cap, 1.2 m thick. The sand/clay cap has a different void ratio - effective stress - conductivity relationship than the underlying waste clay and has a buoyant unit weight of 584.05 kg/m^3. This scenario simulates a mature waste pond with a nonuniform initial void ratio profile that is reclaimed by placement of an S/C cap.

Overlying water thickness is 1 m, PTIB. The model cross section map and modelling results are shown in **Figure 2.13,** it can be seen that the new developed numerical model show obvious characteristic of two different layers, and hence is better than other predictions.

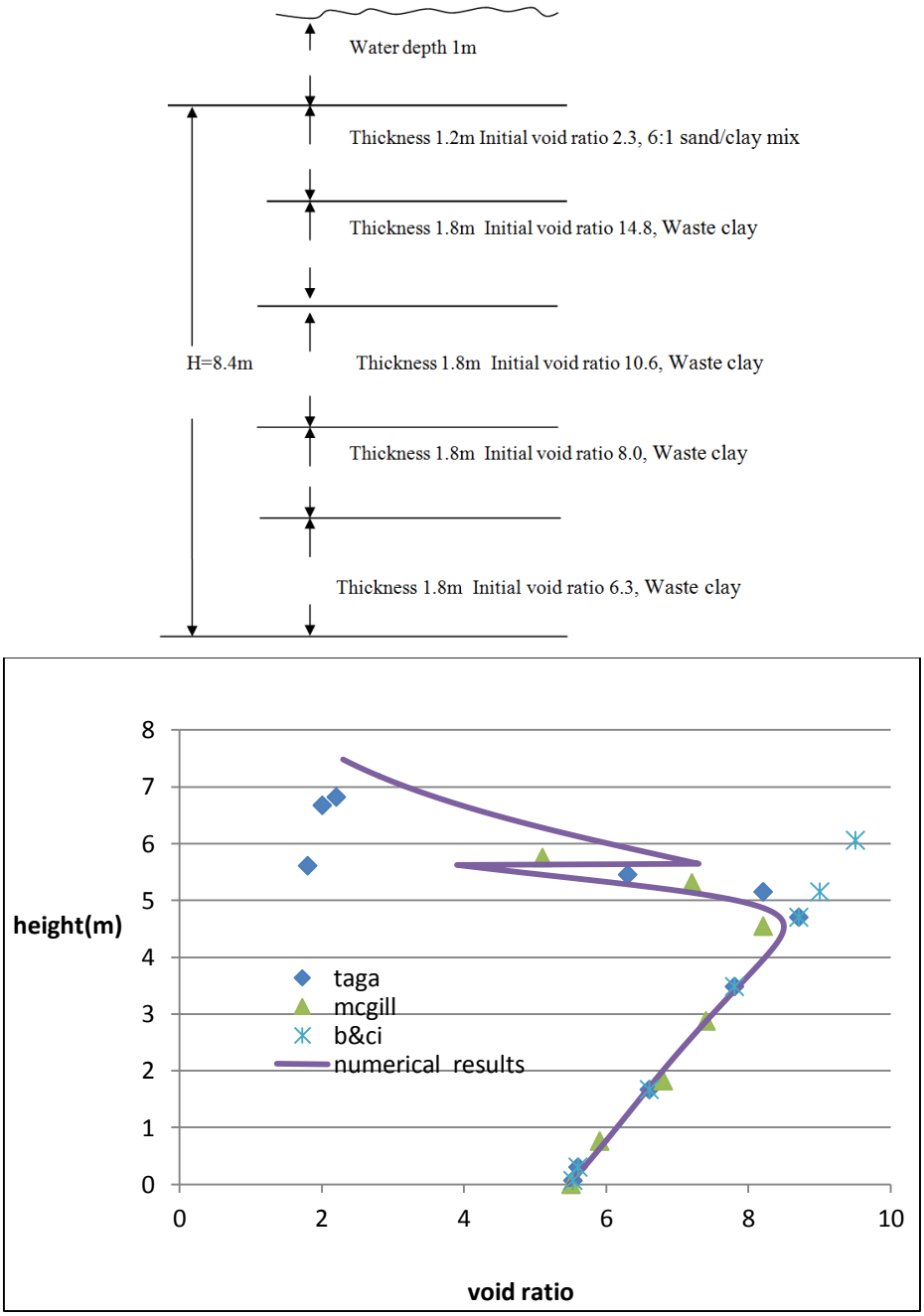

Figure 2.13 Scenario D (multi-layer system) and comparison results (Townsend and Mcvay, 1991), (Comparison of numerical result (line) of this research with other models(scatter plots) - multi-layer consolidation)

2.3.2.2 Verification with other Gibson based model

The Gibson model based numerical model has been applied in shallow compaction. Some researchers have adopted the Gibson model in basin modelling. Wangen applied Gibson's theory in basin modelling and considered the deposition rate as shown in **Equation 2.17** and **2.18** (Wangen, 2010).

The porosity is assumed to be a linear function of the vertical effective stress σ', and the permeability of sediment is constant.

$$\phi = \phi_0 - A\sigma' \tag{2.17}$$

$$\frac{\partial p_{fl}}{\partial t} - \frac{k}{A\mu}\frac{\partial^2 p_{fl}}{\partial z^2} = (\rho_s - \rho_f)g_{ra}w_b \tag{2.18}$$

Where, A is constant (equals sediment compressibility). Other parameters and results are as follows. My numerical model agrees well with his model as shown in **Figure 2.14**, and hence is effective.

parameter	Value	Units
permeability	1.00×10^{-18}	m^2
viscosity	0.001	Pa·s
fluid density	1000	$kg\cdot m^{-3}$
sediment density	2100	$kg\cdot m^{-3}$
sedimentation rate	1000	m/million years
sediment compressibility	1.00×10^{-8}	Pa^{-1}

Table 2.5 Parameters utilized in Wangen's solution.

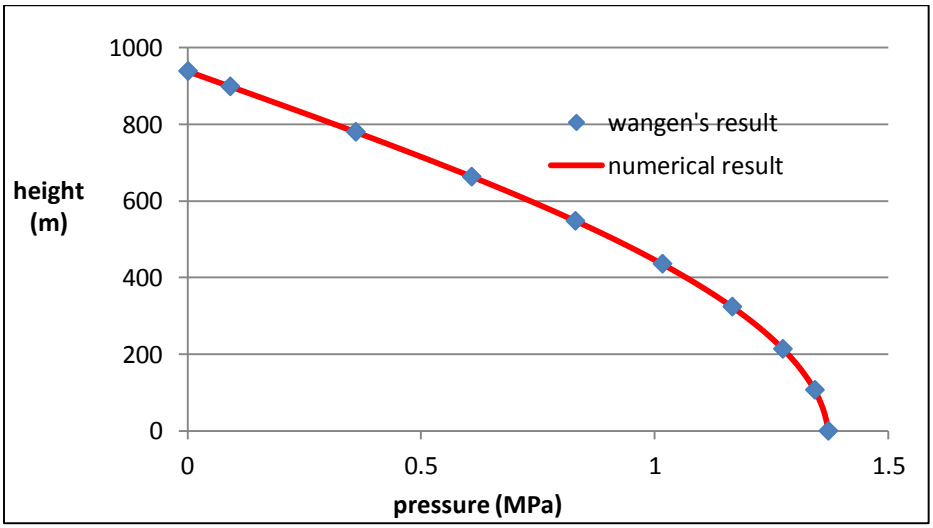

Figure 2.14 Overpressure comparison between numerical results and Wangen's Gibson based solution

2.3.2.3 Verification with other basin modelling model

Comparison between this numerical model and other models, which are already applied in basing modelling, is also conducted. The numerical model is consistent with the widely-used basin modelling equation in both single layer and multi-layer model.

Kooi (1997) developed Domenico and Schwartz's model to form a widely-used one dimensional consolidation equation which considers the water compressibility and sedimentation:

$$(\phi\beta_{fl}+\beta_p)\frac{\partial p_{ex}}{\partial t}=\nabla(\frac{k}{\mu}\nabla p_{ex})+\beta_p(\rho_{gr}-\rho_f)g\nu_{gr}-\phi\beta_{fl}\rho_f g\nu_x \qquad (2.19)$$

Where, ρ_{gr} and ν_{gr} are density and sedimentation rate of the grain material respectively. ϕ is porosity, ρ_f is fluid density, ν_x is subsidence rate comprises contributions from basement subsidence, sea-level change and compaction of the underlying sediment column.

Here the Gibson-based numerical simulation results agree well with Kooi's result, which proves that water compressibility can be ignored in shallow compaction. Normally $\beta_{fl}=10^{-10}pa^{-1}$, this research is limited within 1000m, so the relative volume change amount is less than 10^{-2}, which is negligible. The comparison also proves this.

The parameters of Kooi's model are shown as follows. This numerical model agrees well with his model.

Parameter	Value	Units
sedimentation rate	500	m/ million years
sedimentation time	2	million years
fluid density	1000	Kg/m^3
porosity - effective stress	$\phi=0.5\exp(1.8\times10^{-8}\sigma')$	kPa(σ')
conductivity - porosity	$k=10^{-21.68+4.75\phi}$	m/d(k)

Table 2.6 Parameters utilized in Kooi's solution.

Comparison of Kooi's model and this Gibson-based numerical are shown in the following **Figure 2.15**, fitting curve proves the applicability of Gibson model.

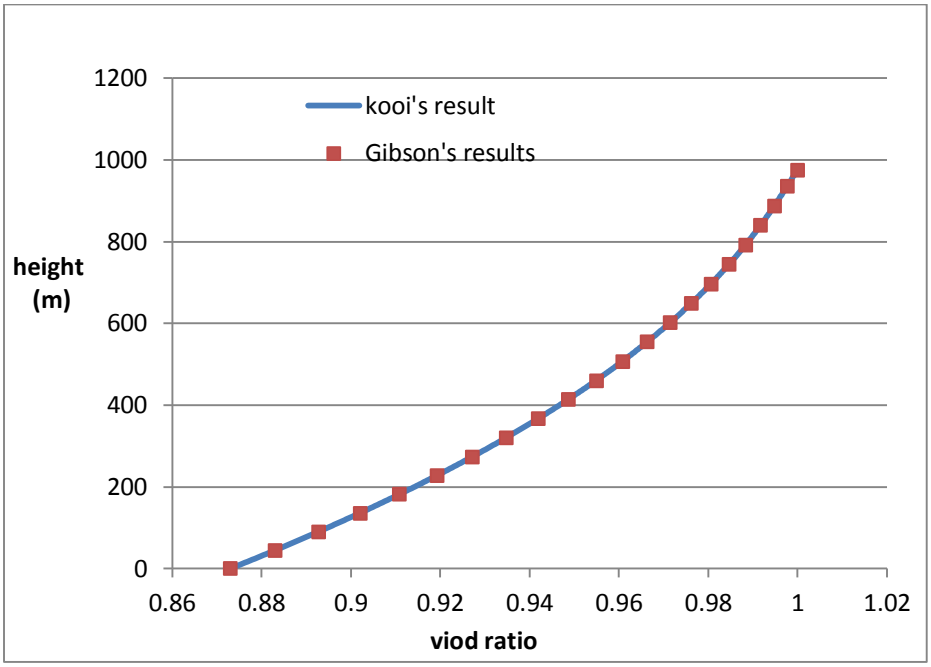

Figure 2.15 Numerical results comparison of Gibson's model and Kooi's model (upper - void ratio distribution comparison, lower - final hydraulic pressure distribution of Gibson based model)

Compared with the Domenico&Schwartz (1991) model, the Gibson model is simpler and large-strain itself (solid coordinate). So for shallow compaction (<1000m), the Gibson model is precise enough.

As described by Wangen, it is now safe to draw the conclusion that there is probably only one exact and reasonable simple solution of overpressure build-up for a basin in a state of constant deposition of sediments, when the porosity is a function of the effective stress (and thereby the overpressure), and that is the Gibson solution (Wangen, 2010).

2.3.3 Large-strain consolidation development

In order to better match experimental data, some development has been achieved based on large-strain consolidation. The numerical simulator takes these developments into consideration.

2.3.3.1 Pre-Consolidation Behaviour

According to considerable evidence (Pollock, 1988; Suthaker, 1995) from large-strain consolidation tests, the compressibility of sediment may exhibit pre-consolidation behaviour. This behaviour makes the use of the power law function questionable and the Weibull

function is employed for study as this function can capture the pre-consolidation behaviour and offers a better coefficient of determination.

$$e = A - B\exp(-E(\sigma')^F) \tag{2.20}$$

Where, A, B, E and F are laboratory determined parameters.

2.3.3.2 Creep Compression Analysis

Creep compression is based on compression behaviour observation of the fine tailings in both field and laboratory. Therefore total deformation is a combination of independent creep compression and consolidation. A creep function is postulated and it is expressed as follows (AGRA, 1997):

$$e^d = M\exp[eN] \tag{2.21}$$

Where, e^d is total deformation, *M* and *N* are experimentally determined parameters. This creep function is fitted from experimental data of creep rates versus void ratio.

The second model is based on a concept of strain rate presented by Leroueil et al (Leroueil et al., 1985). It is performed by assuming a constitutive relationship in a form of $e = f(\sigma', e^d)$.

$$A = G - H\exp[-I(e^d)^j] \tag{2.22}$$

Where *G*, *H*, *I* and *J* are experimental determined parameters and '*A*' is from $e = A(\sigma')^B$.

2.3.3.3 Layering Consolidation Analysis

Jeeravipoolvarn et al simulated the long-term consolidation of oil sands tailings (Jeeravipoolvarn et al., 2009). The model consists of a circular column, with a thickness of 10 m. It is assumed that the tailings are initially homogeneous and deposited instantaneously. The deformation boundary conditions consist of a lower boundary that is fixed in place, and an upper boundary that is free to deform.

In Jeeravipoolvarn's research, the use of a large-strain consolidation theory to predict compression behaviour of oil sands fine tailings does not agree well with experimental data. To search for a possible explanation of this discrepancy, history matching (adjust property parameters numerical to fit the experimental results) was performed by three approaches, namely a pre-consolidation, a creep compression and a hydraulic conductivity layering

consolidation. Results indicate that the conventional approach can lead to a large error, considerations of a pre-consolidation and creep compression do not improve prediction and channelling phenomena could be a major reason of the discrepancy observed between the theory and the experiment.

For the consolidation analysis of layers, the assumption of 'hydraulic conductivity-void ratio' follows the form of $K = Ce^D$ is made, where 'C' and 'D' are parameters. The hydraulic conductivity parameter D of the soil layers is assumed to range between the upper and lower limits of the experimental data in **Figure 2.16**. The upper and lower limits are assumed to represent maximum channelled system and homogenous system respectively.

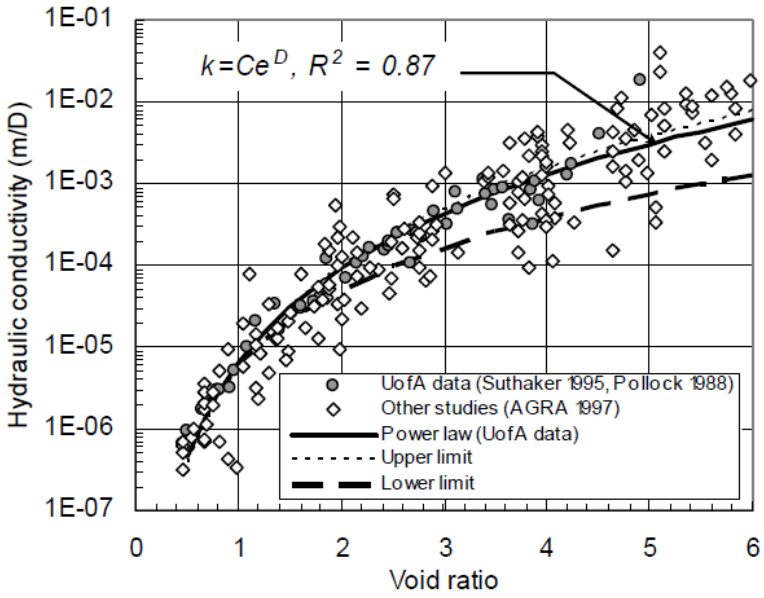

Figure 2.16 Hydraulic conductivity of different fine tailings, splashes and limit line come from publication data, 'power law line' comes from splashes data regression (Jeeravipoolvarn et al., 2009)

Jeeravipoolvarn selected an arbitrary distribution of the hydraulic conductivity parameter D for optimum history matching and the distribution is plotted against normalized thickness, H/H_o, in **Figure 2.17**.

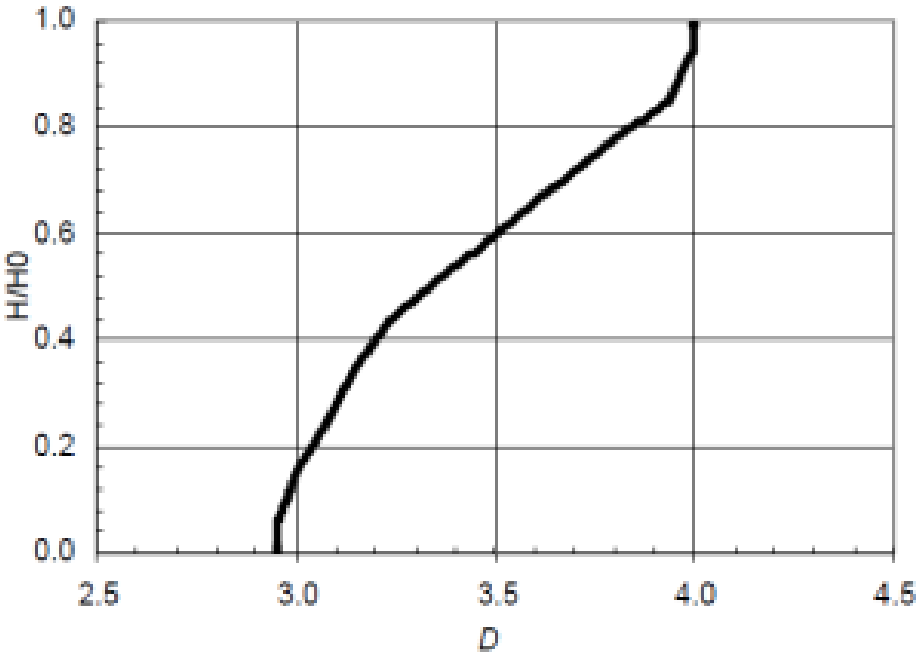

Figure 2.17 Hydraulic conductivity parameter D vs. H/H_o (Jeeravipoolvarn et al., 2009)

2.3.3.4 Sedimentation and consolidation

Pane and Schiffman presented a method to link sedimentation and consolidation together (Pane and Schiffman, 1985). They proposed that for a value of void ratio greater than a certain void ratio, the effective stress becomes zero and the finite strain consolidation equation reduces to Kynch's equation (Kynch, 1952). They introduced an interaction coefficient - ψ (function of void ratio), which connects the processes of sedimentation and consolidation via the effective stress equation as follows:

$$\sigma = \psi(e)\sigma' + p \tag{2.23}$$

Where, σ is total stress, p is pore pressure. The interaction coefficient is a monotonic function of the void ratio. There are two reasonable forms of the coefficient, one has a step function changing the coefficient from 0 in a suspension stage to 1 in a soil stage; the other form is a gradual change of the interaction coefficient. Shodja and Feldkamp argued that the effective stress equation should be left unchanged due to the fact that in the dispersion region the effective stress should be set to zero (Shodja and Feldkamp, 1993). Distinction between the two processes should be made through constitutive models constructed to describe a material behaviour.

Jeeravipoolvarn examined the use of an interaction coefficient to couple sedimentation and consolidation phenomena with the conventional finite strain consolidation theory (Jeeravipoolvarn et al., 2009). A specific continuous interaction function was implemented and the resulting model was examined.

$$\psi = \begin{cases} \left(\frac{1}{E + Fe^{J}}\right), w > w_t \\ w_f, w \le w_t \end{cases}$$

$$e = \begin{cases} A\left(\frac{\sigma'}{w}\right)^{B}, e > e_s \\ A(\sigma')^{B}, e > e_s \end{cases} \qquad (2.24)$$

$$k = Ce^{D}$$

Where, A and B are compressibility parameters, C and D are hydraulic conductivity parameters and E, F and J are interaction coefficient parameters.

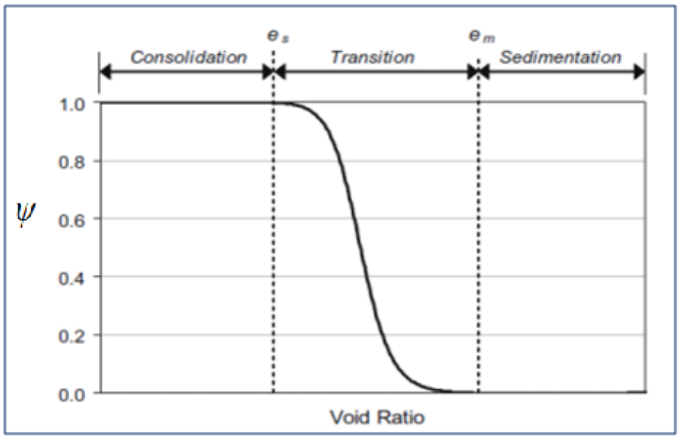

Figure 2.18 Interaction, structural void ratio (e_s) and maximum suspension void ratio (e_m).

An invertible assumption of ψ and constant relationship of 'conductivity - void ratio' are taken, which is still a controversial issue and demands more research.

Jeeravipoolvarn made a programme and verified it with the experiment (Jeeravipoolvarn et al., 2009). This research considers the interaction and is verified with his results as shown in **Figure 2.19**.

Parameters are shown in **Table 2.7**.

Parameter	Value	Units
solids content/ S_i	12.5%	-
initial depth / H	0.36	m
unit weight of soil / γ_s	22.344	kN/m^3
A	3.38	-
B	-0.31	-
C	6.51×10^{-6}	kPa
D	3.82	m/D
E	1.0	kPa
F	1.0×10^{-30}	kPa
J	25.9	-

Table 2.7 Parameters utilized in comparison with Jeeravipoolvarn's model

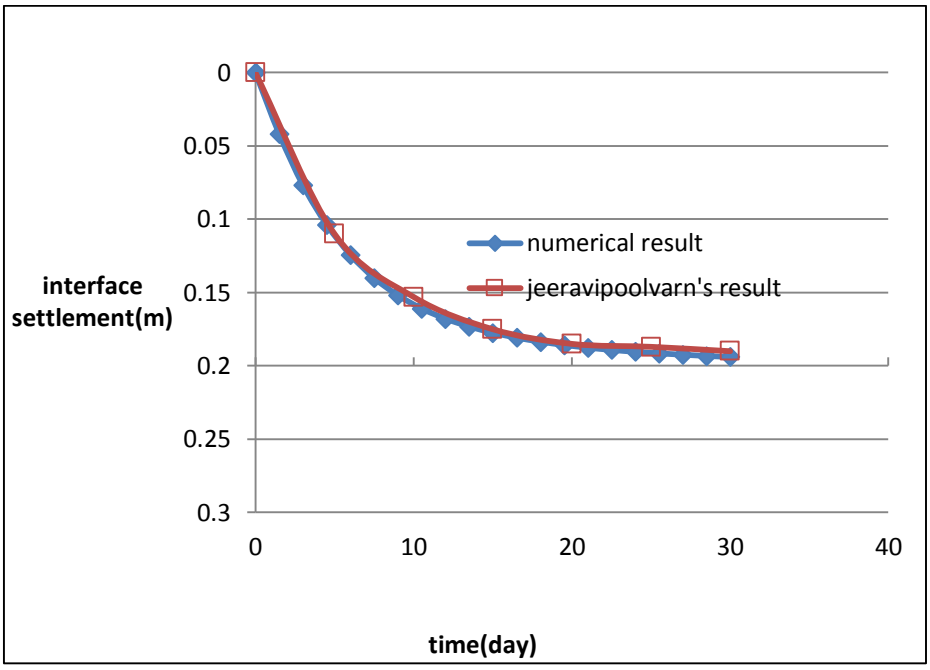

Figure 2.19 Interface settlement verification of the developed numerical code with Jeeravipoolvarn's model

Now we have a verified large-strain numerical simulator, which is capable of simulating many phenomena in the basin evolution.

2.4 Small strain vs. large strain - necessity of large-strain model

In this section, a comprehensive comparison between updating small strain and large strain is provided to show the necessity of using large-strain model.

2.4.1 Theoretical analysis

Terzaghi's model is developed for small-strain deformation where a linear relationship is held for stress and strain, and the conductivity is constant.

As mentioned in verification with Morris's analytical solution, Gibson's equation can be rearranged as follows.

$$\frac{\partial^2 e}{\partial z^2} + \lambda(\gamma_s - \gamma_w)\frac{\partial e}{\partial z} = \frac{1}{g}\frac{\partial e}{\partial t} \tag{2.25}$$

The assumption that λ and g are constant is valid only over limited ranges, and the same limitation applies to the analytical solutions. Attempts to use average λ and g values for large ranges of σ' and e in consolidation analyses will produce poor results (Benson and Sill, 1985; Cargill, 1985; McVay et al., 1986).

For small-strain consolidation (Gibson et al., 1981):

$$\frac{\partial^2 e}{\partial z^2} = \frac{1}{g}\frac{\partial e}{\partial t} \tag{2.26}$$

It can be seen from the comparison between **Equation 2.25** and **2.26,** the small-strain model ignores the effect of self-consolidation that is the second term in **Equation 2.25.** When the effective stress is in linear relationship with void ratio (which is common in piecewise linear approximation), so that λ becomes zero, or the unit weight of the sediment equals that of water, the large-strain consolidation theory will degenerate into small-strain theory (in which g is not constant). Otherwise, a difference is always present, and may accumulate or amplify without correct handling when considering shallow compaction.

Xie and Leo, and Morris compared small-strain (Terzaghi) and large-strain (Gibson) compaction models for a column of sediments with variable volume compressibility. Their results are provided in **Figure 2.20** and **Figure 2.21** for completeness.

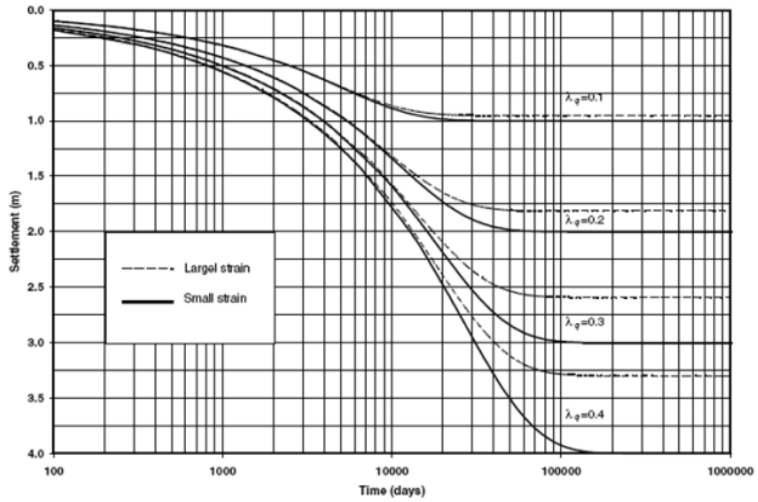

Figure 2.20 The surface settlements calculated using large- and small-strain models vs. time (PTIB) (Xie and Leo, 2004). Note that $\lambda_q = m_{vl} q$ shown on the figure is positively related to the volume compressibility of the sediments under consideration

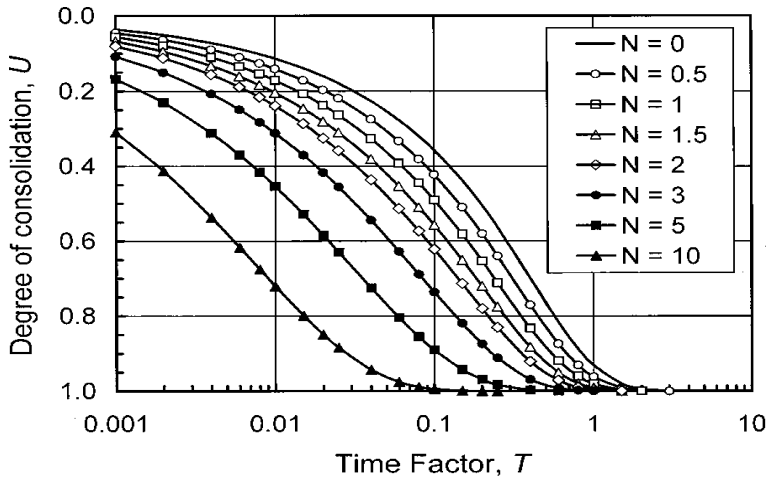

Figure 2.21 Large and small strain surface settlement vs. time (PTIB) (Morris, 2002). Note that $N = \lambda l(r_s - r_w)$, and l is thickness of soil layer in material coordinates. N is positively related to the volume compressibility of the sediment in this case.

According to the results of their analysis, the bigger the volumetric compressibility is, the bigger the difference between small-strain and large-strain result is, for both forced and self-consolidation. Hence, it is not acceptable to apply small-strain theory directly into shallow compaction - large strain.

If the unit weight of soil is equal to that of water, the whole system will not go through consolidation under gravity. This is taken as the reference case, with which all other cases with nonzero self-consolidation are compared. In order to study the proportion of self-

consolidation, a sensitivity comparison is carried out. Relative errors compared with zero self-consolidation (absolute value of the ratio between settlement of zero minus nonzero self-consolidation and settlement of zero self consolidation) are shown in **Figure 2.23** - **Figure 2.25**.

Consolidation schematic diagram follows **Figure 2.2**, no overlying water and no surcharge, PTIB, self-consolidation to steady state. 90% clay content material is adopted for analysis (Ma and Couples, 2008), as shown in **Figure 2.22**. The unit weight of soil is chosen to cover a wide range of possible sediments. Other model parameters are shown in **Table 2.8**.

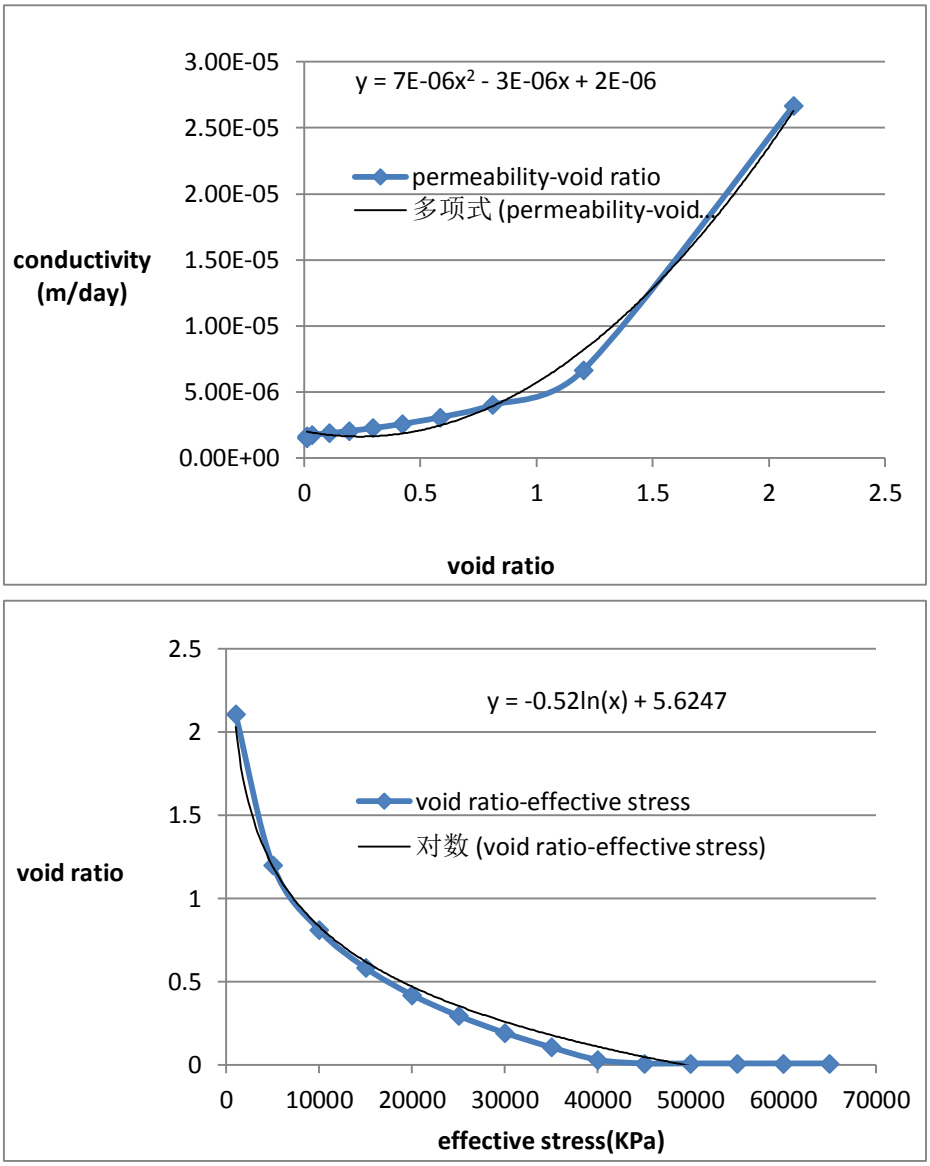

Figure 2.22 Properties and fitting function of 90% clay content, upper - conductivity-void ratio and fitting function of 90% clay content, lower - void ratio-effective stress and fitting function of 90% clay content (Ma and Couples, 2008)

Parameter	Value	Units
unit weights of soil variation / γ_s	[1.2,1.6,2.0,2.4,2.8,3.2]×9.8	kN/m^3
initial effective stresses	[200,600,1000,1400,1800,2200]	kPa
conductivity - void ratio/ $k-e$	$k=7\times10^{-6}e^2-3\times10^{-6}e+2\times10^{-6}$	m/d(k)
void ratio - effective stress / $e-\sigma'$	$e=5.6247-0.52\ln(\sigma')$	kPa(σ')
initial thickness variation	[0.1,1,10,20,40,60,80]	m

Table 2.8 Parameters utilized in self-consolidation evaluation

(1) Influence of initial thickness:

The influence of self-consolidation increases with the increase of initial thickness and unit weight of soil, and the increase rate gradually slows down (can be seen from curve's slope change and variation of spaces between adjacent curves). The influence decreases with increase of effective stress, and the decrease rate gradually decreases (can be seen from variation of spaces between adjacent curves) as shown in **Figure 2.23**.

(2) Influence of unit weight of soil:

Influence of self-consolidation increases with the increase of unit weight of soil (soil density). The influence increases with increase of initial thickness, and the increase rate gradually slows down. The influence decreases with increase of effective stress, and the decrease rate gradually slows down as shown in **Figure 2.24**.

(3) Influence of initial effective stress:

It can be seen from **Figure 2.25**, the influence of self-consolidation decreases with the increase of effective stress. The influence increases with increase of initial thickness/ unit weight of soil, and the increase rate gradually slows down.

Results analyses show that influence of self-consolidation increases with the increase of soil density and initial thickness, while decreases with the increase of effective stress, resulting in the maximum error of 10%.

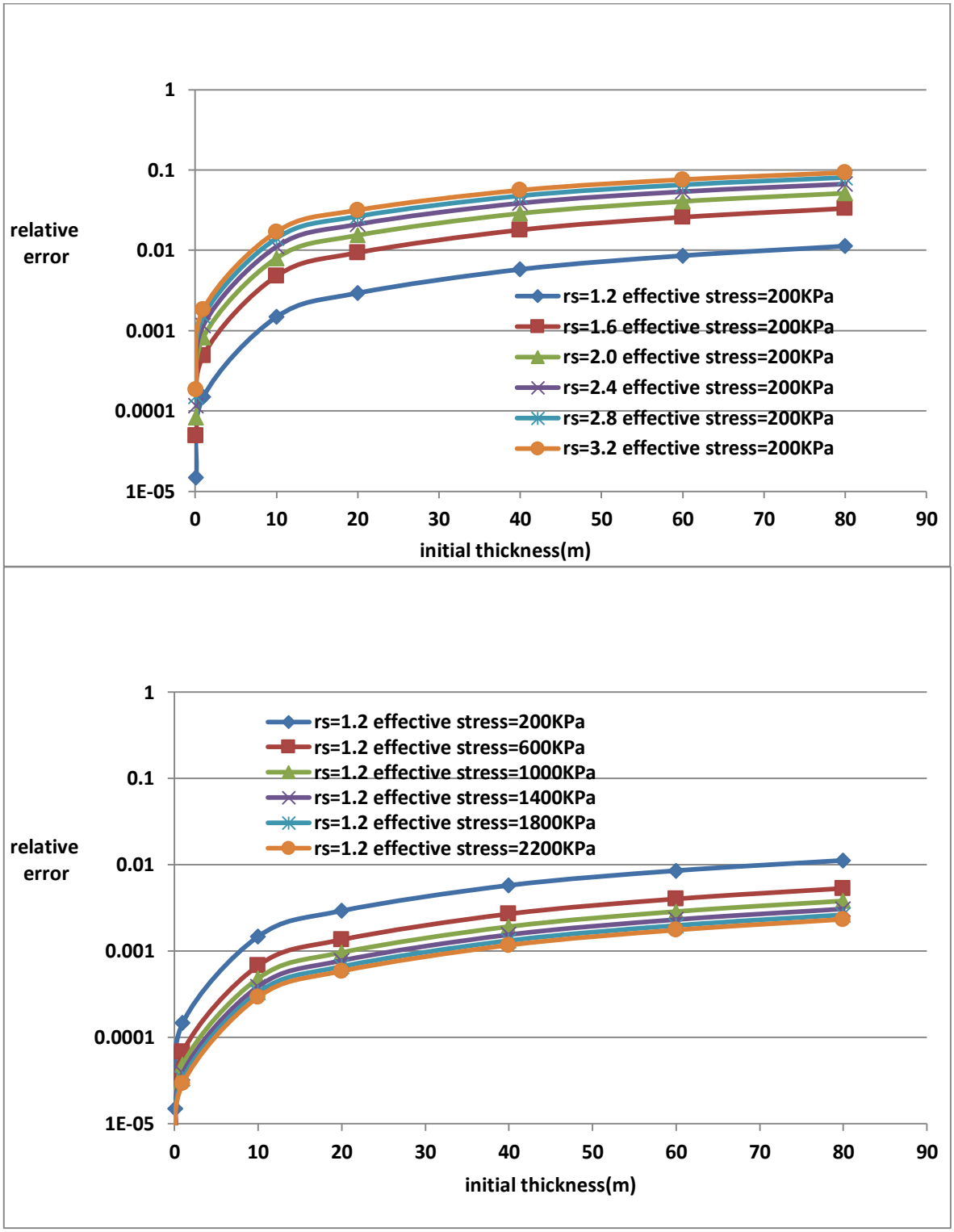

Figure 2.23 Influence of initial thickness on relative error, (relative error is absolute value of the ratio between settlement of zero minus nonzero self-consolidation and settlement of zero self consolidation. 'rs' is unit weight of soil, equals γ_s, h is initial sediment thickness)

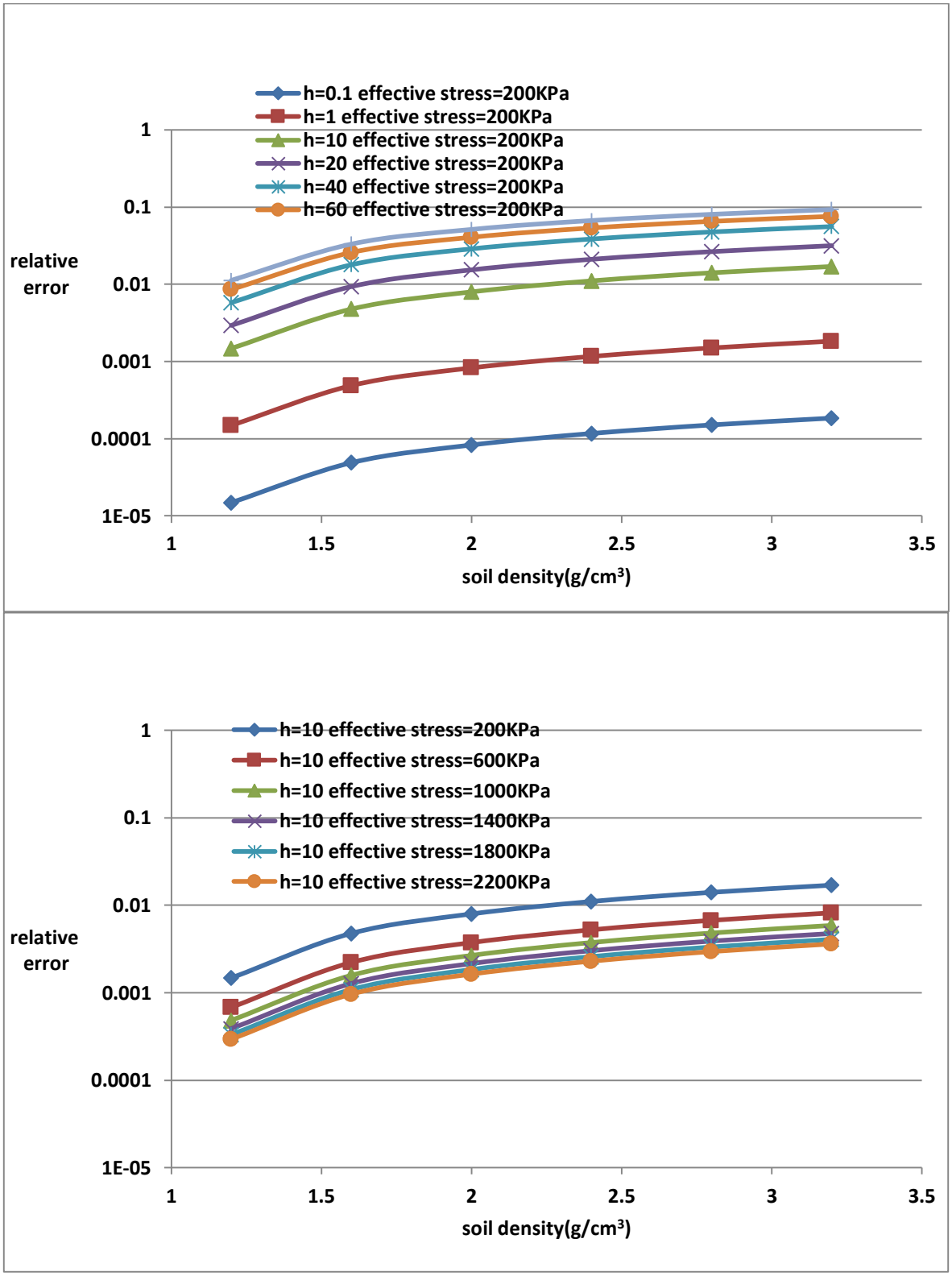

Figure 2.24 Influence of unit weight of soil on relative error, (relative error is absolute value of the ratio between settlement of zero minus nonzero self-consolidation and settlement of zero self consolidation, 'h' is initial sediment thickness)

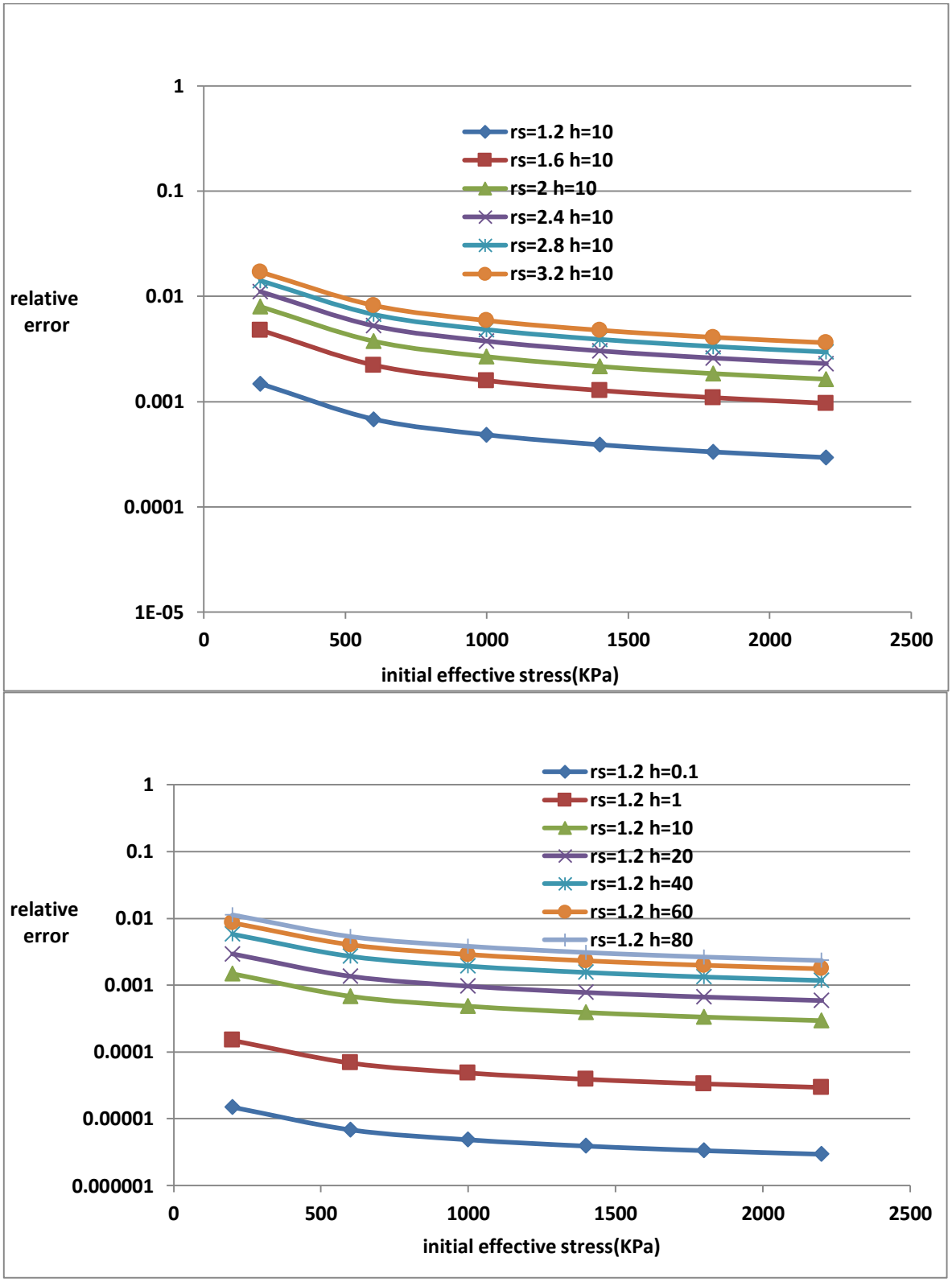

Figure 2.25 Influence of initial effective stress on relative error, (relative error is absolute value of the ratio between settlement of zero minus nonzero self-consolidation and settlement of zero self consolidation, 'rs' equals γ_s, 'h' is initial sediment thickness)

2.4.2 Calculation comparison of Gibson model and updating Terzaghi model

Terzaghi theory is for small-strain consolidation, while Gibson theory for large-strain consolidation, and there is no clear boundary between the two models. Moreover 'Terzaghi' is in continuous development, it is different from its original in practical application.

In Terzaghi's equation, conductivity, void ratio and compressibility can change separately or combined. By combining piecewise linear approximation of soil properties, meshes updating, time and space step control technology, the Terzaghi model has been successfully applied in large-strain consolidation problems (Fox and Berles, 1997).

Real non-linear soil properties other than piecewise linear approximation, meshes updating, time and space step control technology are utilized to make Terzaghi close to Gibson as much as possible. In order to compare the two models, implicit finite difference method is used for the two models simultaneously.

Updating Terzaghi calculation flow graph is shown as follows:

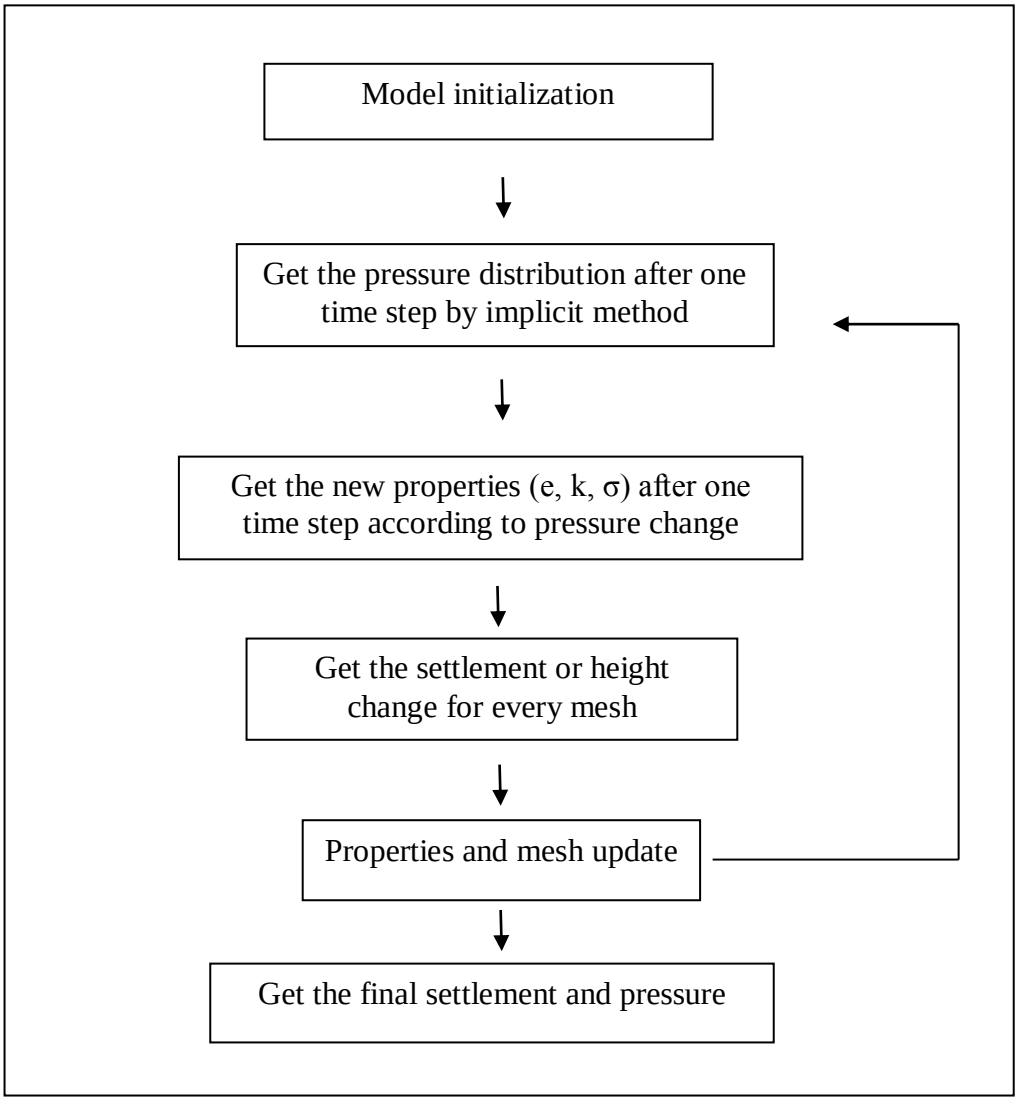

Figure 2.26 Calculation flow of updating Terzaghi's model

A model is designed to compare Gibson and the updating Terzaghi's model. Consolidation schematic diagram follows **Figure 2.2**, 90% clay content material is adopted for analysis, initial effective stress is 500 kPa, PTIB, and initial thickness is 10m and no overlying water. Terzaghi and Gibson share the same time and space step initially (100 time steps for 10000 years, and 50 cells for 10m). It can be seen from **Figure 2.27**, when time step increases 10 times (1000 time steps for 10000 years), there is almost no difference for Gibson model, but updating Terzaghi's model changes greatly, and becomes closer to Gibson model. The same trend applies when time step increases 10 times again (10000 time steps for 10000 years). Moreover, though with a small time step of 10 days, overpressure difference between Terzghi and Gibson is obvious as shown in **Figure 2.28**.

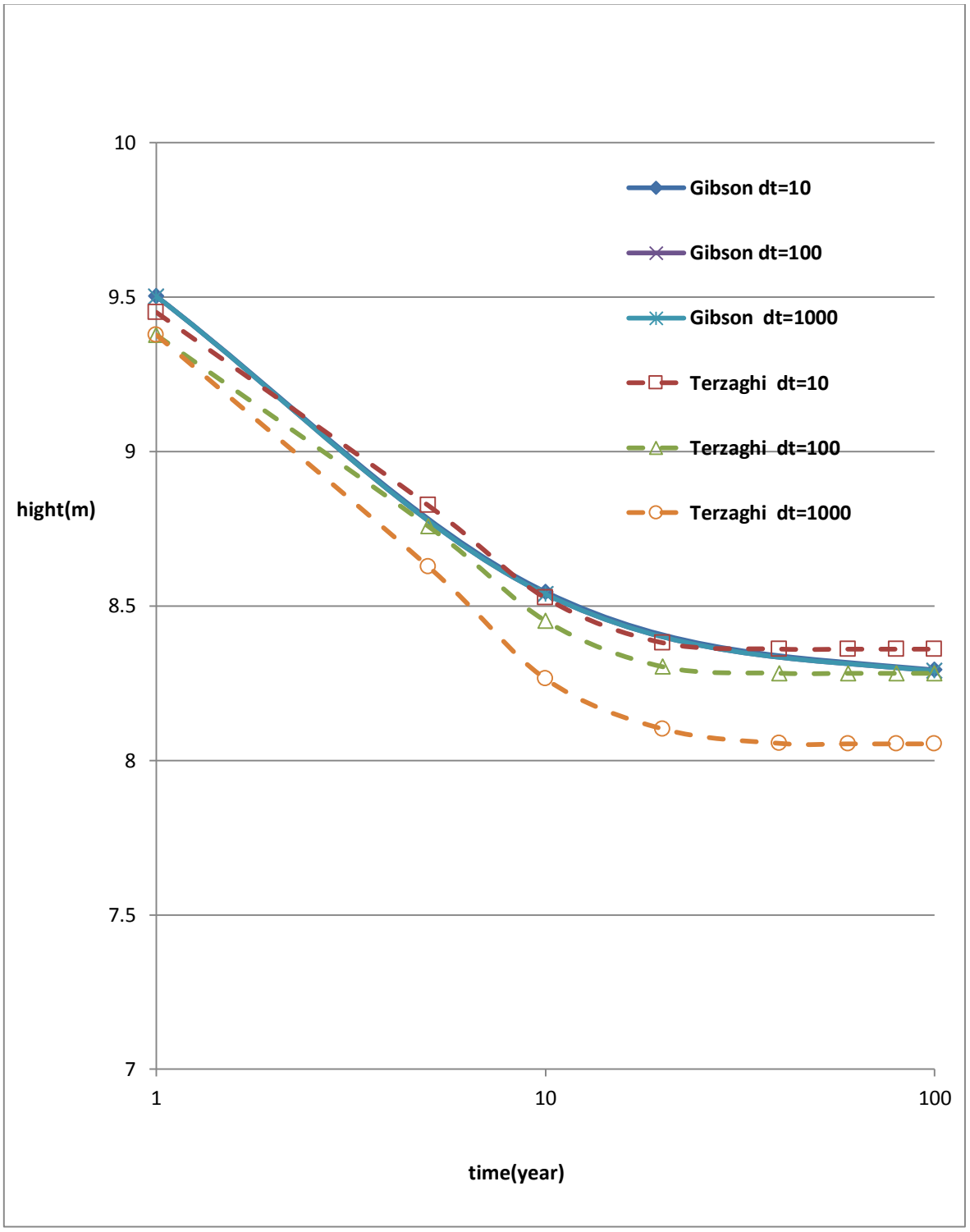

Figure 2.27 Comparison of thickness evolution between updating Terzaghi and Gibson model with different time steps, in which 'dt' is time step in days.

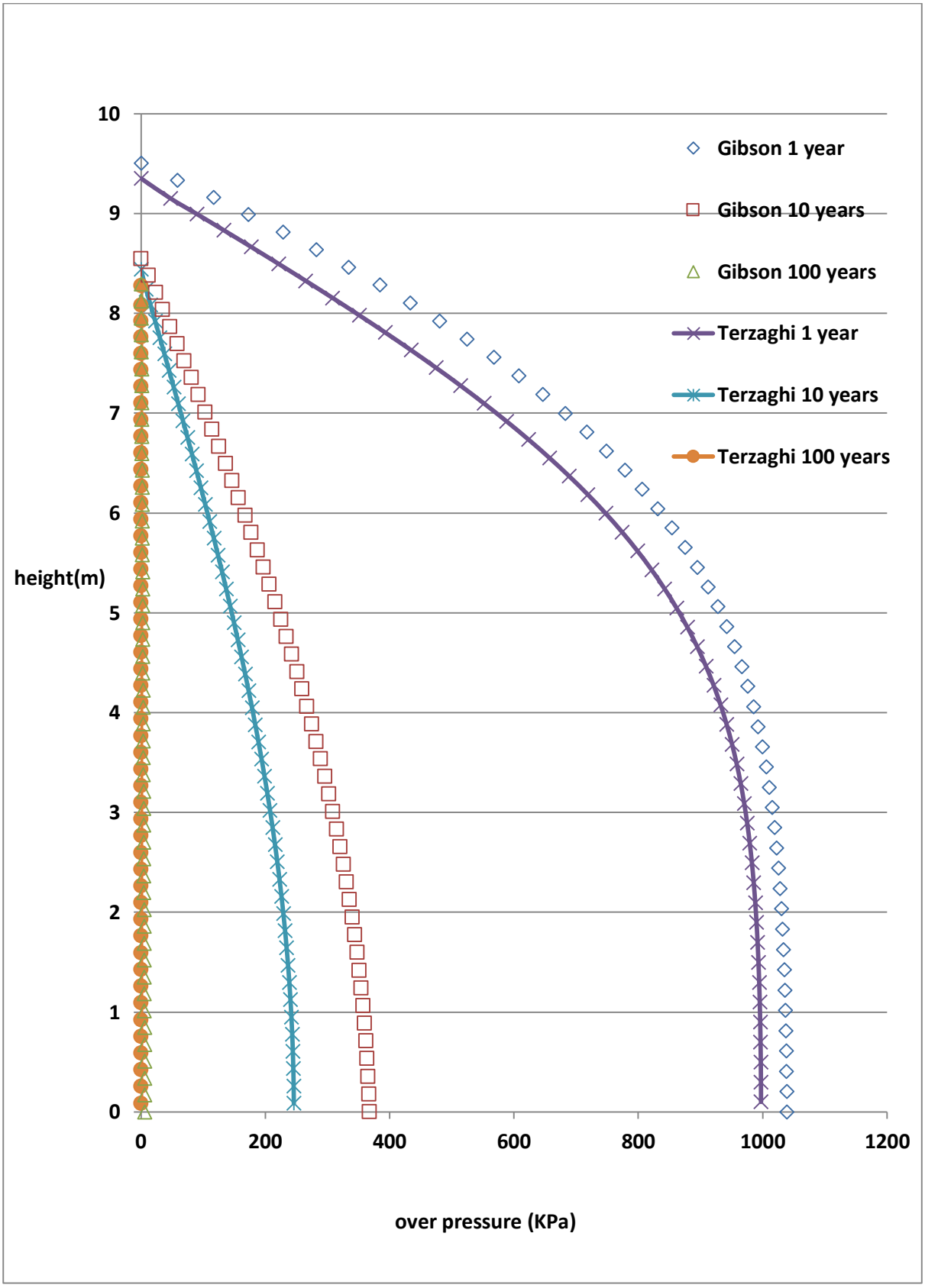

Figure 2.28 Comparison of overpressure results between updating Terzaghi and Gibson model (time step = 10 day)

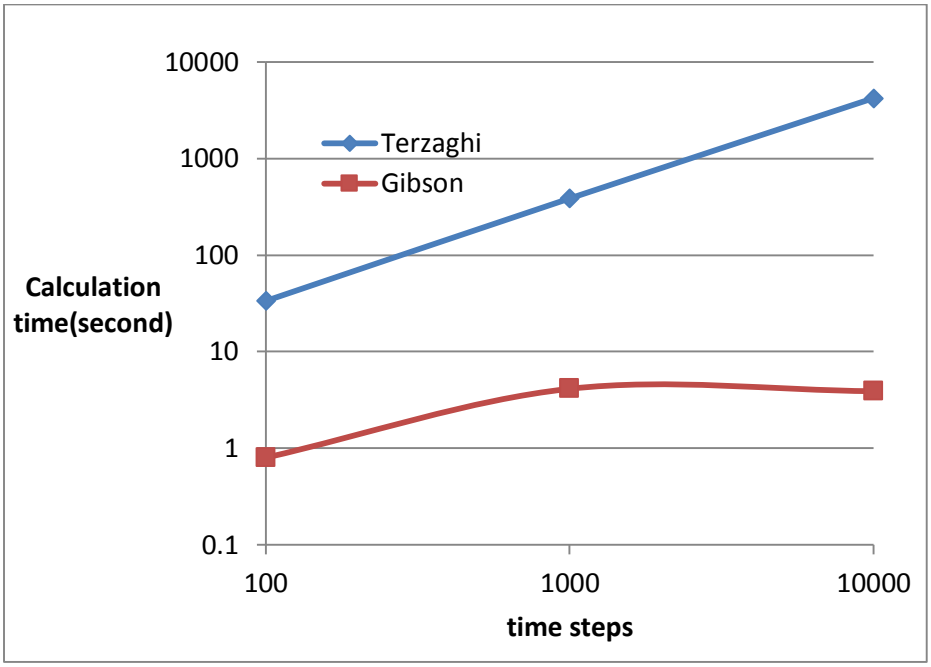

Figure 2.29 Calculation time comparison of Terzaghi and Gibson model

Moreover, updating Terzaghi is too time-consuming compared with Gibson model. As shown in **Figure 2.29**, Gibson computation time is 0.798791 seconds and Terzaghi's is 33.505038 seconds for 100 time steps. As for 1000 time steps, Gibson computation time 4.122612 seconds, Terzaghi 385.36 seconds. As for 10000 time steps, Gibson computation time 3.893294 seconds, Terzaghi 4202.95456 seconds (CPU: Inter core i7-2600, 3.40GHz).

The last point, error induced by the updating Terzaghi method will accumulate and expand. In order to evaluate the error variation of updating Terzaghi model with burial depth growing or surcharge increasing, surcharge increases 1000 kPa and then keeps constant in every 10000 years, which stands for the increment of sediment depth. During the process, time steps keep the same for these two models (100 steps for 10000 years). Dimensionless displacement equals displacement/initial thickness.

As can be seen from **Figure 2.30** and **Figure 2.31**, updating Terzaghi model compresses faster than Gibson model, Terzaghi-Gibson difference proportion increases from 500 kPa to 17.5MPa. The increment gradually slows down, finally changes into decrease.

While for the shallow compaction, this result means that the accumulative 'error' or 'deviation' of using updating Terzaghi model is increasing with time going on or buried depth increasing.

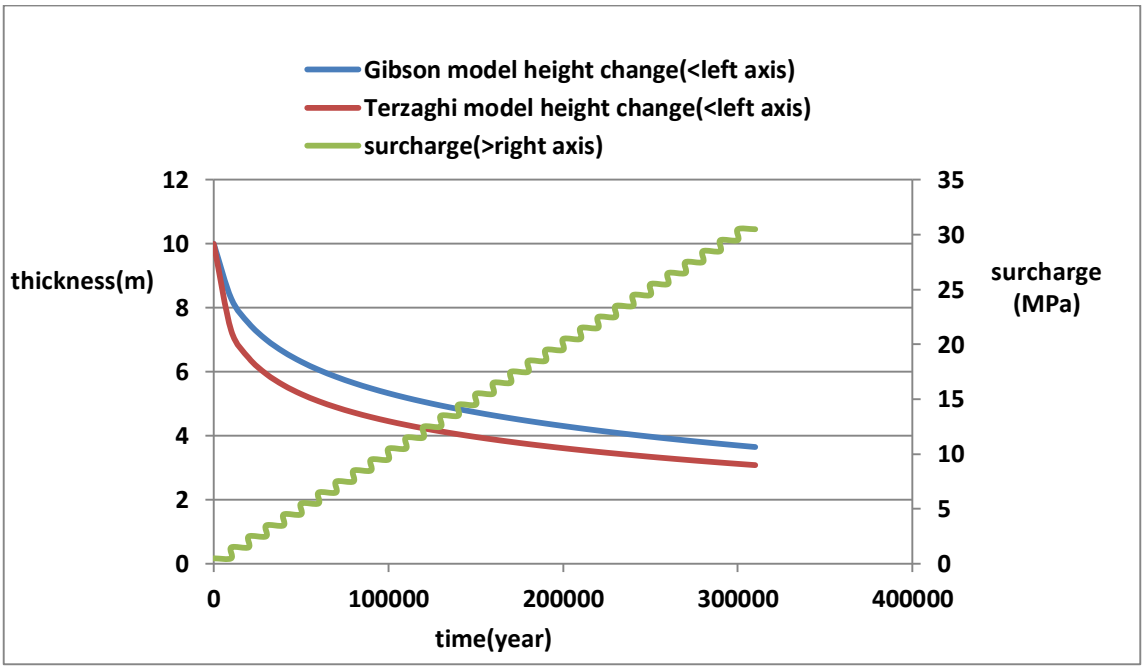

Figure 2.30 Comparison of sediment thickness evolution between updating Terzaghi and Gibson model

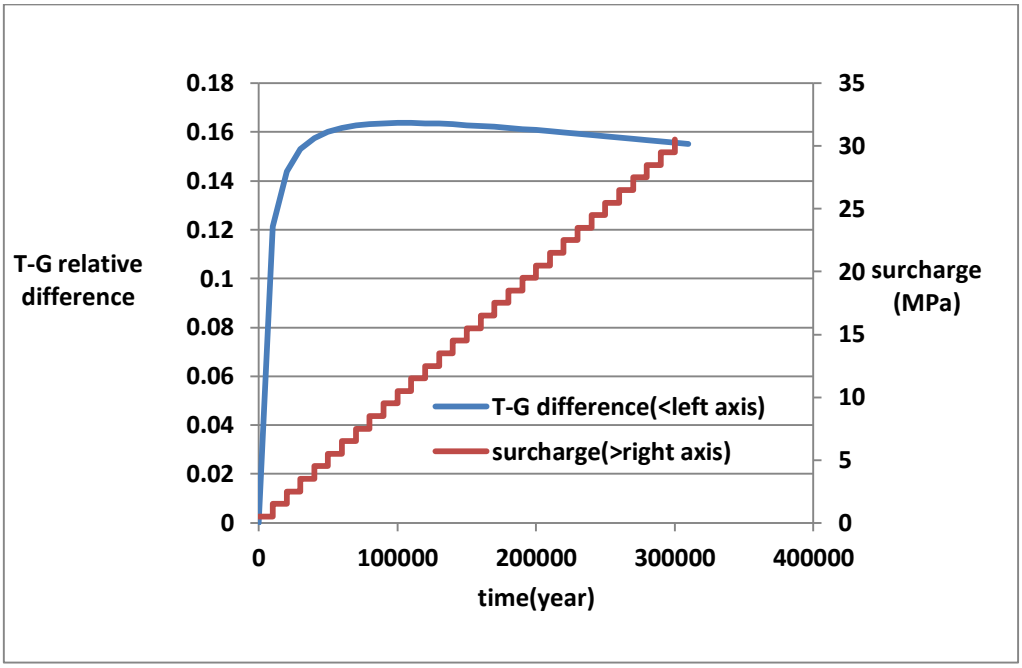

Figure 2.31 Relative error evolution of updating Terzaghi model compared with Gibson model

Also there are some limitations for updating Terzaghi model, final settlement should be small to ensure the small strain in each step, which means both the time step and stress change should be small enough. Hence, local refine meshes and time step encryption should be used in some stress intense change region for small-strain model.

According to this PTIB model, calculation amount/time of Terzaghi model and accumulative total difference from Gibson model will increase greatly with the subsequent sedimentation in basin modelling.

Considering that this research object is shallow compaction, it is now safe to draw the conclusion that Gibson consolidation model is more convenient and accurate than small-strain ones (including modified ones) in large-strain shallow compaction.

2.5 Limitations of 1D model – necessity of multi-dimensional research

There are some limitations for 1D model in basin modelling in both mechanics and fluid flow, which will be illustrated by the following analysis based on a simple heterogeneous basin setting.

2.5.1 Laterally heterogeneous model

Sediment transport and overpressure generation (and dissipation) are coupled primarily through the impact of effective stress on subsidence and compaction, with consequent

impacts on flow properties. You and Person (2008) used mathematical modelling to explore the interactions between groundwater flow and diffusion-controlled sediment transport within alluvial basins in a half-graben setting. Because of lateral variation in vertical permeability, proximal basin facies (generally coarser, with few fine-grained intervals) will have pore pressure close to hydrostatic levels, while distal fine-grained facies can reach near lithostatic levels of pore pressure due to a lack of vertical flow pathways. Lateral variation in pore pressure leads to differential compaction, which deforms basins in several ways. Differential compaction bends isochronal surfaces across the sand-clay interface.

You and Person (2008) restricted their analysis to continental alluvial rift basins where fluvial sediment transport processes dominate. They assumed a simple, half-graben basin configuration and purely vertical subsidence. As shown in **Figure 2.32**, proximal facies of the basin undergoes maximum subsidence and is proximal to the sediment source. The subsidence rate is assumed to decrease linearly from proximal end to the distal edge of the basin. There is no subsidence at the distal edge of the basin.

They made several assumptions about sediment supply to make it easier to focus on the relationship between overpressure generation, sediment compaction, and sedimentation. These include:

(1) The basin is hydrologically closed.

(2) Only alluvial sediment transport is considered.

(3) Sediment supply is specified along only one side of the basin.

(4) The initial elevation of basement is chosen as datum (i.e. sea level or 0m).

(5) Only two (high permeability sand and low permeability clay grained) facies are represented.

Models represent coarse grained facies as typical fan-head to mid-fan deposition in an alluvial fan, which is a mixture of conglomerate, sandstone and some silt; models represent fine grained facies as mid-fan to distal fan, which is a mixture of silt and clay. Coarse grained sediments are assumed to be much more permeable and deposited proximal to the sediment source area. The maximum deposition rate is at the position of distance-0 km, this rate Linear changes to zero at distance-100 km, as shown in **Figure 2.33**. Other parameters are shown in **Table 2.9**.

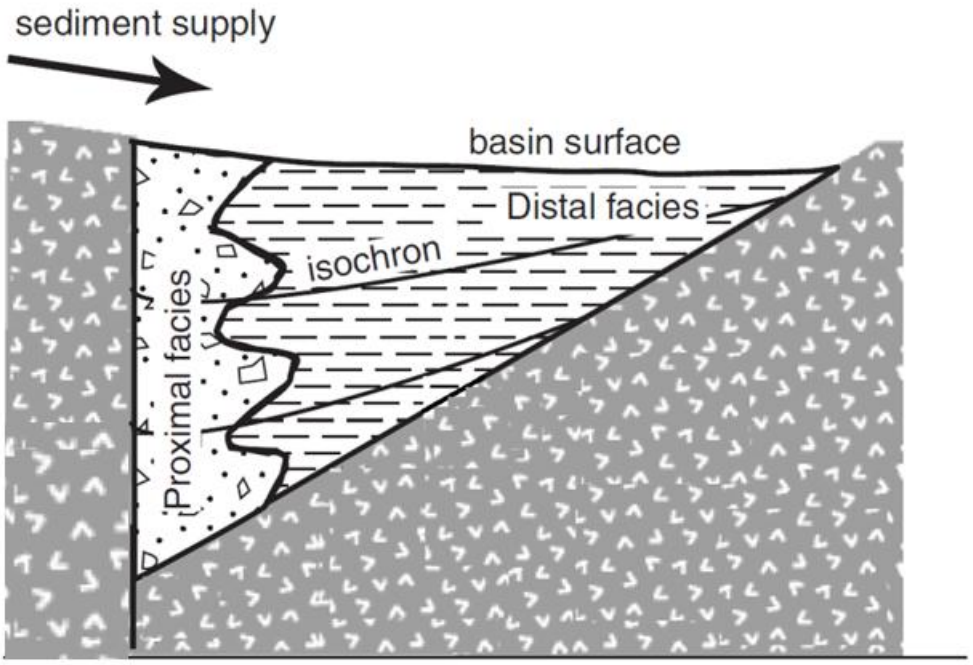

Figure 2.32 Schematic diagram depicting processes and selected variables considered in alluvial rift basin (You and Person, 2008).

Firstly, a homogeneous basin of coarse grained facies with permeability of $10^{-10}m^2$ is simulated as shown in **Figure 2.33**. Because of selective deposition and other sorting mechanism, an alluvial basin can seldom be treated as homogeneous. The model assigns permeability representative of relatively coarse and fine grained facies. **Figure 2.34** presents a simulation where sediment transport variables (i.e. sediment supply, subsidence rate, etc.) are fixed. There is a nine order of magnitude contrast in permeability between the proximal facies ($10^{-10}m^2$) and distal fine-grained facies ($10^{-19}m^2$). The proximal facies, with a higher permeability, compact significantly more than the distal facies. This is also indicated by the fact that isochrones bend steeply near the sand-clay front forming a hinge line.

The position of sand-clay front retreats at the top of the basin and the overall basin length is reduced. Reduction in basin length is less compared with the situation in **Figure 2.33** a-c while retreat in sand-clay front is more. The reason for less reduction in basin length for this run is that distal face does not compact as much as the previous homogeneous case (where distal face had a permeability of $10^{-10}m^2$). Two reasons may answer for this enhanced retreat of sand-clay front:

(1) Extra accommodation spaces created by compaction.

(2) Dynamic feedback of sediment transport and compaction.

Because of differential compaction, the topography of basin surface also changes (bending of isochron surfaces as shown in **Figure 2.34**). Because sediment transport is proportional to change of topography of basin surface, more sediment is deposited near the sand-clay front because topography changes greatly here. This cause the sand-clay front to retreat more compared with the homogeneous case (**Figure 2.33** a-c).

Overpressure profile (**Figure 2.34**) in this run can be divided into two parts: the proximal part which is near hydrostatic, and the distal part which is near lithostatic. Porosity reduces greatly with depth in proximal part. The distal part, on the other hand, hardly lost any porosity during filling of basin because pore pressure helps to support the vertical load.

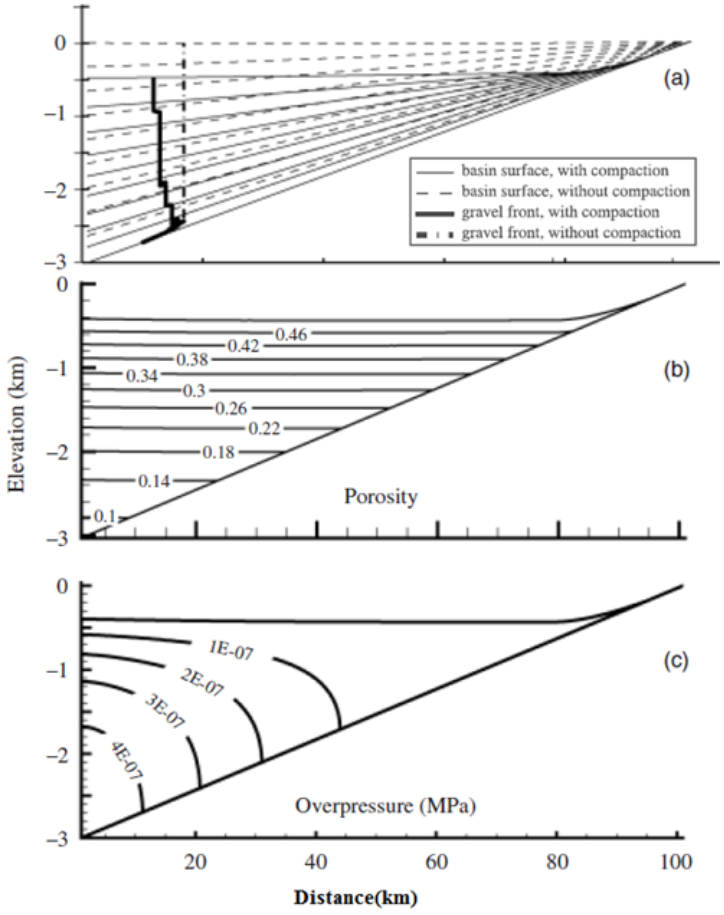

Figure 2.33 Modelling results of homogeneous model after 10Ma deposition. (a)-(c) are results from a homogeneous basin of coarse grained - sand facies with permeability of $10^{-10}m^2$. (a) is comparing isochrones and position of sand-clay front of this basin with a basin that has no compaction at all. (b) is showing contours of porosity of this basin. (c) is showing contour of hydraulic overpressure of this basin (You and Person, 2008).

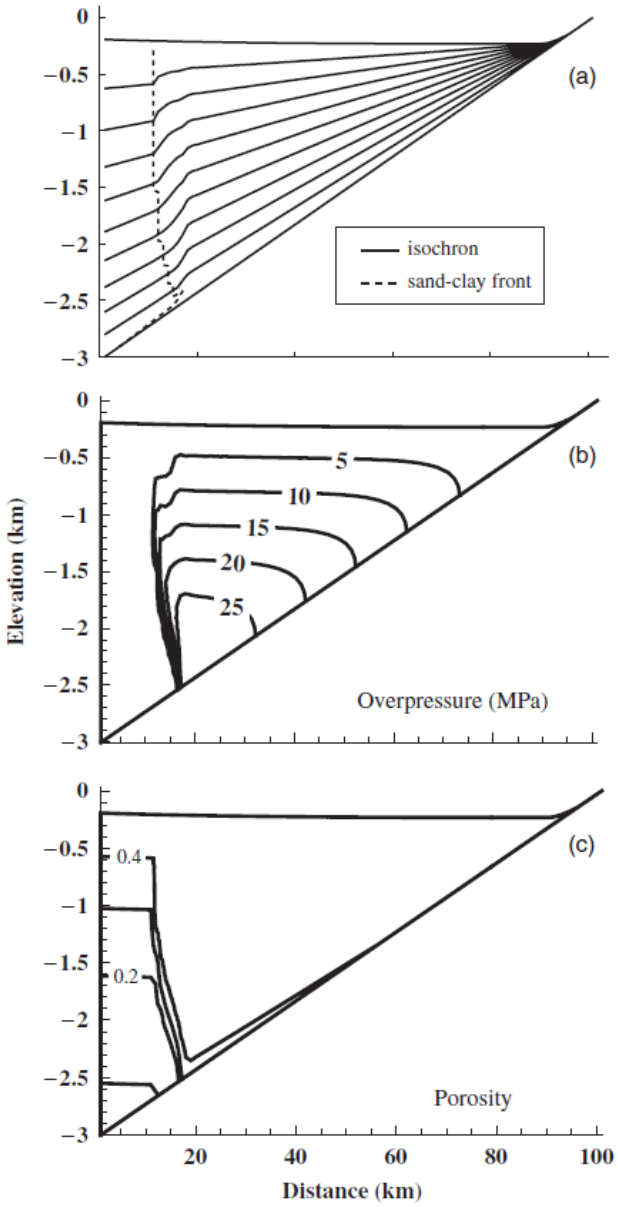

Figure 2.34 Modelling results of heterogeneous model after 10Ma deposition. Permeability of proximal face, landward of sand-clay front, is $10^{-10}m^2$ while permeability of distal face is $10^{-19}m^2$. (a) shows isochrones and position of sand-clay front in a heterogeneous basin. (b) contour of overpressure in this basin. (c) contour of porosity of this basin (You and Person, 2008).

2.5.2 Limitations of 1D model

1D model is applied to the continental alluvial rift basins. Corresponding parameters are shown in **Table 2.9**.

Parameter	Value	Units
density of water	1.0×10^3	kg/m^3
density of sediments	2.6×10^3	kN/m^3
deposition rate (left boundary of proximal, **Figure 2.32**)	3.0×10^{-7}	km/year
initial void ratio	1.0	-
effective stress - void ratio (coarse - proximal part)	$\sigma' = 3.2 \times 10^4 \ln(\frac{e}{1+e})$	kPa(σ')
effective stress - void ratio (fine - distal part)	$\sigma' = 3.2 \times 10^3 \ln(\frac{e}{1+e})$	kPa(σ')
permeability (coarse - proximal part)	1.0×10^{-10}	m^2
permeability (fine - distal part)	1.0×10^{-19}	m^2
Subsidence time	10.0	million years

Table 2.9 Parameters utilized in lateral heterogeneous model

Gibson-based 1D model simulation results at distance of 0 and 40 km (coordinate as shown in **Figure 2.34** c, '0 and 40' are positions that benefit later illustration) are presented in the following.

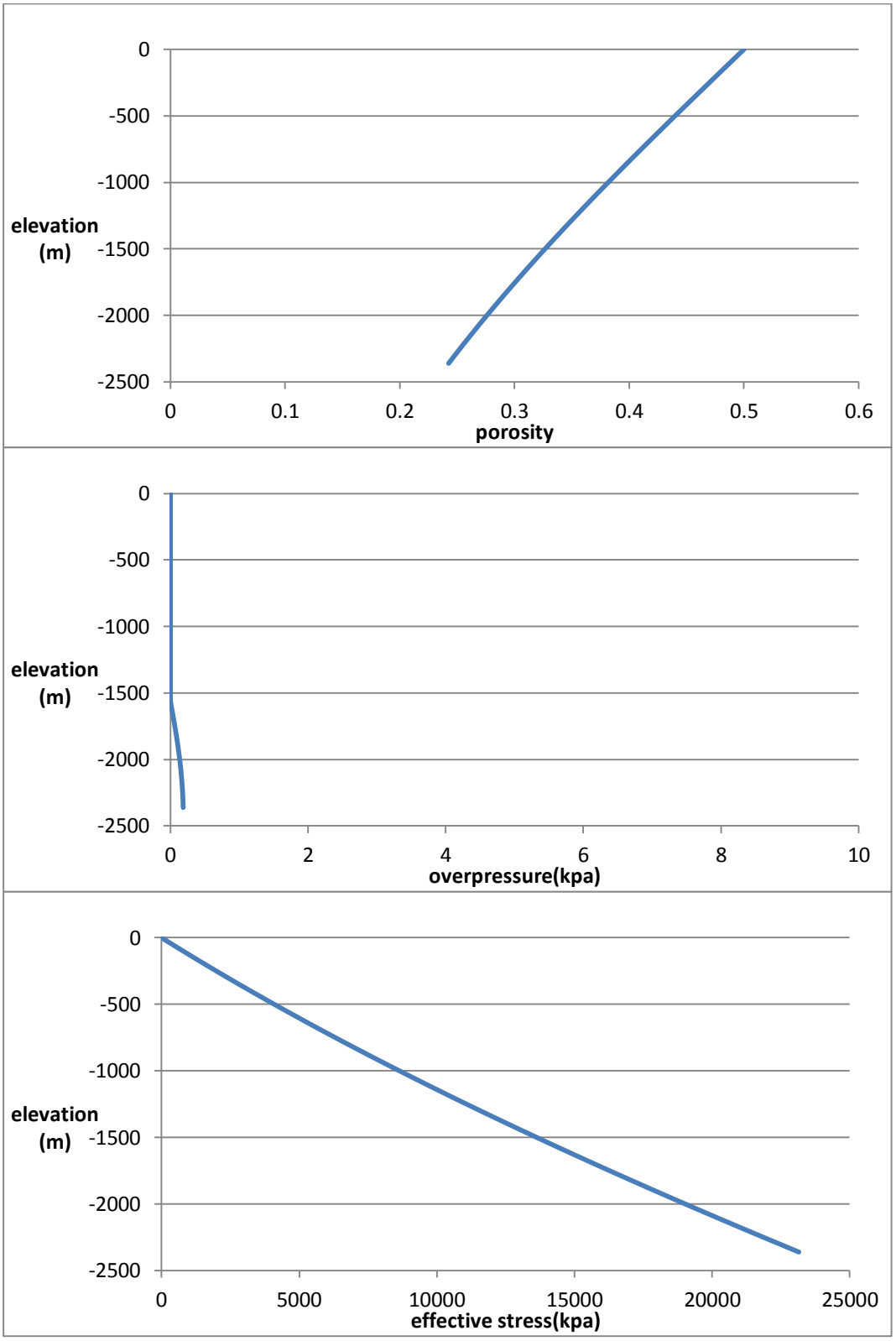

Figure 2.35 Simulation results at distance 0 km (coarse - proximal part), upper - porosity distribution, middle - overpressure distribution, lower - effective stress distribution

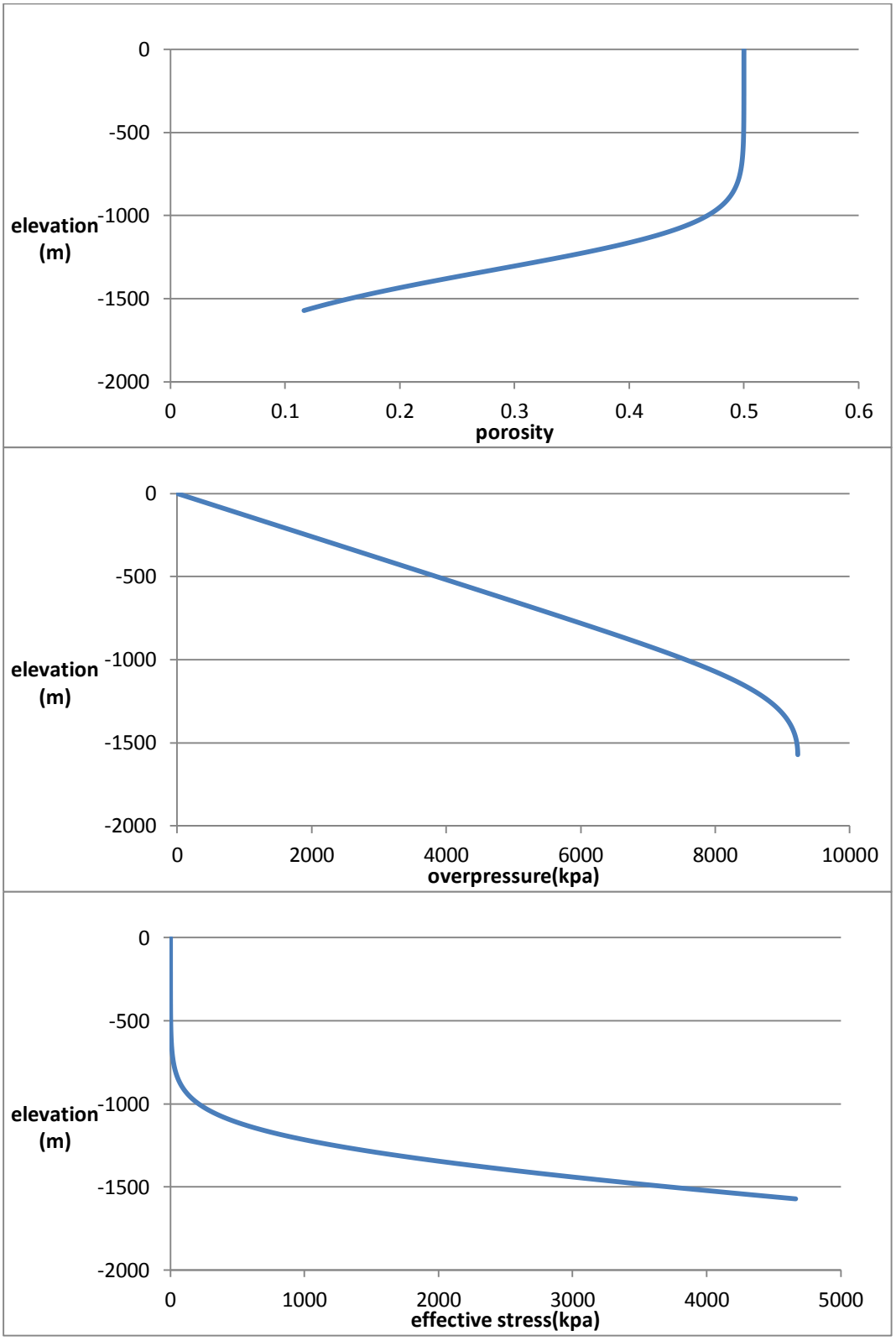

Figure 2.36 Simulation results at distance 40 km (fine - distal part), upper - porosity distribution, middle - overpressure distribution, lower - effective stress distribution

As can be seen from **Figure 2.34**, there are great differences between Gibson based model and You&Person's model for simulation results at distance 40 km (data deficient of You&Person's modelling limits precise comparison of the two models together). Horizontal flow and lateral deformation are supposed to answer for the difference. There are nearly no overpressure at distance 0 km due to high conductivity for the two models.

Compared with You and Person's model, there are two major obvious drawbacks for the 1D Gibson based model:

Firstly in pore pressure distribution, fluid flow is limited in vertical direction only and hence no horizontal flow in the Gibson based model. Hence fluid in the fine - distal part is not able to flow out through the coarse-proximal part, therefore no pressure gradient in horizontal direction as shown in **Figure 2.34** b. Also, the pore pressure is not continuous in horizontal direction when materials of two adjacent columns are different.

Secondly there are no horizontal deformations in the mechanics of the Gibson model. Correspondingly, the sand-clay front position keeps constant. Overpressure and basin evolve along two different paths.

Multi-dimensional models are necessary to better describe basin evolution when considering heterogeneous, multi-dimensional fluid flow and deformation.

2.6 Model application - Ursa Region, Gulf of Mexico

This section presents an example in which compaction/overpressure processes are expressed. The numerical tool is used to assess the history of rapid deposition under deepwater. However the numerical results do not agree well with observed overpressure data. The conclusion reached is that the discrepancies are due to effects that are not captured in 1D.

2.6.1 Ursa Region Geology

The Ursa Region is located 200 km southeast of New Orleans on the continental slope of the Gulf of Mexico. It is a salt-withdrawal mini-basin in 800 - 1400 meters of water, with sediments derived from late Pleistocene deposition by the Mississippi River system. The seafloor dips to the southeast and a zone of slope failures is present to the east of the Mars - Ursa region (**Figure 2.37**). The basin was well described by IODP a large number of researchers (Eaton, 1999; Flemings et al., 2005; Gay and IODP, 2005; Long et al., 2008; Winker and Booth, 2000; Winker and Shipp, 2002).

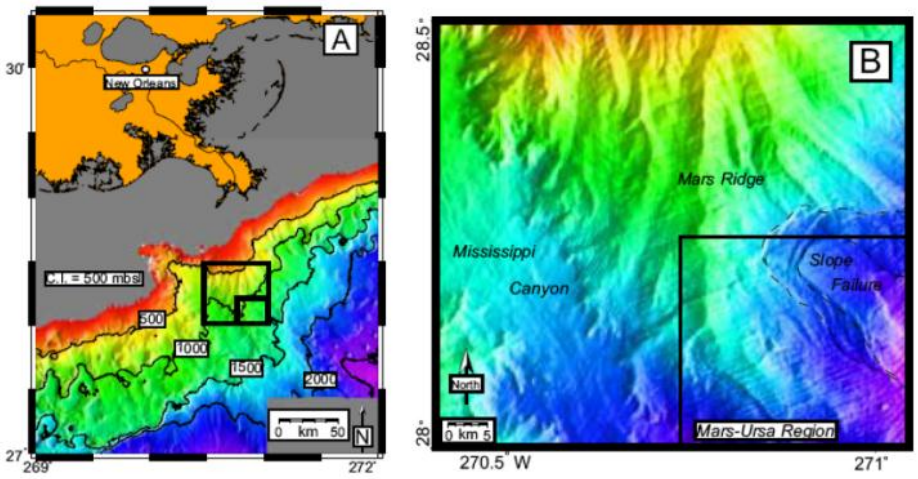

Figure 2.37 A: Base map showing Gulf of Mexico bathymetry and location of Ursa Region. B: Close up of Ursa Region showing the Mississippi Canyon and a submarine slope failure (Sawyer et al., 2007).

This study focuses on the shallow portions of Ursa Region above 1000 meters below seafloor (mbsf), over an area of approximately 900 square kilometres (**Figure 2.38**). This depth interval includes as its base the thick sandy package, called the Blue Unit (near1000m depth bellow sediment-water interface), and the sediments that overlie it (**Figure 2.39**).

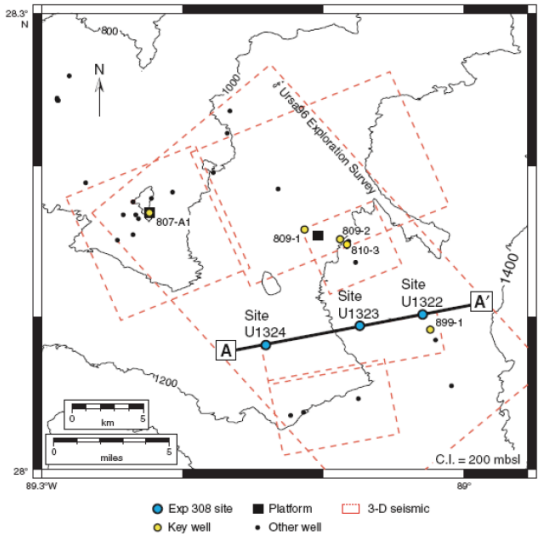

Figure 2.38 Ursa region study area, with survey limits (red lines), reference well 810-3, location of IODP drill sites U1324 and U324, and seismic cross - section A-A' indicated (Christopher, 2006; Flemings et al., 2005; Gay and IODP, 2005).

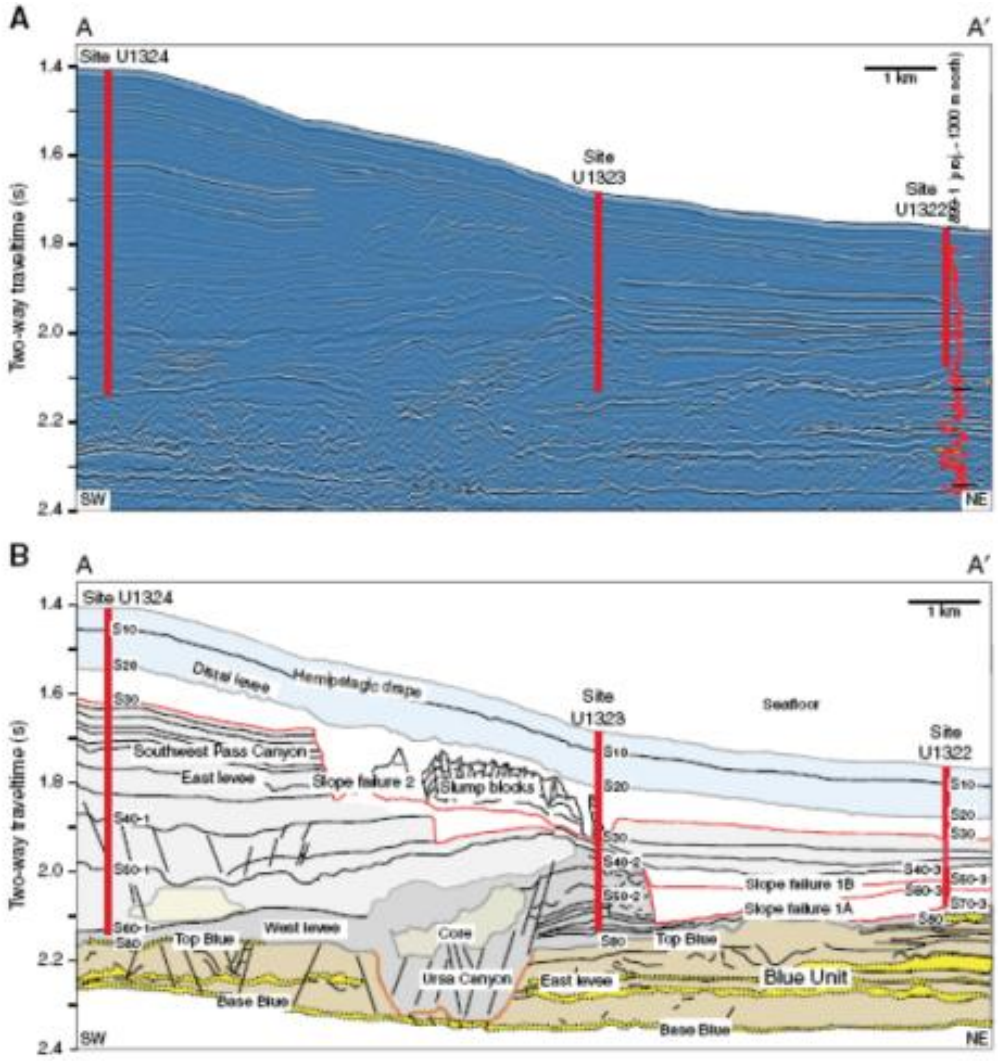

Figure 2.39 Seismic cross-section of Ursa Region showing interpreted sediment facies and major packages simulated in consolidation model. The 1-D Ursa model approximates a vertical section along U1324 (Christopher, 2006).

The Blue Unit is a unit of interbedded sand and mud, which extends over 150 km laterally. It is the thickest in the south-western part of the study area and becomes thinner in the north-eastern. The base of the Blue Unit is flat while the top reflects post-depositional erosion or other modification. The area is incised by two channel levee systems, the Ursa Canyon and the Southwest Pass Canyon. These systems have mud rich levees with sandy channel fill. They cut through the Blue Unit in an approximately north-south orientation. Above the channel levee systems, several mass transport complexes (MTCs) have been interpreted from seismic data (Christopher, 2006; Gay and IODP, 2005; Long et al., 2008). The geological history of this location has created a laterally-heterogeneous sequence of fine-grained sediments.

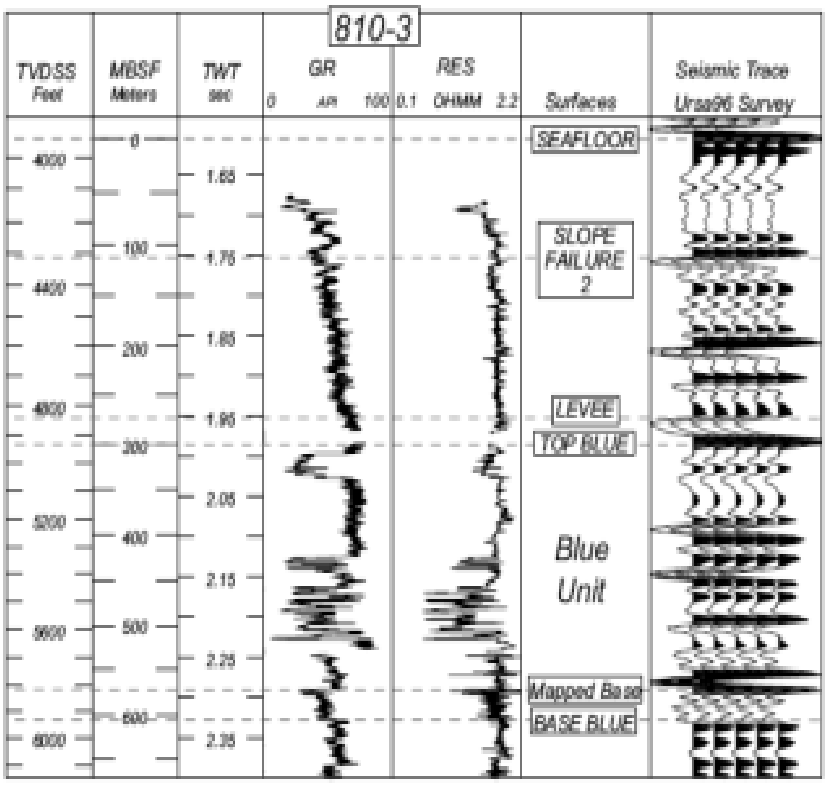

Figure 2.40 A representative well-log showing the gamma-ray (GR) and resistivity (RES) profiles with depth at well 810-3 in the Ursa Region. The Blue Unit is identified by a significant decrease in the GR and resistivity logs and shows layers of interbedded sand and shale (Sawyer et al., 2007).

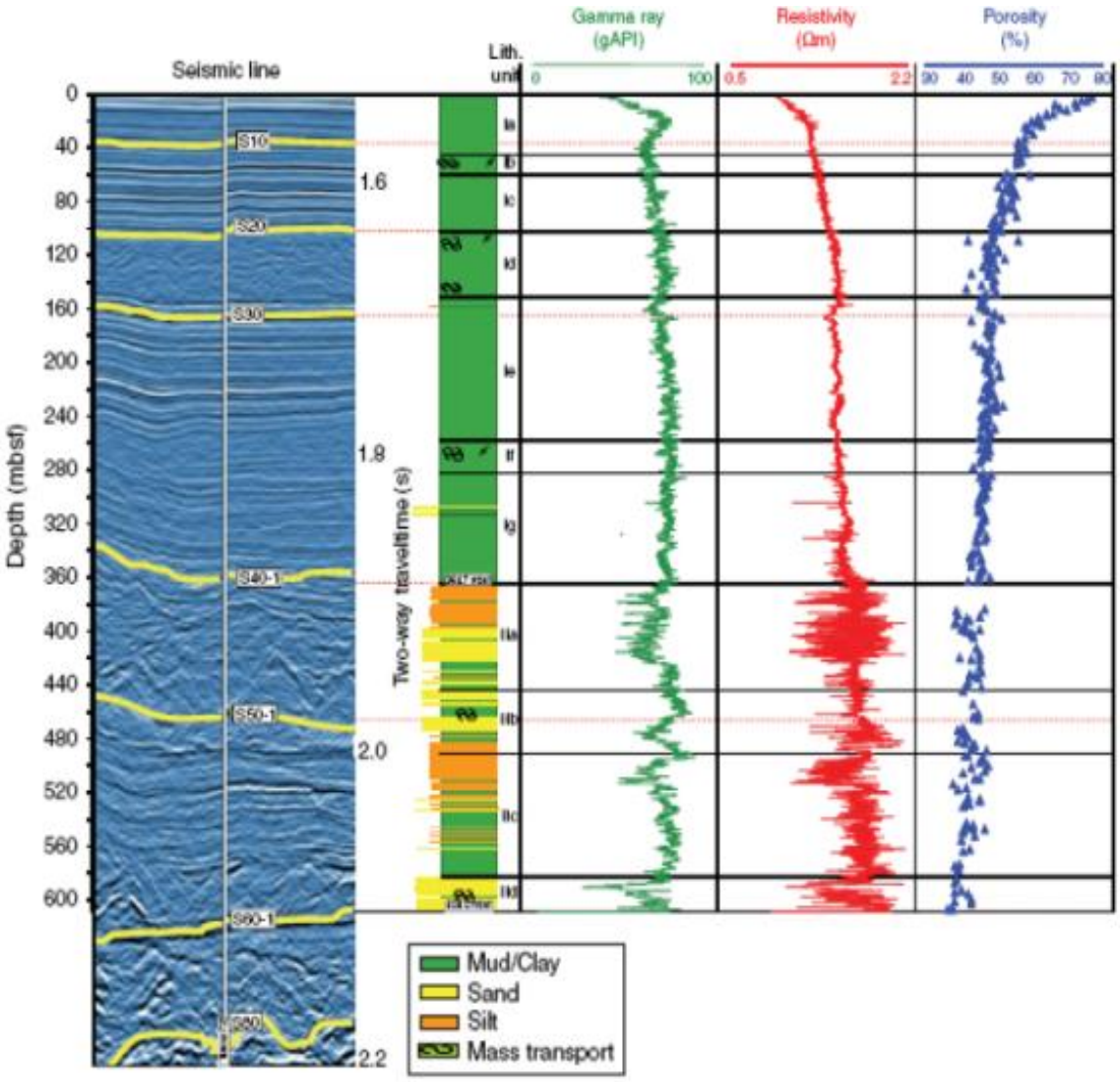

Figure 2.41 Well log from Site U1324 showing gamma ray, resistivity and porosity data for the 600 m of sediment above the Blue Unit at Ursa. A lithology key and seismic line is shown to identify key units (Christopher, 2006).

The Ursa Region system is of particular interest as an over-pressured system, which has been extensively mapped and drilled. Overpressure at Ursa is attributed to rapid deposition of the shallow sediments during the late Pleistocene, and no causes from thermal or diagenetic reasons, nor to lateral transfer of fluid energy from elsewhere. Average sedimentation rate for Ursa Region was calculated to be 1.5 cm/y from seismic data. The presence of the foraminifera Globorotalia flexuosa at the Base of Blue Unit (as shown in **Figure 2.40**) puts this datum at approximately 70 thousand years (ka) ago ((Sawyer et al., 2007; Winker and Booth, 2000). Seismic surface S60 is dated to be approximately 60 ka, while surface S30 is dated at 25 thousand years.

The overpressure distribution has made drilling through the Blue Unit difficult and costly (Eaton, 1999). This study seeks to further assess the overpressure field of the Ursa Basin by 1D modelling.

Christopher (2006) used the following compaction model to analyze the overpressure evolution of Ursa Basin as shown in **Equation 2.27** (Gordon and Flemings, 1998).

$$\frac{\partial p}{\partial t} = \frac{k(1-\phi)^2}{\mu St \rho_f g_{ra}} \frac{\partial^2 u}{\partial z^2} + \beta_p \frac{\phi}{(1-\phi)St} \frac{\partial \sigma'}{\partial t}$$
$$St = \frac{\phi \beta_p}{(1-\phi)} \tag{2.27}$$

This one-dimensional hydrodynamic model simulates the evolution of pressure and porosity in sedimentation. The first term on the right hand side models pressure diffusion. The controlling parameters for pressure diffusion are conductivity (k), fluid viscosity (μ), and porosity (ϕ). St is a storage coefficient dependent on porosity and matrix compressibility (β_p). g_{ra} is acceleration due to gravity, and ρ_f is fluid density. The second term on the right hand side is a source term due to sediment loading. This term is primarily controlled by the sedimentation rate. Compared with Gibson's model, this model is directly based on the physical process of pressure build-up and dissipation, moreover it considers the sedimentary effect. However, it ignores the effect of self-consolidation and hence may underestimate overpressure.

2.6.2 1-D simulation parameters

Two one-dimensional models of the Ursa Region are constructed as representative vertical sections based on the seismic cross-section and well U1324 (**Figure 2.41**). The sediments consist of four major litho-stratigraphic layers: Base shale, Blue Unit, Subunit II and Subunit I (from bottom to top). Subunit I (0 - 340 mbsf at Site U1324) is characterized by predominantly mud with some evidence of mass transport deposits. Subunit II is composed of interbedded silt, sand and mud with more frequent traces of mass transport deposits. This lithofacies describes the sediments from 340 mbsf to the top of the Blue Unit at Site U1324.

Simulation constants such as fluid density, viscosity and gravity are listed in **Table 2.10**.

Parameter	Symbol	Value	Units
fluid Density	ρ_f	1024	kg/m^3
grain Density	ρ_s	2720	kg/m^3
reference porosity	ϕ_0	0.61	-
matrix compressibility	β_p	1.48 x 10^{-7}	Pa^{-1}
viscosity	μ	1.00	cp

Table 2.10 Simulation parameters in Ursa Region modelling

Layer thicknesses were defined based on the depths measured at Site U1324. For layers not penetrated by the IODP well, layer thicknesses were estimated from seismic data. The base shale was assigned a thickness of 150 m, which corresponds to 10 thousand years of sediments accumulating at the sedimentation rate of 0.015 m/y. As an initial test boundary condition, the base of the model was defined as a non-flow boundary. Fluid flow is laterally restricted in the model by imposing non-flow boundaries on the sides.

Approximate ages for the base of the Blue Unit (70 thousand years), surface S60 (60 thousand years) and surface S30 (25 thousand years), given in the IODP preliminary report, are used to calculate the sedimentation rates required to produce the existing sediment thicknesses (**Table 2.11**, **Table 2.12**). Total simulation time is 80 thousand years to include deposition of the shale layer below the Blue Unit.

The seismic surfaces are identified and age dates are given as appropriate. The representative lithofacies used to model the layers are identified at **Figure 2.42** and **Figure 2.43**. Flow is laterally restricted and a non-flow boundary is imposed at the base.

Layer	Thickness (m)	Sedimentation rate (m/y)	Timing of deposition (thousand years)
Subunit I Seafloor to S20	100	0.007	0-15
Subunit I S20 – S30	60	0.006	15-25
Subunit I S30 – S40	180	0.014	25-38
Subunit II S40 – S60	300	0.014	38-60
Subunit II S60 – S80	30	0.006	60-65
Blue Unit	150	0.015	65-75
Base shale	150	0.015	75-85

Table 2.11 The Ursa Region U1324 models are comprised of multiple layers with varying thicknesses, sedimentation rates and timing of deposition

Layer	Thickness (m)	Sedimentation rate (m/y)	Timing of deposition (thousand years)
Subunit I Seafloor to S20	90	0.006	0-15
Subunit I S20 – S30	40	0.004	15-25
Subunit I S30 – S40	20	0.002	25-38
Subunit II S40 – S60	90	0.004	38-60
Subunit II S60 – S80	10	0.002	60-65
Blue Unit	150	0.015	65-75
Base shale	150	0.015	75-85

Table 2.12 The Ursa Region U1322 models are comprised of multiple layers with varying thicknesses, sedimentation rates and timing of deposition.

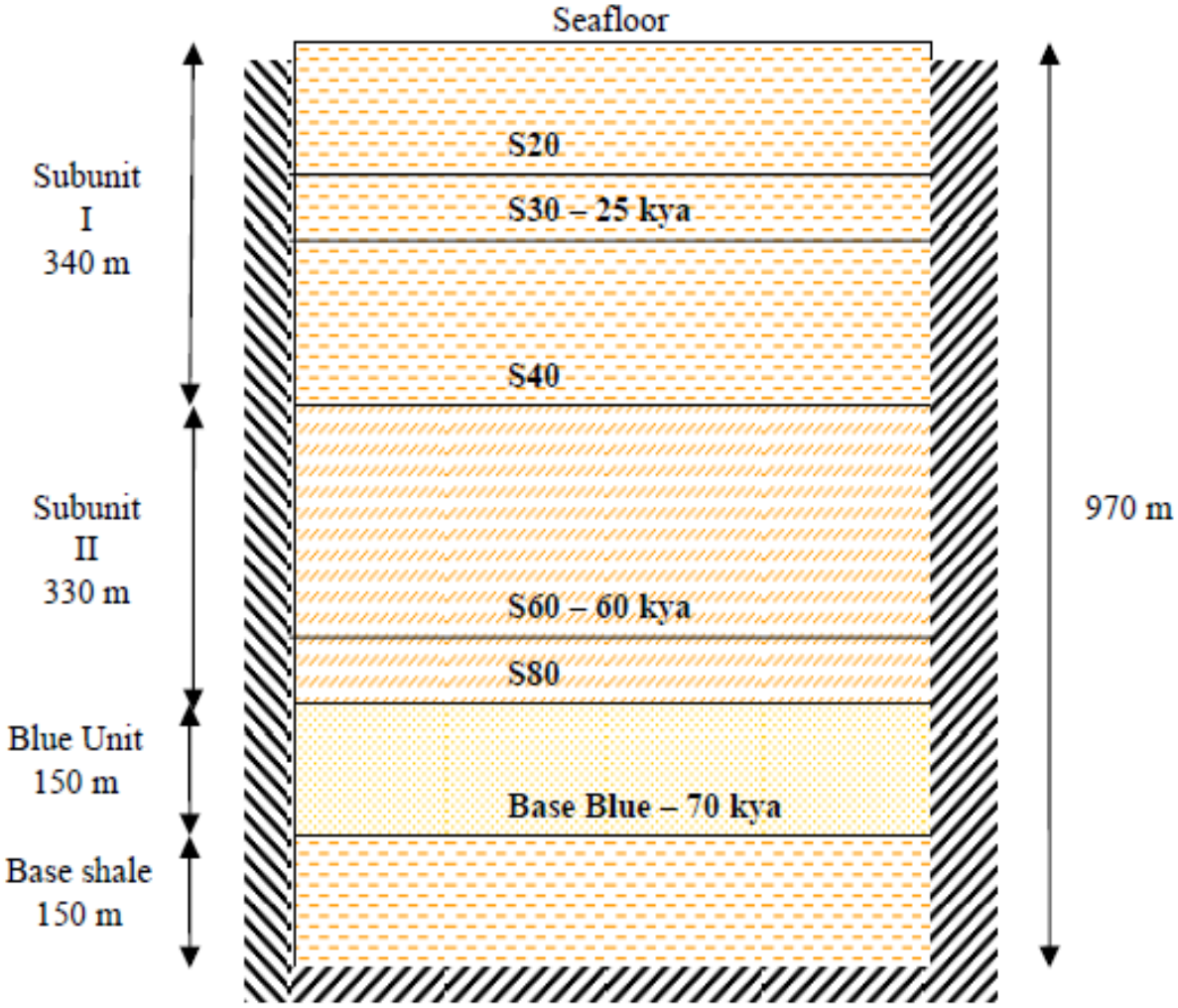

Figure 2.42 1-D version of the Ursa Region at Site U1324 layers identified from seismic and well-log ties (Christopher, 2006).

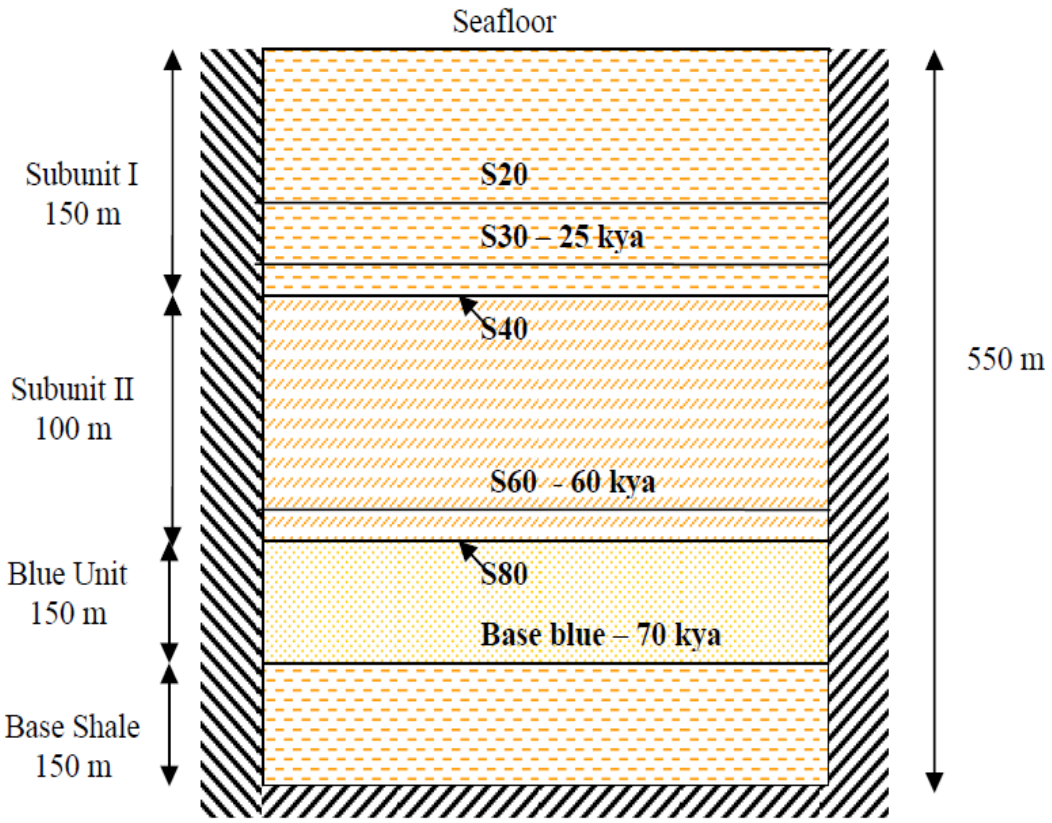

Figure 2.43 1-D version of the Ursa Region at Site U1322 layers identified from seismic and well-log ties (Christopher, 2006).

The lithology and hydraulic conductivity of the Ursa Basin was characterized using representative conductivity - porosity functions for the lithological layers defined from seismic and core descriptions. Consolidation experiments on saturated core samples from several depths at Site U1324 were performed to determine the relationship between hydraulic conductivity and porosity for the Ursa sediments (Long et al., 2008). These relationships were used to approximate Subunit I and Subunit II lithofacies. For the Blue Unit, 10% - 90% shale content material is adopted, with data from Caprocks project phase II (Ma and Couples, 2008).

Model parameters of different materials are shown in the following:

(1) Sub Unit I:

$$k = 3.5839\times10^{-10}\exp(\frac{e}{0.112}),\ (k\ \text{- m/d});\ e = 0.8 - 0.4126\log_{10}(\frac{\sigma'}{3\times10^{3}}),\ (\sigma'\ \text{- kPa}).$$

(2) Sub Unit II:

$$k = 1.3072\times10^{-9}\exp(\frac{e}{0.1015}),\ (k\ \text{- m/d});\ e = 0.45 - 0.2478\log_{10}(\frac{\sigma'}{7\times10^{3}}),\ (\sigma'\ \text{- kPa}).$$

(3) Blue Unit: there are no hard data for this layer, a wide range of materials are utilized in the modelling. Hence, 10%, 30%, 50%, 70%, 90% clay contents and pure sand are adopted for evaluation.

As for sand,

'conductivity - void ratio' relationship is: $k = 426.47e^{7.1747}$, (k - m/d)

'void ratio - effective stress' relationship is : $e = 2.421 - 0.2\ln(\sigma')$, ($\sigma'$ - kPa)

The pure sand conductivity is 9 orders greater than that of most clays. It is unpractical to consider two conductivities of 9 orders' differences in numerical calculation. Moreover conductivity increase exerts little effect on overpressure and thickness evolution when conductivity reaches a certain value, as shown in **Figure 2.46**. Hence, conductivity of 7 orders less than pure sand is adopted for Blue layer.

(4) Base shale adopts material of sub Unit I (no hard data).

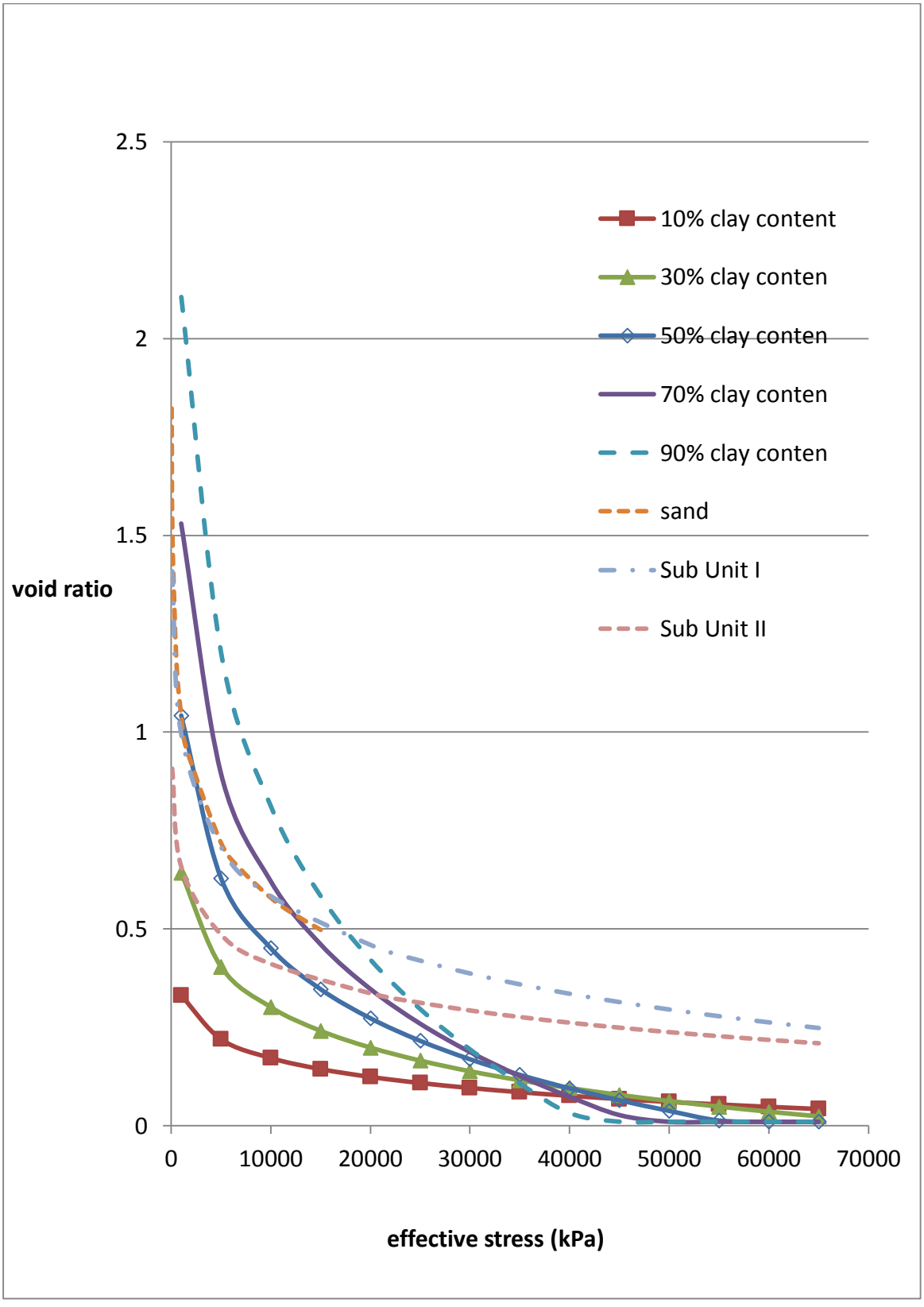

Figure 2.44 All effective stress – void ratio relationships utilized in modelling (Christopher, 2006; Ma and Couples, 2008).

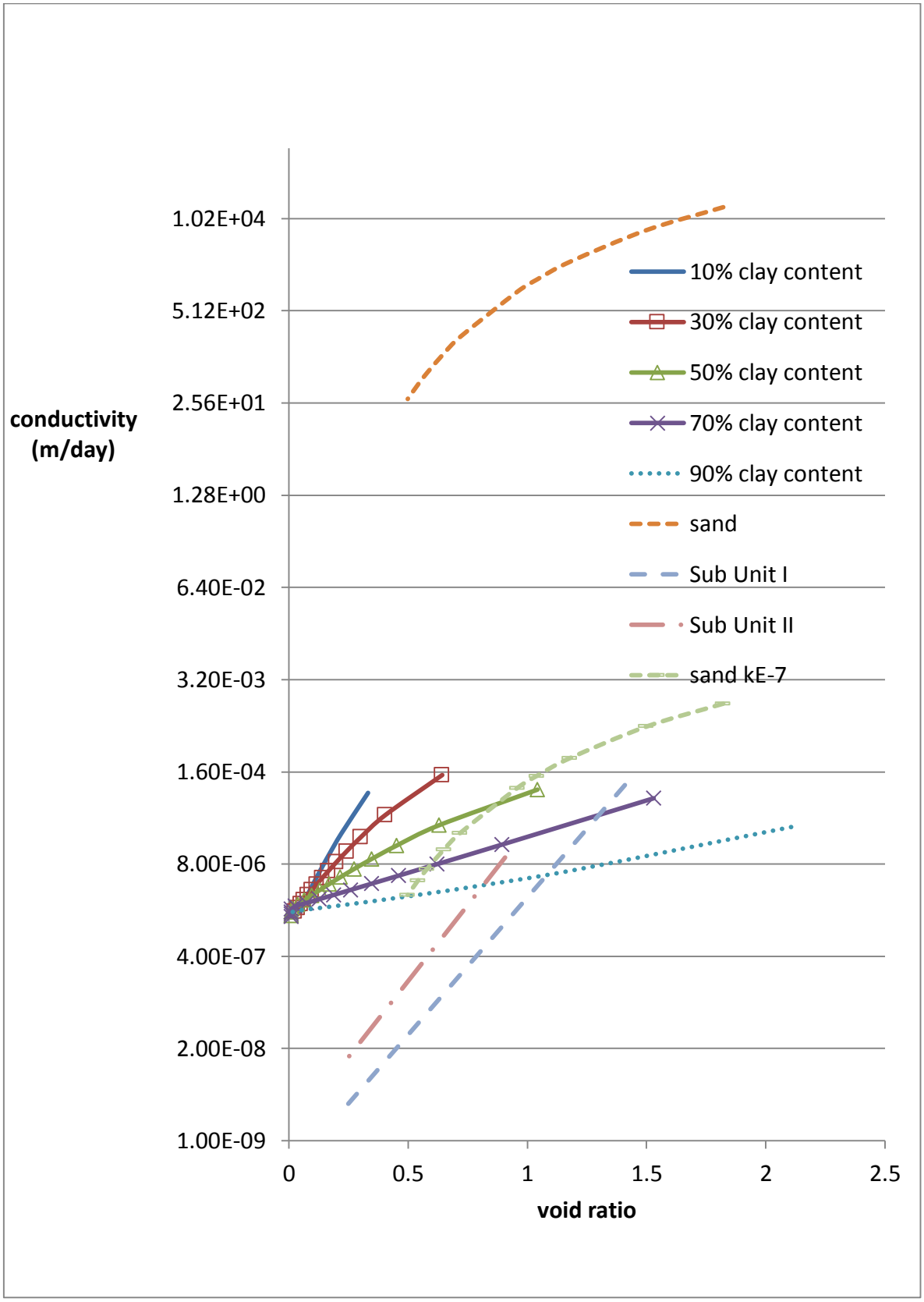

Figure 2.45 All conductivity – void ratio relationships ('sand kE-7' means sand conductivity reduces 7 orders) utilized in modelling (Christopher, 2006; Ma and Couples, 2008).

2.6.3 Modelling results

Overpressure prediction of Site U1324 is shown in **Figure 2.46**. For 0-50 mbsf, this research meets the IODP estimation well, both nearly zero-overpressure, while Christopher (2006) over predicts IODP estimation. Between 50 - 200 mbsf, this research and Christopher both over predict IODP estimation. Between 200 - 400 mbsf, this research and Christopher's overpressures closely approach the IODP estimation. Below 400 mbsf, the Christopher's model predicts only 80% of the overpressure estimated by the IODP. Overpressures prediction of this research is closer but over predicts IODP estimation. The highest overpressure will generate when all materials are Unit II (lower conductivity).

Overpressure prediction of Site U1324 is shown in **Figure 2.47**. For 0-50 mbsf, this research meets the IODP estimation well, both nearly zero-overpressure. This research over predicts IODP estimation deeper than 50 mbsf.

The following points need special attentions:

(1)Variation of materials in Blue unit exerts small influence on the final overpressure distribution.

(2) As shown in **Equation 2.27**, Gordon and Flemings' model ignores the effect of self-consolidation and this may answer for the underestimation of overpressure.

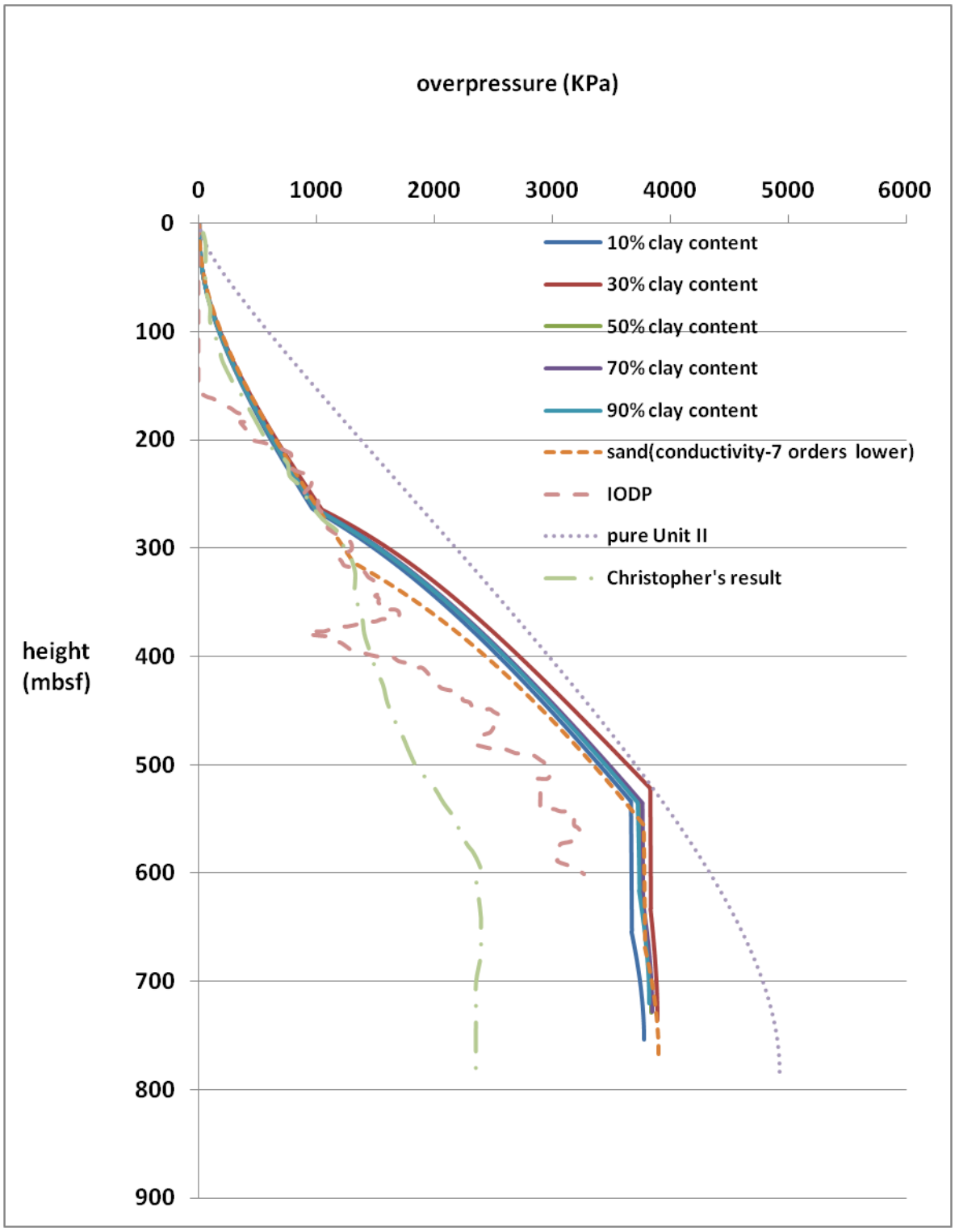

Figure 2.46 Overpressure prediction and IODP estimation for Site U1324

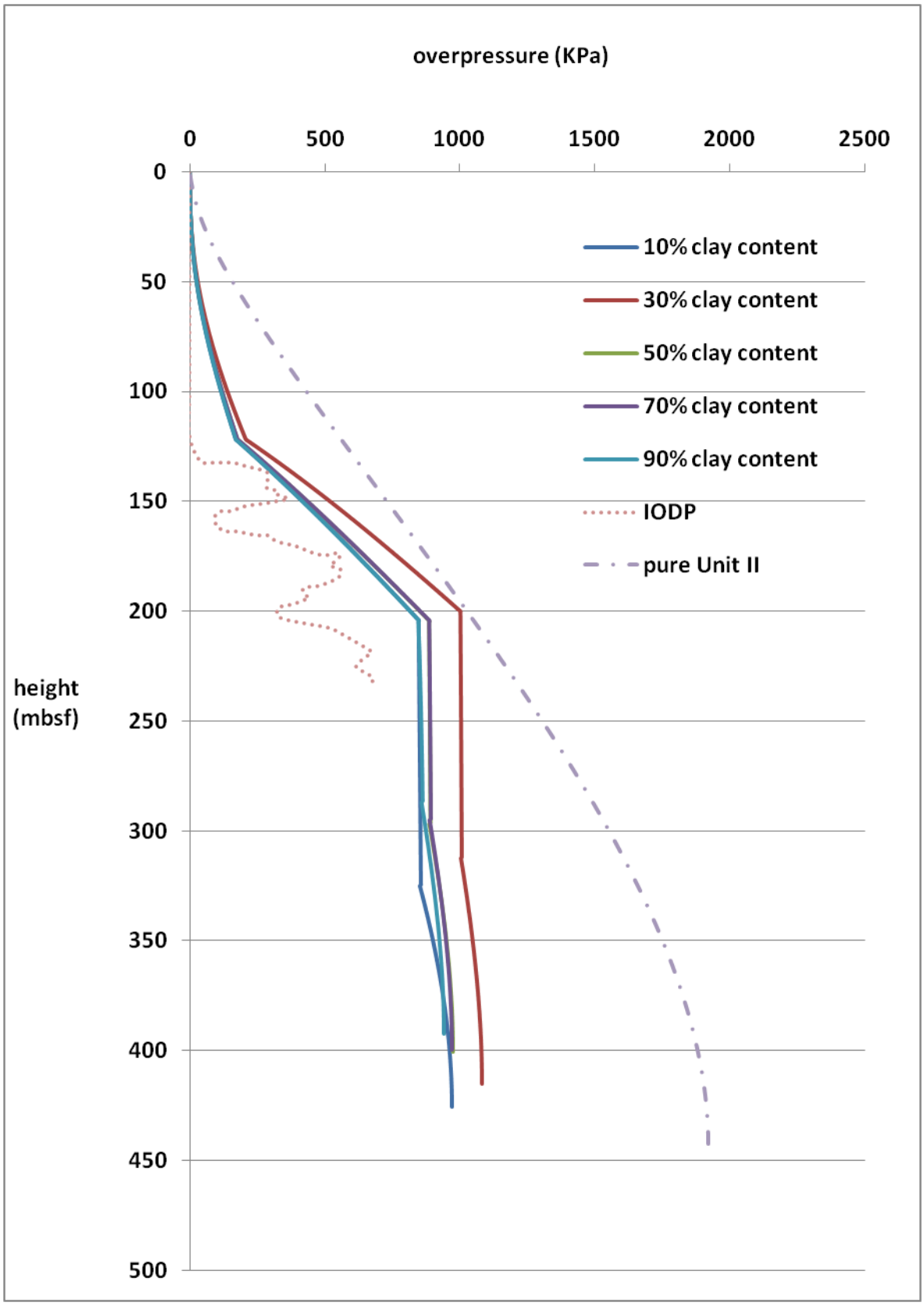

Figure 2.47 Overpressure prediction and IODP estimation for Site U1322.

As mentioned above, the sedimentation rates in Christopher's model are those which would give the current thicknesses without consolidation. However, the final thicknesses are obviously smaller than the current thicknesses as shown in **Figure 2.46** and **Figure 2.47**. This research tries to find the optimized/approximate-right sedimentation rates that result in the current thicknesses after consolidation. Site U1324 and Site U1322 are utilized for illustration, in which Blue Unit is 10% clay content material.

This correction of sedimentation rates leads to an even higher prediction of overpressure for Site U1324 as shown in **Figure 2.48**. The optimized sedimentation rates are shown in **Table 2.13**, there are small differences on the final thickness between the current thicknesses and modelling thickness as shown in **Table 2.14**. This tend also applies in Site U1324 as shown in **Figure 2.49**, **Table 2.15** and **Table 2.16**.

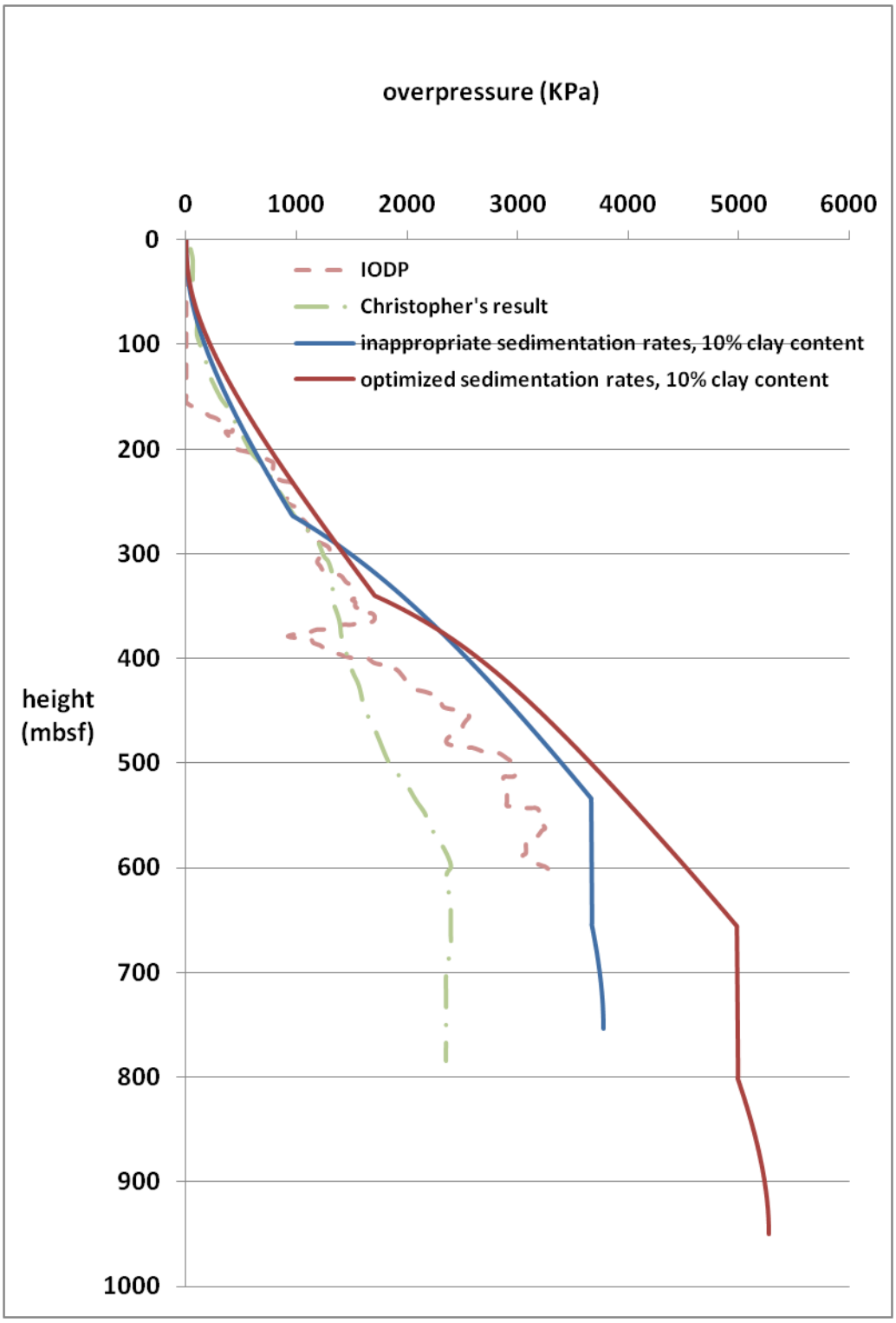

Figure 2.48 Overpressure prediction of different sedimentation rates and IODP estimation for Site U1324

Layer	Initial thickness (m)	Timing of deposition (thousand years)	Sedimentation rate (m/y)
Subunit I Seafloor to S20	130	15	0.008667
Subunit I S20 – S30	90	10	0.009000
Subunit I S30 – S40	240	13	0.018462
Subunit II S40 – S60	330	22	0.015000
Subunit II S60 – S80	60	5	0.012000
Blue Unit	185	10	0.018500
Base shale	225	10	0.022500

Table 2.13 The optimized sedimentation rates for Site U1324

Layer	Modelling thickness (m)	Current thickness (m)	Relative difference of modelling thickness from current thickness
Subunit I Seafloor to S20	103.3413	100	0.033413
Subunit I S20 – S30	69.09227	60	0.151538
Subunit I S30 – S40	168.0683	180	0.066287
Subunit II S40 – S60	283.3762	300	0.055413
Subunit II S60 – S80	32.64193	30	0.088064
Blue Unit	144.2826	150	0.038116
Base shale	149.1818	150	0.005454

Table 2.14 Relative difference of modelling thicknesses from current thicknesses for Site U1324

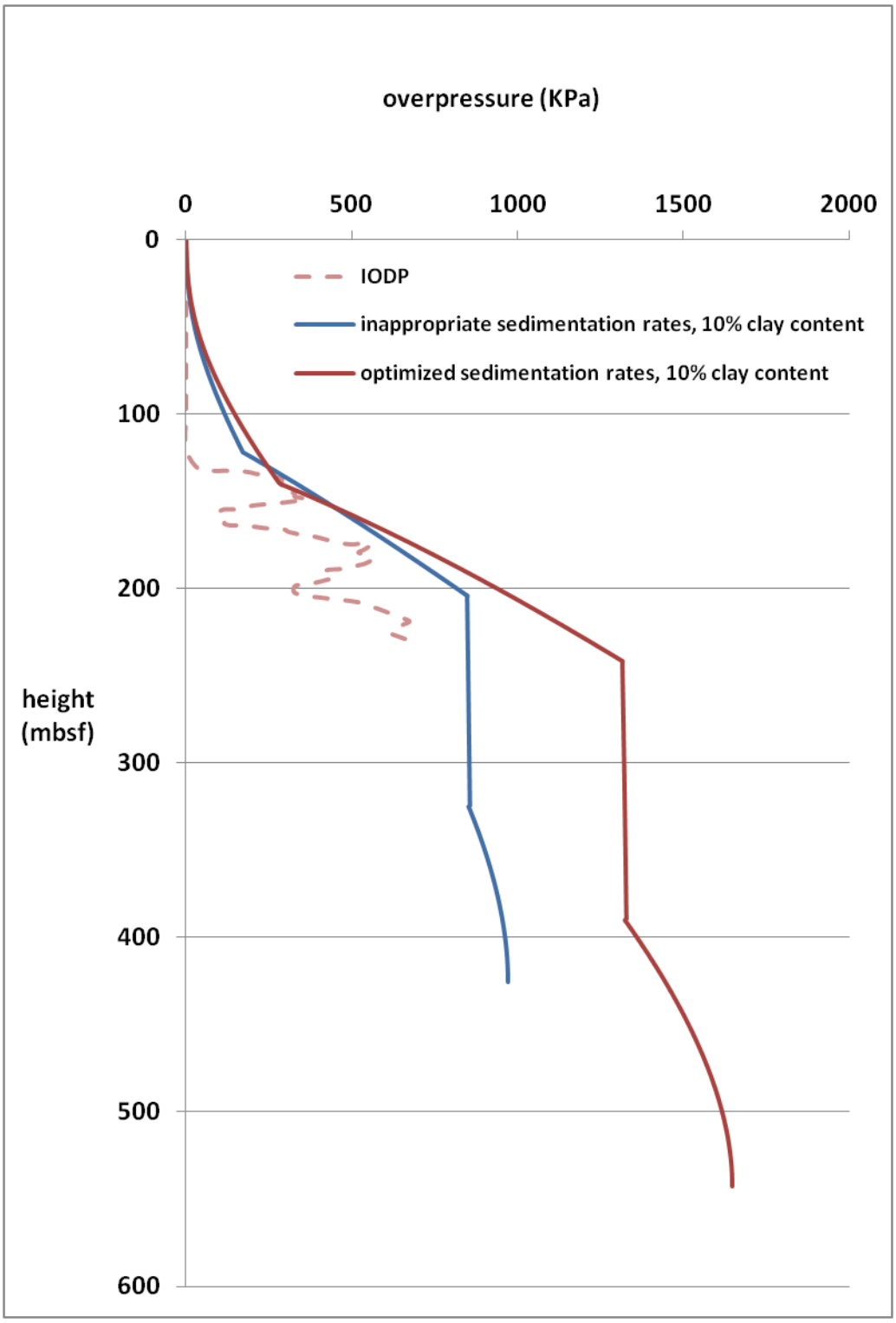

Figure 2.49 Overpressure prediction of different sedimentation rates and IODP estimation for Site U1322

Layer	Initial thickness (m)	Timing of deposition (thousand years)	Sedimentation rate (m/y)
Subunit I Seafloor to S20	100	15	0.006667
Subunit I S20 – S30	50	10	0.005000
Subunit I S30 – S40	30	13	0.002308
Subunit II S40 – S60	110	22	0.005000
Subunit II S60 – S80	20	5	0.004000
Blue Unit	190	10	0.019000
Base shale	230	10	0.023000

Table 2.15 The optimized sedimentation rates for Site U1322

Layer	Modelling thickness (m)	Current thickness (m)	Relative difference of modelling thickness from current thickness
Subunit I Seafloor to S20	77.1805	90	0.142439
Subunit I S20 – S30	39.55083	40	0.011229
Subunit I S30 – S40	23.1855	20	0.159275
Subunit II S40 – S60	86.41796	90	0.039800
Subunit II S60 – S80	15.90837	10	0.590837
Blue Unit	147.7504	150	0.014997
Base shale	152.6937	150	0.017958

Table 2.16 Relative difference of modelling thicknesses from current thicknesses for Site U1322

2.6.4 Model application conclusion

The new developed simulator is applied to study the sedimentation of Ursa Region in Gulf of Mexico. However the numerical results from the simulator do not agree well with observed overpressure data.

Many factors may explain the over prediction. Firstly, the data utilized in the model may not be fully representative. IODP curves, with many turning points, show the characteristics of multi-layer system. The assumption of 4 layers may not be enough, and therefore a finer-scale simulation is required.

Secondly, horizontal flow and mass transport process need to be considered. The plot of overpressure versus depth shows that at several places there are reductions in pressure with increase in depth. These "regressions" can be induced by lateral fluid flow, and hence cannot be explained within a 1D flow regime. Lateral fluid flow may bring overpressure decrease or increase. Moreover, the existence of mass transport deposits, and their sudden loading or unloading effects, is not fully considered.

Correspondingly, the following improvements are required to address the problems. Firstly, a more fine-scale model and consolidation parameters should be adopted in the 1D model. Secondly, multi-dimensional models are required to solve the problems of lateral fluid flow and mechanical-loading heterogeneity.

2.7 Discussion and Conclusion for one dimensional large-strain shallow compaction simulator development

In comparison with other large-strain consolidation models, the Gibson model is reasonable simple, and has been further developed, in this thesis work, into a partial large-strain basin modelling simulator. The simulator can be applied to complex geological processes such as complex loading and unloading conditions.

The developed model is applied to Ursa Region, Mississippi canyon area, Gulf of Mexico. However, it over-predicts the pressure of Ursa region with respect to what has been estimated from the Integrated Ocean Drilling Program. IODP curves, with many turning points indicate the assumption of 4 layers may not be enough, and therefore a finer-scale simulation or upscaling is required. And multi-dimensional models are required to address the problems of lateral fluid flow and mechanical-loading not along vertical direction only. Similarly, the results on the laterally heterogeneous alluvial rift basin model show that multi-dimensional models are necessary to better describe basin evolution when considering lateral heterogeneous, multi-dimensional fluid flow and deformation.

It is then concluded that upscaling and multi-dimensional large-strain model are necessary.

Chapter 3 One dimensional large-strain consolidation upscaling

This chapter studies 1D upscaling methods and upscaled properties of multi-layer systems. An analytical upscaling method for both small-strain and large-strain consolidation based on some simplifications is presented firstly in **Chapter 3.1**. Multi-layer small-strain (Terzaghi) and large-strain (Gibson) consolidation is solved with the transform matrix and Laplace transformation.

Secondly, with the numerical simulator developed in **Chapter 2**, sedimentation characteristics of multi-layer system are studied in **Chapter 3.2**. Analytical upscaling can provide intuitive guidance. Numerical upscaling will provide a more comprehensive understanding. Sedimentation of semi-infinite layers is common, such as channel levee systems. Large-strain consolidation of layered systems is studied by numerical methods in **Chapter** 0.

Inversion of deposited sediments' petrophysical properties is important for accurate basin modelling. Thirdly, this research demonstrates that soil properties of large-strain consolidation can be obtained through inversion in **Chapter 3.4**. Furthermore, the inversion technique is extended for multi-layer system. Similar to well testing, this study shows that it is feasible to obtain heterogeneous sediments' properties using this approach.

These research areas reveal the compaction behaviours of heterogeneous multi-layer systems, and propose feasible upscaling technologies.

3.1 Analytical solution and upscaling for multi-layer consolidation

As mentioned above, the effects of intra-block heterogeneity must be taken into account by upscaling. The weighted average method is commonly used in geotechnical engineering for multi-layer systems at present, which is not supported by theoretical derivation. In what follows, multi-layer small-strain (Terzaghi) and large-strain (Gibson) consolidation is solved with the transform matrix and Laplace transformation. The results match the numerical results and other analytical solutions well. According to the method of transform, matrix which considers the properties of multi-layer consolidation, an upscaling method is developed.

There are small-strain and large-strain consolidations in geotechnical engineering, Terzaghi consolidation theory is widely used for small-strain consolidation. Small-strain consolidation

is easy-to-use, so Terzaghi and its improved methods are still widely used in geotechnical engineering and other fields (Kauerauf and Hantschel, 2009; Terzaghi, 1929; Terzaghi, 1943). As for the analytical solution, it is relative easy to obtain and widely used. In terms of large-strain consolidation, Gibson consolidation theory is more effective (Gibson et al., 1967; Gibson et al., 1981; Gibson et al., 1982). The solutions of Gibson's equation are primarily based on a numerical method, but some analytical solutions have been provided under certain conditions (Morris, 2002; Xie and Leo, 2004).

As for the multi-layer systems, analytical solutions such as state space, three-dimensional transfer matrix solution (Ai et al., 2008) and differential quadrature method (Chen et al., 2005), have been created. Moreover, a great deal of research has been conducted on multi-layer consolidation, both small-strain and large-strain consolidation (Abbasi et al., 2007; Ai et al., 2011; Cai et al., 2007; Chen et al., 2005; Geng, 2008; Lee et al., 1992; Schiffman and Stein, 1970; Xie et al., 1999; Xie et al., 2002).

However, two main drawbacks are discovered in those researches. One is that the analytical solutions are valid under restricted conditions, the other is that none of the research focuses on upscaling and supplying integral properties for the multi-layer consolidation systems, although they have provided accurate solutions for the multi-layer consolidation systems. In order to better describe the multi-layer consolidation system on the whole for both small and large-strain, a method combining Laplace transform and transfer matrix analysis is used to solve and upscale the multi-layer Terzaghi and Gibson consolidation.

3.1.1 Analytical solution and upscaling for multi-layer Terzaghi consolidation

3.1.1.1 Governing equations of solution and upscaling for multi-layer Terzaghi consolidation

It is necessary to point out that according to the principle of effective stress, total stress increments is bear by effective stress and pore stress:

$$\sigma' = \sigma - P \tag{3.1}$$

According to **Equation 3.1**, the following equation with the variable of effective stress increments can be obtained, which will benefit our solutions.

$$C_{\mathrm{v}} \frac{\partial^2 \sigma'}{\partial z^2} = \frac{\partial \sigma'}{\partial t} \tag{3.2}$$

The commonly-used weighted average method generates a consolidation coefficient - C_v for the whole multi-layer system according to **Equation 3.3**.

$$C_v = \frac{\sum_{i=1}^{n} h_i \times C_{v_i}}{\sum_{i=1}^{n} h_i} \tag{3.3}$$

In this research, transformation matrix is utilized to connect parts of the multi-layer system. The Laplace transform is a widely-used integral transform with many applications in physics and engineering. Stehfest numerical inversion of Laplace transforms is adopted in this research (Stehfest, 1960). According to the integral multi-layer transformation matrix and transformation matrix between different layers, the distribution of effective stress increments and excess pore pressure can be obtained. Moreover, results are verified with implicit finite difference numerical solutions.

Consolidation schematic diagram follows **Figure 2.2**, no overlying water, PTIB. Schematic plot of multi-layer Terzaghi consolidation is shown in **Figure 3.1**.

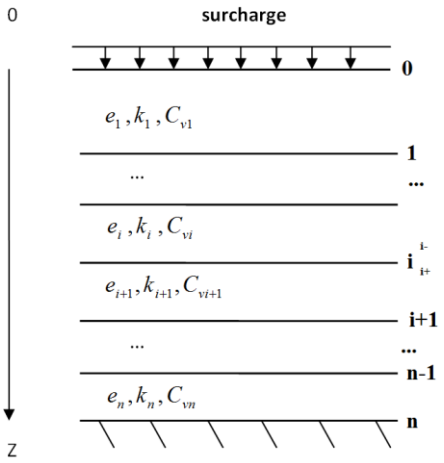

Figure 3.1 Schematic plot of multi-layer Terzaghi consolidation (positive axis direction is from 0 to z)

Laplace transform of **Equation 3.2** about time t:

$$C_v \frac{\partial^2 \tilde{\sigma}'(z,s)}{\partial z^2} = s\tilde{\sigma}'(z,s) - \sigma'(z,0) \tag{3.4}$$

Where $\tilde{\sigma}'(z,s)$ is the Laplace transform of $\sigma'(z,t)$.

At the beginning of consolidation, according to effective stress principle, pore pressure is equal to overburden stress, so that is zero initial effective stress, thus **Equation 3.5** can be obtained.

$$C_v \frac{\partial^2 \tilde{\sigma}'(z,s)}{\partial z^2} = s\tilde{\sigma}'(z,s) \tag{3.5}$$

The general solution of the ordinary differential **Equation 3.5** is as follows:

$$\tilde{\sigma}'(z,s) = c_1 \exp(\beta z) + c_2 \exp(-\beta z) \tag{3.6}$$

Where, c_1 and c_2 are constants, $\beta = \sqrt{\frac{s}{c_v}}$.

Combining **Equation 3.6** and its partial derivative, the following expression can be derived:

$$\begin{bmatrix} \tilde{\sigma}'(z,s) \\ \frac{\partial \tilde{\sigma}'(z,s)}{\partial z} \end{bmatrix} = \begin{bmatrix} \exp(\beta z) & \exp(-\beta z) \\ \beta \exp(\beta z) & -\beta \exp(-\beta z) \end{bmatrix} \begin{bmatrix} c_1 \\ c_2 \end{bmatrix} \tag{3.7}$$

When $z = 0$:

$$\begin{bmatrix} \tilde{\sigma}'(0,s) \\ \frac{\partial \tilde{\sigma}'(0,s)}{\partial z} \end{bmatrix} = \begin{bmatrix} 1 & 1 \\ \beta & -\beta \end{bmatrix} \begin{bmatrix} c_1 \\ c_2 \end{bmatrix} \tag{3.8}$$

Then it can be shown that:

$$\begin{bmatrix} \tilde{\sigma}'(0,s) \\ \frac{\partial \tilde{\sigma}'(0,s)}{\partial z} \end{bmatrix} = \begin{bmatrix} \frac{1}{2}[\exp(-\beta z) + \exp(\beta z)] & \frac{1}{2\beta}[\exp(-\beta z) - e\exp(\beta z)] \\ \frac{\beta}{2}[\exp(-\beta z) - \exp(\beta z)] & \frac{1}{2}[\exp(-\beta z) + \exp(\beta z)] \end{bmatrix} \begin{bmatrix} \tilde{\sigma}'(z,s) \\ \frac{\partial \tilde{\sigma}'(z,s)}{\partial z} \end{bmatrix} \tag{3.9}$$

And when z_i is not zero:

$$\begin{bmatrix} \tilde{\sigma}'(z_i,s) \\ \frac{\partial \tilde{\sigma}'(z_i,s)}{\partial z} \end{bmatrix} = \begin{bmatrix} 1 & 1 \\ \beta & -\beta \end{bmatrix} \begin{bmatrix} \exp(\beta z_i) & 0 \\ 0 & \exp(-\beta z_i) \end{bmatrix} \begin{bmatrix} \frac{\beta}{2\beta \exp(\beta z)} & \frac{1}{2\beta \exp(\beta z)} \\ \frac{\beta}{2\beta \exp(-\beta z)} & \frac{-1}{2\beta \exp(-\beta z)} \end{bmatrix} \begin{bmatrix} \tilde{\sigma}'(z,s) \\ \frac{\partial \tilde{\sigma}'(z,s)}{\partial z} \end{bmatrix} \tag{3.10}$$

Then the relationship between top surface stress and bottom stress can be derived.

When considering the equation of continuous stress, and flow conservation, between two layers, the relationship between different layers can be derived.

$$k_i \frac{\partial \tilde{\sigma}'(z_i^-, s)}{\partial z} = k_{i+1} \frac{\partial \tilde{\sigma}'(z_i^+, s)}{\partial z} \tag{3.11}$$

$$\tilde{\sigma}'(z_i^-, s) = \tilde{\sigma}'(z_i^+, s) \tag{3.12}$$

Combine **Equation 3.11** and **3.12**.

$$\begin{bmatrix} \tilde{\sigma}'(z_i^-, s) \\ \frac{\partial \tilde{\sigma}'(z_i^-, s)}{\partial z} \end{bmatrix} = \begin{bmatrix} 1 & \\ & \frac{k_{i+1}}{k_i} \end{bmatrix} \begin{bmatrix} \tilde{\sigma}'(z_i^+, s) \\ \frac{\partial \tilde{\sigma}'(z_i^+, s)}{\partial z} \end{bmatrix} \tag{3.13}$$

Stress distribution in the same layer and in the interface can be derived respectively by using **Equation 3.10** and **Equation 3.13**. With equation of each layer combined together, a transform matrix T can be obtained to express the relationship between $z = 0$ and $z = z_n$.

$$\begin{bmatrix} \tilde{\sigma}'(0, s) \\ \frac{\partial \tilde{\sigma}'(0, s)}{\partial z} \end{bmatrix} = T \begin{bmatrix} \tilde{\sigma}'(z_n, s) \\ \frac{\partial \tilde{\sigma}'(z_n, s)}{\partial z} \end{bmatrix} \tag{3.14}$$

Here, this example only considers the situation of permeable top surface and impermeable bottom for illustration.

Boundary condition:

$$\mathrm{z} = 0, \mathrm{u}(\mathrm{z}, \mathrm{t}) = 0;\ \mathrm{z} = \mathrm{z}_{\mathrm{n}}, \frac{\partial \mathrm{u}(\mathrm{z}, t)}{\partial \mathrm{z}} = 0 \tag{3.15}$$

The corresponding Laplace transformation,

$$z = 0, \tilde{\sigma}'(0, s) = \frac{\sigma}{s}; z = z_n, \frac{\partial \tilde{\sigma}'(z_n, s)}{\partial z} = 0 \tag{3.16}$$

Hence

$$\tilde{\sigma}'(z_n, s) = \frac{\sigma}{T_{11} S} \tag{3.17}$$

Where σ is pressure on the surface, T_{11} is the value of first column and first row of T.

With $\tilde{\sigma}'(z_n, s)$, the stress at each upper point $\tilde{\sigma}'(z, s)$ can be obtained by the transformation matrix. Moreover the real stress distribution can be derived by the inverse of Laplace transformation.

As for an n-layer consolidation system, the multi-layer consolidation transform matrix is:

$$T_1 = \begin{bmatrix} \frac{1}{2}[\exp(-\beta_1 h_1) + \exp(\beta_1 h_1)] & \frac{k_2}{k_1}\frac{1}{2\beta_1}[\exp(-\beta_1 h_1) - \exp(\beta_1 h_1)] \\ \frac{\beta_1}{2}[\exp(-\beta_1 h_1) - \exp(\beta_1 h_1)] & \frac{k_2}{k_1}\frac{1}{2}[\exp(-\beta_1 h_1) + \exp(\beta_1 h_1)] \end{bmatrix}$$

$$T_i = \begin{bmatrix} \frac{1}{2}[\exp(-\beta_i h_i) + \exp(\beta_i h_i)] & \frac{k_{i+1}}{k_i}\frac{1}{2\beta_i}[\exp(-\beta_i h_i) - \exp(\beta_i h_i)] \\ \frac{\beta_i}{2}[\exp(-\beta_i h_i) - \exp(\beta_i h_i)] & \frac{k_{i+1}}{k_i}\frac{1}{2}[\exp(-\beta_i h_i) + \exp(\beta_i h_i)] \end{bmatrix} \tag{3.18}$$

$$T_n = \begin{bmatrix} \frac{1}{2}[\exp(-\beta_n h_n) + \exp(\beta_n h_n)] & \frac{1}{2\beta_n}[\exp(-\beta_n h_n) - \exp(\beta_n h_n)] \\ \frac{\beta_n}{2}[\exp(-\beta_n h_n) - \exp(\beta_n h_n)] & \frac{1}{2}[\exp(-\beta_n h_n) + \exp(\beta_n h_n)] \end{bmatrix}$$

$$\begin{bmatrix} \tilde{\sigma}'(0, s) \\ \frac{\partial \tilde{\sigma}'(0, s)}{\partial z} \end{bmatrix} = T_1 \cdot \cdot T_i \cdot \cdot T_n \cdot \begin{bmatrix} \tilde{\sigma}'(z_n, s) \\ \frac{\partial \tilde{\sigma}'(z_n, s)}{\partial z} \end{bmatrix}, \quad i = 2,3.....n-1$$

The commonly-used weighted average method will lead to the following weighted average method transform matrix:

$$\begin{bmatrix} \tilde{\sigma}'(0, s) \\ \frac{\partial \tilde{\sigma}'(0, s)}{\partial z} \end{bmatrix} = \begin{bmatrix} \frac{1}{2}[\exp(-\beta z_n) + \exp(\beta z_n)] & \frac{1}{2\beta}[\exp(-\beta z_n) - \exp(\beta z_n)] \\ \frac{\beta}{2}[\exp(-\beta z_n) - \exp(\beta z_n)] & \frac{1}{2}[\exp(-\beta z_n) + \exp(\beta z_n)] \end{bmatrix} \begin{bmatrix} \tilde{\sigma}'(z_n, s) \\ \frac{\partial \tilde{\sigma}'(z_n, s)}{\partial z} \end{bmatrix} \tag{3.19}$$

When: $t \to \infty, s \to 0, \beta \to 0$, by applying the following Taylor expansion **Equation 3.20**.

$$e^x = \sum_{n=0}^{\infty} \frac{x^n}{n!} \tag{3.20}$$

Multi-layer transform matrix, that is **Equation 3.17**, will develop into **Equation 3.21**.

$$\begin{bmatrix} \tilde{\sigma}'(0,s) \\ \dfrac{\partial \tilde{\sigma}'(0,s)}{\partial z} \end{bmatrix} = \begin{bmatrix} 1 & -(h_n + \sum_{i=1}^{n-1} \dfrac{k_n}{k_i} h_i) \\ 0 & \dfrac{k_n}{k_1} \end{bmatrix} \begin{bmatrix} \tilde{\sigma}'(z_n,s) \\ \dfrac{\partial \tilde{\sigma}'(z_n,s)}{\partial z} \end{bmatrix} \tag{3.21}$$

The weighted average method transform matrix, that is **Equation 3.19**, will develop into **Equation 3.22.**

$$\begin{bmatrix} \tilde{\sigma}'(0,s) \\ \dfrac{\partial \tilde{\sigma}'(0,s)}{\partial z} \end{bmatrix} = \begin{bmatrix} 1 & -z \\ 0 & 1 \end{bmatrix} \begin{bmatrix} \tilde{\sigma}'(z,s) \\ \dfrac{\partial \tilde{\sigma}'(z,s)}{\partial z} \end{bmatrix} \tag{3.22}$$

It can be concluded that, when conductivity in different layers are nearly the same, the weighted average method can be used for the whole multi-layer system, which is the situation of homogenous.

3.1.1.2 Verification

Lee et al (1992) presented an analytical solution for multi-layer small-strain consolidation. The analytical solution provided here is verified against the results of Lee et al, as shown in the following **Figure 3.2**. The parameters of Lee's model are shown in **Table 3.1**. The model cross section map follows the illustration in **Figure 2.2**, no overlaying water, PTIB. The simplified cross section map of 4 layers follows **Figure 3.1**.

Layer number	C_v (m^2/d)	k (m/d)	Thickness(m	m_{vl} (Pa^{-1})
1	0.0038	2.4049×10^{-6}	3.048	6.41×10^{-5}
2	0.0178	0.7132×10^{-5}	6.096	4.07×10^{-5}
3	0.0051	1.0150×10^{-6}	9.144	2.034×10^{-4}
4	0.0064	2.5451×10^{-6}	12.192	4.07×10^{-5}

Table 3.1 Parameters of Lee's model

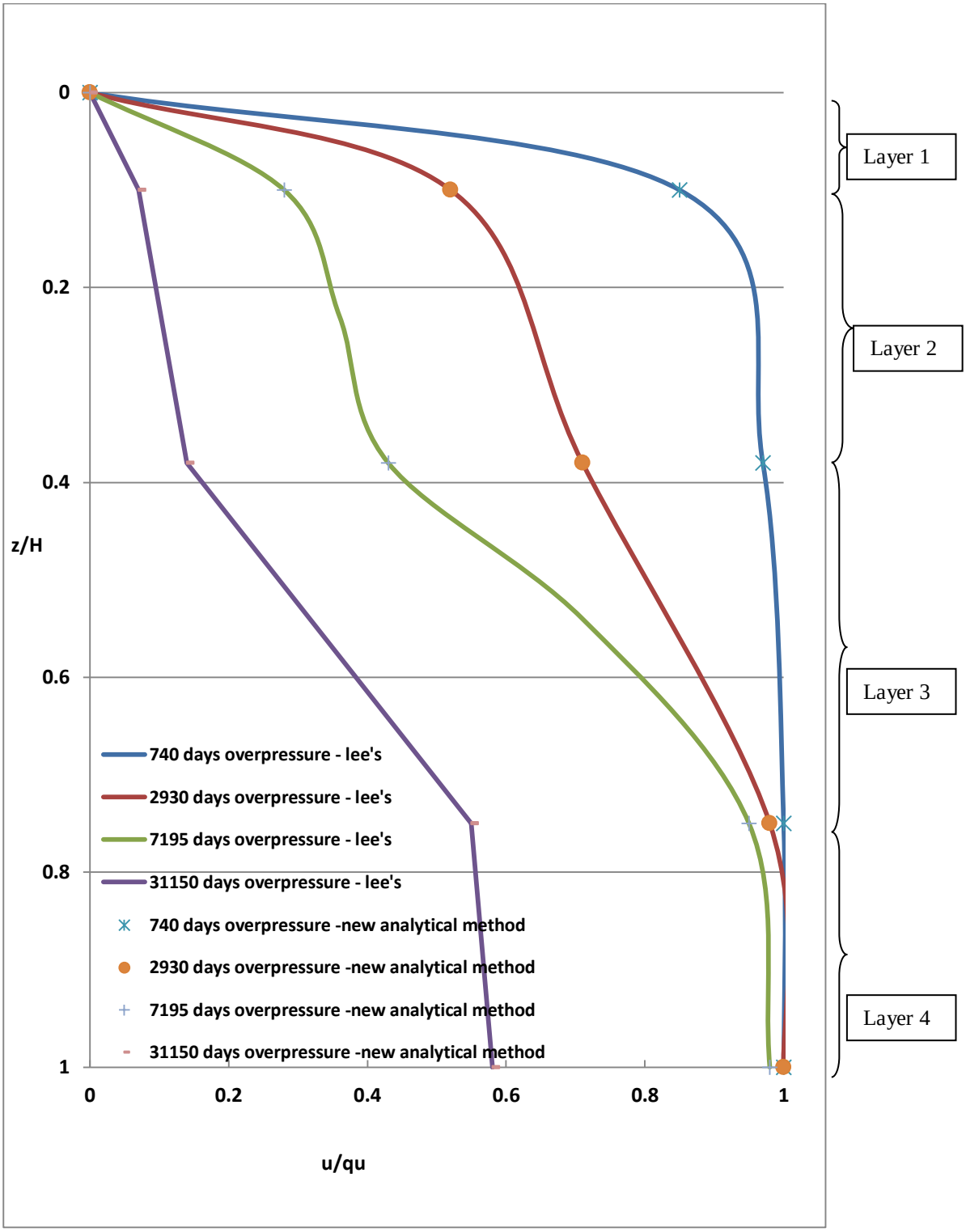

Figure 3.2 Numerical overpressure-results verification with Lee's analytical solution - PTIB, scatter plot is the results of the developed new analytical method, line plot is the analytical solution of Lee (q_u is surcharge on the surface, H is thickness of multi-layer system) (Lee et al., 1992)

In order to compare different upscaling methods, an implicit finite difference numerical model is developed. Analytical results are also compared with the implicit finite difference

numerical solution for verification in the following model. A simplified cross section map is also provided as shown in **Figure 3.3**, for no overlaying water and PTIB.

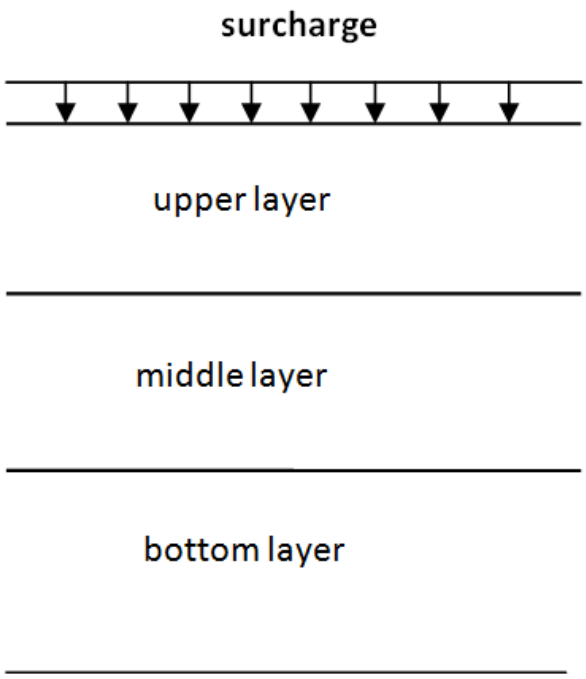

Figure 3.3 The cross section map for three different layers with surcharge

The parameters of the three different layers are shown in **Table 3.2**, and comparison results are shown in **Figure 3.4**. Hence, a conclusion can be reached that this method can be applied to multi-layer Terzaghi consolidation compaction. It should be noted that the values of m_{vl} and surcharge ensure the small strain, and nearly no settlement can be seen in **Figure 3.4**. The small changes in thickness are shown in **Figure 3.5**.

Lay	C_v (m^2/s)	k (m/s)	Thickness(m	m_{vl} (kPa^{-1})
upper	3.125×10^{-8}	1.038×10^{-12}	1.02	3.3948×10^{-6}
middle	2.662×10^{-8}	6.8403×10^{-12}	1.02	2.6221×10^{-5}
bottom	3.125×10^{-8}	1.038×10^{-12}	1.02	3.3948×10^{-6}

Table 3.2 Model parameters utilized in the three-layer model

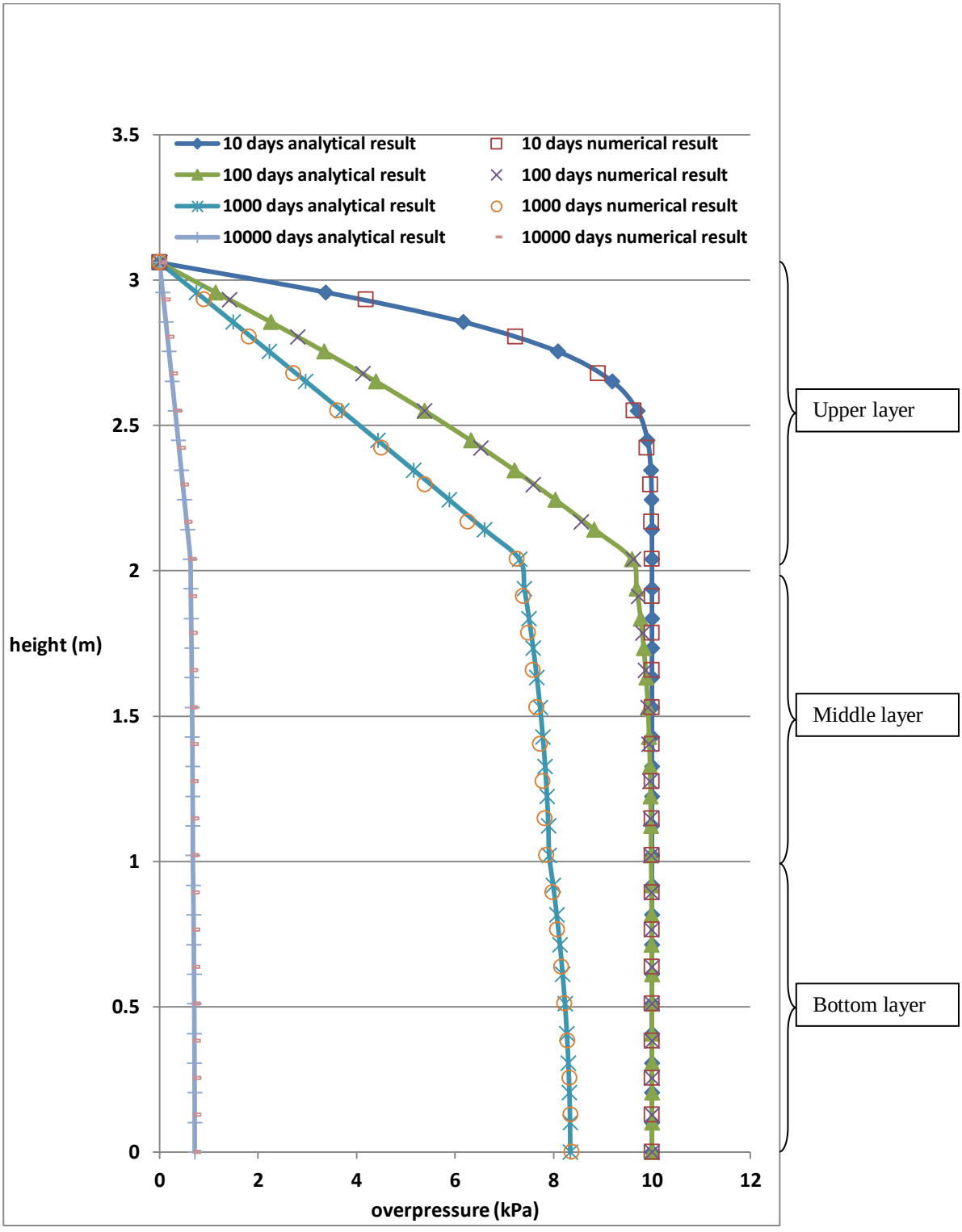

Figure 3.4 Comparison of overpressure evolution for three layers with different properties

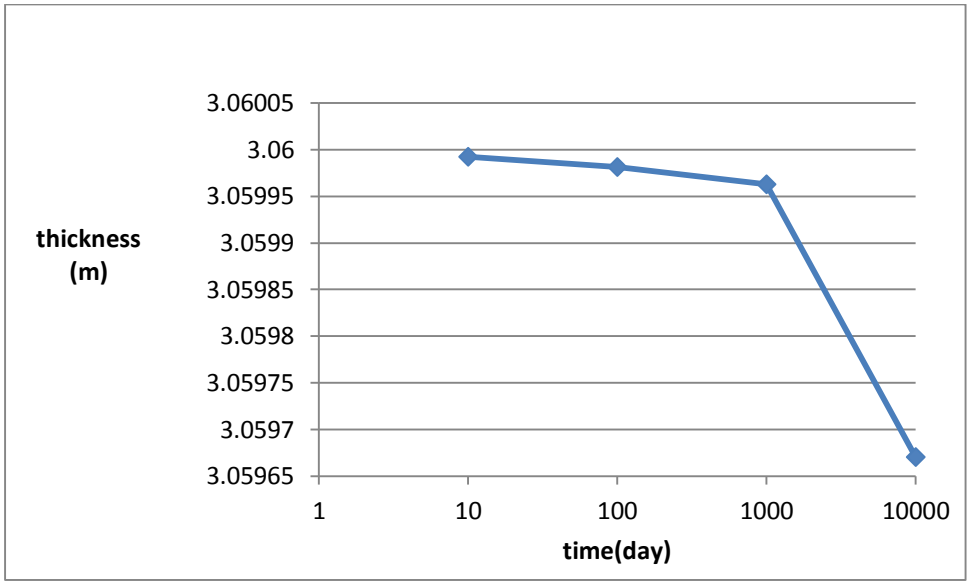

Figure 3.5 Small changes in thickness of the three-layer model

3.1.1.3 Comparison of different upscaling methods

T represents the multi-layer system. A new C_v is needed to represent the whole multi-layer system. With the new C_v, a new transform matrix for the multi-layer consolidation T' can be obtained. The new C_v should be the one that make the minimum of **Equation 3.23**.

$$\sqrt{(T'(1,1)-T(1,1))^2+(T'(1,2)-T(1,2))^2+(T'(2,1)-T(2,1))^2+(T'(2,2)-T(2,2))^2} \quad (3.23)$$

To be special, under the condition of PTIB, it can be found that $\frac{\partial\tilde{\sigma}'(z_n,s)}{\partial z}=0$, so $\tilde{\sigma}'(0,s)=T(1,1)\times\tilde{\sigma}'(z_n,s)$. This provides a thought of using a homogeneous layer's $T(1,1)$ to represent multi-layer heterogeneous consolidation. A new β is required to fit the value of $T(1,1)$. The example of the before-mentioned three layers with different properties is used to illustrate. A new C_v can be derived from **Equation 3.24**.

$$\frac{1}{2}[e^{-\beta z}+e^{\beta z}]=T(1,1) \quad (3.24)$$

C_v changes with time according to **Equation 3.24**, as shown in **Figure 3.6**.

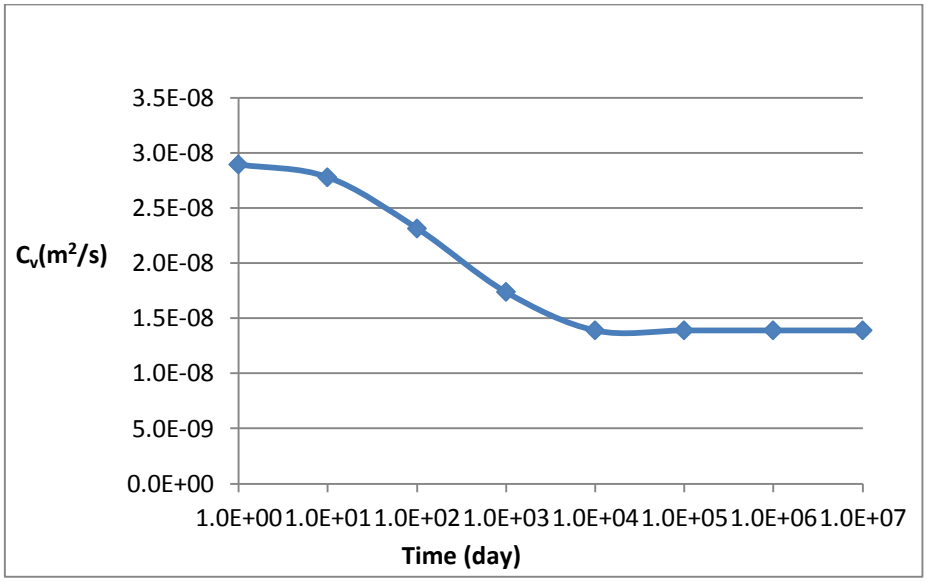

Figure 3.6 Consolidation coefficient variation - c_v changes with time

In light of the long-time consolidation, C_v is set to be 1.4×10^{-8} (m^2/s). A homogeneous layer with the new upscaling C_v can be compared with the three-layer system.

Specially, the transform matrix for a three-layer system is:

$$T_1=\begin{bmatrix} \frac{1}{2}[e^{-\beta_1 h_1}+e^{\beta_1 h_1}] & \frac{k_2}{k_1}\frac{1}{2\beta_1}[e^{-\beta_1 h_1}-e^{\beta_1 h_1}] \\ \frac{\beta_1}{2}[e^{-\beta_1 h_1}-e^{\beta_1 h_1}] & \frac{k_2}{k_1}\frac{1}{2}[e^{-\beta_1 h_1}+e^{\beta_1 h_1}] \end{bmatrix}$$

$$T_2=\begin{bmatrix} \frac{1}{2}[e^{-\beta_2 h_2}+e^{\beta_2 h_2}] & \frac{k_3}{k_2}\frac{1}{2\beta_2}[e^{-\beta_2 h_2}-e^{\beta_2 h_2}] \\ \frac{\beta_2}{2}[e^{-\beta_2 h_2}-e^{\beta_2 h_2}] & \frac{k_3}{k_2}\frac{1}{2}[e^{-\beta_2 h_2}+e^{\beta_2 h_2}] \end{bmatrix}. \qquad (3.25)$$

$$T_3=\begin{bmatrix} \frac{1}{2}[e^{-\beta_3 h_3}+e^{\beta_3 h_3}] & \frac{1}{2\beta_3}[e^{-\beta_3 h_3}-e^{\beta_3 h_3}] \\ \frac{\beta_3}{2}[e^{-\beta_3 h_3}-e^{\beta_3 h_3}] & \frac{1}{2}[e^{-\beta_3 h_3}+e^{\beta_3 h_3}] \end{bmatrix}$$

$$\begin{bmatrix} \tilde{\sigma}'(0,s) \\ \frac{\partial \tilde{\sigma}'(0,s)}{\partial z} \end{bmatrix}=T_1T_2T_3\cdot\begin{bmatrix} \tilde{\sigma}'(z_3,s) \\ \frac{\partial \tilde{\sigma}'(z_3,s)}{\partial z} \end{bmatrix}$$

Meanwhile the commonly-used weighted average method will lead to another C_v. Here C_v = 3.0093×10^{-8} (m^2/s) in the weighted average method, with this C_v, a new β and weighted average transform matrix can be derived. Compared with the exact numerical result (verified with the analytical solution), overpressure will develop in different ways with the new upscaled C_v and weighted average C_v. Overpressure comparisons of the three methods are shown in **Figure 3.7**. It can be seen that the overpressure results of the new upscaling method is closer to the fine scale numerical method than the weighted average method from an overall perspective.

According to **Equation 3.26**, the relative error between the weighted average method or the new upscaling method and the numerical results can be obtained, as shown in **Figure 3.8**.

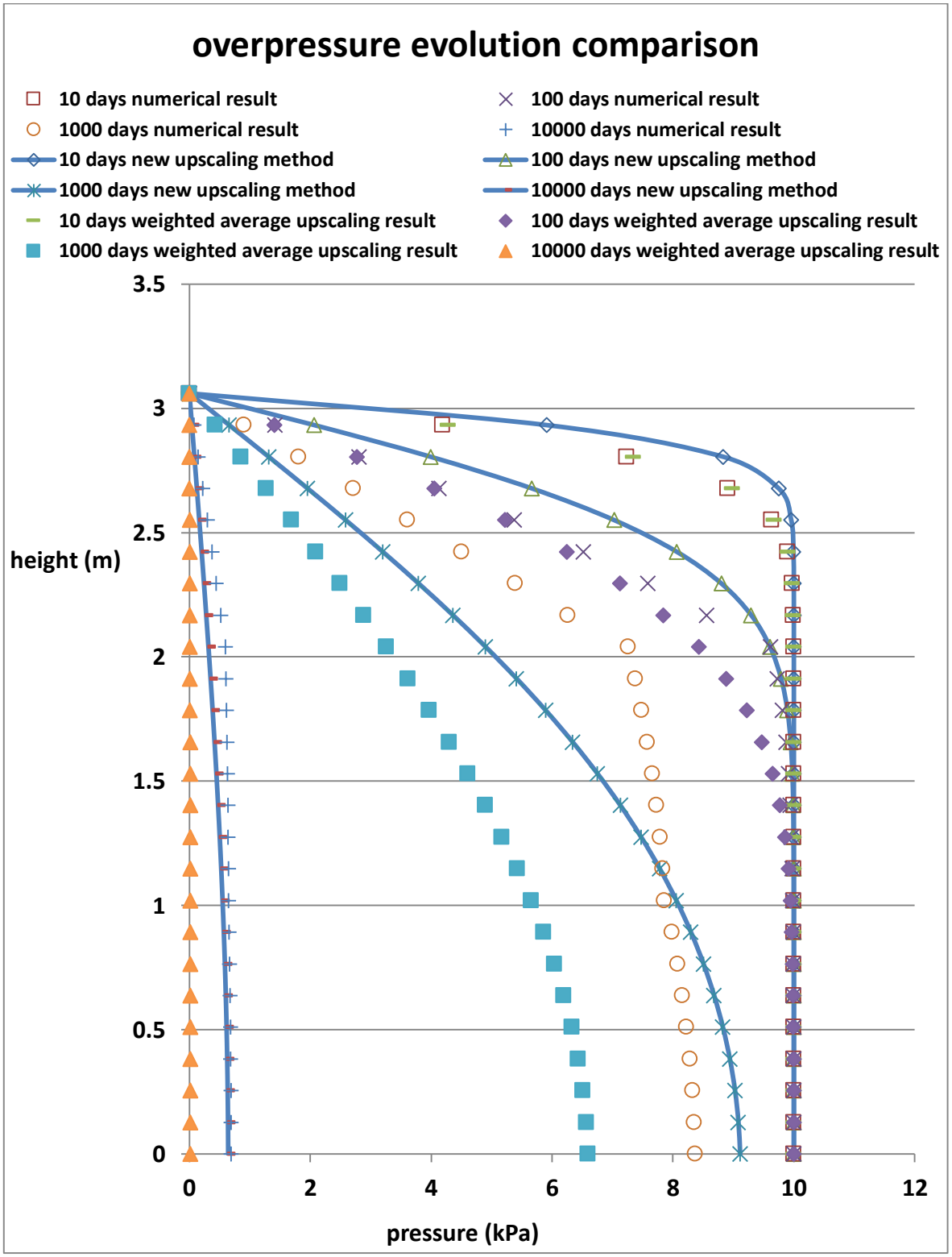

Figure 3.7 Overpressure evolution comparison of the three different methods

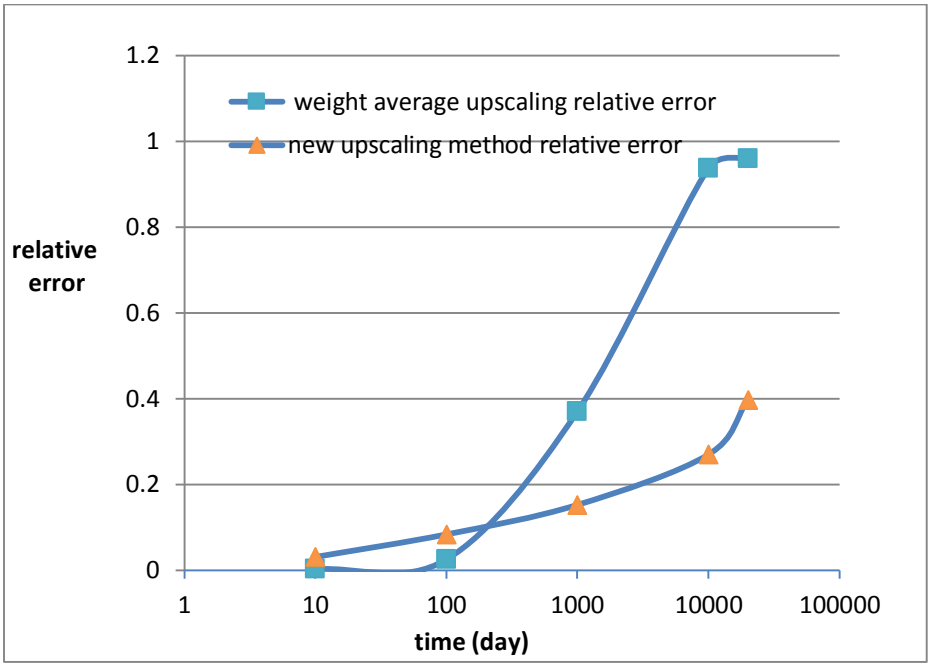

Figure 3.8 Relative errors of the two upscaling methods change with time

$$R = \frac{\sum_{i=1}^{n} \left| u'_i - u_i \right| / u_i}{n} \tag{3.26}$$

Where, u_i is overpressure for mesh 'i' in three-different layers numerical model, u'_i is overpressure for mesh 'i' with the upscaled C_v.

Figure 3.7 indicates that when it comes to 20 000 days, there is nearly no overpressure, hence the multi-layer system's characteristics is studied within 20000 days. As can be seen from **Figure 3.8**, in the first 100 days, the weighted average method is more efficient than the upscaling method, which can be explained as follows.

Fluid flows out through the top surface. The whole system is determined by properties of the first layer before overpressure reduction reaches the second layer, which can be illustrated with the following **Figure 3.9**. Overpressure distributions of 1 homogenous layer (same properties with the upper layer) and 3 heterogeneous layers' consolidation are same. This can explain why the result of changing C_v and the weighted average method compacts faster than the real situation. The possible explanation is bigger C_v of upper layer is applied to the whole layers with small C_v characteristic. The multi-layer consolidation will show the integral properties of the region where overpressure reduction reaches.

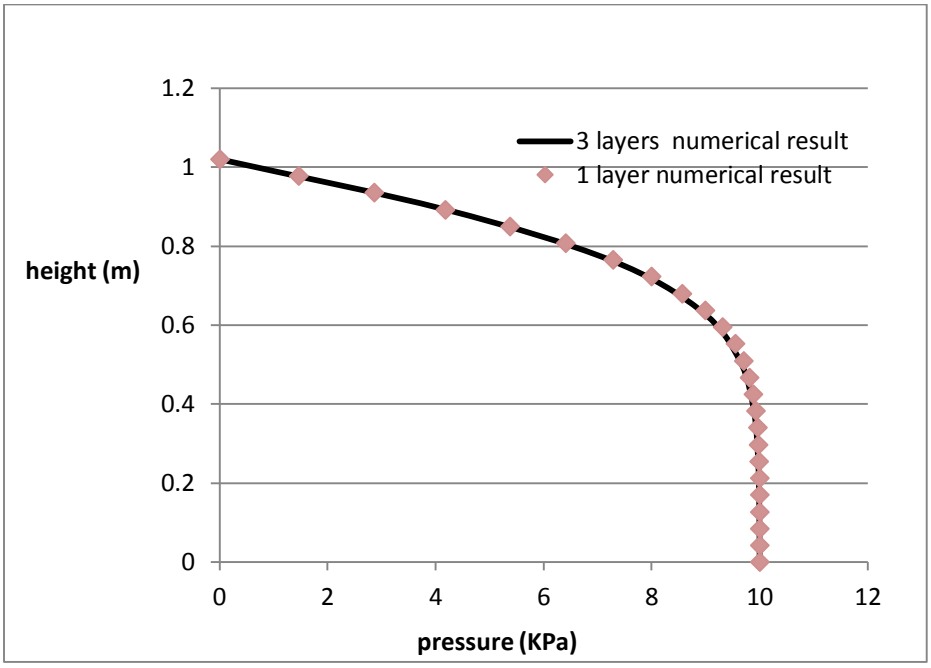

Figure 3.9 Overpressure distribution at 10 days, overpressure result of 1 homogenous layer and 3 layers' consolidation before the pressure reduction reaches the second layer.

3.1.2 Analytical solution and upscaling for multi-layer Gibson consolidation

3.1.2.1 Governing equations of solution and upscaling for multi-layer Gibson consolidation

In order to apply the transfer matrix method to large-strain consolidation, the simplification of Xie et al is adopted to simplify Gibson's equation (Xie and Leo, 2004).

The coefficient of volume compressibility of the soil skeleton for large-strain is defined as **Equation 2.14.** Gibson's equation can be changed to:

$$\frac{1}{\gamma_w}\frac{\partial}{\partial z}[\frac{k(1+e_0)}{(1+e)}\frac{\partial u}{\partial z}] = m_{vl}\frac{1+e}{1+e_0}(\frac{\partial u}{\partial t}-\frac{\partial q_u}{\partial t}) \tag{3.27}$$

Where q_u is surcharge, m_{vl} is constant during consolidation.

The relationship between conductivity k and void ratio is:

$$\frac{k}{k_o} = (\frac{1+e}{1+e_0})^2 \tag{3.28}$$

Where k_o is the initial conductivity at time t = 0. k is often found empirically to be a logarithmic function of the void ratio, e_0 is the initial void ratio.

A load q_u is applied suddenly at t = 0 on the top surface of the model and remains constant thereafter. According to the effective stress principle and Xie's assumption (Xie and Leo, 2004), the relationship between void ratio and excess pore water pressure can be deduced as follows.

$$\frac{1+e}{1+e_0} = \exp(-m_{vl}(q_u - u)) \tag{3.29}$$

With **Equation 2.14** and **Equation 3.29**, **Equation 3.27** can now be changed to the following one, which determines excess pore evolution in Lagrangian coordinates:

$$c_{vo}[\frac{\partial^2 u}{\partial z^2} + m_{vl}(\frac{\partial u}{\partial z})^2] = \frac{\partial u}{\partial t} \tag{3.30}$$

Where c_{vo} is the initial coefficient of consolidation at time t = 0 given by:

$$c_{vo} = \frac{k_o}{m_{vl} r_w} \tag{3.31}$$

The solution to large consolidation theory is facilitated by the following transformation.

$$\omega = \omega(z,t) = \exp(m_{vl} u) \tag{3.32}$$

In consideration of the permeable top impermeable base (PTIB) boundary condition, with **Equation 3.32** and **Equation 3.30**, equation of Terzaghi form will come up as follows.

$$\begin{aligned} & c_v \frac{\partial^2 \omega}{\partial z^2} = \frac{\partial \omega}{\partial t} \\ & \omega(0,t) = 1 \\ & \frac{\partial \omega}{\partial z}(H,t) = 0 \\ & \omega(H,0) = \exp(m_{vl} q_u) \end{aligned} \tag{3.33}$$

Then the transfer matrix can be used for solutions and upscaling of multi-layer Gibson consolidation. In order to use the transfer matrix method, ω should be continuous, hence different layers share the same m_{vl}, then according to **Equation 3.31**, what upscaled is actually k_o, i.e. conductivity upscaling.

3.1.2.2 Verification

The analytical solution is compared with the developed implicit finite difference numerical code for verification. The model cross section map follows **Figure 3.3**, PTIB and no overlying water.

A three-layer model is used for comparison, with the surcharge 1×10^5Pa, γ_s = 26.950kN/m^3, γ_w = 10.045kN/m^3, other parameters are shown in **Table 3.3**.

Lay	m_{vl} (Pa^{-1})	k_o (m/s)	e_0	Thickness(m)
1(surface)	4×10^{-6}	1.00×10^{-9}	3	5
2(middle)	4×10^{-6}	1.16×10^{-10}	4	5
3(bottom)	4×10^{-6}	1.04×10^{-9}	5	5

Table 3.3 Large-strain verification model parameters

Figure 3.10 shows the comparison results. Consistent results prove the effectiveness of this method in solving large-strain multi-layer consolidation.

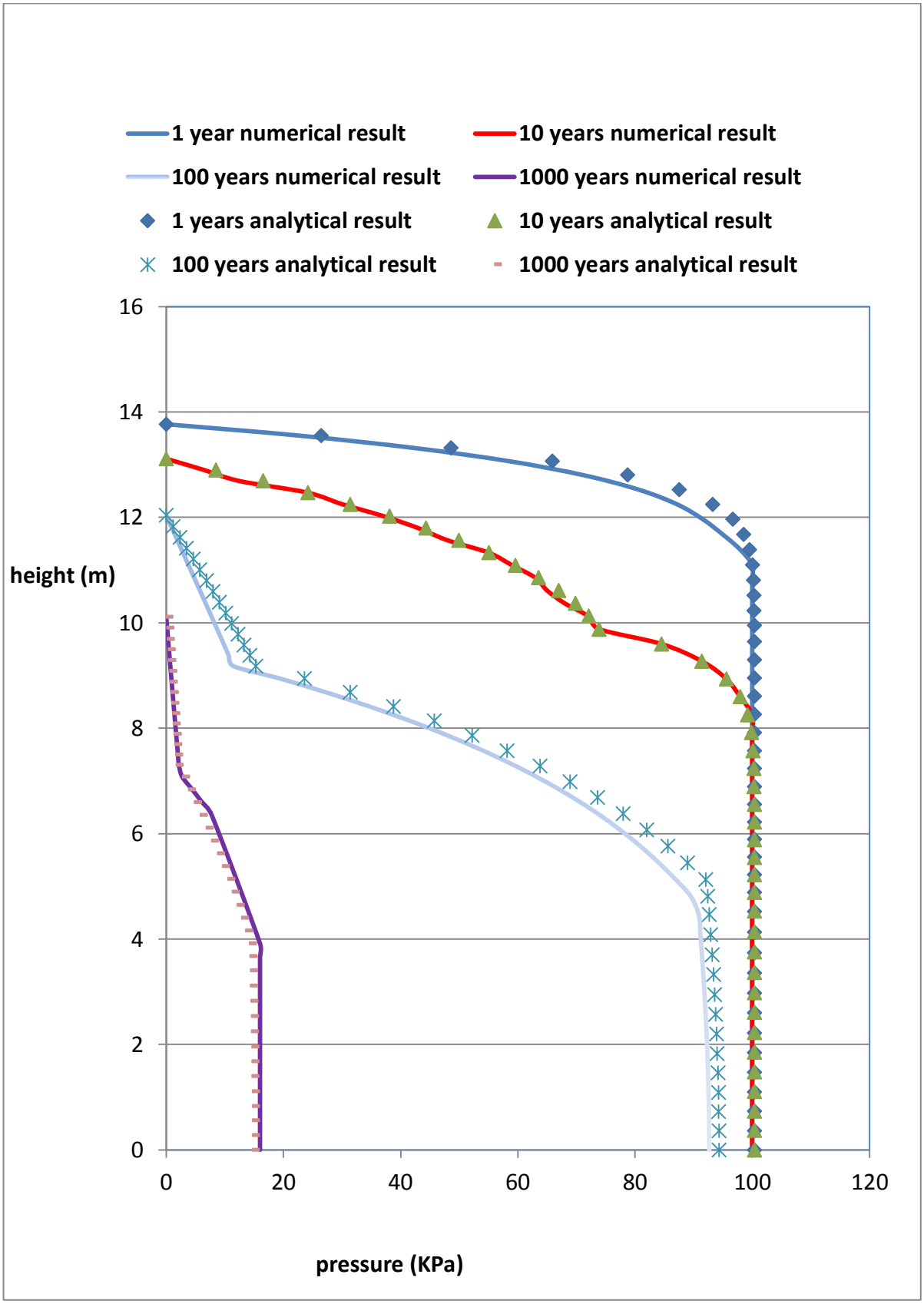

Figure 3.10 Overpressure comparison of three layers with different properties after large-strain consolidation

3.1.2.3 Comparisons of different upscaling methods

In order to evaluate this upscaling method, comparison with the weighted average method is carried out here, using the same three-layer model used in verification.

When it comes to 1000 years, there are nearly no excess pore pressure according to the weighted average method, hence we focus within 1000 years.

The upscaled k_o according to **Equation 3.31** is changing with time as shown in **Figure 3.11**. In consideration of the long geology process, k_o value is set to be 2.8356×10^{-10} (m/s), and C_v is 7.2337×10^{-9} (m^2/s). While for weighted average method, k_o is 7.1867×10^{-10} (m/s), C_v is 1.8333×10^{-9} (m^2/s).

The comparison of the two upscaling methods and the numerical solution are shown in **Figure 3.12**. It can be seen that the overpressure results of this new upscaling method is closer to the fine scale numerical method than the weighted average method from an overall perspective.

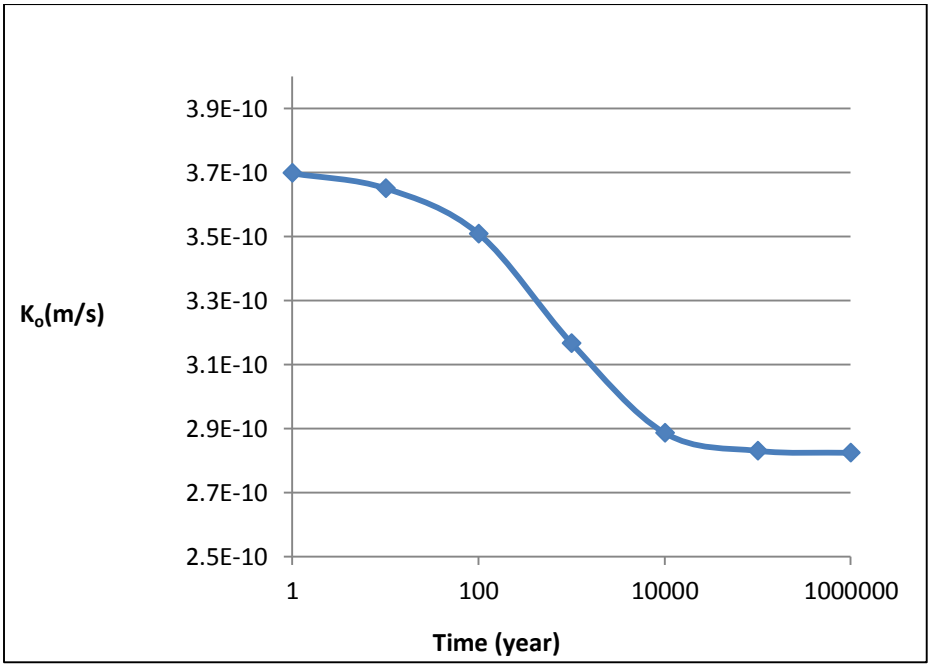

Figure 3.11 Upscaled conductivity - k_o changes with time

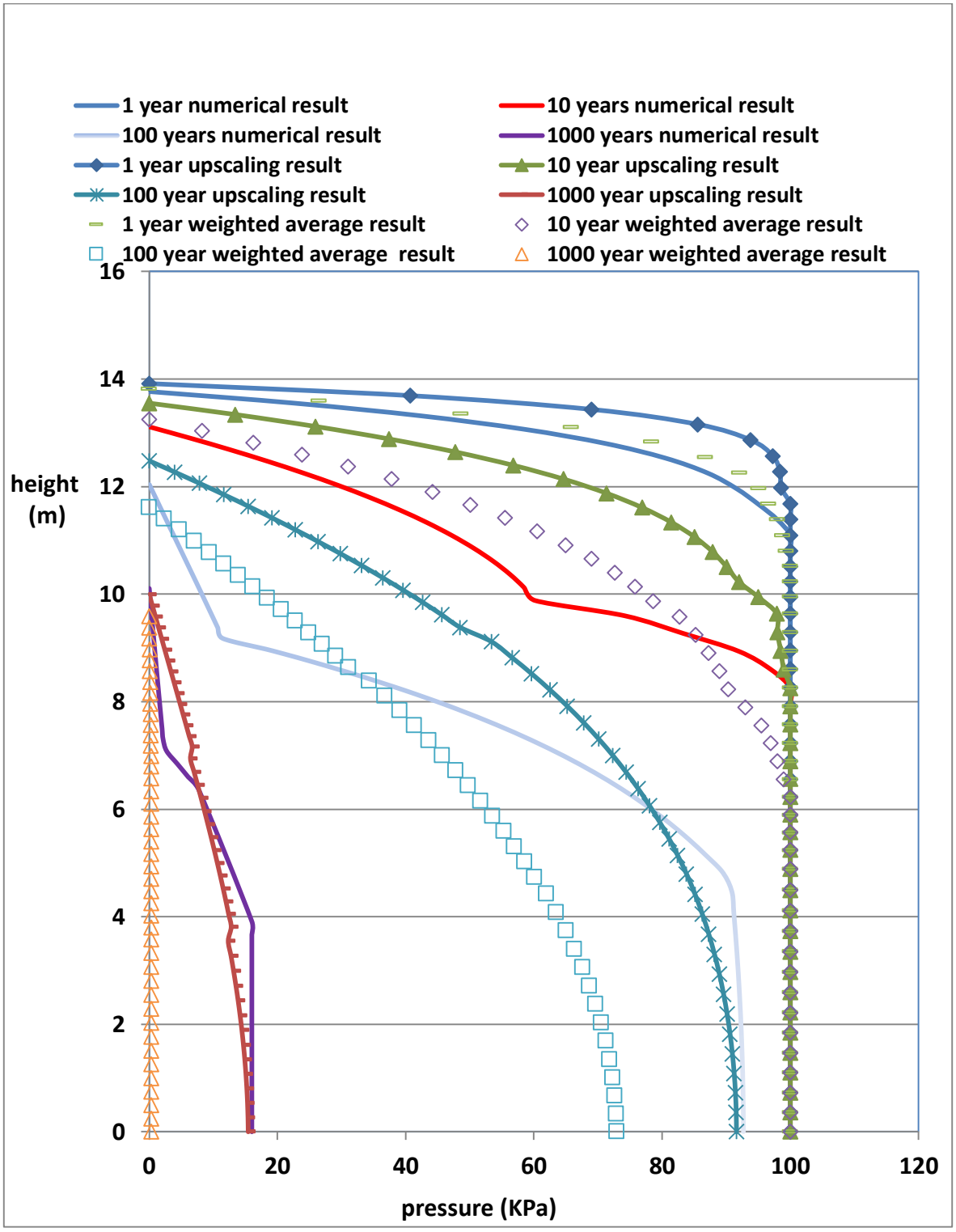

Figure 3.12 Over-pressure evolution comparison of different modelling method, 'scatter diagram' is the weighted average results, 'line' is the fine scale numerical results, 'scatter diagram + line' is the new upscaling results. The new upscaling results plots are more closer to the fine scale results at different time compared with weighted average results overall.

The whole model only shows properties of the first layer before the pressure reduction reaches the second layer, the weighted average k_o is closer to first layer's k_o than the upscaled k_o. Hence, within the first 10 years, results obtained through the weighted average method are closer to the numerical results than the upscaling method. However, as a whole, the upscaling method is more effective than the weighted average method.

The multi-layer system only shows properties of the place where the stimulation has affected, integral properties will change with the increase of affected region. This can partly explain the result of a changing upscaled k_o. This upscaling method is more accurate than the commonly-used weighted average method as a whole.

We can arrive at a conclusion that this upscaling method is more effective than the commonly-used weighted average method for multi-layer large-strain consolidation.

3.1.3 Conclusion for analytical solution

The following conclusions can be drawn from this study.

(1) Multi-layer small-strain (Terzaghi) and large-strain (Gibson) consolidation are solved with the transform matrix and Laplace transformation.

As for the simple Terzaghi's equation, several solutions can handle the multi-layer system efficiently. This solution does not improve previous ones obviously, the results are almost coincident. But when considering upscaling technology for multi-layer systems, the transfer matrix solution has its own advantages, which can upscale the heterogeneous multi-layer system into one homogenous layer, therefore it is more convenient in both physical significance and numerical form.

(2) Based on the method of transform matrix considering the properties of multi-layer consolidation, an upscaling method is put forward, which is more effective than the widely-used weighted average method. The multi-layer systems only show integral properties of the place where the stimulation has affected, integral properties vary with the increase of affected region.

3.2 Numerical study of multi-layer upscaling properties

Two relationships, 'void ratio - effective stress' and 'conductivity - void ratio', are widely used in basin modelling. When facing multi-layer systems, upscaling of these two relationships is needed. The real consolidation is a coupling process of mechanical and fluid flow, upscaling of these two relationships simultaneously is necessary.

3.2.1 Present upscaling

In basin modelling, a general and widely-accepted relationship between void ratio and effective stress is (Ma and Couples, 2008):

$$e = e_0 - \delta \log(\sigma' / \sigma_0') \tag{3.34}$$

Where, δ is a coefficient, e_0 and σ'_0 are void ratio and effective stress respectively taken at reference points, e and σ' are void ratio and effective stress respectively.

This relationship was developed originally from soil mechanics based on extensive laboratory testing. This is believed to be true in most basins up to a burial depth of a few 1000s of meters. For mudstones, after analysing many datasets from all over world, Dewhurst et al found that e_0 and δ are closely related to the clay fraction c, and derived empirical equations based on them (Yang and Aplin, 2004).

$$e = e_{100} - \delta \log(\sigma' / 100) \tag{3.35}$$

$$e_{100} = 0.3024 + 1.6867c + 1.9505c^2 \tag{3.36}$$

$$\delta = 0.0407 + 0.2479c + 0.3684c^2 \tag{3.37}$$

Where, e_{100} is void ratio corresponding to effective stress of 100 kPa.

A neural network technique has been developed, called 'ShaleQuant' (Yang et al., 2004), which estimates the clay fractions from conventional well logs. So when the clay fraction is known, using the compaction equations, the porosity can be determined at each effective stress. This approach, from conventional logs to clay fraction log to porosity at each effective stress, has been widely used in modelling porosity evolution.

Yang et al developed another scheme for upscaling compaction along wells (Yang et al., 1995). That scheme ensures the fine scale and coarse scale models compact exactly the same

amount for any given change in effective stress. The stresses are assumed to be applied at the model top and bottom. Using a depth and void ratio relationship, they derived an equation for upscaled δ * and then e*.

For basin modelling, these compaction relationships, which are typically determined by clay fractions at well-log scales, need to be upscaled for coarse grid cells in the calculations. Here, upscaling is defined as the process to find effective coefficients (e*, δ *), so that when they replace every individual pair of coefficients in a fine scale model, the whole model, i.e. the upscaled model, behaves exactly the same as the finer model in terms of volumetric changes.

Yardley developed a simple volume–weighted upscaling scheme originally for a 1D fine model containing uniform-sized cells (Yardley, 2000). He calculated the effective coefficients as the arithmetic average of the corresponding e and δ over all cells. This scheme is intuitive because the void ratio is lineally related to $\log(\sigma'/\sigma'_0)$. This method could be extended readily to 3D and non-layered systems. However, this scheme is not accurate as the volume change of the upscaled model differs from the corresponding fine model.

$$e^* = \frac{1}{n}\sum e_i \tag{3.38}$$

$$\delta^* = \frac{1}{n}\sum \delta_i \tag{3.39}$$

Ma and Couples, developed another scheme for upscaling (Ma and Couples, 2008). According to definition of compaction upscaling, equivalent (e*, δ *) is needed so that under the same configuration of effective stress the fine and upscaled models should compact exactly the same.

To derive formulae of (e*, δ *), let h_i^v and h_i^s be the void and solid volumes of cell i, then,

$$h_i^v = h_i^s(e_i - \delta_i \ln(\sigma'_i)) \tag{3.40}$$

Therefore, in order for the upscaled model and the fine model to have the same compaction, i.e:

$$\sum h_i^v = \sum h_i^{v^*} \tag{3.41}$$

$$\sum h_i^s (e_i - \delta_i \ln(\sigma'_i)) = \sum h_i^s (e^* - \delta^* \ln(\sigma'_i)) \tag{3.42}$$

Clearly, we can derive (e*, δ *) as below to satisfying up equations:

$$e^* = \sum h_i^s e_i / \sum h_j^s \tag{3.43}$$

$$\delta^* = \sum h_i^s \delta_i \ln(\sigma'_i) / \sum h_j^s \ln(\sigma'_i) \tag{3.44}$$

The above equation shows that the correct calculation must consider the weight the logarithm of effective stresses. It is mainly this weighting issue that leads to errors in Yardley's calculations.

Their analyses led to the following conclusions for 1D consolidation:

(1) Compaction relationships can be upscaled when the effective stresses are known;

(2) If the effective stresses are not known, but the effective stresses are known to be high, and their variation is small, variation would exert little influence on the calculation of effective coefficients. Hence, the effective stresses can be replaced with a simple average effective stress.

(3) If effective stresses are known to be lower at some locations, e.g. at shallow burials or due to fluid over-pressure, and true effective stress distribution is not known, that distribution has to be modelled in order to estimate effective coefficients.

It can be concluded that the heterogeneity of fine-grained sediments must be taken into account in basin modelling especially at shallow burial even under moderate basin fill conditions, and suggests that basin modelling must be extended to be able to take into account those factors that have been ignored so far in basin modelling.

3.2.2 The shortcomings of existing research

There are obvious drawbacks of the above-mentioned research, which only considered the 'void ratio - effective stress' relationship without paying attention to the coupling of 'conductivity - void ratio'. However, the real situation is coupled, only upscaling of these two relationships simultaneously is meaningful. To be specified, initial sediment thickness and final consolidation may be captured by only considering the 'void ratio - effective stress'.

However, the overpressure evolution may be quite different without considering 'conductivity - void ratio'.

As shown in **Chapter 3.1,** the weighted average method could lead to great errors. The upscaling method is more accurate than the commonly-used weighted average method. The multi-layer systems only show integral properties of the place where the stimulation has affected, integral properties will change with the increase of the affected region. A conclusion can be drawn that integral properties of multi-layer systems are changing with time and external stimulation.

Equation 3.44 also indicates that δ* may change with effective stress. In order to fully understand the dynamic evolution of multi-layer $k-e$ and $e-\sigma'$ simultaneously, the following analysis is provided.

3.2.3 Numerical upscaling

In what follows, the upscaling of δ* follows **Equation 3.44**. The fluid flow follows Darcy flow, i.e. $Q=\frac{\kappa A\Delta p}{\mu l}$. The total discharge, Q (units of volume per time, e.g., m^3/s) is equal to the product of the intrinsic permeability of the medium, κ(m^2), the cross-sectional area to flow, A (units of area, e.g., m^2), and the total pressure drop Δp, all divided by the viscosity, μ (Pa s) and the length over which the pressure drop is taking place (l). For a 1D series of grids arrangement, the pore pressure is continuous and flow is conserved. Accordingly, the conductivity for a 1D series of grid is shown in **Equation 3.45.**

$$k^*=\frac{\sum H_i}{\sum \frac{H_i}{k_i}} \tag{3.45}$$

Where, k^* is upscaled conductivity, H_i is height for grid i, k_i is conductivity of grid i.

The compressibility varies with time and between meshes, hence real consolidation time is used rather than dimensionless time.

3.2.3.1 Upscaling of sedimentation layers

The three-layer system is formed by a 1000 years' sedimentation. Initial effective stress is 100 kPa. Consolidation schematic diagram follows **Figure 2.2**, no overlying water, PTIB. Related parameters and simplified schematic diagram are shown as **Figure 3.13**.

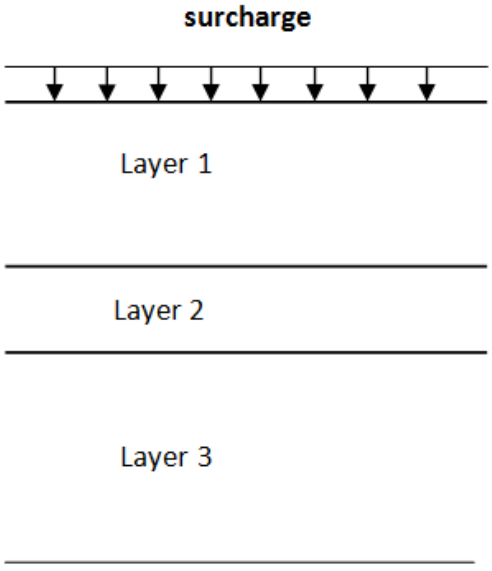

Figure 3.13 The model cross section map for numerical upscaling study with sedimentation

	Initial thickness(m)	Clay content(%)	Sedimentation time(years)
layer 1	45	90	450
layer 2	10	10	100
layer 3	45	90	450

Table 3.4 Model parameters for numerical upscaling study with sedimentation

90% clay content:

$k = 7\times10^{-6}e^2 - 3\times10^{-6}e + 2\times10^{-6}$, ($k$ - m/d); $e = 5.6247 - 0.52\ln(\sigma')$, ($\sigma'$ - kPa).

10% clay content:

$k = 1.2\times10^{-3}e^2 - 2\times10^{-4}e + 1\times10^{-5}$, ($k$ - m/d); $e = 0.8091 - 0.069\ln(\sigma')$, ($\sigma'$ - kPa).

These data for 10% and 90% clay content comes from Caprocks phase II internal report (Ma and Couples, 2008). After the sedimentation, surcharge is applied on the top surface. Additional surcharge changes from 0 to 2000 kPa. Simulation results are presented in **Figure 3.14** to **Figure 3.16**.

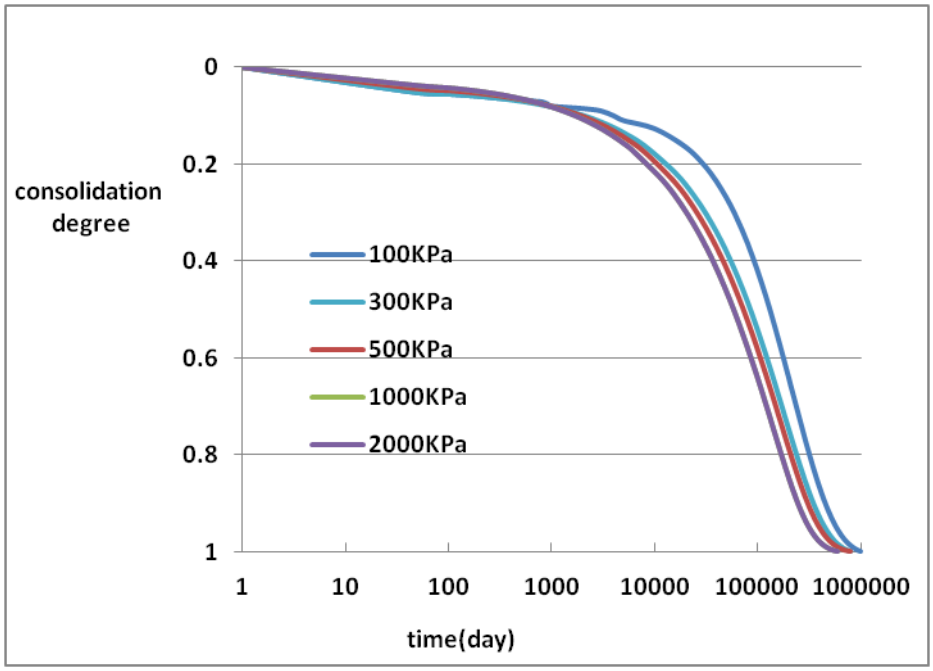

Figure 3.14 Consolidation curve changes with surcharge (surcharge changes as 100 300 500 1000 2000 kPa)

Consolidation curve is an indicator of sediment characteristics. It can be seen from the **Figure 3.14** that the properties of multi-layer systems vary with external stimulation (i.e. surcharge). To be detailed, the upscaling conductivity and δ^* vary with time and surcharge.

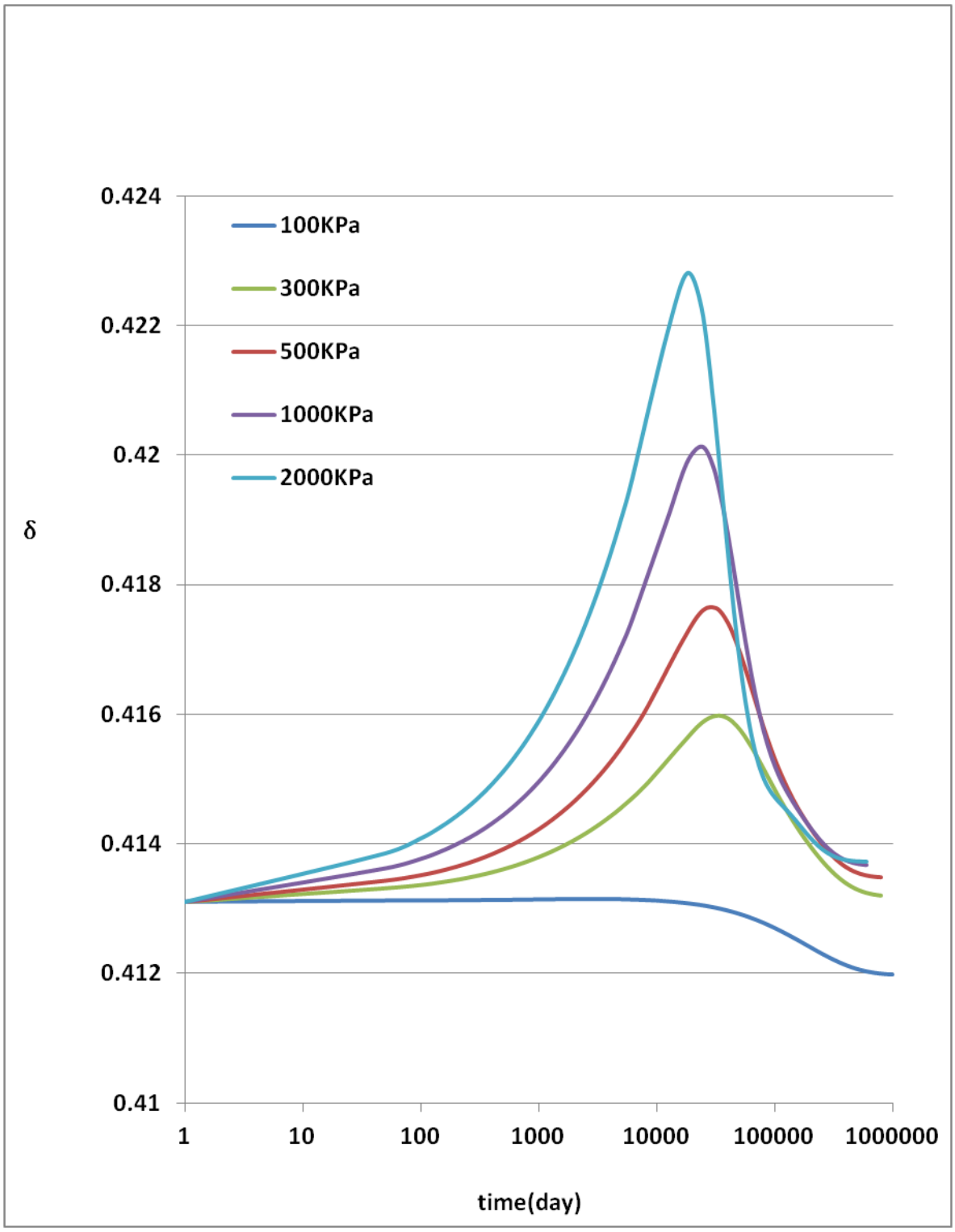

Figure 3.15 Upscaled δ changes with surcharge (surcharge change)

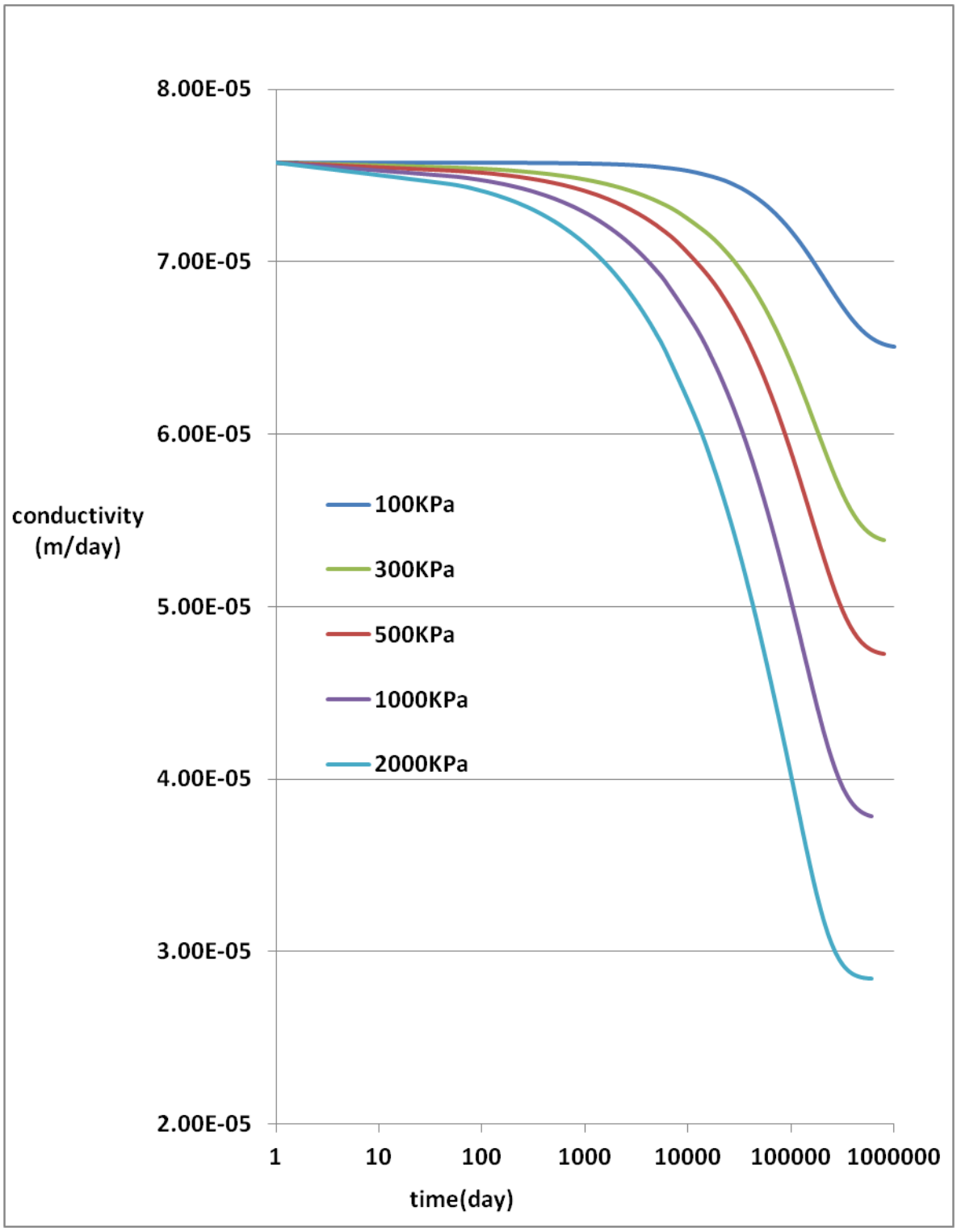

Figure 3.16 Upscaled conductivity changes with external stimulation (surcharge changes as 100 300 500 1000 2000 kPa)

3.2.3.2 Upscaling of multi layer without sedimentation

The three-layer system is formed without sedimentation. Each layer has the same initial effective stress. Initial effective stress is 100 kPa. The model cross section map is the same as **Figure 3.13**. Related parameters are shown as follows.

	Thickness(m)	Clay content(%)
layer 1	45	90
layer 2	10	10
layer 3	45	90

Table 3.5 Model parameters for numerical upscaling study without sedimentation

Surcharge varies from 500 kPa to 5000 kPa. Simulation results are presented in **Figure 3.17** to **Figure 3.19**. The property of multi-layer systems is changing with external stimulation. To be detailed, the upscaling conductivity and δ* are verify with time and surcharge.

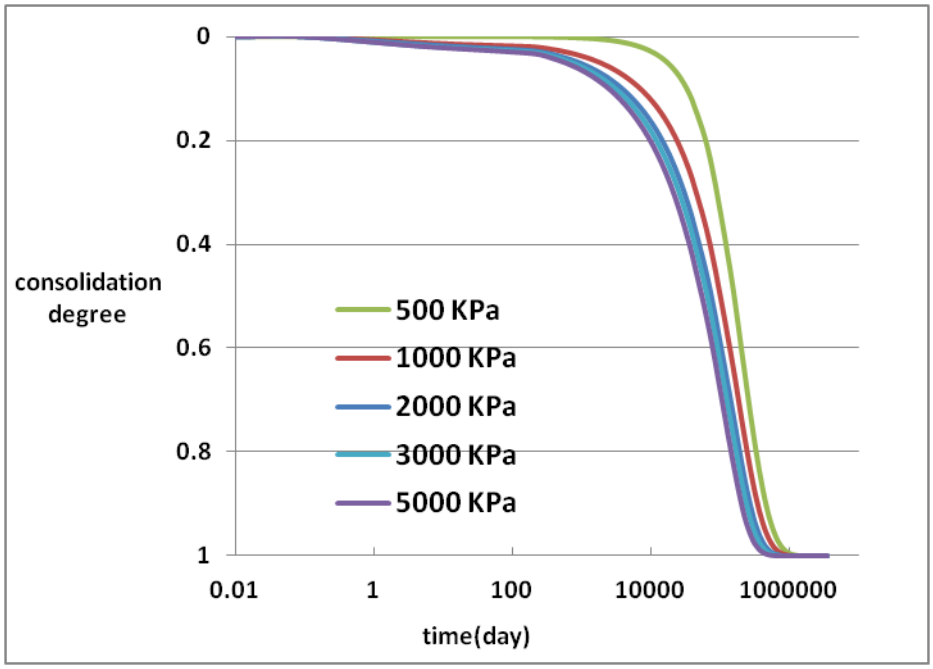

Figure 3.17 Consolidation curve changes with external stimulation (surcharge changes as 500 1000 2000 3000 5000 kPa)

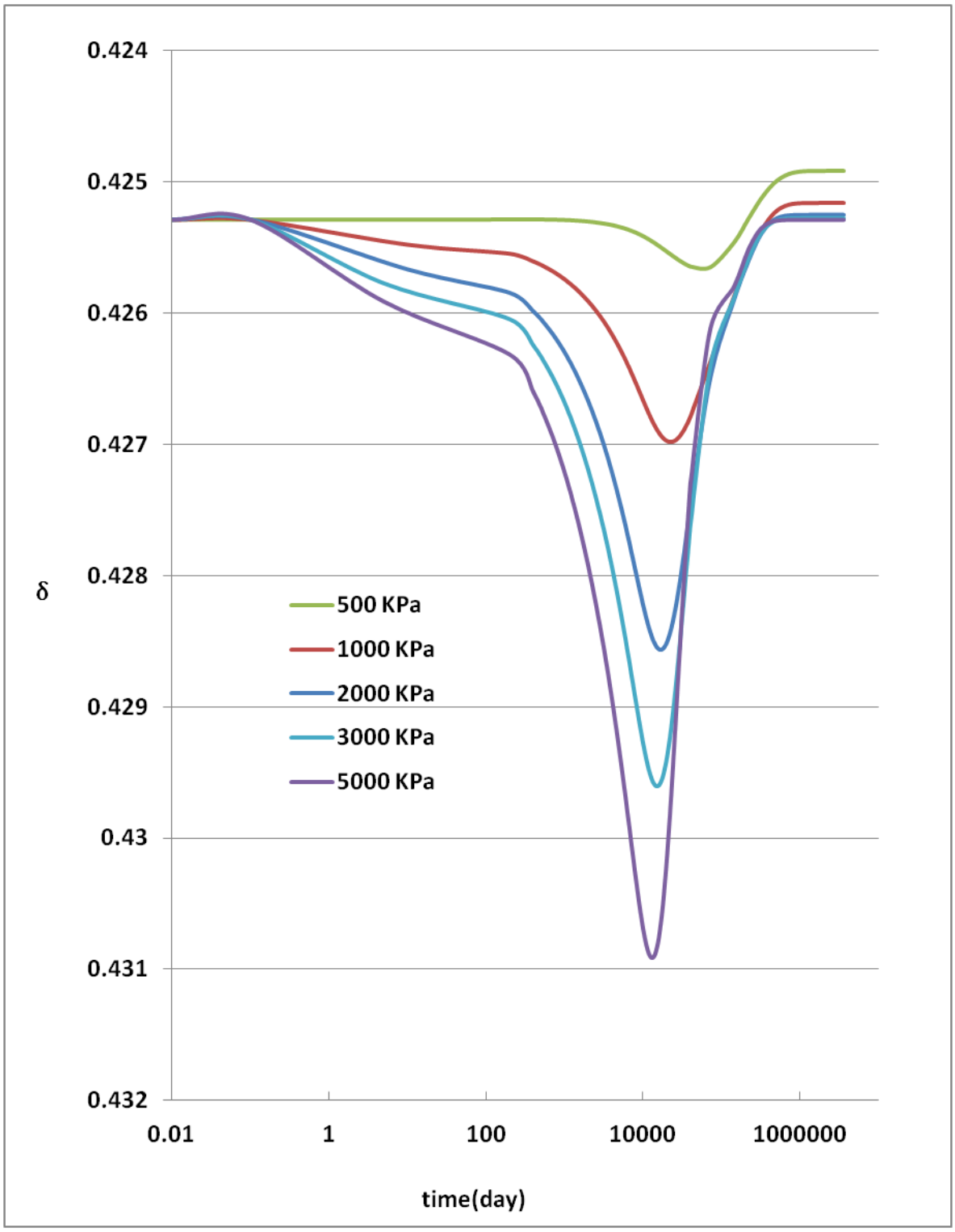

Figure 3.18 Upscaled δ changes with external stimulation

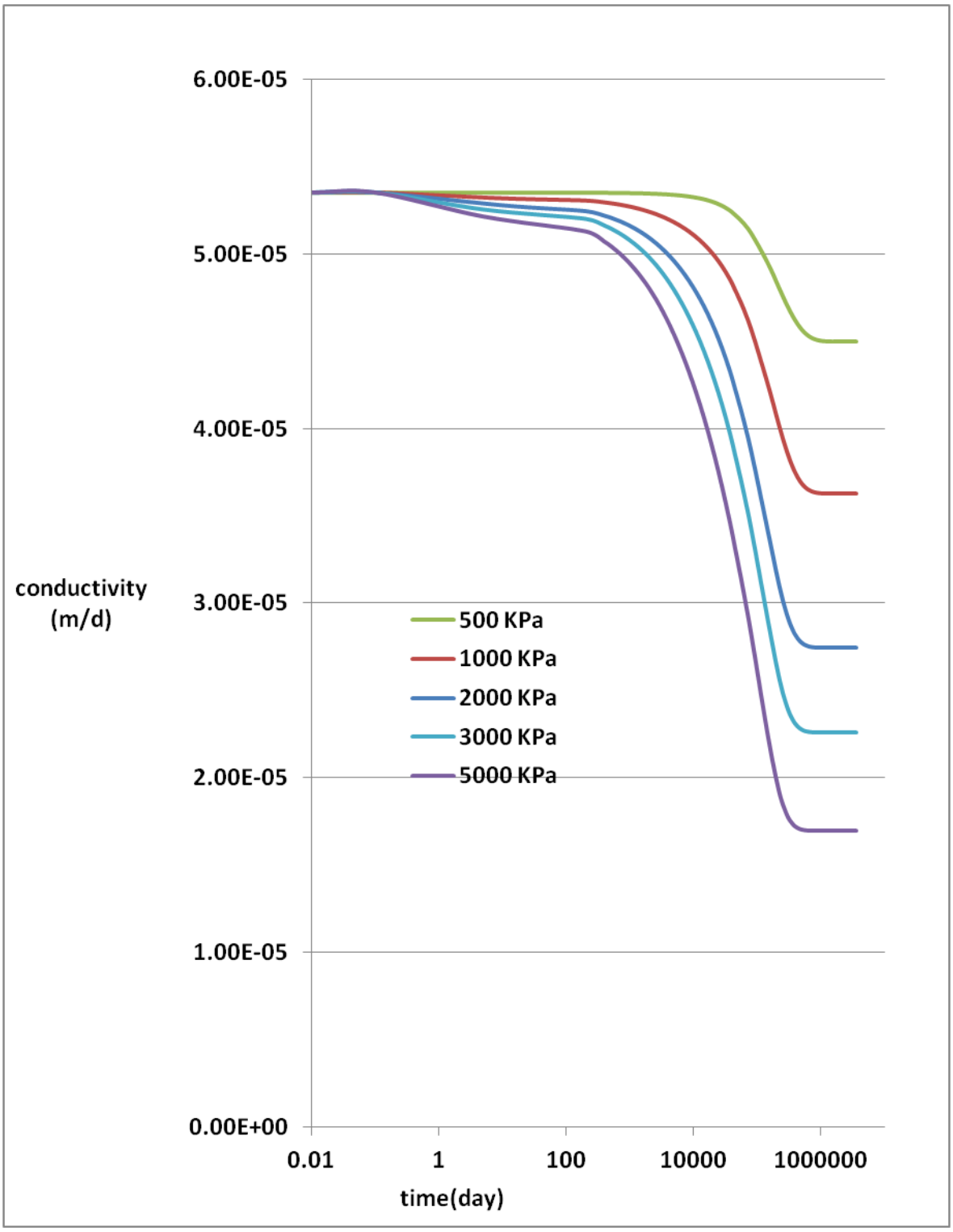

Figure 3.19 Upscaled conductivity changes with external stimulation

3.2.3.3 History matching with dynamic consolidation parameters

Attempt of using dynamic parameters to match numerical results for the model without sedimentation is shown as follows, dynamic δ* and conductivity are shown in **Figure 3.20**

and **Figure 3.21**. The result of thickness based average upscaling is also provided for comparison, in which e* = 4.6064, δ* = 0.4246, surcharge is 1000 kPa. Simulation results are presented in **Figure 3.22** and **Figure 3.23**. However, using dynamic consolidation parameters still generates deviation from the actual fine-scale numerical results.

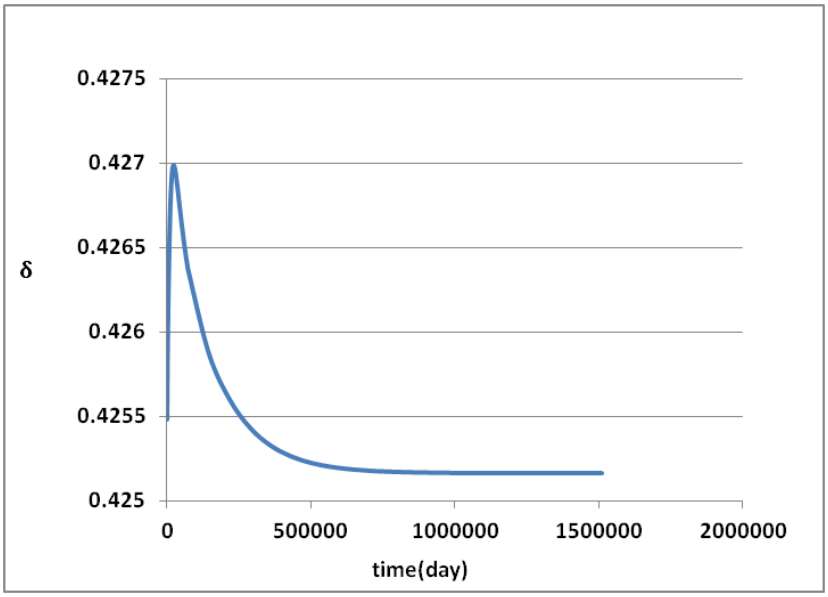

Figure 3.20 Upscaled δ changes with time

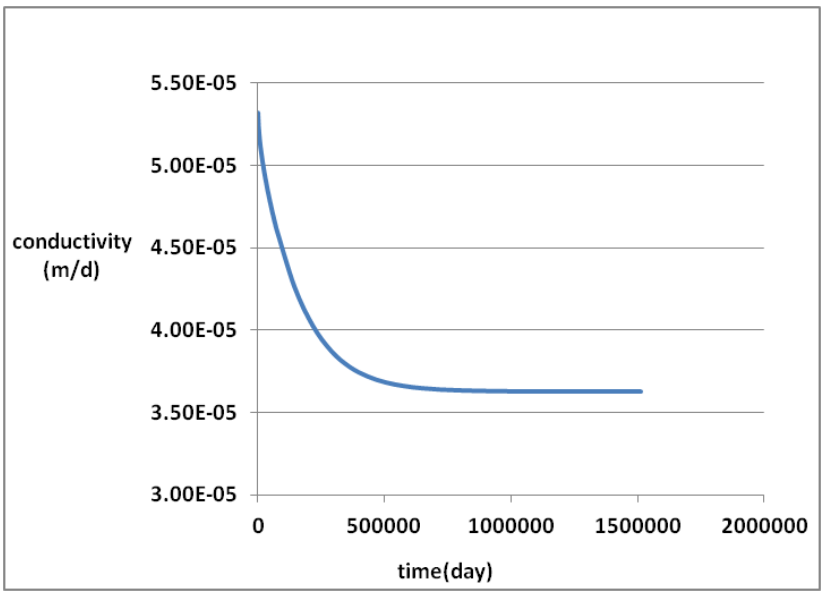

Figure 3.21 Upscaled conductivity changes with time

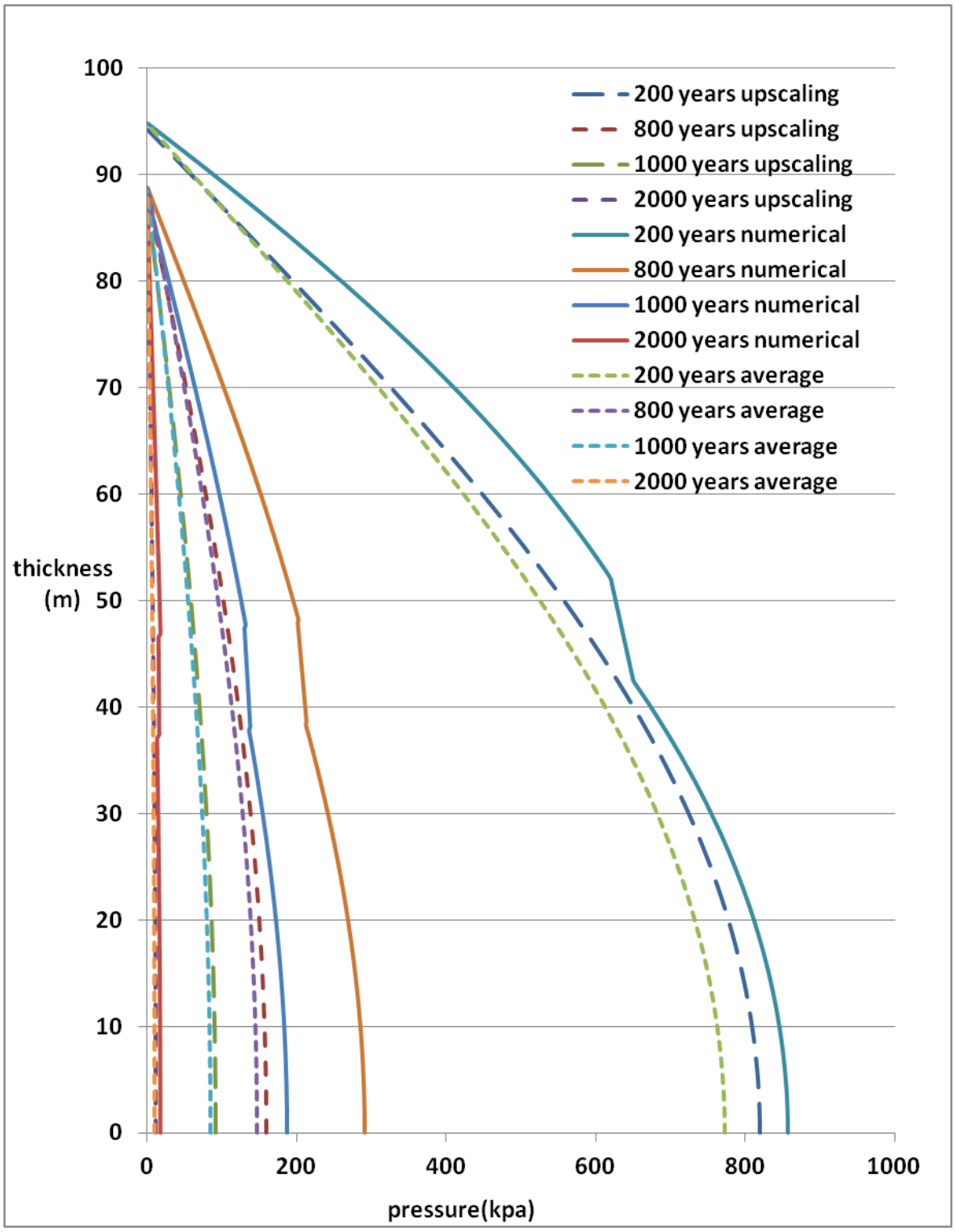

Figure 3.22 Over pressure evolution of different upscaling method, 'xx years numerical' is simulation result of fine scale model, 'xx years average' is simulation result of average upscaling method, 'xx years upscaling' is simulation result of dynamic upscaling method.

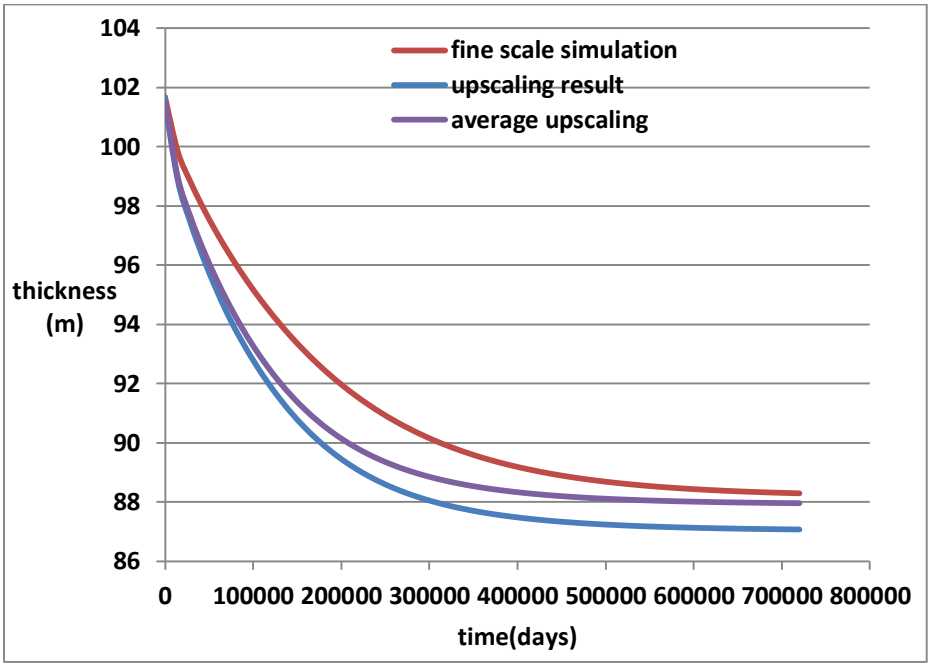

Figure 3.23 Sediment thickness evolution of different simulation method, 'fine scale simulation' is fine scale numerical model, 'average upscaling' is simulation result of average upscaling method, 'upscaling result' is simulation result of dynamic upscaling method.

3.2.4 Discussion and Conclusion for numerical study of multi-layer system

Two relationships, 'void ratio - effective stress', 'conductivity - void ratio', are widely used in basin modelling. The real consolidation is coupled processes of mechanical deformation and fluid flow, only upscaling of these two relationships simultaneously is meaningful.

Multi-layer numerical results show that the properties of multi-layer systems are changing with surcharge and time. It is impossible to use one constant relationship to describe consolidation characteristics. The bigger the surcharge is, the bigger the variations of δ^*(mechanical parameter, can be seen as compressibility to some extent) and conductivity are, the bigger the variation of consolidation curves is. Upscaled conductivity keeps decreasing in the consolidation process, but δ^* is not. Moreover, difference between consolidation with and without considering sedimentary history is obvious.

Initial and final sediment thickness can be captured by only considering the 'void ratio - effective stress'. However, the overpressure and thickness evolution is quite different without considering of 'conductivity - void ratio'. Both dynamic-coarse and weighted average-coarse scale simulation predict a faster consolidation than real fine-scale simulation. But simulation results of dynamic-coarse upscaling are closer to the fine-scale simulation

than that of the average upscaling, such as overpressure and thickness evolution. However, using dynamic consolidation parameters still generates deviation from the actual fine-scale numerical results, hence requires further research.

3.3 1 D large-strain consolidation of layered system

Natural depositional processes frequently give rise to layered sediment having alternating or random layers with different permeability, compressibility and thickness. As shown in **Figure 3.24**, the core Log of Site 1144 from South China Sea shows a sequence of hemipelagites, which are muddy sediments deposited close to continental margins by the settling of fine particles and always likely to form layered systems (Henrich and Hüneke, 2011; Praeger, 2007).

Understanding the consolidation behaviours of these multi-layer systems, which will undergo large-strain consolidation process, is significant for basin modelling. In this research, large-strain consolidation of layered systems is studied by numerical methods. Alternating layers, random layers and impact of surcharge are analysed.

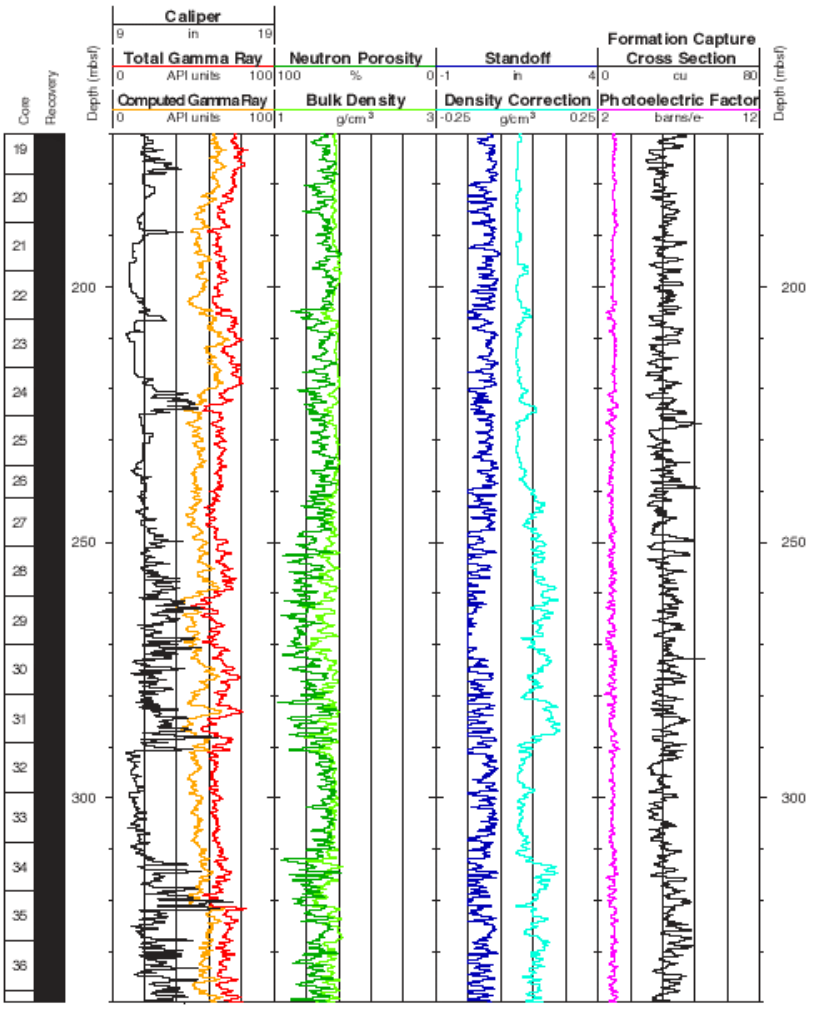

Figure 3.24 Site 1144, South China sea Hemipelagites – Core Log Correlations (Praeger, 2007)

The consolidation behaviour of a two-layer system has received considerable attention in the past. Several investigators have proposed techniques for predicting the one-dimensional consolidation of layered soil systems assuming a system develops a small-strain only (Chen et al., 2005; Davis and Lee, 1969; Liu and Lei, 2013; Xie et al., 2002). Booker and Rowe studied the consolidation of periodically layered deposits, property variation and initial excess pore-pressure distribution were taken into consideration, their simulations show that when the alternating layer reaches a certain value the whole system will follow a single consolidation curve (Booker and Rowe, 1983).

However their studies are based on small-strain theory or simplified large-strain theory. Moreover, they did not consider that properties of different layers may vary randomly, and they did not look at the upscaling. With the purpose of better understanding the consolidation characteristics of large-strain multi-layer systems, large-strain consolidation of layered

systems is studied by numerical methods. Alternating layers and random layers are assumed to follow Gibson's large-strain consolidation. Alternating layers, random layers and influence of surcharge are analysed. Upscaling possibility of multi-layer systems is discussed thereafter. The results are of guiding significance for understanding multi-layer consolidation and upscaling in basin modelling.

The coefficient of volume compressibility of the soil skeleton for large-strain is defined as **Equation 2.14.**

3.3.1 1 D large-strain consolidation of periodically layered system

Periodically layered deposits involving the repetition of layers (**Figure 3.25**) may be characterized by two dimensionless parameters. According to the notation of Booker and Rowe (Booker and Rowe, 1983), these parameters are defined as $a = \frac{m_{vl1}H_1}{m_{vl2}H_2}$ and $b = \frac{k_2 H_1}{k_1 H_2}$, where m_{vli} (i = 1 and 2) is the coefficient of the volume compressibility (m_{vl}) for two layers, respectively, k_i (i = 1 and 2) is the conductivity, and H_i (i = 1 and 2) is the layer thickness.

The model cross section map follows the illustration in **Figure 2.2**, no overlying water, PTIB. The simplified cross section map is also provided as shown in **Figure 3.25**.

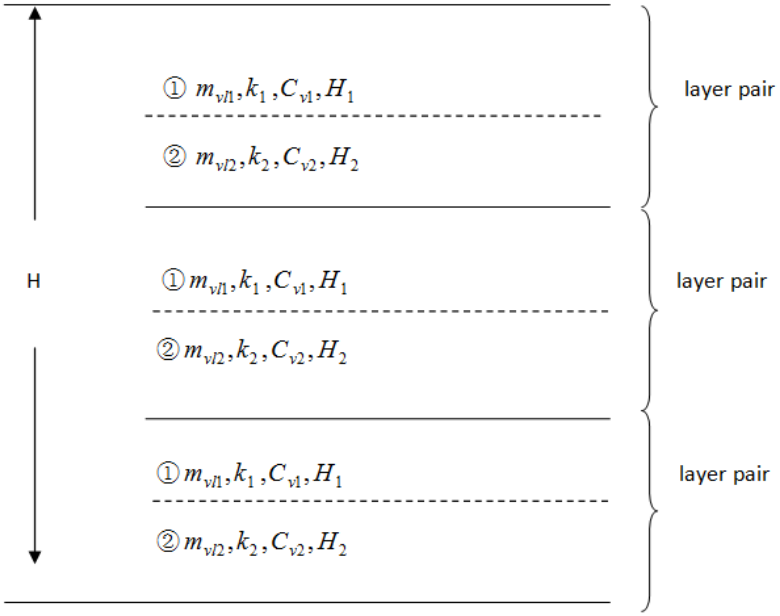

Figure 3.25 Periodically layered stratum

The dimensionless parameters as defined by Booker and Rowe (1983):

$$T = \frac{tC_{eq}}{H^2} \tag{3.46}$$

$$C_{eq} = \frac{k}{m_{vl}\gamma_w} \tag{3.47}$$

Where, C_{eq} is the equivalent consolidation coefficient, k is conductivity corresponding to e_0 in **Equation 3.48.**

In this work, we assume the following constitutive relationships:

'void ratio - effective stress':

$$e = (1+e_0)\exp(-\sigma' m_{vl}) - 1 \tag{3.48}$$

'conductivity - void ratio':

$$k = k_0(1+e)^2 \tag{3.49}$$

It should be noted that **Equation 3.48** is derived from **Equation 2.14,** assuming that m_{vl} is a constant, while in **Equation 3.49** k_0 is constant in a layer. These assumptions follow Xie and Leo's large-strain consolidation analytical solution (Xie and Leo, 2004), which will benefit the comparison of multi-thin layer systems. Moreover, the conductivity is also in nonlinear relationship with void ratio. Both the compressibility and conductivity are in the scope of basin sediment (Kooi, 1997).

Corresponding parameters are shown in **Table 3.6**.

Parameter	Value	Units
unit weight of water / γ_w	10.045	kN/m^3
unit weight of soil / γ_s	27.636	kN/m^3
initial thickness for each layer / H_i	1.0	m
initial effective stress	1.0	kPa
initial void ratio/ e_0	3.0	-
m_{vl} (bottom layer in the pair of two layers)	1.0×10^{-3}	mPa^{-1}
k_0 (bottom layer in the pair of two layers)	5.4×10^{-6}	m/d
m_{vl} (upper layer in the pair of two layers)	0.5×10^{-3}	mPa^{-1}
k_0 (upper layer in the pair of two layers)	5.4×10^{-5}	m/d
surcharge	100.0	kPa

Table 3.6 Parameters utilized in periodically layered deposits

Reverse arrangement is to exchange the upper and bottom layers in the pair. Layer pair numbers, as shown in **Figure 3.25**, change as: [2 4 8 16 32 64 128]. C_{eq} is defined through m_{vl} = 1×10^{-3} and k_0 = 5.4×10^{-6}. Consolidation schematic diagram follows **Figure 2.2**, no overlying water, PTIB.

As shown in **Figure 3.26** - **Figure 3.28**, for a = 0.5, b = 10 (positive arrangement), the increase of the number of layer pairs will decrease the rate of consolidation. For a = 2, b = 0.1 (reverse arrangement) the rate of consolidation is much faster, the rate of consolidation increases with the increase of the number of layer pairs.

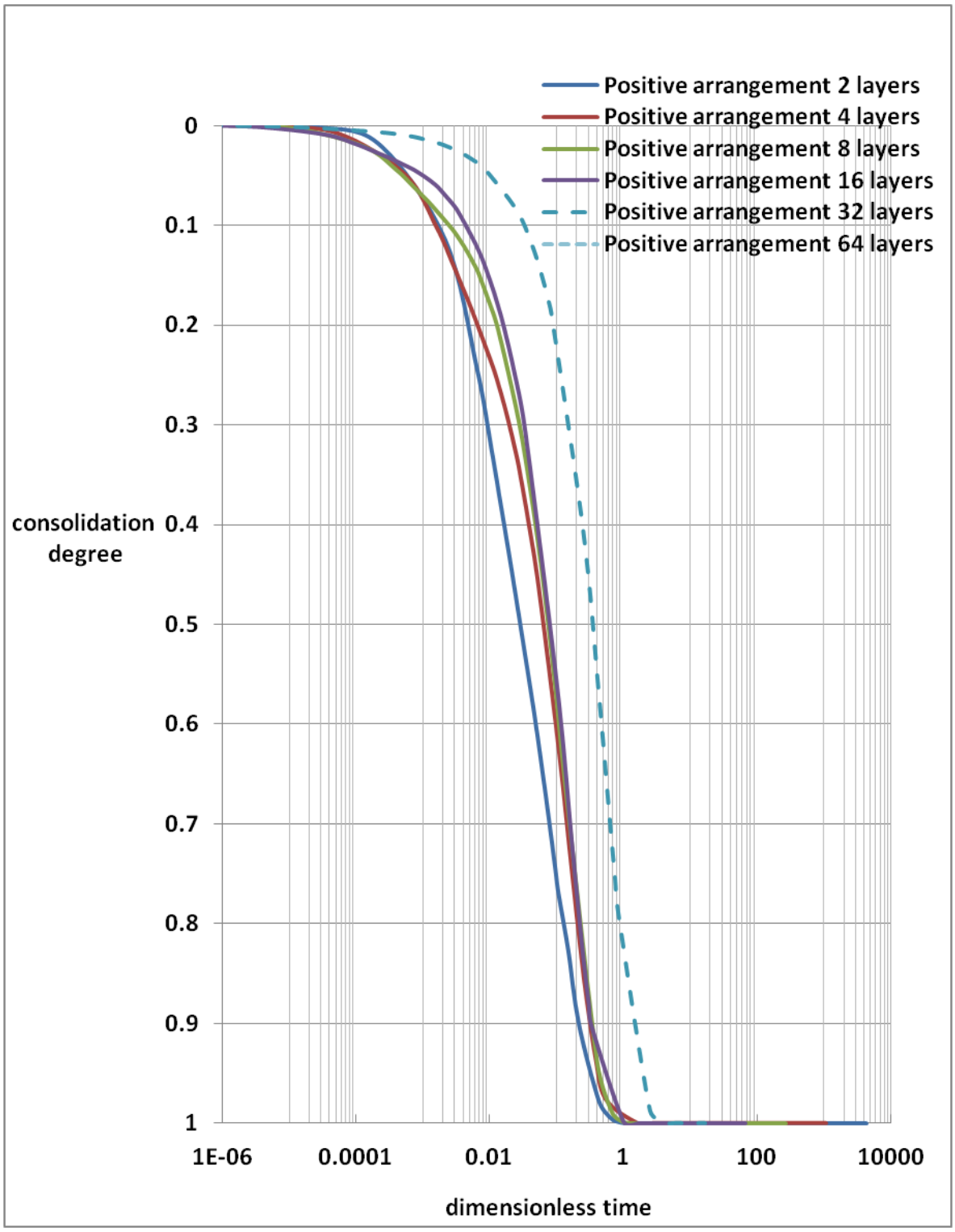

Figure 3.26 Consolidation curves of the positive arrangement

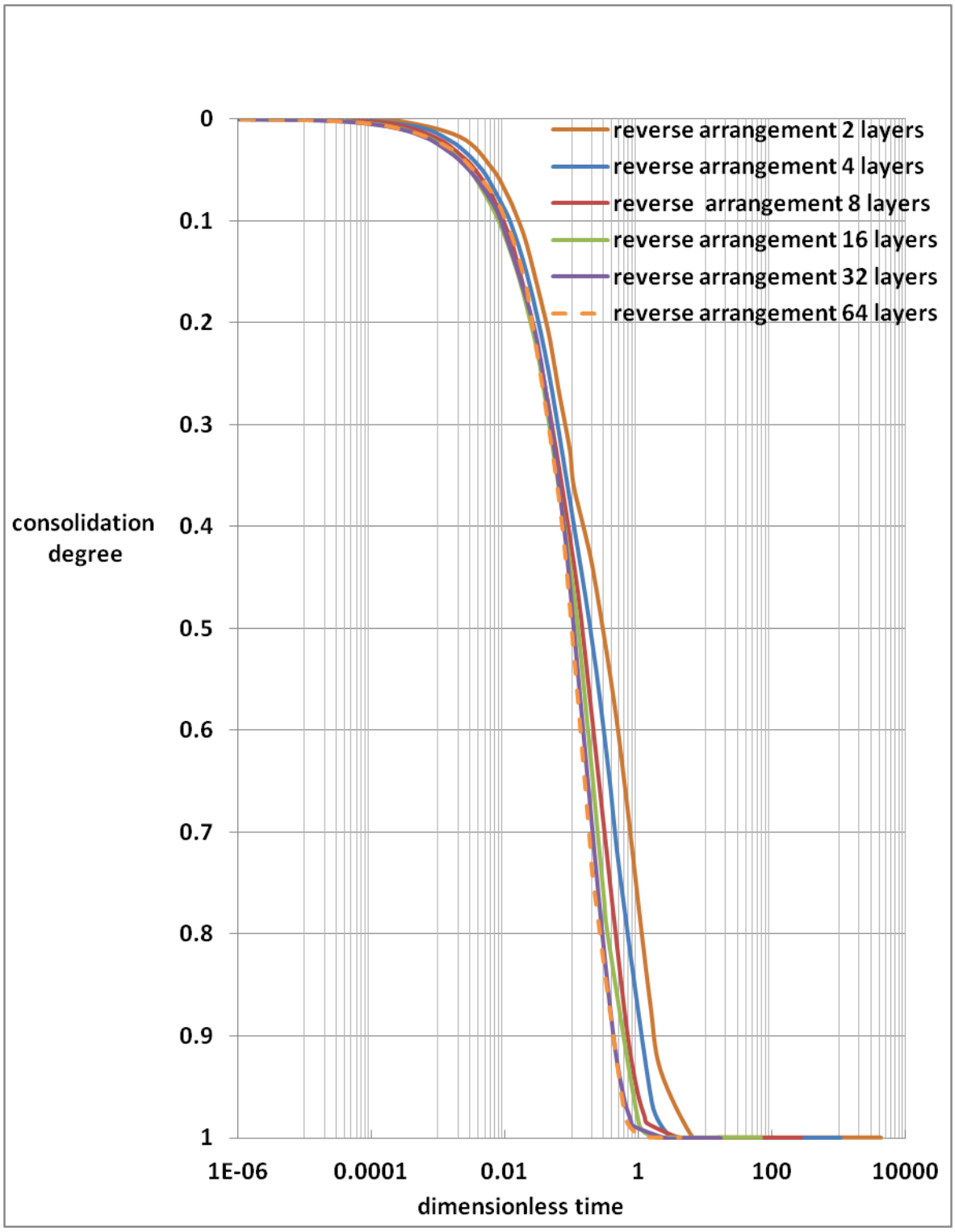

Figure 3.27 Consolidation curves of the reverse arrangement

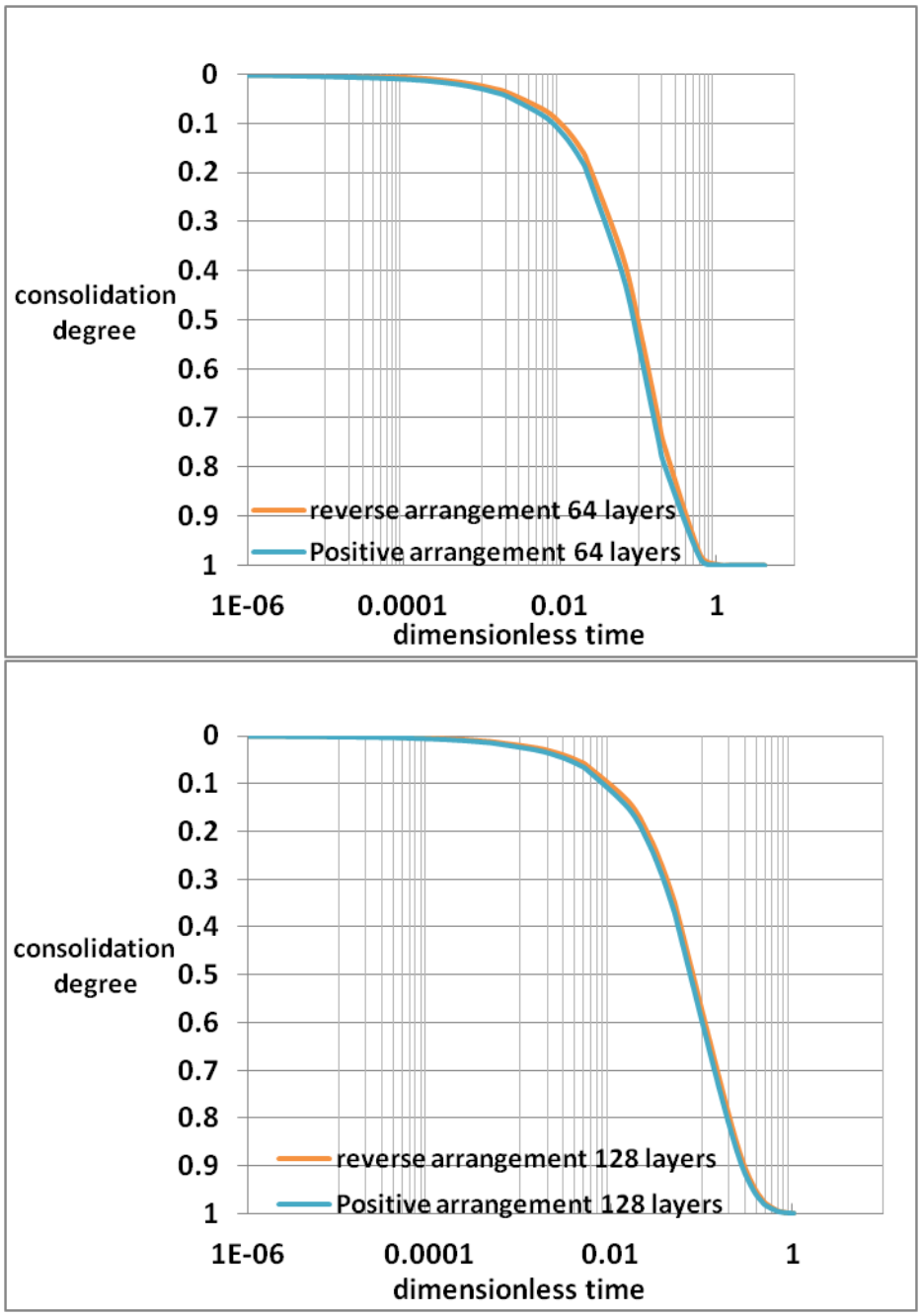

Figure 3.28 Overlapping consolidation curves, upper – 64 different layers, lower – 128 different layers.

When layer numbers reach 64, there is nearly no difference, when the layer number reaches 128 there will be two overlapping curves, which means that the multi-layer system can be treated as 'homogeneous' no matter how arrangement is.

3.3.2 Sensitivity analysis

In order to better understand this 'homogeneous' evolution, a sensitivity analysis is designed here. Layer number changes as: [2 4 6 8 10]. In the two layer pair, bottom layer m_{vl} = 1×10^{-3}, k_0 = 5.4×10^{-5}. For the upper layer m_{vl} change as: [0.8, 1, 1.2] ×10^{-3} kPa^{-1}, k_0 change as: 5.4×10^{-5}/[10, 1, 0.1], which corresponds to a = [0.8, 1, 1.2], b = [0.1, 1, 10], C_{eq} is defined according to bottom layer.

As might be anticipated, layering can exert a significant effect on the consolidation times for a deposit with only a few layer pairs. Viewed as a whole from **Figure 3.29 - Figure 3.30**, the consolidation time T50/T90 (the times required for 50% and 90% consolidation) curves converge fairly rapidly when layer number is small. But when the layer pair numbers reach a certain value, it results in a constant dimensionless consolidation time, which means one unique consolidation curve.

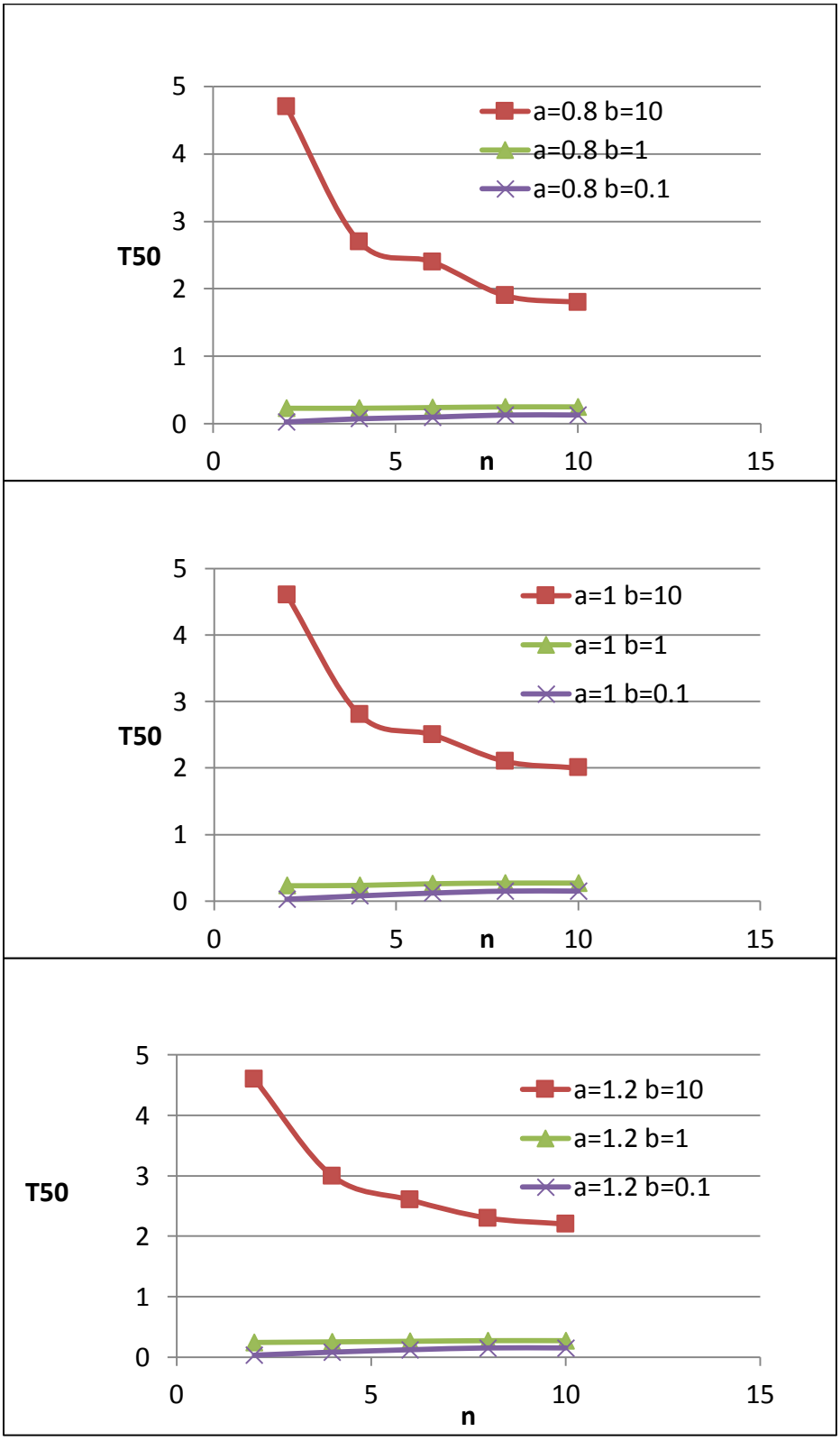

Figure 3.29 Variation of T_{50} with layer number

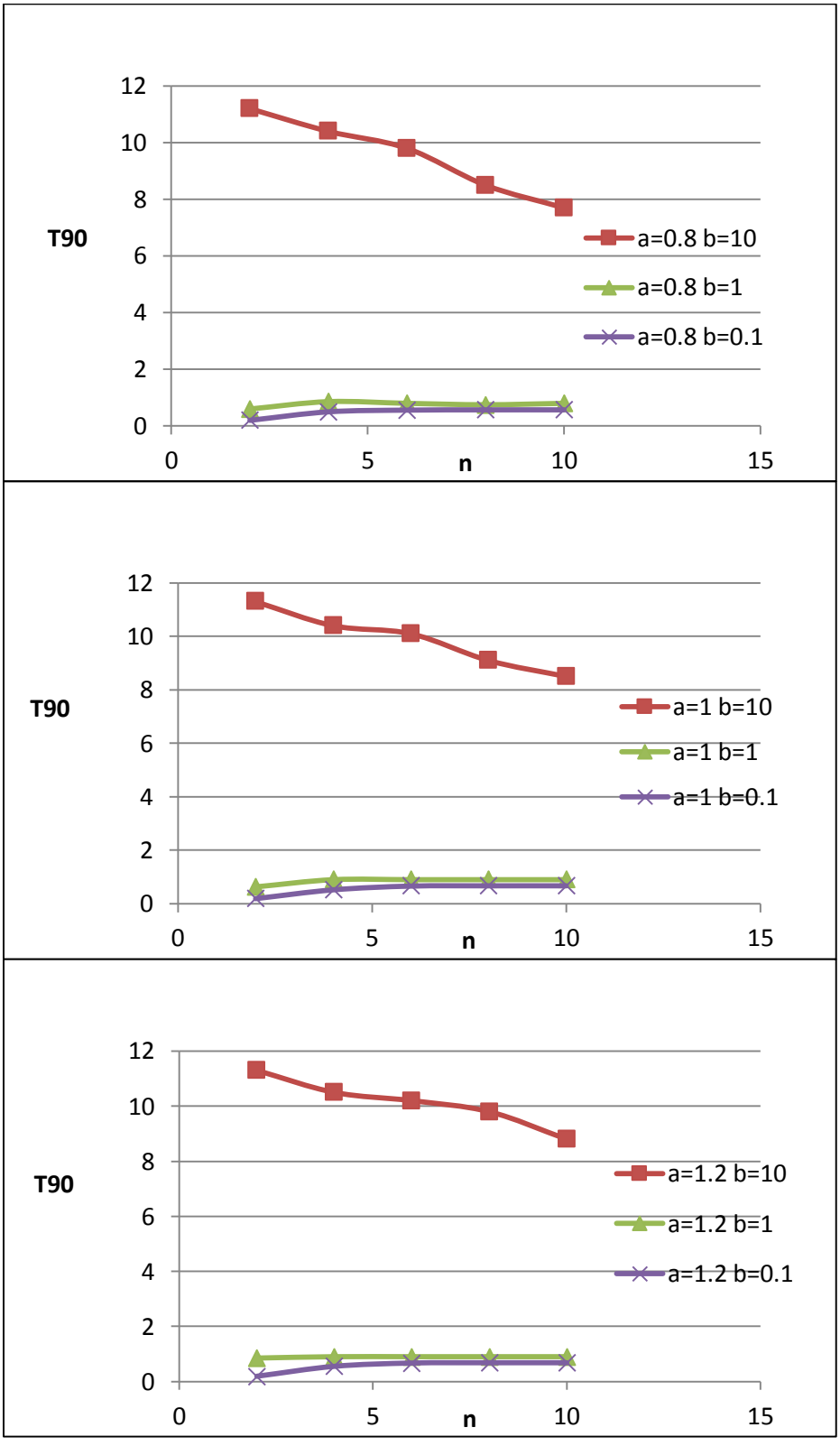

Figure 3.30 Variation of T_{90} with layer number

3.3.3 Consolidation characteristic of layers with random properties

3.3.3.1 Conductivity change

(1)Conductivity varies within a factor of 10.

Layer number change as: [8 16 32 64 128], m_{vl} = 1×10^{-3}, k_0 varies randomly between 5.4×10^{-6} and 5.4×10^{-5}, there are two sets of layer for each layer number, C_{eq} is defined through k_0 = 5.4×10^{-6}.

It can be seen from **Figure 3.31**, difference of consolidation curves decreases with the increase of layer number. When layer numbers reach 64, there are nearly two overlapping curves, which means the multi-layer system then can be treated as 'homogeneous'.

(2)Conductivity varies within a factor of 50.

Layer number change as: [8 16 32 64 128]. m_{vl} = 1×10^{-3}, k_0 varies randomly between 5.4×10^{-6} and 2.7×10^{-4}, there are two sets of layer for each layer number. C_{eq} is defined through k_0 = 5.4×10^{-6}.

Figure 3.32 indicates that difference of consolidation curves decreases with the increase of layer number. When layer numbers reach 128, there are nearly two overlapping curves, which means the multi-layer system then can be treated as 'homogeneous'.

Hence, we may come into the conclusion that the bigger the variation of conductivity, the more layers will be needed to reach a homogenized property.

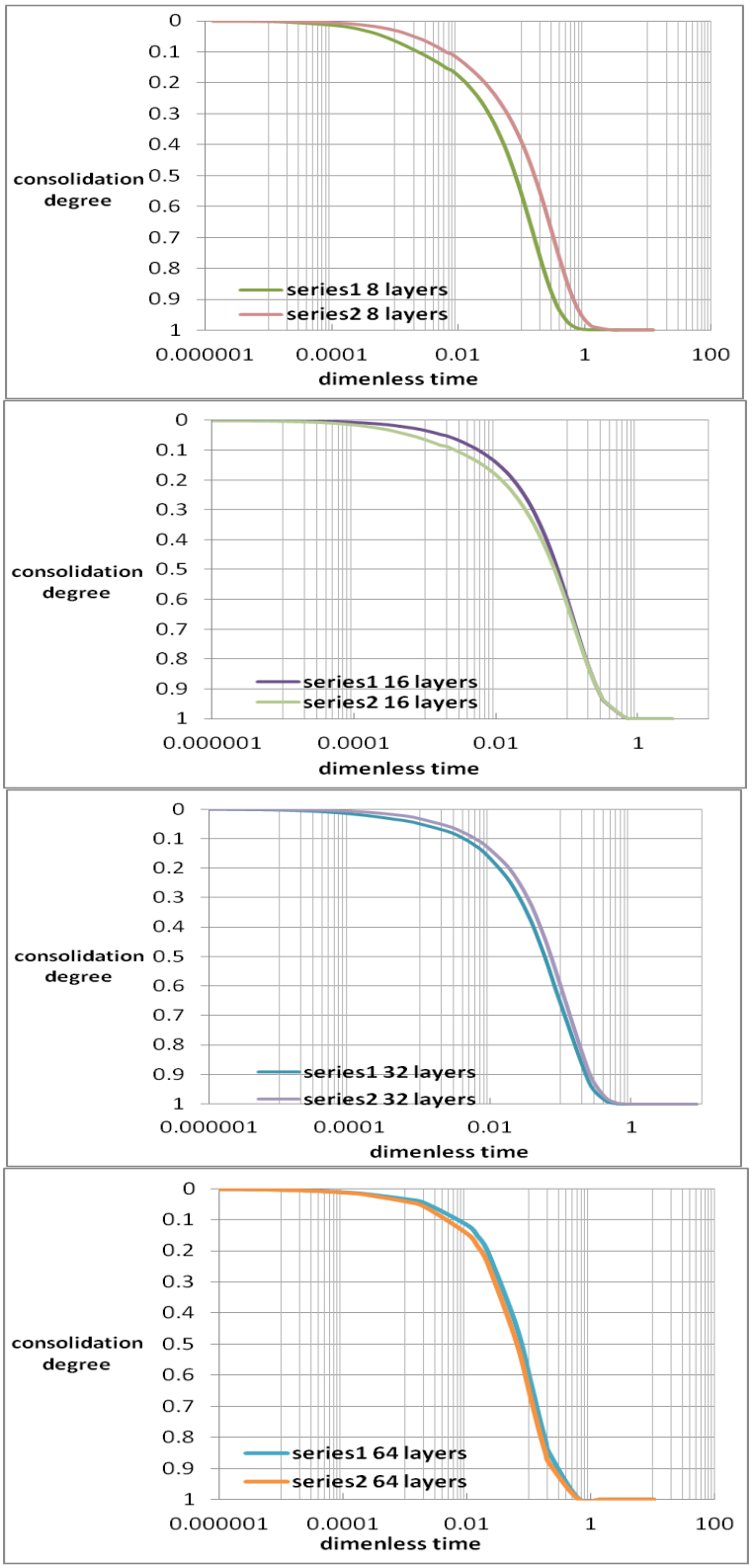

Figure 3.31 Consolidation curves change with layer number (Conductivity varies within a factor of 10)

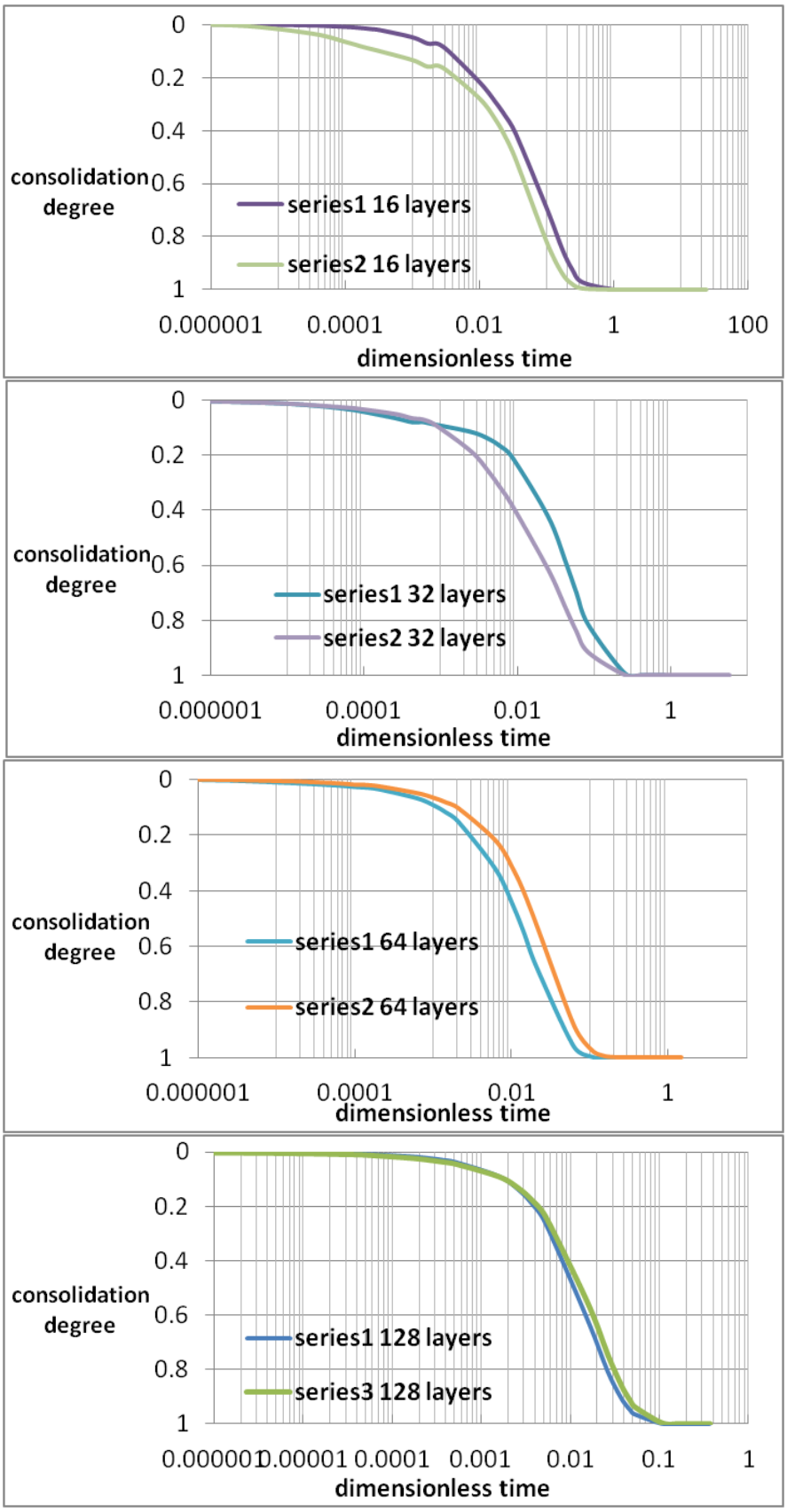

Figure 3.32 Consolidation curves change with layer number (Conductivity varies within a factor of 50)

3.3.3.2 Compressibility change

(1)Compressibility varies within a factor of 2.

Layer number changes as: [8 16 32 64]. k_0 = 5.4×10^{-5}, m_{vl} varies randomly between 1×10^{-3} and 2×10^{-3}, there are two sets of layer for each layer number. C_{eq} is defined through m_{vl} = 1×10^{-3}.

Figure 3.33 shows that difference of consolidation curves decreases with the increase of layer number. When the layer number reaches 16, there will be two overlapping curves, which means the multi-layer system can be treated as 'homogeneous'.

(2)Compressibility varies within a factor of 3.

Layer number changes as: [8 16 32 64]. k_0 = 5.4×10^{-5}, m_{vl} varies randomly between 1×10^{-3} and 3×10^{-3}, there are two sets of layer for each layer number. C_{eq} is defined through m_{vl} = 1×10^{-3}.

Figure 3.34 reveals that difference of consolidation curves decreases with the increase of layer number. When layer number reaches 16, there is small difference. When the layer number reaches 32 there will be two overlapping curves, which means the multi-layer system can be treated as 'homogeneous'.

It can be concluded that the bigger the variation of compressibility is, the more layers will be needed to reach a homogenized property.

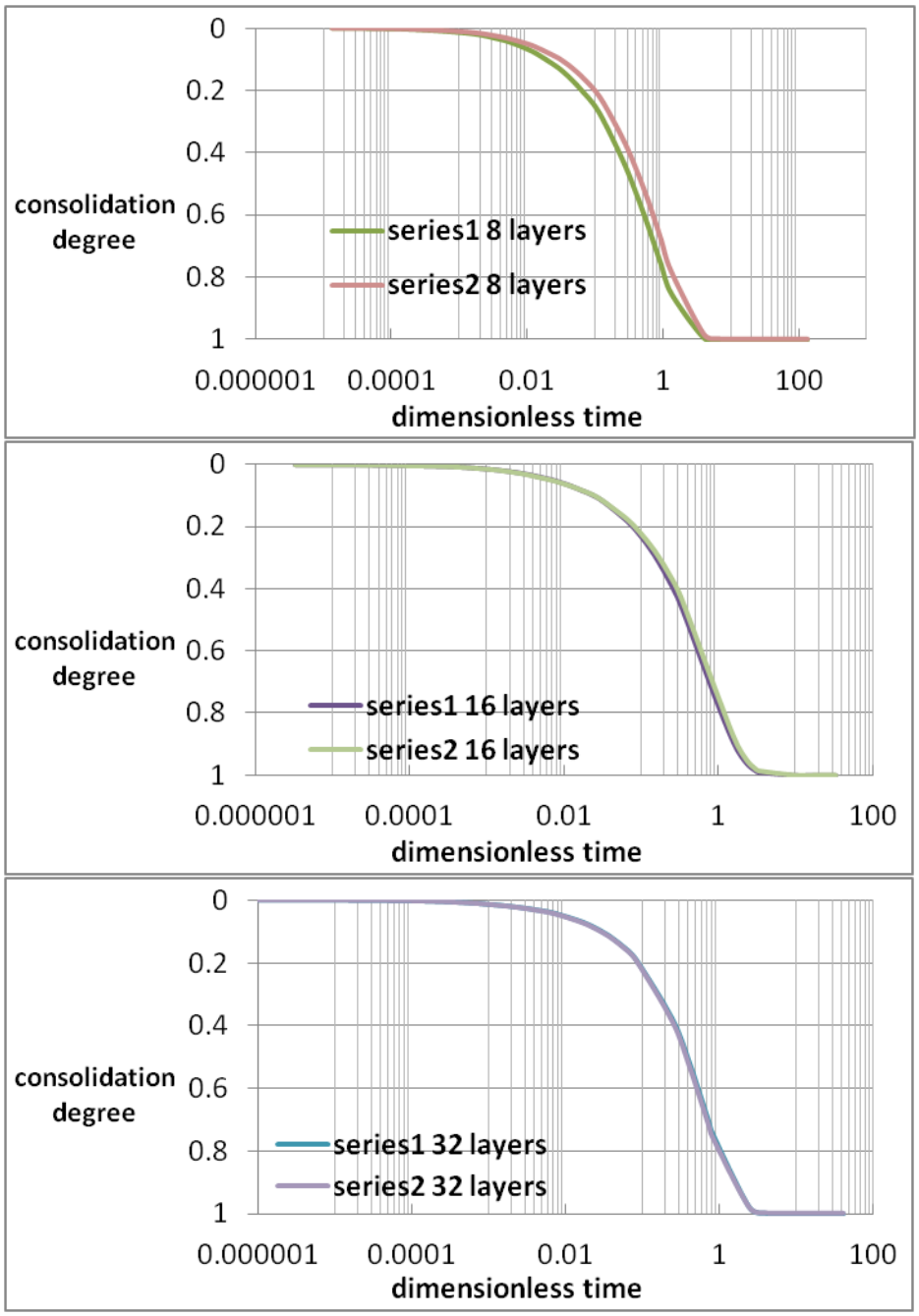

Figure 3.33 Consolidation curves change with layer number (Compressibility varies within a factor of 2)

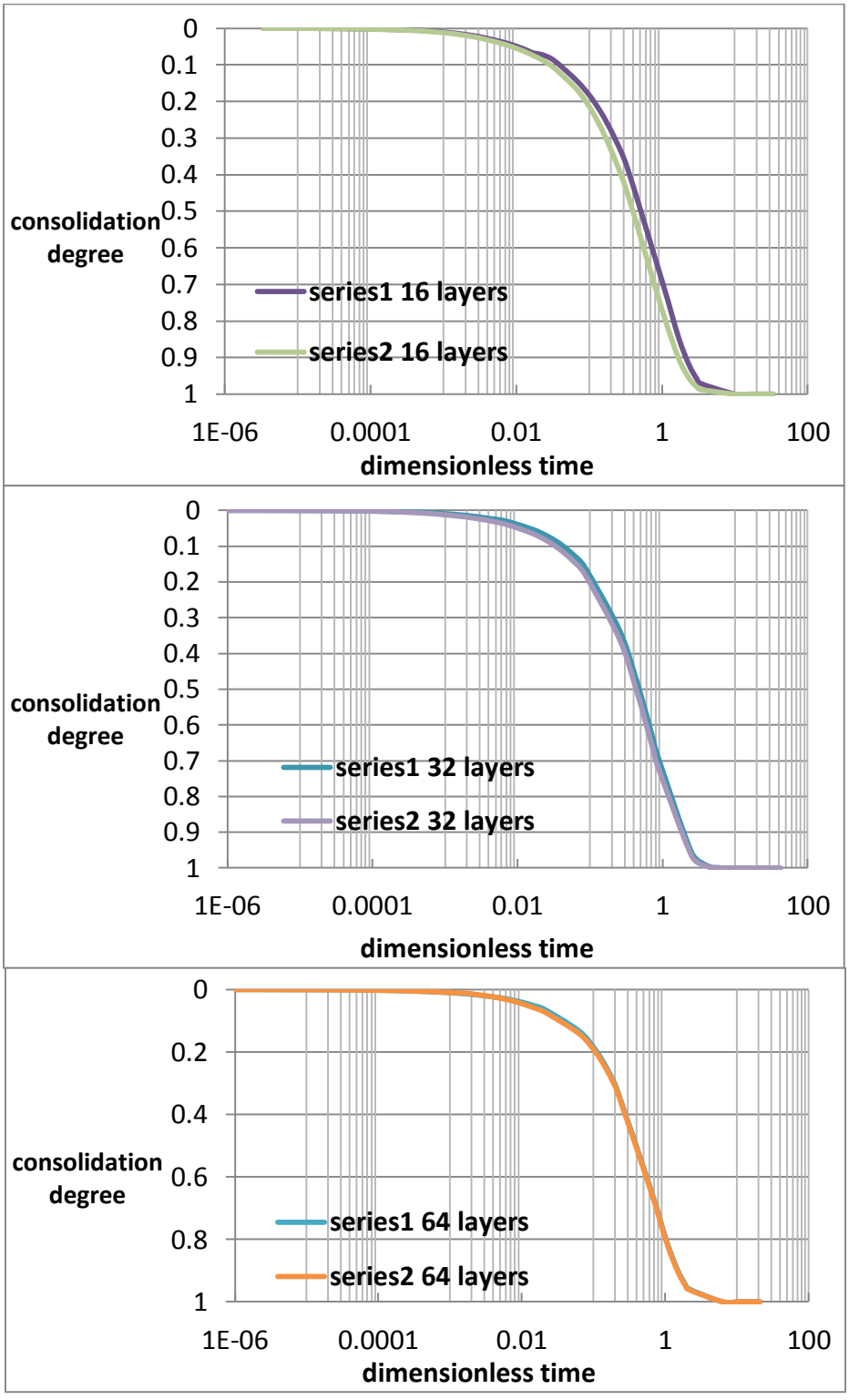

Figure 3.34 Consolidation curves change with layer number (Compressibility varies within a factor of 3)

3.3.3.3 Conductivity and compressibility change together

Layer number changes as: [8 16 32 64 128]. k_0 varies randomly between 5.4×10^{-6} and 5.4×10^{-5}, m_{vl} varies randomly between 0.5×10^{-3} and 1×10^{-3}, there are two sets of layer for each layer number. C_{eq} is defined through $m_{vl} = 0.5\times10^{-3}$, $k_0 = 5.4\times10^{-6}$.

It can be seen from **Figure 3.35**, difference of consolidation curves decreases with the increase of layer number. When layer numbers reach 64 there is small difference. When the layer number reaches 128, there will be two overlapping curves, which means the multi-layer system can be treated as 'homogeneous'.

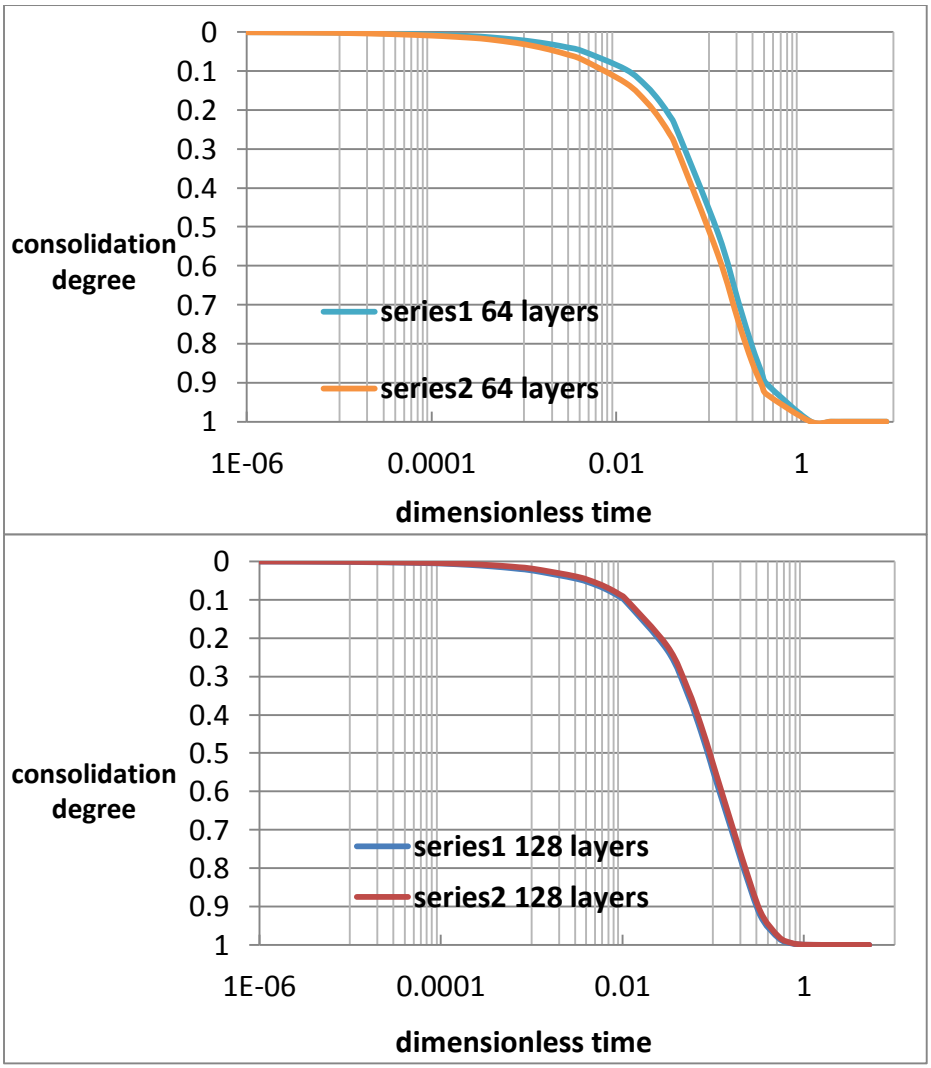

Figure 3.35 Consolidation curves change with layer number (Conductivity and compressibility change together)

3.3.4 Effect of surcharge variation

Consolidation of the 64 homogenized multi-layer system with random k and m_{vl} under different surcharges is analysed here. Surcharge changes as [100 400 700] kPa. There are two sets of random materials for each loading condition. k_0 varies between 5.4×10^{-6} and 1.08×10^{-5} randomly, m_{vl} varies between 0.5×10^{-3} and 1×10^{-4} randomly. C_{eq} is defined through $m_{vl} = 0.5\times10^{-3}$, $k_0 = 5.4\times10^{-6}$. There are 2 sets of layers for each surcharge.

As shown in **Figure 3.36**, instead of keeping constant, consolidation curves change with surcharge variation. The biggest variation occurs at about T = 0.02, with time going on consolidation curves evolve into a same line.

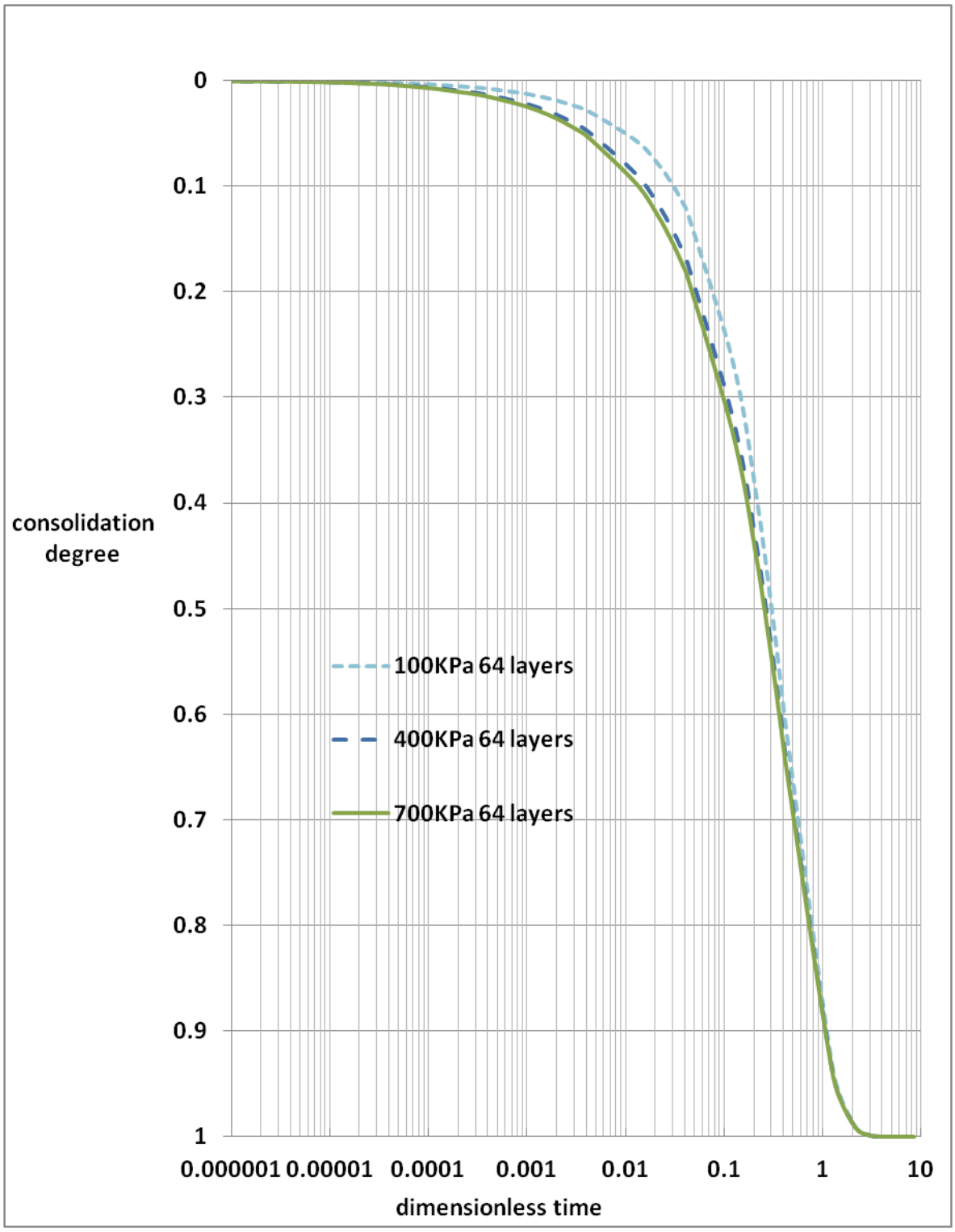

Figure 3.36 Consolidation curves change with surcharge

3.3.5 Multi-layer upscaling analysis

It is feasible to use one type of material to stand the whole multi-layer system when considering the homogenized properties. Accompanying with curve fitting method, conductivity varies within a factor of 10 is used for illustration.

However, no constant consolidation parameters generate the same consolidation curve in curve fitting process, as **Figure 3.37** shows the optimal fitting results. **Chapter 3.1** provides explanation, the characteristics of multi-layer systems vary with time and out stimulation (surcharge). Considering the change of properties, it is impossible to find a set of fixed relationship to stand for the multi-layer system.

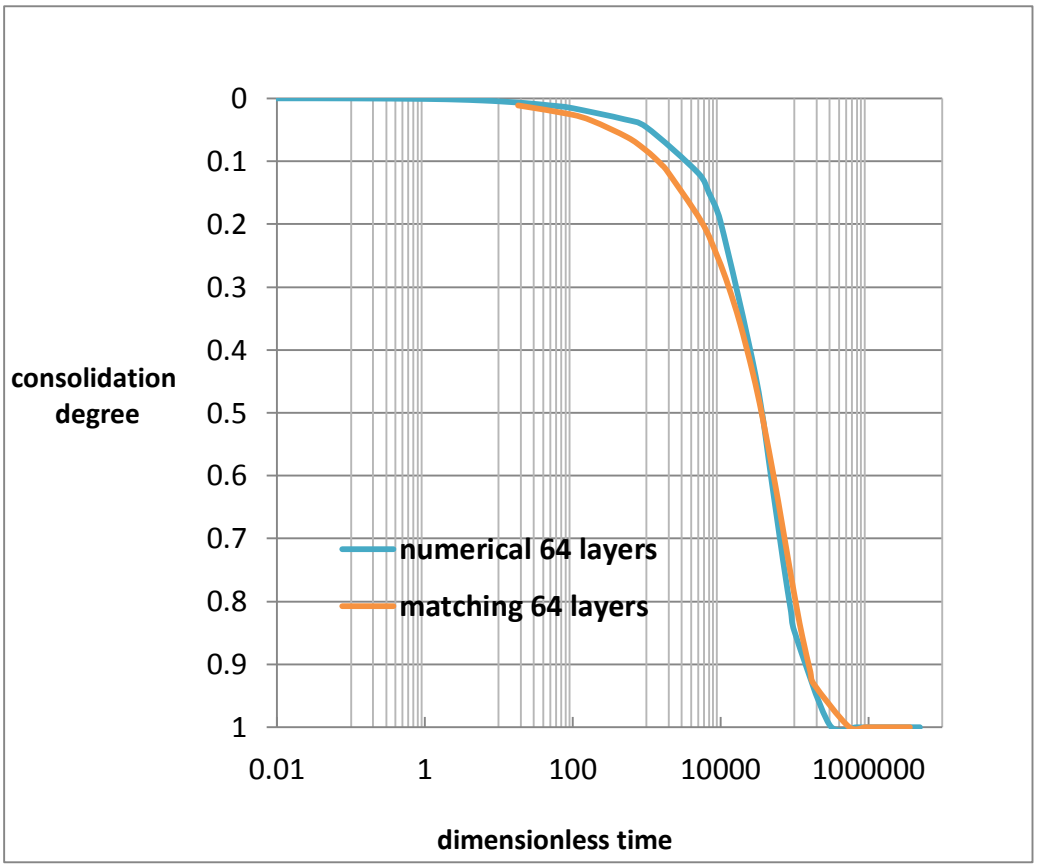

Figure 3.37 Consolidation curve fitting result

3.3.6 Theory extension

3.3.6.1 Permeable top and Permeable bottom (PTPB)

There are two different consolidation patterns, Permeable top impermeable bottom (PTIB) and Permeable top Permeable bottom (PTPB), PTPB shows the same trend with PTIB.

Moreover, despite variation of initial pore pressure distribution, all result in a homogenized consolidation curve when layer number reaches a certain value. PTPB example is provided as **Figure 3.38** shows. With a view to the limitation of writing length, these cases are omitted.

Layer number changes as: [8 16 32 64], two random series provided for each layer number. k_0 changes between 5.4×10^{-6} and 16.2×10^{-6} randomly, m_{vl} changes between 1×10^{-3} and 2×10^{-3} randomly, C_{eq} is defined through $m_{vl} = 1\times10^{-3}$, $k_0 = 5.4\times10^{-6}$.

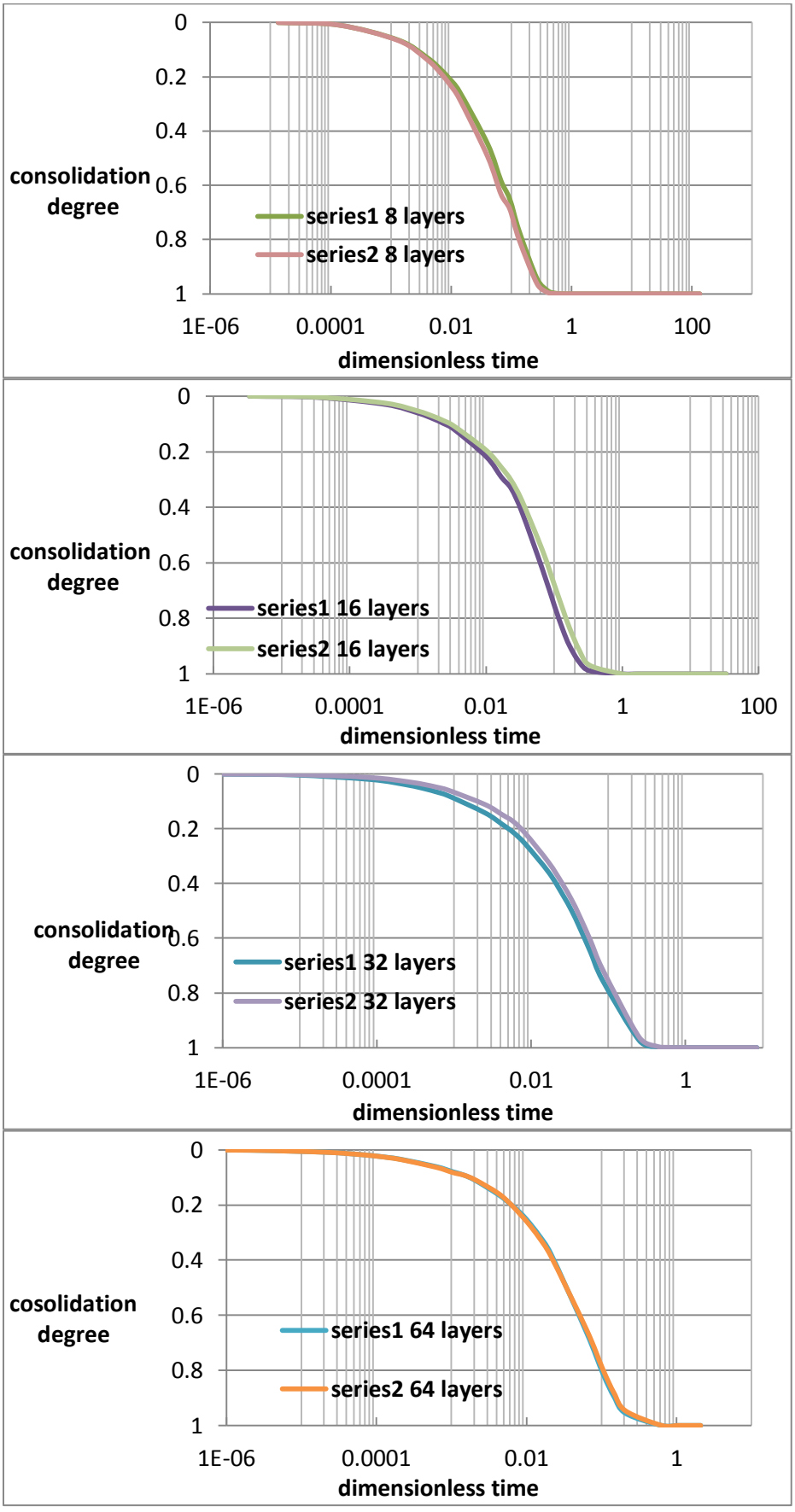

Figure 3.38 Consolidation curves change with layer number for PTPB

3.3.6.2 Small-strain consolidation

There is no clear dividing line between small-strain and large-strain consolidation theory. With the increase of confined pressure, conductivity will decrease and can be treated as constant. In the meanwhile high volume compressibility will ensure small strain. The conclusion is similar as large-strain consolidation.

3.3.6.3 Influence of periodically arrangement

Similar to the notation of Booker and Rowe (Booker and Rowe, 1983), since all water must eventually flow to the surface, the rate of consolidation is largely controlled by the conductivity of the top sub layer. If the upper sub layer is relatively thick and impermeable, the distribution of initial excess pore pressure will not greatly affect the rate of consolidation and in all cases consolidation will be relatively slow. Conversely, the initial pore pressure distribution significantly affects the rate of consolidation and in these cases consolidation will be faster. This tends can also be applied to multi-layer large-strain consolidation as can be seen from the study of periodically layered system. The significance of this study to basin modelling is that if the less permeable layer is relatively thick and on the top, the distribution of initial excess pore pressure will not greatly affect the rate of consolidation and consolidation will be relatively slow. The whole system will show a less permeable characteristic and overpressure can be maintained for a long time. If the less permeable layer is at the base, the initial pore pressure distribution significantly affects the rate of consolidation and consolidation will be faster. However, this effect decreases with the increase of layer number.

3.3.7 Discussion and Conclusion for 1D consolidation of layered system

In this part, large-strain consolidation of layered systems is studied by numerical methods. Alternating layers, random layers and influence of surcharge are analysed.

(1) When the alternating layer reaches a certain value, the whole system will follow a single consolidation curve both for small-strain and large-strain deformation. A sensitivity analysis demonstrates that the number of layers exerts a great influence on consolidation time.

(2)In the real sedimentation, compressibility and conductivity change randomly. When the random layer reaches a certain value, the whole system will follow a single consolidation

curve. The bigger the variation of compressibility and conductivity is, the more layers will be needed to reach a single consolidation curves.

Consolidation curves stand for the nature of multi-layer system. The significant meaning for upscaling is that when alternating layer pair reaches a certain value the whole system follows one consolidation curve.

(3)Curve fitting results show that it is impossible to find a set of fixed relationship to match the multi-layer consolidation, which means direct upscaling is impossible.

(4)The homogenized multi-layer consolidation curves (64 random layers) change with surcharge, the curves coincide with each other at the beginning, the biggest variation occurs at about T = 0.02. With time going on consolidation curves nearly evolve into a same line, the variation between curves become smaller with the increase of surcharge.

These conclusions may provide meaningful guidance for upscaling in basin modelling.

3.4 Large-strain consolidation properties inversion and upscaling

In the petroleum industry, a well test is the execution of a set of planned data acquisition activities to broaden the knowledge and understanding of hydrocarbons properties and characteristics of the underground reservoir where hydrocarbons are trapped. Similar to well test, inversion of deposit sediments' petrophysical properties is possible and very important for accurate basin modelling.

Precise description of the deposit sediments' properties is significant for basin modelling. However, in many cases, it is impossible to obtain the consolidation properties directly. The revolution in sensor and information technology has made possible extensive monitoring during construction or consolidation, or under an external stimulation, coupled with inversion analysis to obtain the unknown soil parameter.

The goal of inverse problem solving is to determine the values of unknown model parameters from measured quantities by assuming a model that relates the two. Normally the forward problem can be expressed in a matrix form. The general forward problem has the following matrix form:

$$y = h_{trans} \cdot x \tag{3.50}$$

Where x represents the input vector (unknown), y is output vector (measured quantities), h_{trans} is transformation matrix.

There are a number of techniques to find the unknown parameters (Press, 2002; Santamarina and Fratta, 2005), such as Direct Inversion (DI), Least Squares Solution (LSS), and Regularized Least Squares Solution (RLSS).

If the h_{trans} is invertible, the Direct Inversion method is applicable, and the unknown parameters are obtained as:

$$x = h_{trans}^{-1} \cdot y \tag{3.51}$$

When h_{trans} is not invertible, other methods should be used.

Narsilio did some research on small-strain consolidation inversion (Narsilio, G. A., 2006). In his research the matrix forms of Terzaghi from finite differences constitute the forward problem and generate synthetic 'measured' data of the excess pore pressure vector - u. Then, the goal is to determine the C_v profiles versus depth from these 'measured' data.

The finite difference equation is expressed in matrix form in order to use matrix based on inversion methods:

$$\Delta u = h_{trans} \cdot C_v \tag{3.52}$$

Where Δu is overpressure difference between two given time.

Geotechnical engineers often face important discrepancies between the observed and the predicted behaviour of geo-systems. Sometimes it is induced by the ubiquitous spatial variability in soil properties. The most common type of soil variability is layering. However, natural soil deposits can exhibit large variability in both vertical and horizontal dimensions as a result of deposition history, chemical or biogenic effects. What is more, due to the limitation of log data and computation ability, detail modelling of each small layer is impossible. Therefore, the effects of intra-block sediment heterogeneity must be taken into account by upscaling. Inversion technique gives us enlightenment to upscale the properties of multi-layer system. This research makes an attempt to upscale the properties of multi-layer system by inversing

In this research, a large-strain consolidation finite difference code based on Gibson model is developed firstly, and on this base inversion technique for large-strain consolidation is developed. Townsend's sedimentation model is adopted for verification thereafter. Then inversion technique is extended for upscaling.

3.4.1 Large-strain consolidation inversion theory

Somogyi rearranged the continuity and fluid flow relationships (Somogyi, 1980), the governing equation becomes:

$$\frac{\partial}{\partial z}[\frac{k}{\gamma_w(1+e)}]\frac{\partial u}{\partial z}+\frac{k}{\gamma_w(1+e)}\frac{\partial^2 u}{\partial z^2}+\frac{de}{d\sigma'}\frac{\partial u}{\partial t}-\frac{de}{d\sigma'}[(G_s-1)\gamma_w\frac{d(\Delta z)}{dt}]=0 \qquad (3.53)$$

Then with the difference of void ratio and overpressure, we can invert the soil properties. Normally, void ratio data is obtained through experiment, which is highly dependent on drilling and coring, so it is not reliable and unable to update. It is unpractical to obtain the small change of void ratio data by log data in a short period of time, but practical of using pore pressure. The equation of Somogyi is equal to Gibson in physical significance. Hence Somogyi's equation can be used for properties inversion if we have pore pressure stimulation in a short time.

3.4.2 Solution

An implicit finite difference method is used to solve the Gibson/Somogyi's equation, exponential form is utilized for illustration. As for the Gibson model, equation with the variable of void ratio e, the matrix forms from finite differences is shown as follows.

$$e=A(\sigma')^B, k=Ce^D, e_i^{t+1}-e_i^t=Ee_{i-1}^t+Fe_i^t+Ge_{i+1}^t \qquad (3.54)$$

Where E, F, G are function of A, B, C, D, time step, space step, t is time step. A, B, C, D, are constants which stand for the soil properties, are unknown. As a matter of course, four equations, that mean at least six continuous points in finite difference, are needed for a homogeneous soil, as shown in the **Figure 3.39**.

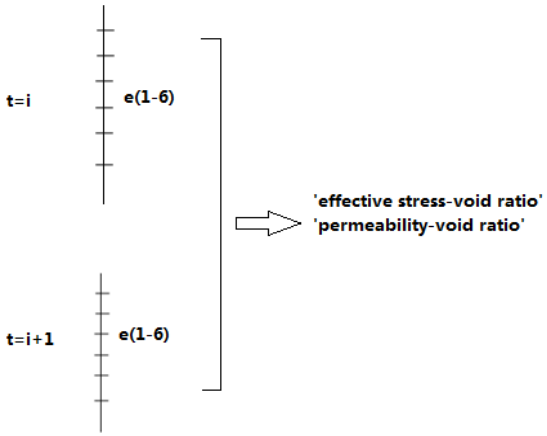

Figure 3.39 Nodes cross section map for inversion

Multi-layer means more sets of points are required. Least Squares Solution (LSS) is applied to solve these nonlinear equations.

3.4.3 Verification

3.4.3.1 Verification with analytical solution

Xie and Leo obtained Gibson's analytical results (Xie and Leo, 2004). The inversion technology is verified with the analytical solution. Verification parameters are shown in the following **Table 3.7**. The model cross section map follows the illustration in **Figure 2.2**, PTIB, and no overlying water.

Parameter	Value	Units
unit weight of soil / γ_s	27.5	kN/m^3
initial thickness / H	0.1	m
e_0	3.0	-
m_{vl}	4.0	mPa^{-1}
k_0	10^{-9}	m/s
initial effective stress	10	kPa
load increment/ q_u	100	kPa
water level above the initial top surface of the layer	1	m

Table 3.7 Parameters utilized in comparison with Xie's solution.

$\sigma' - e$ and $k - e$ relationships :

$k = 5.4 \times 10^{-6}(1+e)^2$, ($k$ - m/d);

$\sigma' = 10 - 250(\ln(1+e) - \ln(4)) = 356.573 - 250\ln(1+e)$, ($\sigma'$ - kPa).

Considering the setting of Xie and Leo (Xie and Leo, 2004), '250' and '5.4×10^{-6}' are set to be unknown parameters. Two unknown parameters require two equations, that is 4 nodes when considering two boundary nodes.

Initial condition is consolidation after 0.1 day. Time step is 0.001 days, space step is 0.0025 m. there are 10 nodes in all, node number 4 5 6 7 (1 - 10 from bottom to up) is utilized for calculation.

Initial pressure and pressure of after 0.01 days for node 4 - 7 are shown in the following table.

Node	Initial overpressure(kPa)	Next step overpressure(kPa)
4	99.74317315805443	99.72533314741391
5	98.50644787078167	98.46061683056962
6	95.11296038821480	95.01507422743269
7	87.01632340369378	86.84885430125055

Table 3.8 Overpressure data for different nodes

Node	Initial void ratio	Next step void ratio
4	2.99187140267343	2.99158655272381
5	2.97284432577138	2.97211607417427
6	2.91994409841326	2.91840956573879
7	2.79566602137827	2.79312424568401

Table 3.9 Void ratio data for different nodes

Solution with void ratio and overpressure variation are provided, results are shown in the table as follows.

Inversion through void ratio:

	Real value	Initial value/set1	Result/set1	Residual
Set1	250	255.00	251.79	0.19711×10^{-5}
	5.4×10^{-6}	5.80×10^{-6}	5.36×10^{-6}	-4.15368×10^{-6}
Set2	250	245.00	248.50	0.19198×10^{-5}
	5.4×10^{-6}	5.00×10^{-6}	5.43×10^{-6}	-4.04481×10^{-6}
Set3	250	100.00	105.06	-0.71184×10^{-6}
	5.4×10^{-6}	5.00×10^{-6}	1.29×10^{-6}	1.43533×10^{-6}
Set4	250	25.00	27.11	-0.35759×10^{-6}
	5.4×10^{-6}	5.80×10^{-5}	4.99×10^{-5}	-3.68833×10^{-6}
Set5	250	100.00	103.89	0.84980×10^{-6}
	5.4×10^{-6}	5.00×10^{-5}	1.30×10^{-6}	1.72479×10^{-6}

Table 3.10 Solutions with void ratio variation

Inversion through overpressure:

	Real value	Initial value/set1	Result/set1	Residual
Set1	250	260.00	255.38	-0.66174×10^{-3}
	5.4×10^{-6}	5.60×10^{-6}	5.40×10^{-6}	1.60476×10^{-5}
Set2	250	245.00	244.86	-0.65647×10^{-3}
	5.4×10^{-6}	5.00×10^{-6}	5.63×10^{-6}	4.93985×10^{-6}
Set3	250	100	102.14	-0.58494×10^{-3}
	5.4×10^{-6}	5.00×10^{-5}	1.35×10^{-6}	1.45677×10^{-4}
Set4	250	200.00	203.60	-0.63579×10^{-3}
	5.4×10^{-6}	5.40×10^{-5}	6.77×10^{-6}	0.38595×10^{-5}
Set5	250	20	22.44	-0.54450×10^{-3}
	5.4×10^{-6}	5.40×10^{-7}	6.14×10^{-6}	2.29790×10^{-4}

Table 3.11 Solutions with overpressure variation

3.4.3.2 Verification with experiment

Here we use Townsend's A model, self-consolidation, for illustration as shown in **Chapter 2.3.2** (Townsend and Mcvay, 1991). Due to the better fitting and the existence of void ratio data, void ratio data is utilized for inversion. Firstly numerical model is adjusted to fit the experiment results. Then void ratio variation is used for inversion. Time step is 1 day, space step is 6.13×10^{-3} m, Node number equals 100, Initial void ratio equals 14.80, node number from 1 to 100 as from bottom to top. Nodes i = 4, 5, 6, 7 are selected to form 4 equations for illustration, moreover nodes i = 3, 8 are also necessary.

After the first step, void ratio distribution from node i = 1 to i = 10 are shown in the following table.

Initial void ratio	Void ratio after 1day
14.8	10.12201179
14.8	13.18421559
14.8	14.24190555
14.8	14.60723331
14.8	14.73341808
14.8	14.77700250
14.8	14.79205663
14.8	14.79725635
14.8	14.79905234
14.8	14.79967268

Table 3.12 Model parameters utilized in verification with experiment

Two set of initial values are provided, results are shown in the table as follows.

Real value	Initial value/set1	Result/set1	Initial value/set2	Result/set2
7.72	7.72	7.720001	7.92	7.720000573
-0.22	-0.22	-0.22	-0.32	-0.220000035
2.532×10^{-7}	2.00×10^{-7}	2.53×10^{-7}	2.00×10^{-6}	2.532×10^{-7}
4.65	4.65	4.65000055391654	4.63	4.649999799

Table 3.13 Inverting results in verification with experiment

It is then concluded that soil properties can be inverted. However, due to the strong nonlinearity, inversion is only effective over a limited range. It is necessary to narrow the scope of parameters by combining with other information during the actual operation.

3.4.4 *Inversion based upscaling*

As for the multi-layer system, soil properties can be acquired by inversion for each layer separately. With the purpose of upscaling properties for the whole multi-layer system, this inversion method is evaluated under different conditions.

In the following calculation, ‘void ratio - effective stress’ and ‘conductivity - void ratio‘ will be in the form of **Equation 3.55**.

$$e = A - B\ln(\sigma'),\ k = Ce^{D} \tag{3.55}$$

Where A, B, C, D, are constants which stand for the soil properties.

A three-layer system is adopted for illustration. The three-layer system is permeable top impermeable bottom as shown in **Figure 3.13**, model parameters are shown in **Table 3.14**.

Layer	Thickness(m)	Clay content (%)	Node number(node)
layer 1	20	90	45(156-200)
layer 2	20	10	110(46-155)
layer 3	20	90	45(1-45)

Table 3.14 Model parameters for inversion based upscaling

Overburden pressure 500 kPa, initial effective stress 500 kPa, time step is 10 days, space step is 0.132m.

Due to the limitation of log data and computation ability, fine-scale modelling of each small layer is impossible, such as 1 or 2 nodes, or even no node for some layer. In this inversion calculation, 6 nodes is needed, two nodes for each layer, nodes, void ratio of first (consolidation of 100 years) and next step (10 days after the first step) are shown in the following table.

Node	100 year	After 10 days
e(15)	2.20660823	2.20657983
e(30)	2.21931839	2.21929207
e(70)	0.363329046	0.363326022
e(95)	0.369014532	0.369011416
e(105)	0.371419698	0.371416541
e(130)	0.377809712	0.377806440
e(170)	2.42186287	2.42184568
e(185)	2.40924559	2.40923703

Table 3.15 Void ratio data for inversion based upscaling

Maximum errors on void ratio of all nodes are also provided. Initial value, results and maxim error for all nodes are shown in **Table 3.16**. Comparison between results (1) and real numerical result is shown in **Figure 3.40**. Further improvement of the error requirements is also studied. Initial value, results and required error for all nodes are shown in **Table 3.17**, which is not satisfactory result.

	Initial value				Results				
	A	B	C	D	A	B	C	D	Max errors
1	3.00	0.30	1.00×10^{-6}	3.00	3.00	0.30	1.00×10^{-6}	3.00	7.5150×10^{-4}
2	3.00	0.30	1.00×10^{-5}	2.50	3.00	0.30	2.00×10^{-14}	2.50	1.5390×10^{-11}

Table 3.16 Initial value, results and maxim error for all nodes

	Initial value				Results				Max errors
	A	B	C	D	A	B	C	D	
1	3.00	0.25	1×10^{-5}	5.00	3.000000	0.2544639	0	5.006905	$<1\times10^{-30}$
2	5.00	0.25	1×10^{-5}	6.00	-7.528870+ 0.009144395 55864i	6.003149+ 0.009712689429 25i	0	0.2040539+ 0.00221837635 371i	$<1\times10^{-25}$
3	3.80	0.30	1×10^{-5}	9.00	3.805638	0.2943618	0	9.005638	$<1\times10^{-25}$

Table 3.17 Initial value, results and required error for all nodes with a higher accuracy requirement

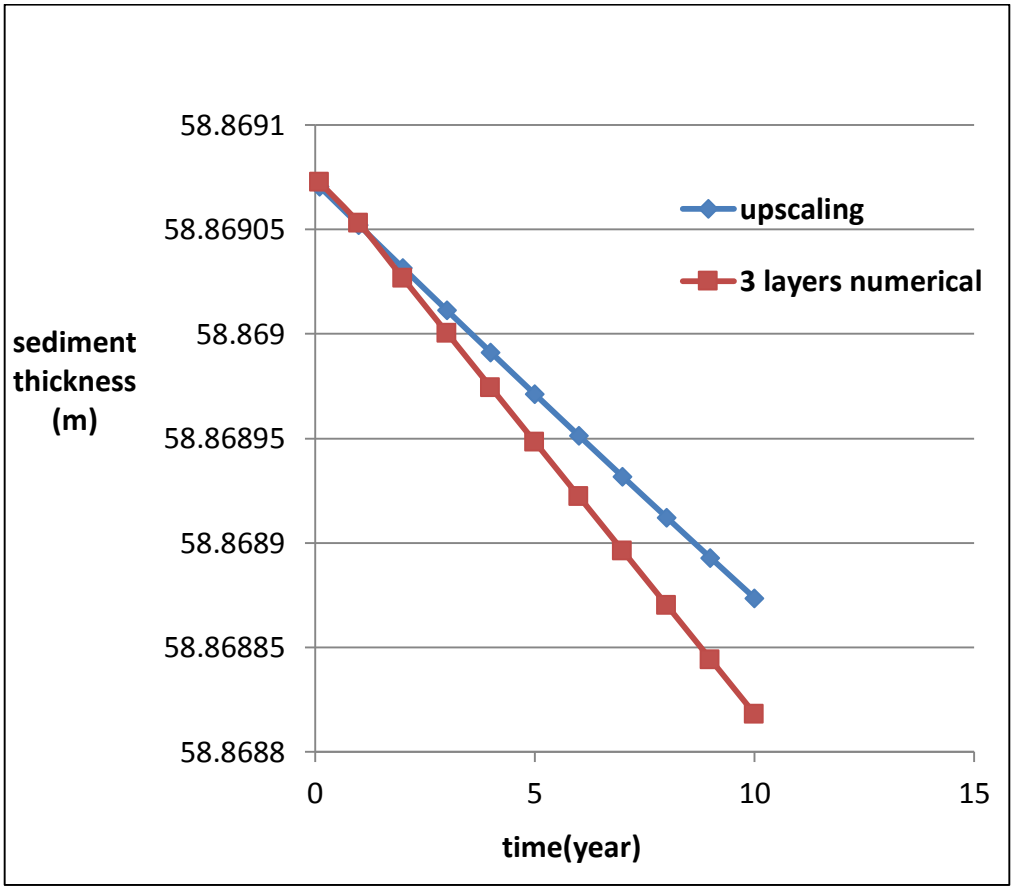

Figure 3.40 Sediment thickness evolution comparison between three-layer numerical model and upscaling model

3.4.5 Conclusion for inversion based upscaling

An inversion method for large-strain consolidation is developed in this part. This method can be used to invert the soil characters. However, due to the strong nonlinearity, inversion is only effective over a limited range. It is necessary to narrow the scope of parameters by combining with other information in actual operation.

This inversion technique is extended for multi-layer system properties upscaling successfully. However, difference between upscaling and fine-scale simulation increases over time, which

coincides with the nature that parameters of multi-layer system is changing with time. As for the multi-layer system, parameters are changing with external stimulation and time. Hence one set of constant parameters will not fit the consolidation process and a piecewise linear method is required.

3.5 Discussion and Conclusion

(1)This research reveals the changing nature of multi-layer properties. The suggested upscaling method considering time range is better than the weighted average method.

Based on the method of the transform matrix, which considers the properties of multi-layer consolidation, an upscaling method is put forward for both small-strain and large-strain consolidation. The integral properties of multi-layer system change with the increase of affected region and hence are changing. Multi-layer numerical results reveal that the properties of multi-layer systems are changing with surcharge and time. It is impossible to use one constant relationship to describe consolidation characteristics, which proves the insufficiency of most direct upscaling methods.

(2) An upscaling method is proved for semi-infinite layers.

When the number of alternating layers reaches a certain value, the whole system will follow a single consolidation curve. A sensitivity analysis shows that layer number has a great effect on the time for the system to consolidate. For a system of layers with random property each, when the layers reach a certain value, the whole system will follow a single consolidation curve too. The bigger the variations of compressibility and conductivity are, the more layers will be needed to reach a single consolidation curve.

(3) Since the consolidation is a coupled process of mechanical compaction and fluid flow, upscaling must deal with two relationships, 'void ratio - effective stress' and 'conductivity - void ratio', simultaneously. Numerical analysis showed that these two upscaled relationships are changing in the consolidation process for multi-layer system.

However, even if the changing nature has been taken into account, upscaling does not lead to a consolidation closely matching that of detailed numerical simulation, and therefore this warrants a further study into the causes.

(4) Sediments' petrophysical properties can be inverted, and this inversion technique can be extended to multi-layer systems' petrophysical upscaling.

This research showed that soil properties of large-strain consolidation can be obtained through the inversion of known pore pressure data. The inversion technique has been extended to upscaling successfully.

Similar to well testing, this study proves the feasibility of getting heterogeneous sediments' properties through pressure simulation, which has an important industrial application value.

Chapter 4 Two dimensional large-strain shallow compaction simulator selection and verification

For simulation and modelling of coupled phenomena occurring during basin evolution, the mechanical aspects of sediment at deformation are generally assumed to be restricted to vertical compaction characterized by a simple relationship between the effective vertical stress and the rock porosity. However, as described in **Chapter 2.5**, basin modelling needs to account for multi-dimensional mechanical processes and thus needs to consider multi-dimensional constitutive models in order to better understand basin evolution. This is further reinforced in **Chapter 4.1**.

Elastic-plasticity is a more general formulation than simple 1D consolidation, which, in principle, allows for the consideration of horizontal deformations and those which vary laterally. The Modified Cam Clay elastic-plastic material model is a general but widely-accepted way of modelling coupled hydro-mechanical processes in fine-grained materials as shown in **Chapter 4.2** and **Chapter 4.3**. For example, it can simulate the 1D mechanical compactions of sediments up to 50 MPa of vertical effective stress, but can also be employed to simulate much more complicated deformations as shown in **Chapter 4.4**.

It is utilized in this research because it is a low-sophistication example of a whole class of material models that could be considered. The purpose of the research, described in this and the subsequent Chapter, aims to assess the benefits of considering multiple dimensions, and also to identify some of the challenges that remain to be resolved, when adopting a realistic materials perspective on basin processes. In principle, the Modified Cam Clay model, or an alternate, could be used to develop a new basin modelling simulation tool. However, since the purpose of this work is to justify the need for that sort of bespoke development, it is deemed appropriate to use an existing implementation to allow those specific aims to be met. Here, the choice is to use the commercial tool FLAC, which uses the Modified Cam Clay model, as a functional numerical tool. FLAC's capabilities are assessed via comparison with experimental results in this Chapter, and its use to address some challenging problems arising in basin modelling is treated in the subsequent Chapter.

4.1 Development of multi-dimensional simulation

One dimensional models have limitations as described in **Chapter 2.6** and **2.5**. They will show their limitations in dealing with horizontal stress, strongly dipping layers, structural

discontinuities or anisotropic mass rock properties, etc. Moreover, some phenomena can only be studied in a multi-dimensional arrangement. Such as the Mandel-Cryer effect, in which the induced pore pressure becomes higher than the applied pressure for a saturated soil. It was first described by Mandel (1953) for a triaxial soil sample and by Cryer (1963) for a spherical soil sample. This phenomenon is strongly related with the Poisson's ratio (Cryer, 1963). In order to capture this effect mathematically, a three-dimensional consolidation theory is required (Schiffman et al., 1969).

A three-dimensional mechanical constitutive model based on the theory of critical state is necessary for modelling three-dimensional deformations in sedimentary basins. And it should be a function of the effective stress tensor and able to reproduce porosity evolution under conditions of uni-dimensional compaction, in a range of stresses corresponding to the depths of predominant mechanical compaction. The elastic-plastic Modified Cam Clay constitutive law is recalled as a satisfactory approach to define the stress-strain relationship for fine-grained sediments (Djeran Maigre and Gasc Barbier, 2000; Luo et al., 1998; Pouya et al., 1998).

Basins exhibit time and space variations that demand multi-dimensional analysis. Multiple dimensions are considered in current basin modelling tools for fluid flow and thermal modelling, but the existing commercial basin modelling tools still are based on 1D consolidation methods for the mechanical aspects of basin development. It might be presumed that the lack of multi-dimensional mechanics in current basin modelling is because there has not been sufficient evidence that the limitations or errors associated with the 1D consolidation approach are important enough to warrant the significant changes associated with changing to a true multi-dimensional formulation of the mechanical aspects. This research uses a multi-dimensional approach to assess the hydro-mechanical responses of a basin-like system, as a step towards establishing the case for making major changes to the way that basin modelling is undertaken.

4.2 Multi dimensional consolidation theory for basin modelling

4.2.1 Theory of Modified Cam Clay model

The formulation of the original Cam Clay model as an elastic-plastic constitutive law is presented by Roscoe and Schofield (1963). The original Cam-Clay model is based on the assumption that the soil is isotropic, elastic-plastic, and deforms as a continuum. Roscoe and

Burland (1968) proposed the modified Cam clay model. The difference between the Cam Clay model and the Modified Cam Clay model is that the yield surface of the Modified Cam Clay model is described by an ellipse (Roscoe and Burland, 1968; Roscoe and Schofield, 1963). A description and systematic study of the model can be found in the text by Muir Wood (Muir Wood, 1990). This model is an elastic-plastic constitutive model with a nonlinear hardening and softening law (hardening and softening refer to changes of the yield condition), which depends on the pre-consolidation pressure of the soil (which is a way of accounting for prior consolidation steps). The model determines the response of the soil according to the specific volume or void ratio, a deviator stress (q) and a mean effective stress (p').This model is based on an isotropic material, but does account for anisotropic 2D or 3D stress states. The Modified Cam Clay model is an associated plastic flow model, in which the yield surface is defined as an ellipse with no strength at the origin and zero pre-consolidation pressure. When the stress state lies within the yield surface, the material is elastic, and as the stress state crosses the yield surface, both plastic volumetric and deviatoric strains will develop. The material is either incrementally contractive or dilative depending on if it is dense or loose compared to the critical state. At the critical state the sample will undergo only deviatoric strain and therefore will not harden or soften. Sustained shearing of a soil sample eventually leads to a state in which further shearing can occur without any changes in stress or volume. This means that under this condition, known as the critical state, the soil distorts at a constant state of stress with no volume change. This state is called the Critical State and characterized by the Critical State Line (CSL). This model has a relatively simple formulation and is compatible with critical state soil mechanics and certain idealized clays. Yield surfaces of Cam Clay model and Modified Cam Clay model are shown as following.

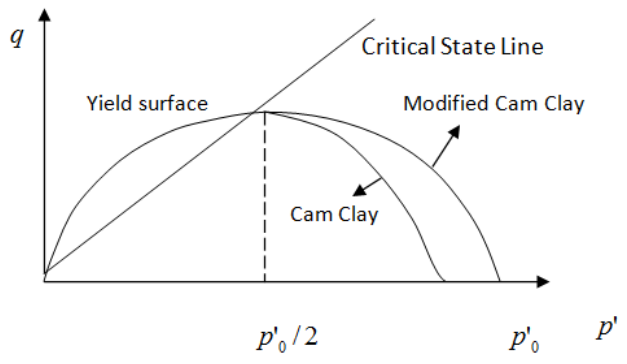

Figure 4.1 Cam Clay and Modified Cam Clay model

This model captures the observed essential stress-strain behaviours of clay, including hardening and softening dilatation. But this model also shows its limitations when there are sharp corner on the failure surface, or anisotropy in the material. And the shear deformation is not fully expressed. Predictions of undrained tests using the law of Modified Cam Clay model always show no variation in mean effective stress before yielding, which is not always true.

4.2.2 Fitting a Modified Cam Clay model to sediment deformation experimental data

Numerous experimental methods have been developed to examine the mechanical compaction of fine-grained sediments over a wide range of effective stresses. The usual one-dimensional description of sediment deformation, based on a phenomenological relationship between porosity and the vertical effective stress, does not provide information about the horizontal stress, although the presumed value of horizontal stress is often based on the so-called k_o ratio. These loading conditions inspire the oedometric experimental design in which a disk-shaped sample is subjected to an axial load while being prevented from expanding laterally. But, since the lateral stress is not known in such experiments, data from typical oedometric tests is not readily useful for calibrating a Modified Cam Clay material model.

However, in the research of Ahmad et al (1998), a special oedometric cell was conceived. This cell allows measurement of the lateral stress during oedometric compaction and so enables us to elaborate a three-dimensional model of mechanical behaviour. Four varieties of fine-grained sediments were studied by this cell on a large scale of strain and stresses. The Modified Cam Clay model was used for fitting the experimental data and it was shown that this model can reproduce the mechanical compaction of sediments up to 50 MPa of vertical effective stress (corresponding to burial depths of 3000 m), if its parameters are deduced from oedometric (zero lateral strain) data.

In the accompanying research of Luo et al, the elastic-plastic Modified Cam Clay material law was recalled as a satisfactory approach to define the stress-strain relationship for fine-grained sediments (Luo et al., 1998). This provides a solid foundation for numerical modelling of the hydro-mechanical problems related to sedimentary basin evolution. The slow sedimentation process, whereby the geological structure is progressively built, can be accounted for by incremental deposition of layers. Note that a numerical implementation of a material law, such as the Modified Cam Clay model, may not work well under all possible

model conditions, so there is a need to discover whether a chosen implementation can address the particular problem envisaged.

In order to model the experimental compaction of clays as completely as possible, it is necessary to apply the hydro-mechanical coupled three-dimensional theory into saturated porous media. In the research of Djeran Maigre and Gasc Barbier, the identification of the parameters of Modified Cam-clay model was measured by special oedometric experiments at steady state. The compaction experiments were simulated in transient and steady state (Djeran Maigre and Gasc Barbier, 2000). The specially-designed oedometric cell permits the experimental compaction of samples in the range of 0.1–50MPa, representing the in situ state of natural clays to be found at 2 or 3 km depth. Besides, it permits to access to the three-dimensional mechanical parameters that are needed for the modelling. Porosity, stress state and hydraulic conductivity are observed as a function of the compaction. The general linear relationship between void ratio and logarithm of applied stress is verified for the total range of stress as shown in **Figure 4.2**. The various behaviours can be explained by the nature of clay particles, their organisation in aggregates and their orientation as a function of compaction degree. This work reveals the significance of considering mechanical, mineralogical and micro-structural aspects of clays for a better understanding of their properties.

The hydraulic conductivity can be measured at each compaction stage using the method of differential pore pressure. A hydraulic pressure is applied separately on two parallel faces of the sample and controlled up to 20 MPa, the volume of water expelled is then measured. The hydraulic conductivity is measured on each different compaction levels when the sample has a stabilized length. The measured hydraulic conductivity can be expressed as a function of void ratio ($k = Ae^B$) related parameters are shown as **Figure 4.3**.

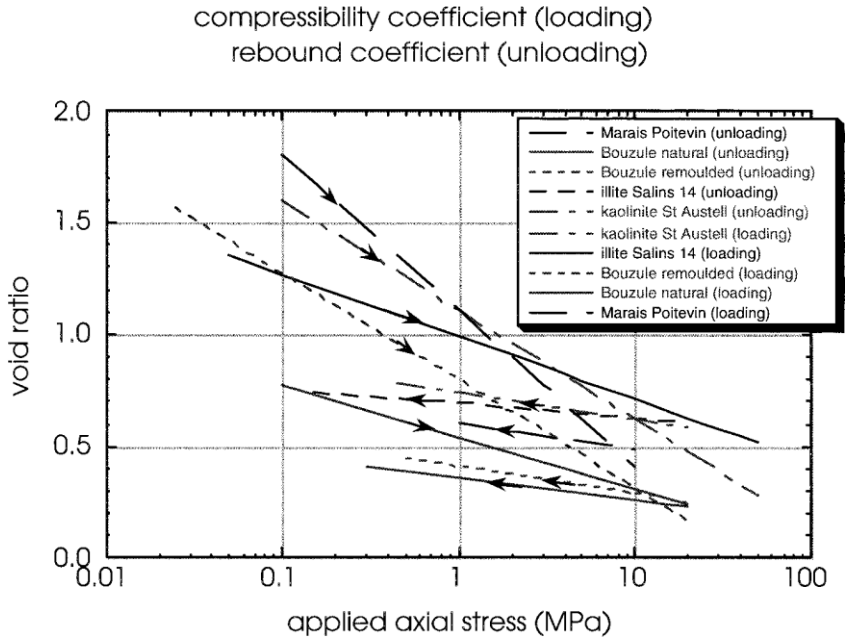

Figure 4.2 Evolution of void ratio on steady state for loading and unloading versus the logarithm of axial applied stress for four clays (Djeran Maigre and Gasc Barbier, 2000).

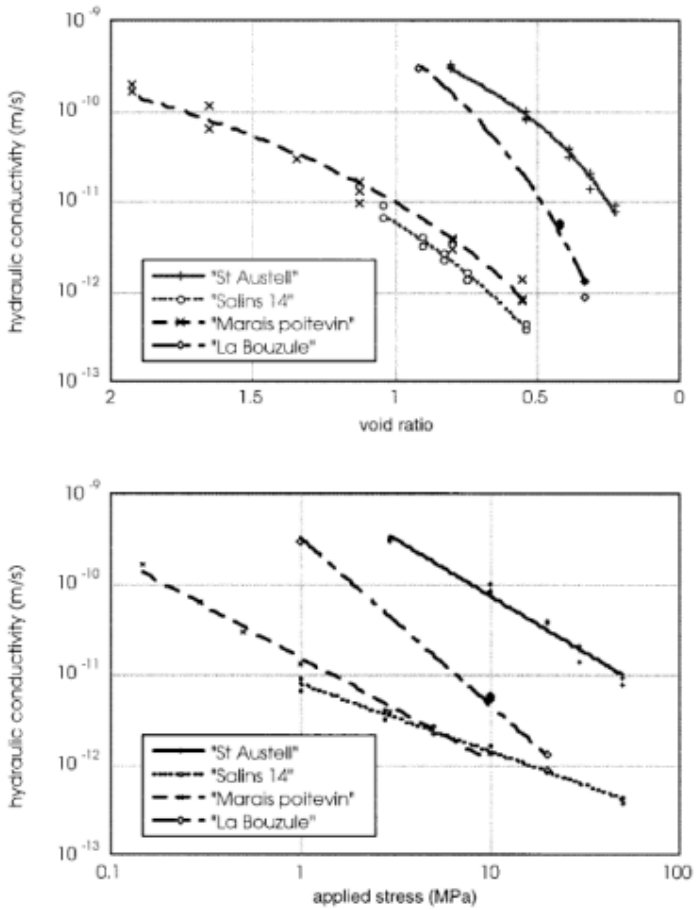

Figure 4.3 Evolution of measured conductivity as a function of void ratio and as a function of applied stress for four clays (Djeran Maigre and Gasc Barbier, 2000).

Clay	λ'	κ'	υ	M	ϕ^0
St Austell kaolinite	0.21	0.087	0.15	1.08	27
Salins 14 illite	0.12	0.045	0.14	1.17	29
La Bouzule clay	0.21	0.084	0.15	1.19	30
Marais Poitevin mud	0.30	0.073	0.17	1.33	33

Table 4.1 Cam Clay model properties for different clays (Djeran Maigre and Gasc Barbier, 2000).

clay	A	B
St Austell kaolinite	5.6×10^{-10}	2.94
Salins 14 illite	5.8×10^{-12}	4.43
La Bouzule clay	5.4×10^{-10}	5.54
Marais Poitevin mud	9.8×10^{-12}	4.17

Table 4.2 Coefficients of permeability for different clays (Djeran Maigre and Gasc Barbier, 2000).

With the above-mentioned researches, it is now quite reasonable to utilize the Modified Cam Clay model in our research.

4.3 FLAC introduction

Complexity in geotechnical engineering includes non-linear material properties, complex loading patterns and non-simple geometries. For these problems numerical simulations are often used to examine surcharges and displacements from various types of loading.

FLAC, Fast Lagrangian Analysis of Continua, is distributed by Itasca Consulting Group and is able to solve a wide range of geotechnical problems involving changing loading, multiple material models, structural elements and pore fluid. FLAC is a commercially available, two-dimensional finite difference software, its free academic version has a limitation on cell number. In this research, the academic version of FLAC is adopted for the simulation of shallow compaction.

4.4 Model verification with experiment

The correctness of FLAC's Modified Cam Clay is verified by simulating the experimental data of Djeran Maigre and Gasc Barbier. Here Marais Poitevin mud is selected for comparison, a two dimensional model is utilized according to real sample size, 50mm in width and 80mm in high, the comparison result is shown as follows. Djeran Maigre and Gasc Barbier have simulated the experimental process with numerical finite differences method. Their simulation also presented for comparison as follows.

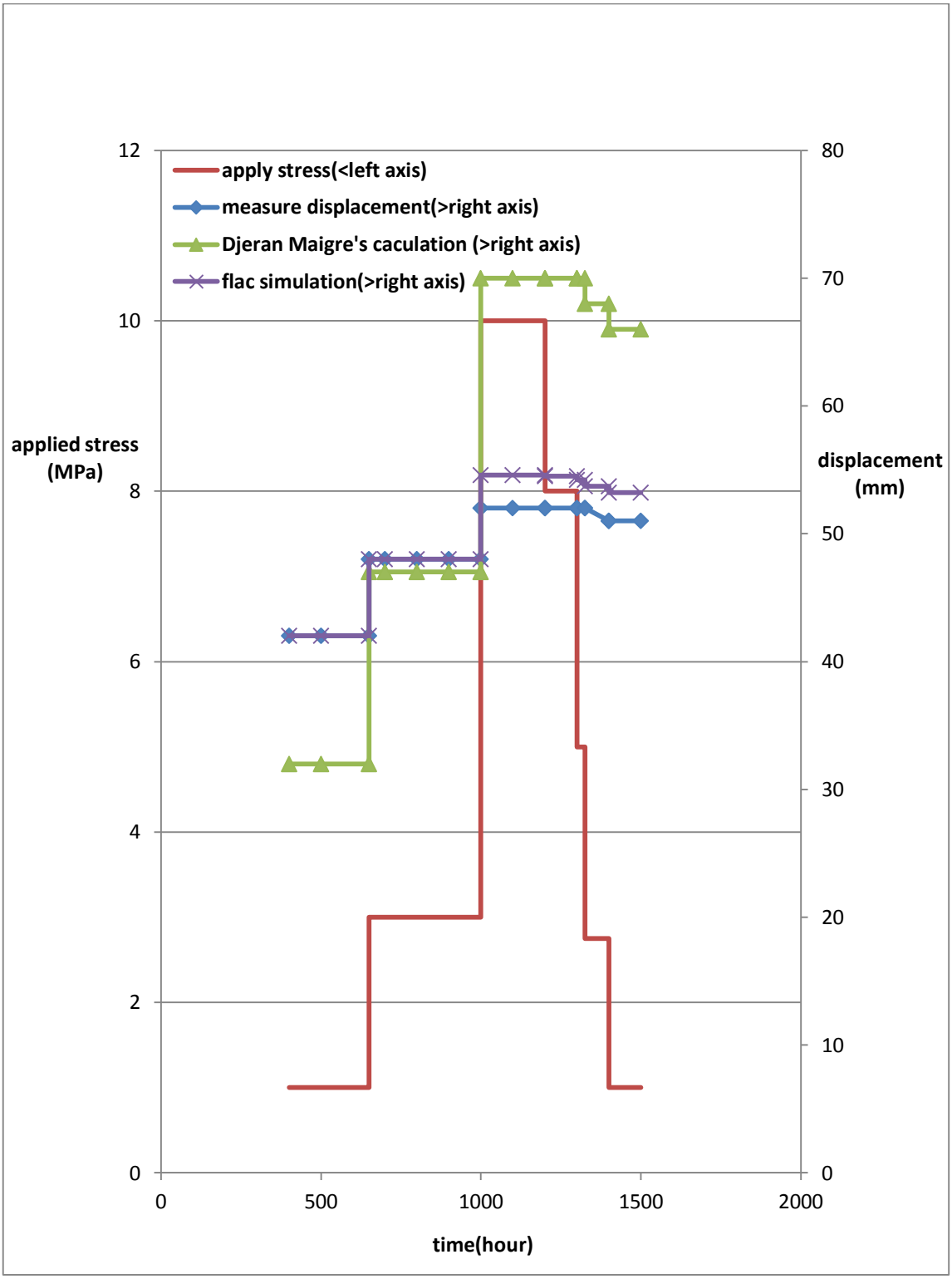

Figure 4.4 Comparison between experimental and calculated displacements as a function of time

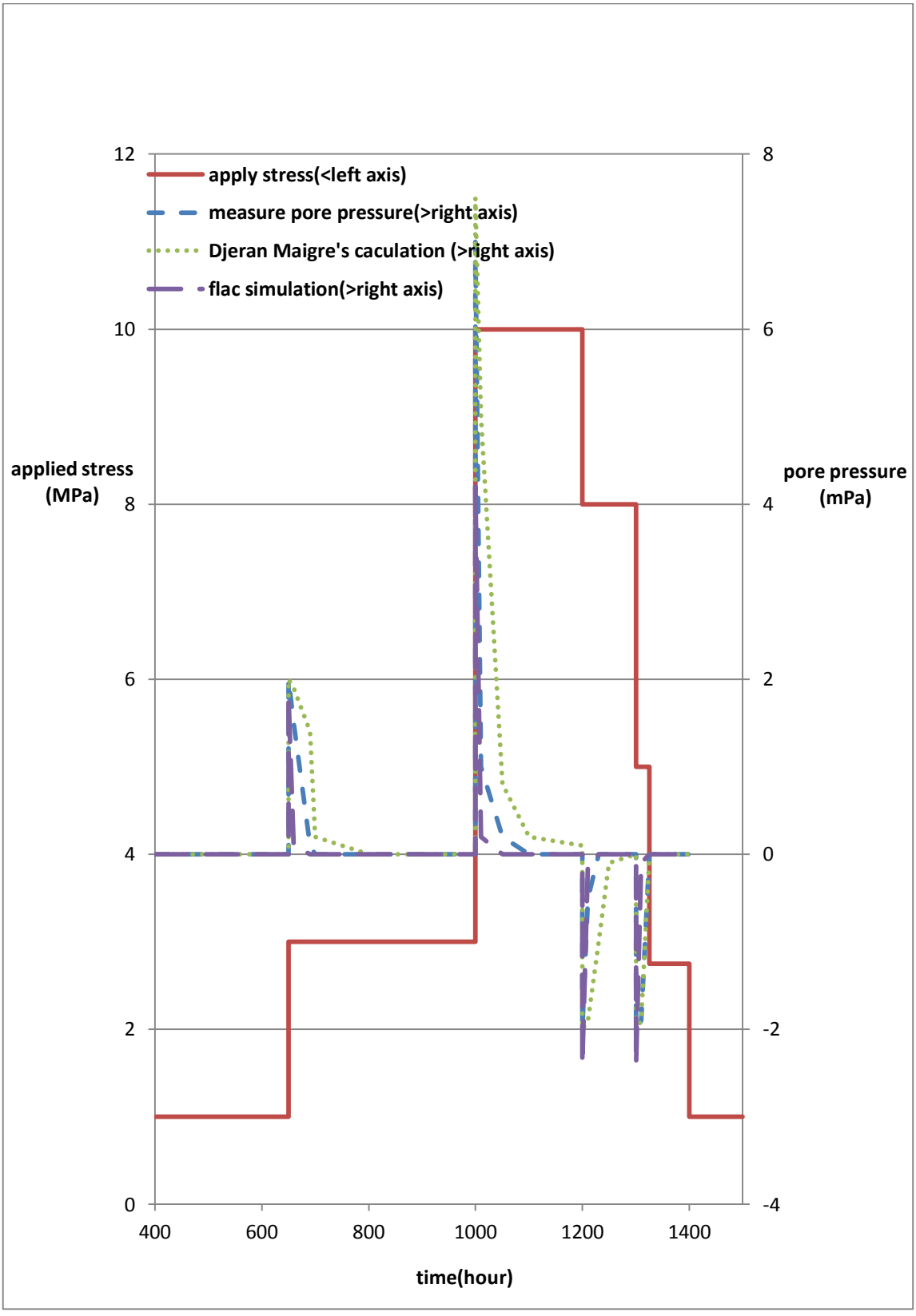

Figure 4.5 Comparison between experimental and calculated pore pressure as a function of time

From the comparison results, FLAC Modified Cam Clay model is able to capture the evolution of Modified Cam Clay material both in displacement and pore pressure, which is a fluid-structure interaction process. Displacement results of FLAC are closer to measured data than Djeran Maigre's. However, pore pressure in the FLAC simulations dissipates more quickly than both Djeran Maigre's and measured data. The "spikes" that are calculated by FLAC, when the loading is changed, are artefacts of the implementation, which is optimised for smooth loadings.

4.5 Model verification with analytical solution and limitations

Though Modified Cam Clay model can capture the characteristics of clay materials, FLAC Modified Cam Clay model show its limitations when facing some situations which will be illustrated in this part.

4.5.1 Numerical discretization for sedimentary deposit

Normally, the numerical approach requires discretization of sedimentary deposit: each new sediment layer is deposited at once on the top of the previously existing structure, underlying layers undergo a sudden pore pressure increase, then the pressure gradually decreases. Such phenomena are quite different from the progressive sedimentation.

As shown in **Figure 4.6**, the amplitude of each pressure pulse is a function of the discretization, i.e. of the assumed deposit thickness, each pressure pulse being followed by a relaxation period. Therefore, in order to simulate progressive loading and a reasonable pressure history, one should deposit very thin layers (Luo et al., 1998). For a nominal average rate of deposition, small increments of deposition amount to short time steps.

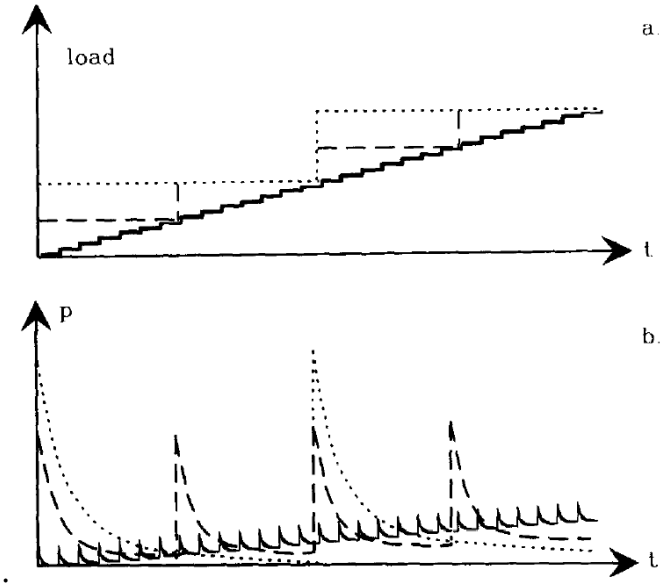

Figure 4.6 Evolution of pressure during sedimentation with finite increments (Luo et al., 1998). (a) various discretization of the incremental load. (b) evolution of excess pore pressure corresponding to the various discretization presented in (a).

The decrease of pore pressure during relaxation results in increase of effective stress. This plastic extension has to be controlled numerically and therefore the relaxation of pressure also needs to be controlled. This is possible through the use of a time-step estimated from the ratio of cell size square and diffusion coefficient, which takes into account the hydraulic conductivity and the stiffness of the medium (Luo et al., 1998).

4.5.2 Verification with analytical solution

Montgomery (2010) provided an examination of the FLAC software for an undrained triaxial test on Modified Cam Clay. In his research, the internal stresses in the element are initialized to the confining pressure to simulate an isotropic consolidated sample. The sample is initially saturated and the bulk modulus of water is defined to simulate the compressibility of water. Groundwater flow is turned off to simulate an undrained test. As plastic volumetric strains try to accumulate, the sample is unable to change volume due to saturation and the pore pressure will increase or decrease depending on whether the sample is trying to contract or dilate. The ratio of pre-consolidation pressure to current mean effective stress is known as the over-consolidation ratio (OCR). Two samples were simulated to capture this behaviour. One was a lightly over-consolidated sample (OCR = 1.5) which is loose compared to the critical state, and a heavily over-consolidated sample (OCR = 20) which is denser than the critical state. Model parameters are shown in **Table 4.3**.

Parameter	Value
λ': loading line slope	0.088
κ': unloading line slope	0.031
ϕ^{o}: angle of internal friction	22.6^{o}
Shear modulus	3000(kPa)
Pre-consolidation pressure	150(kPa)

Table 4.3 Selected material parameters for Modified Cam Clay (Montgomery, 2010).

To validate results of the numerical solutions, an analytical solution was used from Muir Wood (Muir Wood, 1990). This solution solves the stresses in an undrained triaxial test at yielding and critical state. A formula is also presented to calculate the stress path of the material between the initial yield point and the critical state. Results of the analytical solutions for both the highly and lightly over-consolidated samples are presented in **Figure 4.7**. The predicted responses are consistent with general critical state theory in that the loose sample contracts and generates positive pore pressure, while the over-consolidated sample dilates and generates negative pore pressure.

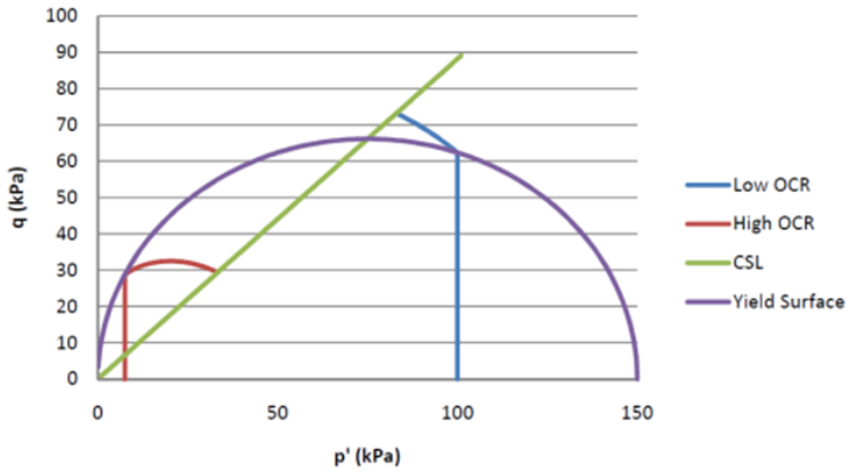

Figure 4.7 Analytical solution to Modified Cam Clay loading, 'CSL' means critical state line, 'OCR' means over consolidation ratio, (Montgomery, 2010).

The numerical simulation is conducted with three different loading rates. The loading is applied at a constant rate of strain on the top of the model. The slowest loading rate is 0.01% strain per step, which is increased to 0.5% strain per step and then to 10% strain per step. This increase in loading is meant to raise the equivalent step size of the simulation and gauge the effects on the results.

Figure 4.8 shows the response of the lightly over-consolidated sample to each of the three loading rates. **Figure 4.9** shows the response of the heavily over-consolidated sample. The figures show that the effective stresses predicted by the numerical models are in agreement regardless of the step size. Note that effective stress lines (0.01%, 0.5% and 10% strain per step correspond to low, medium and high velocity-effective in both **Figure 4.8** and **Figure 4.9**) and analytical results lines overlap each other.

Although the effective stress path is in good agreement regardless of the step size，the total stress paths show how large steps can adversely affect results. Only the step size of 0.01% (low velocity-total in both **Figure 4.8** and **Figure 4.9**) produces a reasonable total stress path while the larger step sizes produce total stress paths, which oscillate around the correct line (0.5% and 10% strain per step correspond to medium and high velocity-total in both **Figure 4.8** and **Figure 4.9**).

In an undrained test pore pressures represent the sample attempting to change volume, but because the test is undrained this contraction or dilation occurs in the form of pore pressure. The pore pressure can be thought of as representative of the volumetric strains which would occur in a drained test. **Figure 4.10** shows the pore pressure response of both the lightly and heavily over-consolidated samples. Pore pressures are only shown for the smallest step size because other paths are very erratic as suggested by the total stress paths shown in the other figures. As expected, the lightly over-consolidated sample undergoes contraction and positive pore pressure generation. The heavily over-consolidated sample experiences contraction at first and then dilation.

It is then concluded that only small steps generate reasonable simulation results on pore pressure, effective and total stress.

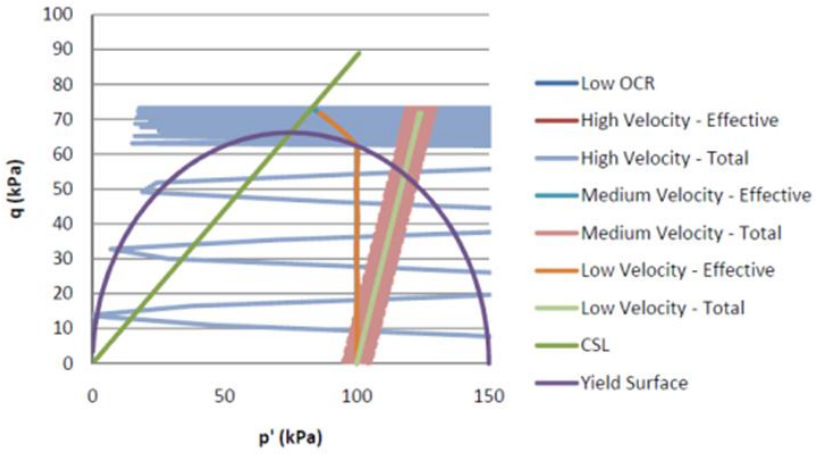

Figure 4.8 Combined plot of all stress paths for low OCR Cam clay (Montgomery, 2010). (low, medium and high velocity-effective correspond to effective stress evolution of 0.01%, 0.5% and 10% strain per step, low, medium and high velocity-total correspond to total stress evolution of 0.01%, 0.5% and 10% strain per step)

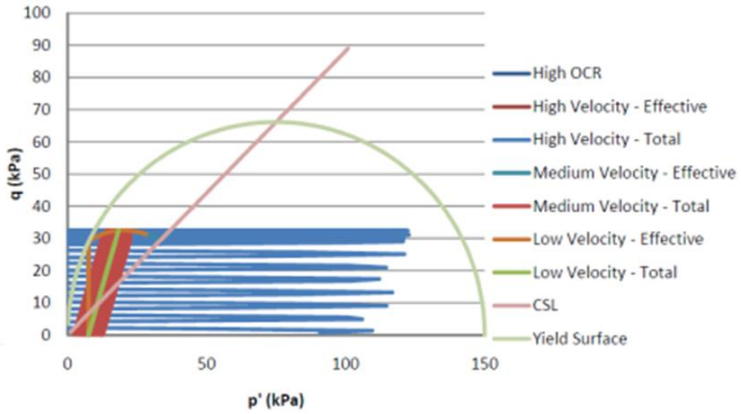

Figure 4.9 Combined plot of all stress paths for high OCR Cam clay (Montgomery, 2010). (low, medium and high velocity-effective correspond to effective stress evolution of 0.01%, 0.5% and 10% strain per step, low, medium and high velocity-total correspond to total stress evolution of 0.01%, 0.5% and 10% strain per step)

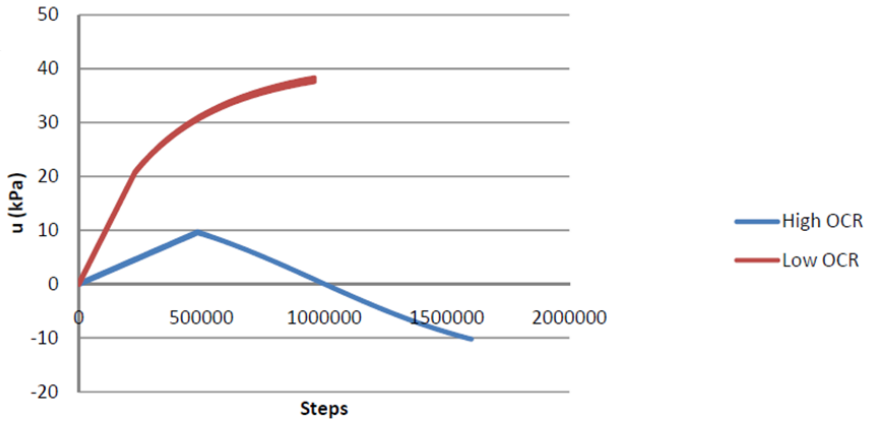

Figure 4.10 Pore pressure response of both the high and low OCR samples (Montgomery, 2010).

4.5.3 Limitation of FLAC's Modified Cam Clay model in basin modelling

When the sample is loaded very quickly, the pore pressure will suddenly spike or drop in response to the imposed strains. This would normally alter the effective stress of the sample, but in FLAC the constitutive model is only given displacements and velocities from which it produces stress and strains. Because the rate of strain is controlled by loading, FLAC adjusts the total stress to maintain the proper strain rate. This adjustment occurs as the sample tries to maintain equilibrium under large strains. In reality, the samples would likely form tension cracks when the effective stress drops to zero, but the numerical solution prevents this and the error manifests itself in the total stress. Another drawback is the generation of negative pressure, which may be a numerical expression of vaporisation and variation of saturation.

These are related with problems in basin modelling, such as sudden loading/ unloading. When sudden unloading happens, negative pore pressure will generate in the simulation. When loading happens, zero effective pressure and fracture will generate. The indistinctness of mechanism and numerical solution for negative pore pressure and fracture makes the existing basin modelling suspect. Note that these simulation artefacts are exacerbated by the explicit formulation of FLAC, and that an implicit formulation may be a better choice for developing suitable simulation methods for use in basin modelling.

Similar to the 1D modelling, the continuous sedimentation process is divided into multi-steps' addition of sediment with a certain thickness. In a word, FLAC and Modified Cam Clay model can not simulate the full process of sudden loading and unloading.

Normally, in soil engineering this sudden loading is modelled in two stages. In the first stage, mechanical equilibrium occurs, without flow, the second stage allows flow. In this research fluid-structure interaction is always utilized. However, both of them are not consistent with reality, which include fracturing and other phenomena.

4.6 Conclusion

(1) Modified Cam Clay model is proved to be able to capture the elastic-plasticity of sediment under a range of loading arrangements.

(2)A two dimensional large-strain FLAC modelling method based on Modified Cam Clay model is verified. It can be applied to complex mechanics processes, such as loading, unloading and horizontal stress/strain.

(3)There are limitations for Modified Cam Clay and FLAC when considering sudden loading and unloading.

Chapter 5 Numerical Upscaling Approach for Modified Cam Clay

Upscaling properties is significant for lowering computational requirements of simulation while honouring local heterogeneities in sediment properties, which apply equally or even more so to a 2D basin modelling. In this chapter, a numerical upscaling technique for elastic-plastic properties is proposed. Heterogeneous Modified Cam Clay materials can be upscaled to a homogenous anisotropic elastic material in elastic deformation and a homogenous Modified Cam Clay material in elastic-plastic deformation. Complex facies, property distributions and anisotropic deformation have been considered in this upscaling technique. This upscaling technology is applied in a case study associated with North Africa basin sedimentation thereafter.

5.1 Upscaling characteristics

Mechanical Earth Models are comprehensive geological models, which include in-situ stress magnitudes/directions and heterogeneous maps of sand/clay mechanical properties. The main motivation for upscaling is to reduce simulation CPU requirements in view of multiple realizations and fine scale heterogeneous property models.

Several analytical techniques have been developed for upscaling and homogenization of elastic media. Mackenzie used a self-consistent model to determine the equivalent elastic properties of a material composed of three phases (Mackenzie, 1950). Other analytical formulations for equivalent elastic media calculation have also been developed (Backus, 1962; Budiansky, 1965; Hashin, 1955; Hill, 1965; Salamon, 1968). Although different assumptions are considered in these approaches, a common element is their consideration of a simplified stratified facies configuration, which is not appropriate for the complex facies configurations that can be encountered in basins (e.g. levees and channels, MTDs, etc).

Numerical techniques for upscaling of elastic properties are not common. Elkateb proposed a mathematical expression for determination of equivalent elastic modulus for a simplified layer cake model with isotropic elastic deformation (Elkateb, 2003). However, the deformation behaviour of many materials depends upon orientation.

Complex facies and property distributions and anisotropic deformation have rarely been considered in previous upscaling techniques.

A numerical upscaling technique for elastic properties was proposed by Khajeh (2012). The technique is similar to local upscaling of conductivity, but it is applied to elastic properties. The methodology is demonstrated on a synthetic 2D example based on sand/shale distributions typical of the McMurray oil sands deposit located in northern Alberta, Canada.

Based on Modified Cam Clay material and numerical elastic properties upscaling method, numerical upscaling techniques for Modified Cam Clay material properties are proposed in this research. Modified Cam Clay materials are upscaled to anisotropic variable elastic material in elastic range, and Modified Cam Clay material in elastic-plastic range. Complex facies, property distributions and anisotropic deformation have been considered.

5.2 Modified Cam Clay material upscaling in elastic conditions

5.2.1 Elastic upscaling theory

The numerical upscaling of elastic properties is shown in **Figure 5.1**. The loading process would result in complex deformation in heterogeneous media. After upscaling this system to a single block, the goal is to reproduce the average fine scale deformation in the coarse scale block. The coarse upscaled property is the value that results in the same average displacement had the fine scale model been deformed.

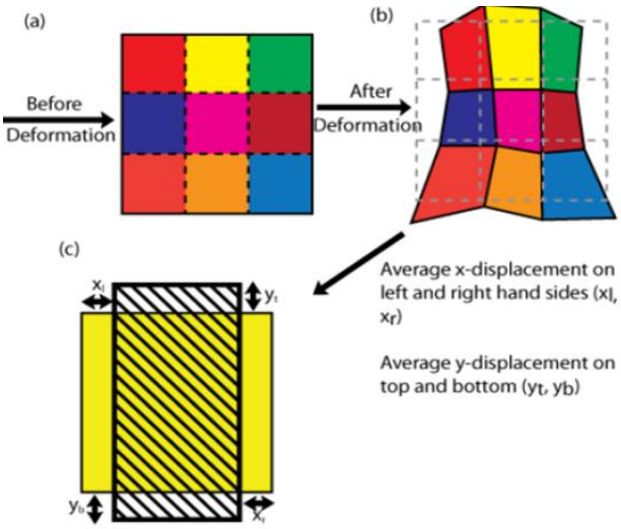

Figure 5.1 Conceptual framework for numerical upscaling (Khajeh, 2012).

It is assumed that X - Z is the plane of symmetry (i.e. same properties in X and Z directions) corresponding to horizontal directions, and Y direction is vertical direction. In the work of Khajeh (2012), Hooke's Law in the case of transverse isotropy and plane strain can be simplified as:

$$\begin{bmatrix} \varepsilon_{xx} \\ \varepsilon_{yy} \\ 0 \\ \varepsilon_{xy} \end{bmatrix} = \begin{bmatrix} 1/E_x & -\upsilon_y/E_x & -\upsilon_x/E_x & 0 \\ -\upsilon_y/E_x & 1/E_y & -\upsilon_y/E_x & 0 \\ -\upsilon_x/E_x & -\upsilon_y/E_x & 1/E_x & 0 \\ 0 & 0 & 0 & 1/2G \end{bmatrix} \begin{bmatrix} \sigma_{xx} \\ \sigma_{yy} \\ \sigma_{zz} \\ \sigma_{xy} \end{bmatrix} \tag{5.1}$$

Where, E is Young modulus, υ is Poisson's ratio. Five parameters are required to fully characterize the problem under the above assumptions: E_x, E_y, υ_x, υ_y, G. With good approximation, G (shear modulus) can be determined from the following equation.

$$G_{xy} = \frac{E_x E_y}{E_x(1+2\upsilon_{xy}) + E_y} \tag{5.2}$$

The upscaling process reduces to determining the value of these five parameters for a coarse cell that results in the same average displacement as the fine scale model (**Figure 5.1**). Thus there are four unknowns determined from the uniform stress and strain tensors. The number of equations obtained in a single loading configuration is less than the number of unknowns. Therefore, it is not possible to determine all required values by applying one stress configuration, hence two different stress boundary conditions are considered as shown in **Figure 5.2**, (a) and (b) show the situation of fix left boundary, and stress applied on the right boundary, while the upper and bottom boundary are free to deform; (c) and (d) show the situation of bottom boundary, with stress applied on the upper boundary, while the left and right boundary are free to deform. Then with the applied stresses and averaged displacements, these unknown parameters can be determined.

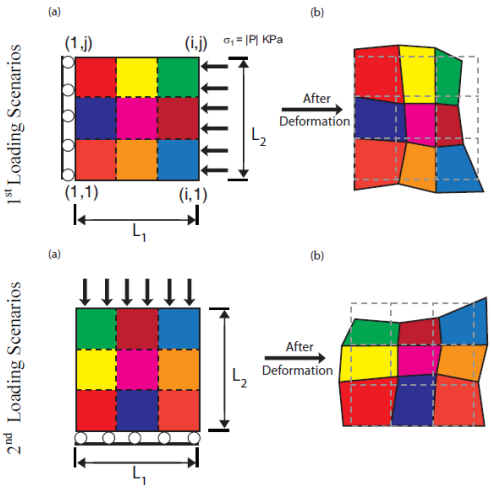

Figure 5.2 Initial boundary conditions for loading scenarios (Khajeh, 2012)

5.2.2 Elastic upscaling workflow and application

To describe the stress - strain relationship, Young's modulus - E, Poisson's ratio - υ, and bulk modulus - K are to be used. Their relationship is shown as follows (so there are only two independent elastic parameters for isotropic materials):

$$E = 3K(1-2\upsilon) \tag{5.3}$$

For soil modelling using the Modified Cam Clay model, the bulk modulus K depends on the mean effective stress $\overline{\sigma}'$, void ratio e, and unloading–reloading line slope κ' as shown in **Figure 5.3** The following equation can be obtained from the unloading–reloading line used for consolidation analysis describing the elastic behaviour of soil:

$$K = \frac{(1+e)\overline{\sigma}'}{\kappa'} \tag{5.4}$$

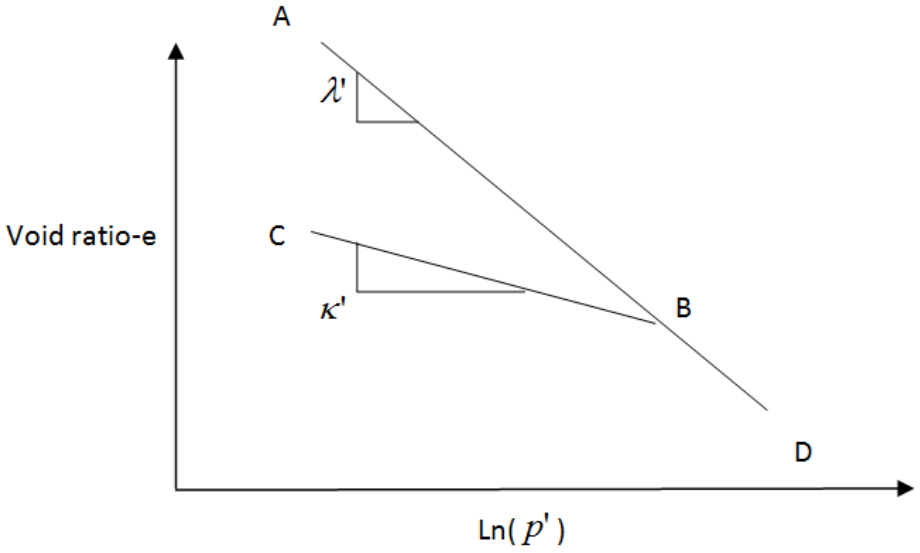

Figure 5.3 The relationship between void ratio and effective stress in Modified Cam Clay model

As can be seen from **Figure 5.3**, 'A - D' is elastic-plastic deformation, which stands for the normal consolidation line. 'C - B' is an elastic deformation process, which stands for unloading/reloading line. It is easy to obtain the Young modulus, which is function of mean effective stress - $\overline{\sigma}'$, void ratio, unloading–reloading line slope, and Poisson's ratio.

$$E = \frac{3(1-2\upsilon)(1+e)\overline{\sigma}'}{\kappa'} \tag{5.5}$$

After obtaining the elastic modulus, the general workflow for upscaling can then be deduced as follows:

Step 1: Set the vertical and horizontal stress conditions, provide a small stress boundary change. Solve the isotropic-heterogeneous Modified Cam Clay model for the boundary of the target coarse scale cell. In this step the elastic tensor is calculated and the non-uniformly deformed body is obtained.

Step 2: Average the displacement on border of the coarse scale body. In this step, the hatched black rectangle is obtained.

Step 3: Calculate the optimal characteristics elastic parameters by least square method, which results in the same stress and strain tensor applied on the uniformly deformed body.

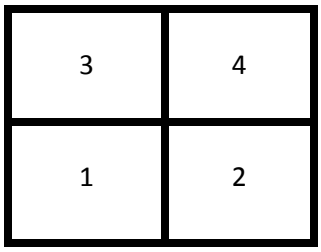

Figure 5.4 Cell arrangement 1: Marais Poitevin mud, 2: La Bouzule clay, 3: Salins 14 illite, 4: St Austell kaolinite. Material properties come from the research of Djeran Maigre and Gasc Barbier (2000).

The model utilized is shown in **Figure 5.4**, the mechanical parameters of four different clays are shown in **Table 4.1**. Two different loading scenarios are shown in **Figure 5.2**.

In view of the failure surface, initial effective stress $\sigma'_{xx} = \sigma'_{yy}$ ($= \sigma'_{zz}$) = 10MPa ensures the elastic deformation of Modified Cam Clay material. Density = 2250 kg/m^3, Poisson's ratio = 0.17. Shear and Young's modulus for each cell are shown as **Table 5.1**.

	Shear modulus (Pa)	Young modulus (Pa)
cell1	1.61×10^8	3.77×10^8
cell2	1.26×10^8	2.94×10^8
cell3	3.15×10^8	7.37×10^8
cell4	1.52×10^8	3.56×10^8

Table 5.1 Cell shear and Young's modulus

Upscaling results:

(1) Applied compressive stress on right boundary: -10.1 MPa (1% higher than the initial stress).

Correspondingly, fix x direction displacement on the left boundary. Other boundaries applied stress: -10.0 MPa. Calculation results are shown in the following table.

Average boundary displacement	Modified Cam Clay model (m)	Equivalent elastic model	Relative error
horizontal	2.42×10^{-4}	2.42×10^{-4}	0.17%
vertical	5.33×10^{-5}	5.36×10^{-5}	0.51%

Table 5.2 Calculation results with additional stress on right boundary

(2) Applied stress on upper boundary: -10.1 MPa (1% higher than the initial stress)

Fix y direction displacement on the bottom boundary. Others boundaries applied stress: -10 MPa. Calculation results are shown in **Table 5.3**.

Average boundary displacement	Modified Cam Clay model (m)	Equivalent elastic model	Relative error
horizontal	2.9870×10^{-5}	2.9977×10^{-5}	0.36%
vertical	1.4051×10^{-4}	1.4076×10^{-4}	0.18%

Table 5.3 Calculation results with additional stress on upper boundary

The least square method is utilized to solve equations containing x/y strain. Corresponding upscaling calculation results are shown in **Table 5.4**, with the sum of residual squares 8.659×10^{-4}.

Parameter	Initial value	Results	Residual
E_x	4.00×10^{8}	4.38×10^{-8}	1.258×10^{-2}
E_y	3.00×10^{8}	3.91×10^{-8}	0.513×10^{-2}
υ_x	0.1000	0. 438786	1.259×10^{-2}
υ_y	0.1093	0. 113291	2.286×10^{-2}

Table 5.4 Upscaling results for elastic upscaling

As depicted by Khajeh, various upscaling ratios (upscaling ratio is defined as the ratio of upscaled and original cell size) are considered to assess the upscaling methodology. The average error increases with upscaling ratio (Khajeh, 2012).

It is then concluded that in the elastic range, by adopting upscaling procedure mentioned above, heterogeneous Modified Cam Clay materials can be upscaled to a homogenous anisotropic elastic material in elastic deformations.

5.3 Modified Cam Clay material upscaling in elastic-plastic range

5.3.1 Elastic-plastic upscaling theory

In order to benefit the upscaling of Modified Cam Clay materials, the following elastic-plastic matrix form is adopted. Elastic-plastic matrix stands for properties of Modified Cam Clay material. Similar to upscaling in the elastic range, what is needed is to find the equivalent parameters for the elastic-plastic matrix.

$$\begin{Bmatrix} \mathrm{d}\varepsilon_v \\ \mathrm{d}\varepsilon_s \end{Bmatrix} = \frac{2\eta(\lambda'-k')}{(1+e)(m^2+\eta^2)} \begin{bmatrix} \frac{\lambda'(m^2+\eta^2)}{2\eta} - \eta & 1 \\ 1 & \frac{2\eta}{m^2-\eta^2} \end{bmatrix} \begin{Bmatrix} dp' \\ dq \end{Bmatrix} \tag{5.6}$$

Where, ε_v and ε_s are strain induced by dp' and dq respectively, e is void ratio, η equals q/p', p' is effective mean stress, q is deviatoric stress, m is the slope of the critical state line.

It needs to determine λ' κ' m e for the elastic-plastic matrix. Under the assumption of homogeneous stress condition across/in upscaling area, the following calculation method is adopted.

For a single cell:

$$e = a + b\ln(\sigma') \tag{5.7}$$

For a genetic unit that contains many elements:

$$\bar{e} = \frac{\sum_{i=1}^{n} a_i}{n} + \frac{\sum_{i=1}^{n} b_i}{n}\ln(\sigma') \tag{5.8}$$

This equation can then be used to deduce λ' and κ'.

Void ratio upscaling adopts the average method for n elements:

$$\bar{e} = \frac{\sum_{1}^{n} e_i}{n} \tag{5.9}$$

Then what needs to be upscaled is only 'm'. The least square method is utilized to deduce this optimized m. Similarly to elastic upscaling, this inversion fitting method is adopted here, detailed procedure are as follows.

Step 1: Set the vertical and horizontal stress conditions, provide a small stress boundary change. Solve the isotropic-heterogeneous Modified Cam Clay model. In this step ε_v and ε_s are calculated and the non-uniformly deformed body is obtained.

Step 2: Average ε_v and ε_s for the coarse scale body.

Step 3: Calculate the optimal elastic-plastic parameters by the least square method which results in the same ε_v and ε_s applied on the uniformly deformed body.

5.3.2 Elastic-plastic upscaling application

Cell arrangement is shown in **Figure 5.5**.

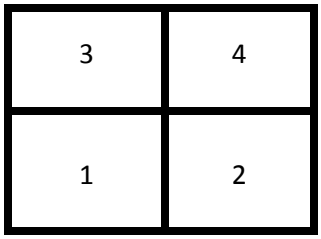

Figure 5.5 Cell arrangement 1: Salins 14 illite, 2: Marais Poitevin mud, 3: St Austell kaolinite, 4: La Bouzule clay

(1) Initial mean effective stress: -10 MPa

Considering the failure surface, initial vertical effective stress σ'_{yy} = -13.636 MPa, horizontal effective stress σ'_{xx} = -8.182 MPa, to ensure the elastic-plastic deformation of Modified Cam Clay material. Addition of $d\sigma'_{yy}$ = 0.1 MPa is applied on the upper boundary, fix lower boundary. Left and right boundaries are applied effective stress of σ'_{xx} = -8.182 MPa.

Upscaling parameters are shown in **Table 5.9** and **Table 5.6**, small relative errors indicate the promising upscaling results.

Upscaling parameter	Value
λ'	0.21
κ'	0.0722
void ratio $\bar{e}$	0.5334
m	1.21561

Table 5.5 Upscaling parameters (Initial mean effective stress: -10 MPa)

Average boundary displacement	Fine-scale model	Coarse-scale model	Relative error
$d\varepsilon_v$	8.9787×10^{-4}	9.0832×10^{-4}	1.150%
$d\varepsilon_s$	5.2886×10^{-4}	5.2339×10^{-4}	1.045%
Average boundary displacement-vertical	2.5387×10^{-4}	2.3461×10^{-4}	8.209%
Average boundary displacement-horizontal	4.9166×10^{-5}	4.7974×10^{-5}	2.485%

Table 5.6 Upscaling results (Initial mean effective stress: -10 MPa)

(2) Initial mean effective stress - 11 MPa

Considering the failure surface, initial effective stress σ'_{yy} = -14.636 MPa, σ'_{xx} = -9.182 MPa, this ensures the elastic-plastic range of Modified Cam Clay material. Addition of $d\sigma'_{yy}$ = 0.1 MPa is applied on the upper boundary, fix lower boundary. Left and right boundaries are applied effective stress of σ'_{xx} = -9.182 MPa.

Upscaling parameters are shown in **Table 5.7** and **Table 5.8**, small relative errors indicate the promising upscaling results.

Upscaling parameter	Value
λ'	0.21
κ'	0.0722
void ratio $\bar{e}$	0.523
m	1.2144

Table 5.7 Upscaling parameters (Initial mean effective stress: -11 MPa)

Average boundary displacement	Fine-scale model	Coarse-scale model	Relative error
$d\varepsilon_v$	8.0533×10^{-4}	8.1353×10^{-4}	1.008%
$d\varepsilon_s$	4.3581×10^{-4}	4.3121×10^{-4}	1.067%
Average boundary displacement - vertical/m	2.0684×10^{-4}	2.1397×10^{-4}	3.332%
Average boundary displacement - horizontal/m	3.7999×10^{-5}	4.3767×10^{-5}	1.318%

Table 5.8 Upscaling results (Initial mean effective stress: -11 MPa)

(3) Upscaling properties variation

It can be seen from the above results that upscaling properties vary with mean effective stress. Difference of ε_v and ε_s between fine-scale and upscaling modelling results are utilized as research object. Generally, error of upscaling increases with the increase of additional pressure, are shown in **Figure 5.6.**

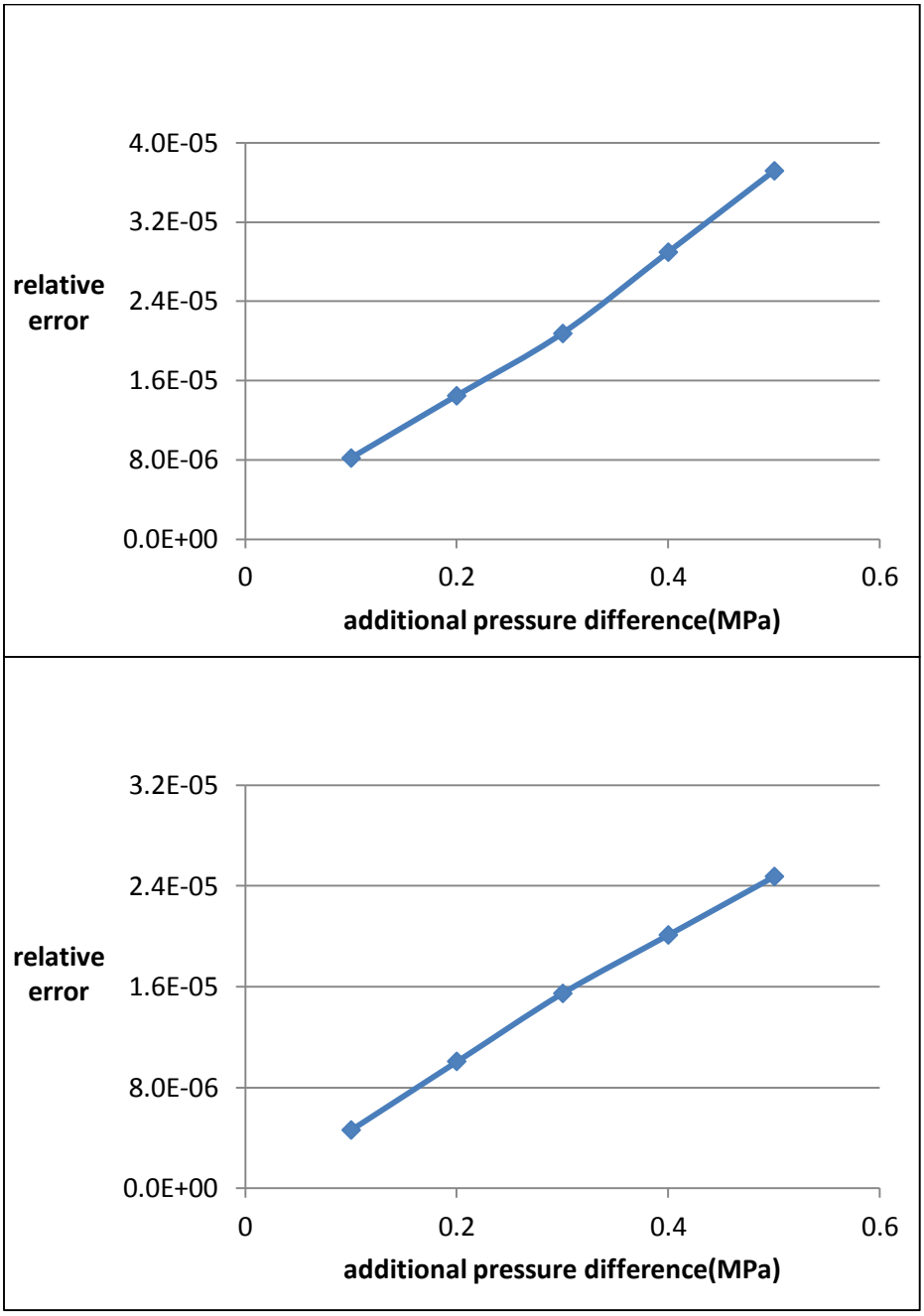

Figure 5.6 Relative error of $d\varepsilon_v$ (upper) and $d\varepsilon_s$ (lower) increases with additional pressure

When stress condition of upscaling region cannot be treated as homogeneous, the mentioned upscaling equation will fail. Then similar to elastic upscaling, λ' κ' m e can all be set to be unknown, and hence more loading conditions (i.e. more equations) are needed to obtain the unknowns. However, more equations do not ensure obvious improvement, the least square method sometimes generates inappropriate parameters.

5.3.3 Verification with classic upscaling model - checkered box

A classic model is utilized for verification of feasibility, corresponding cell arrangement is shown as follows.

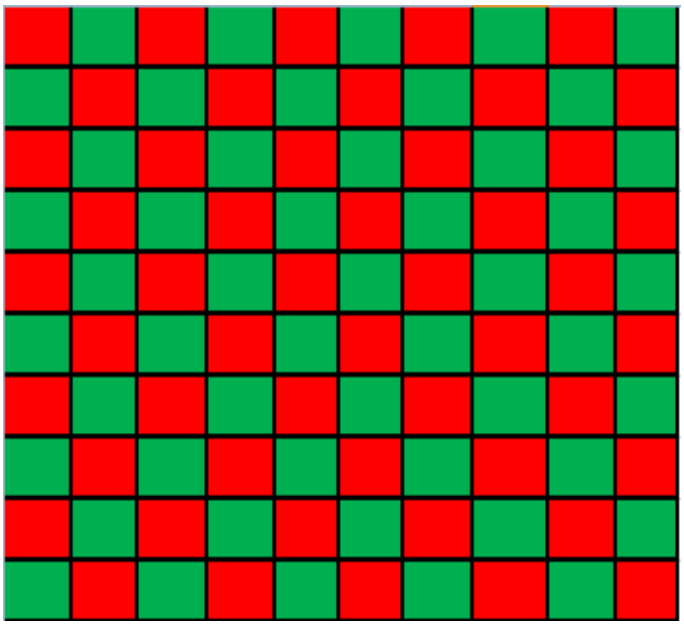

Figure 5.7 Cell arrangement (red: Salins 14 illite, green: Marais poitevin), each small square block is 1×1 m, overall size is 10×10 m.

Upscaling unit are shown in **Figure 5.8**, the whole area is homogenized as shown in **Figure 5.9**. 2×2 cells upscaled to 1 homogeneous cell. Initial mean effective stress is 11 MPa. Considering the failure surface, initial effective stress σ'_{yy} = -14.636 MPa, σ'_{xx} = -9.182 MPa, this ensures the elastic-plastic deformation of Modified Cam Clay material. Addition of $d\sigma'_{yy}$ = 0.1 MPa is applied on the upper boundary, fix lower boundary. Left and right boundaries are applied effective stress of σ'_{xx} = -9.182 MPa.

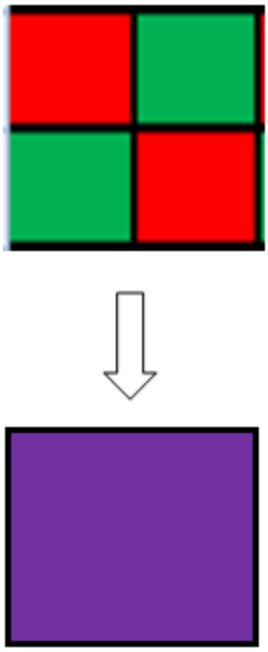

Figure 5.8 Upscaling unit, 4 small square 1×1 m cells upscaled into one 2×2 m cell.

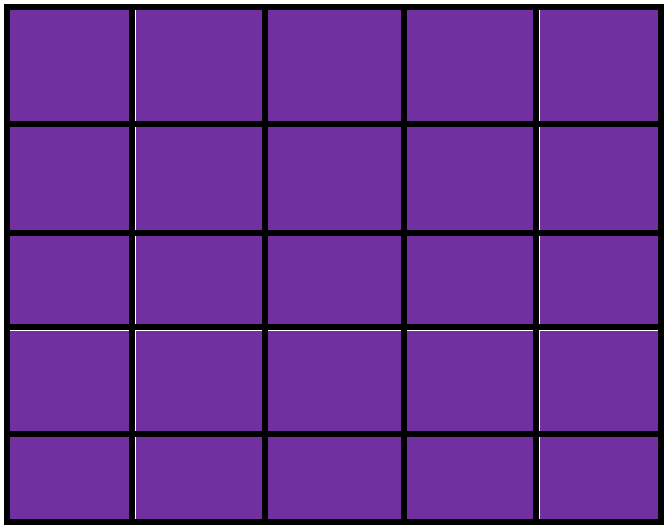

Figure 5.9 Homogeneous coarse-scale model, each small square block is 2×2 m, overall size is 10×10 m.

Modelling results of fine-scale model are shown in **Figure 5.10**. Upscaling results and relative errors are shown in **Table 5.9**.

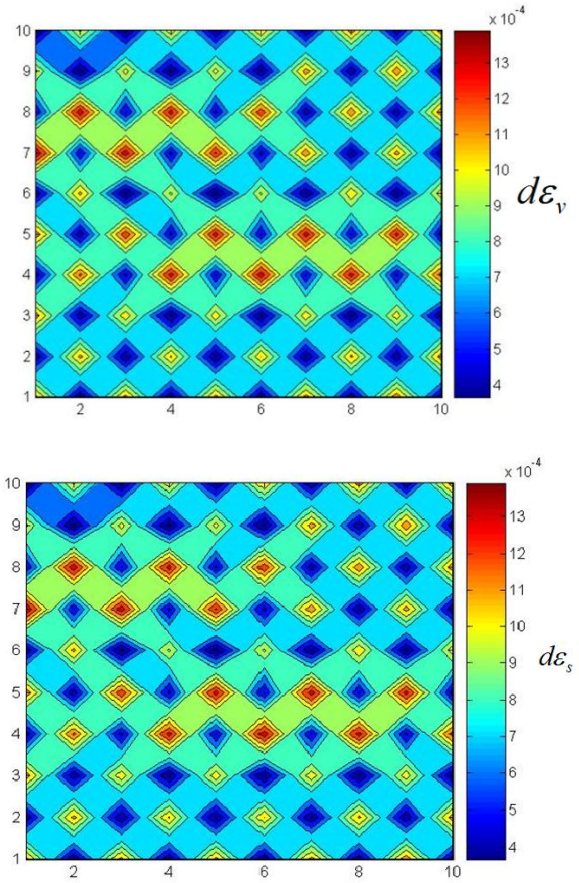

Figure 5.10 Fine-scale model $d\varepsilon_v$ (upper) and $d\varepsilon_s$ (lower)

	Upscaling result	Fine-scale model result	Relative difference of coarse-scale model from fine-scale model
$d\varepsilon_v$	7.65×10^{-4}	7.98×10^{-4}	4.32%
$d\varepsilon_s$	3.67×10^{-4}	3.97×10^{-4}	8.16%
horizontal boundary average displacement	3.42×10^{-5}	2.48×10^{-5}	27.58%
vertical boundary average displacement	1.67×10^{-4}	1.21×10^{-4}	27.63%

Table 5.9 Upscaling results for checkered box model

The application of classic 'checkered-box' model proves the effectiveness of the upscaling method. Upscaling results of ε_v and ε_s are smaller, while the displacement upscaling results are relative higher which is induced by the material contrast of adjacent cells. Displacements, $d\varepsilon_v$ and $d\varepsilon_s$ of two adjacent cells display a marked difference, which can be reflected in **Figure 5.10**.

5.3.4 Channel levees upscaling application

A channel levees system, which is very common in sedimentary basin, is utilized to create a model configuration. This model is used for demonstrating and testing the upscaling approaches. Note that this model is designed to study the upscaling of elastic-plastic materials. For channel levees that are composed of sand, the elastic-plastic clay model may not suit.

The material and arrangement of the fine-scale model is shown in **Figure 5.11**, the upscaling unit is displayed in **Figure 5.12**, 9 heterogeneous small square 1×1 m cells upscaled into one homogeneous 3×3 m cell in the channel levees region. And correspondingly, the coarse-scale model is shown as **Figure 5.13**

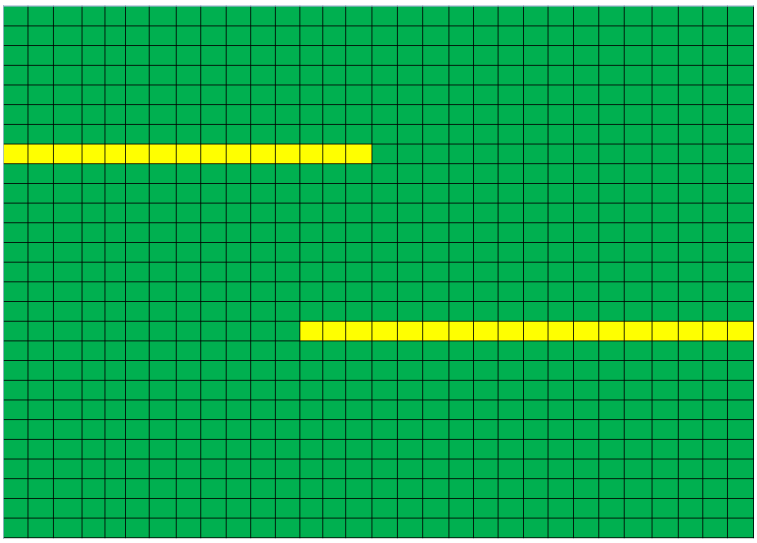

Figure 5.11 Channel levees system. Yellow - Salins 14 illite, Green - Marais Poitevin mud (The fine-scale model is 30×30m, each cell is 1×1m, Salins levees - upper one 15×1m and lower one - 18×1m).

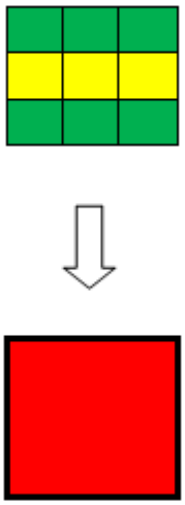

Figure 5.12 Upscaling unit, 9 heterogeneous small square 1×1 m cells upscaled into one homogeneous 3×3 m cell.

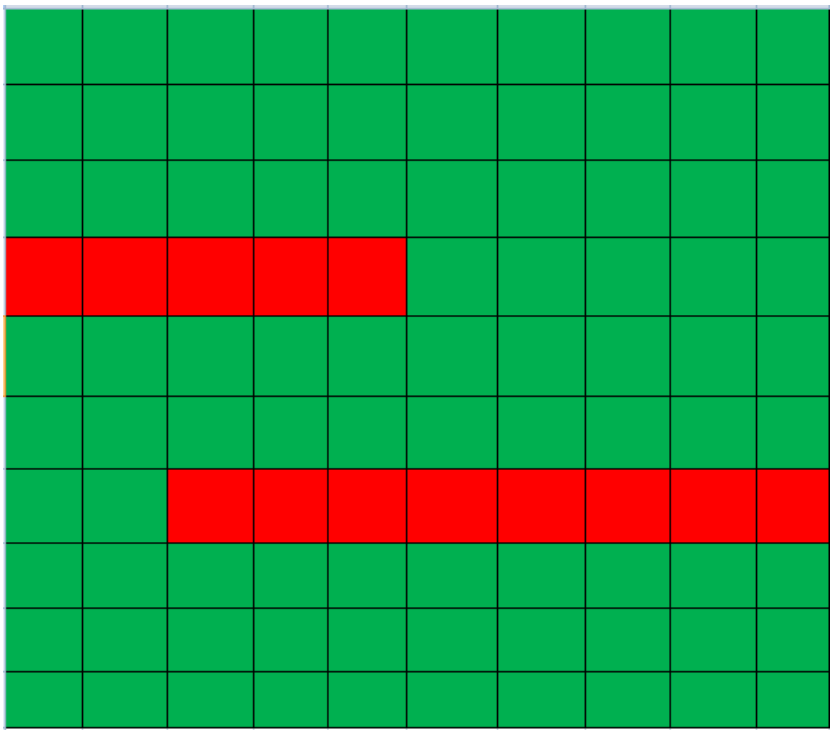

Figure 5.13 Coarse-scale model after upscaling

Considering the failure surface of the Modified Cam Clay material, the initial effective stress state is assigned as σ'_{yy} = -14.636 MPa, σ'_{xx} = -9.182 MPa, at an initial mean effective stress of 11MPa; this ensures the elastic-plastic range of Modified Cam Clay material. Upscaling parameters are deduced by adding a small stress increment on the right boundary (0.01 MPa additional stress). Then a larger load is applied (0.1MPa additional stress on right

boundary) on the whole model to validate the upscaling method. Left boundary is fixed, upper and bottom boundaries remain at constant applied effective stress of σ'_{yy} = -14.636 MPa.

When the 3×3 cells are upscaled into one cell, the whole-model upscaling results are shown in **Table 5.10**, **Figure 5.14** and **Figure 5.15**. Analyses conclude that upscaling captures the characteristics of the two channel levees systems, accompanied with reasonable errors of average boundary displacement. It should be noted that interaction between levees and boundary will generate singular areas (discrete small areas in $d\varepsilon_v$ results) in the background of Marais Poitevin mud.

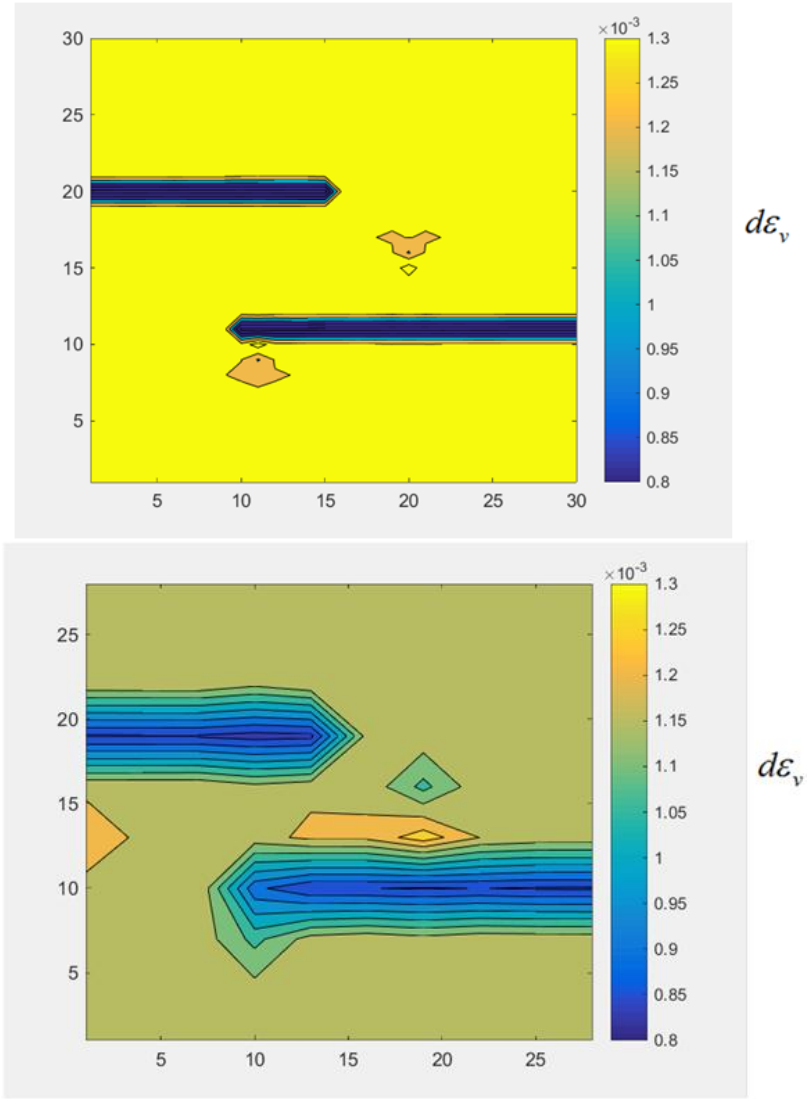

Figure 5.14 $d\varepsilon_v$ results, fine-scale (upper) and coarse-scale (lower) model

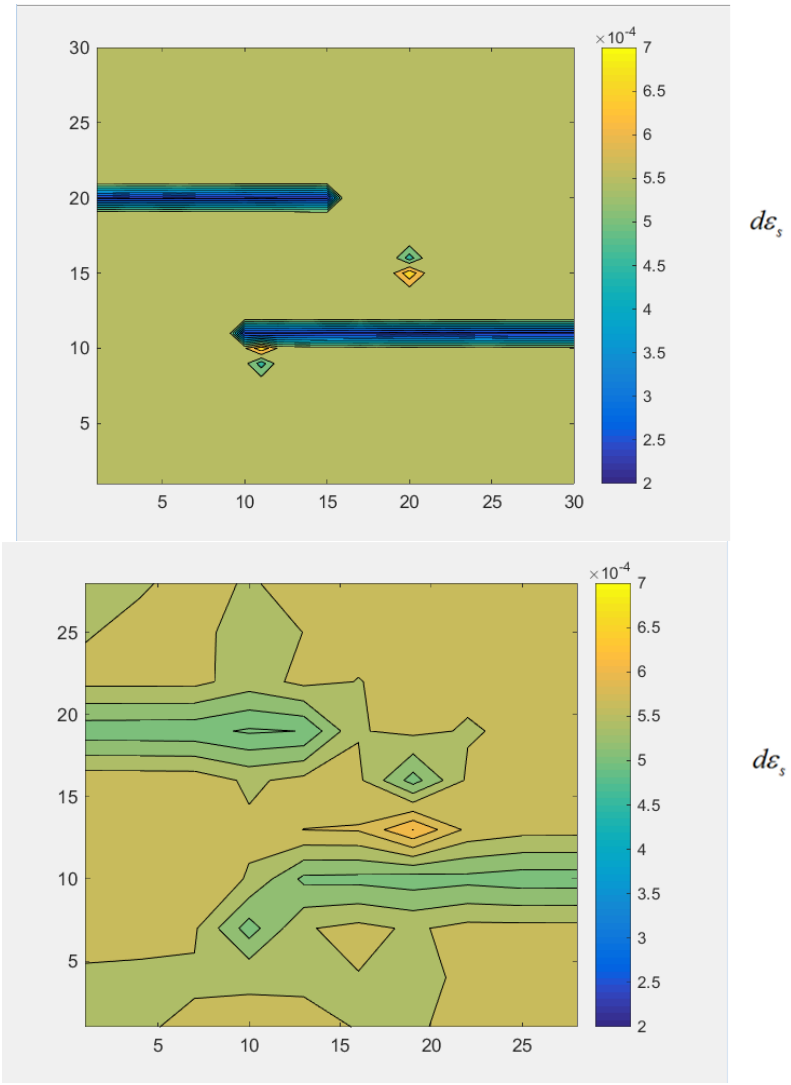

Figure 5.15 Fine-scale model (upper) and coarse-scale (lower) $d\varepsilon_s$ results

Average boundary displacement	Fine-scale model (m)	Coarse-scale model (m)	Relative error of the two results
horizontal	4.8011×10^{-5}	4.8186×10^{-5}	0.363176%
vertical	2.3769×10^{-4}	2.3579×10^{-4}	0.805802%

Table 5.10 Calculation results for the channel levees model

The coarse-scale model captures the characteristics of the channel levees system as shown in **Figure 5.14** and **Figure 5.15**. And the displacement upscaling results are satisfactory.

5.4 Application of Modified Cam Clay model and upscaling method

5.4.1 Model setting

In this section, Modified Cam Clay and the developed upscaling method is applied to a case derived from a real basin located in North Africa, which was examined in the Caprocks project (Georgiopoulou et al., 2008). There are many channel levees in this basin, which

reflects the lateral heterogeneity in both mechanical and fluid flow. Both the fine-scale and coarse-scale model simulate the evolution of this basin, and their modelling results are coincident.

A genetic-unit based seismic facies interpretation is shown as follows:

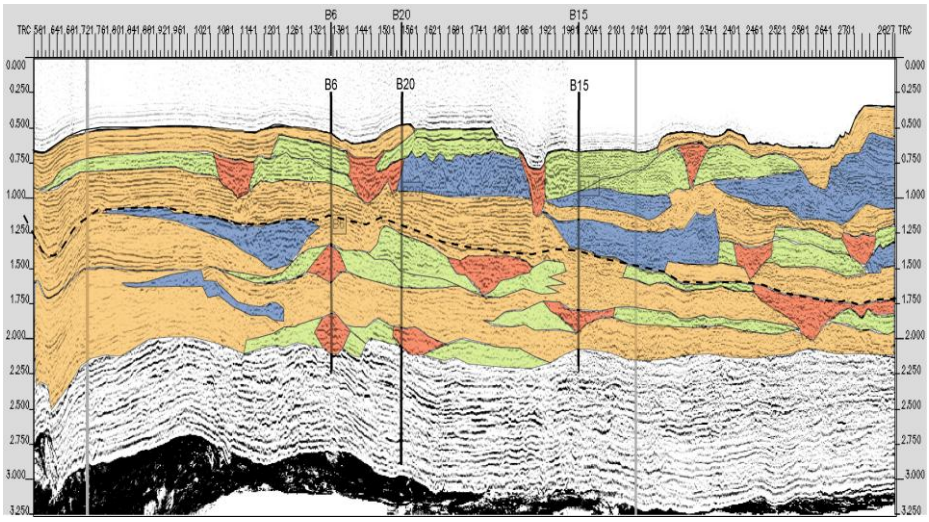

Figure 5.16 Genetic unit based seismic facies of North Africa, from Aggeliki's interpretation (Georgiopoulou et al., 2008).

Considering the shortage of hard data, parameters utilized in modelling are assumed as follows. Sedimentation rate: 50m/0.1 million years - corresponding to one layer' cell of 50 m in depth is added on the top to simulate the sedimentation. Boundary condition: permeable top, impermeable bottom, fixed lateral displacement along right and left boundary.

Low initial stress of sediment will make cell tightly twisted, and hence fail to converge. More cells will solve this problem. In consideration of the limitations of the academic version of FLAC, initial horizontal stress is -0.6 MPa, initial vertical stress is -1.0 MPa, initial pore pressure is hydrostatic.

Genetic unit facies are simplified into the following cell arrangement, in which the main part is assumed to be Salins 14 illite of low conductivity, while the channel levees and MTDs are higher conductivity material (St Austell kaolinite, La Bouzule clay and Marais Poitevin mud).

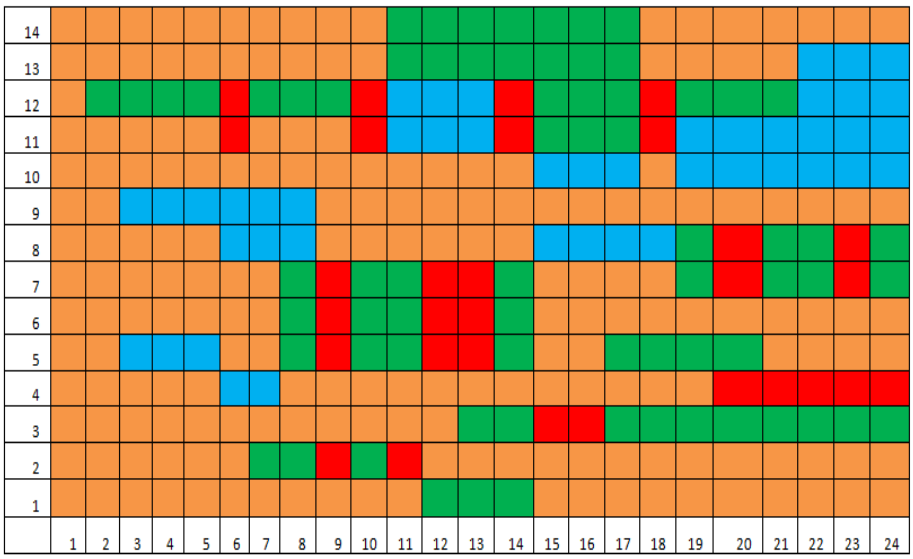

Figure 5.17 Simplified cells arrangement (Yellow: Sa14, Blue: Mp, Green: Labour, Red: Ka st au)

The overall size is 12000 m in width and 700m in height. Each cell is 500m in width, 50m in height for the fine-scale model. In the upscaled model, each cell is 1500m in width, 50m in height, that is 3 cells upscaled into 1 cell in lateral direction. There is no upscaling in the vertical direction in order to meet the requirement of inter cell stress equivalence. The coarse-scale model is shown in **Figure 5.18**, the heterogeneous cells that require upscaling are surrounded by dotted lines.

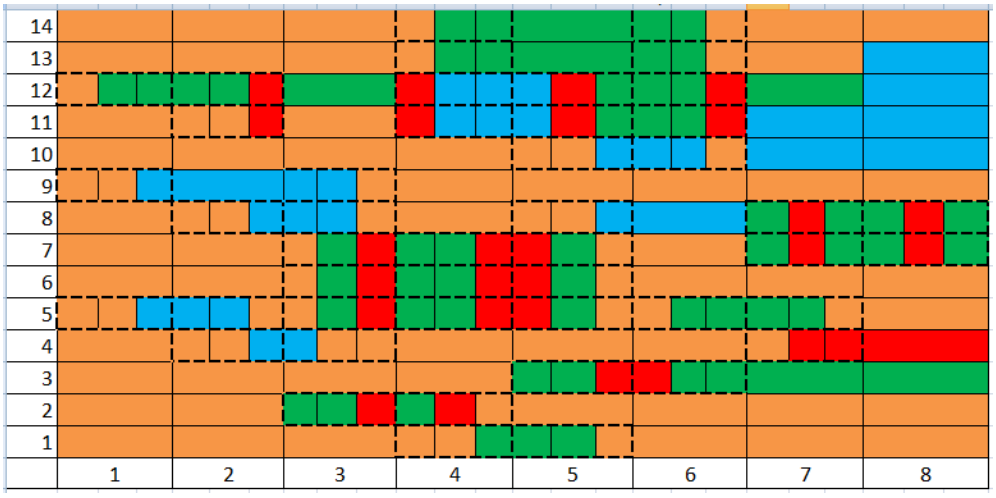

Figure 5.18 Coarse-scale cells arrangement (Yellow: Sa14, Blue: Mp, Green: Labour, Red: Ka st au)

These clay parameters are defined in **Chapter 4,** in order to reduce unknown parameter numbers, all Poisson's ratios are set to be 0.17. However the ultra-low permeability is beyond the scope of conventional materials in basin modelling as shown in **Figure 2.45**.

Moreover this will result in the neglecting of ultra-low flow velocity in FLAC's fluid-structure interaction computation. In order to better describe the evolution of overpressure and meet the limitation of FLAC academic, the conductivities for all materials are 7 orders greater than that defined in **Chapter 4.**

Upscaled conductivity is different in x direction (horizontal) and y direction (vertical):

In x direction, it is series arrangement of three cells, w_i is the length of each cell; in y direction, it is parallel arrangement of three cells of height H.

In lateral direction, series arrangement: $k^* = \dfrac{\sum w_i}{\sum \dfrac{w_i}{k_i}}$

In vertical direction, parallel arrangement: $k^* = \dfrac{\sum w_i k_i}{\sum w_i}$

Updating of upscaled Modified Cam Clay property and conductivity are adopted in the simulation, with the updating frequency of 0.5 MPa per interval/step.

5.4.2 Model results

In order to compare the modelling results of the fine-scale model and updating upscaling model, distribution of permeability, effective stress and pore pressure are presented. The width-height ratio is too large for each cell, practical visual effect of parameters distribution is not easy to observe. 'Square-grid' results, in which the width equals the height for each cell, are utilized although without natural transition between grids. Note that sharp bends and fluctuations are also induced by grid diagram, as the final modelling results shown in the following:

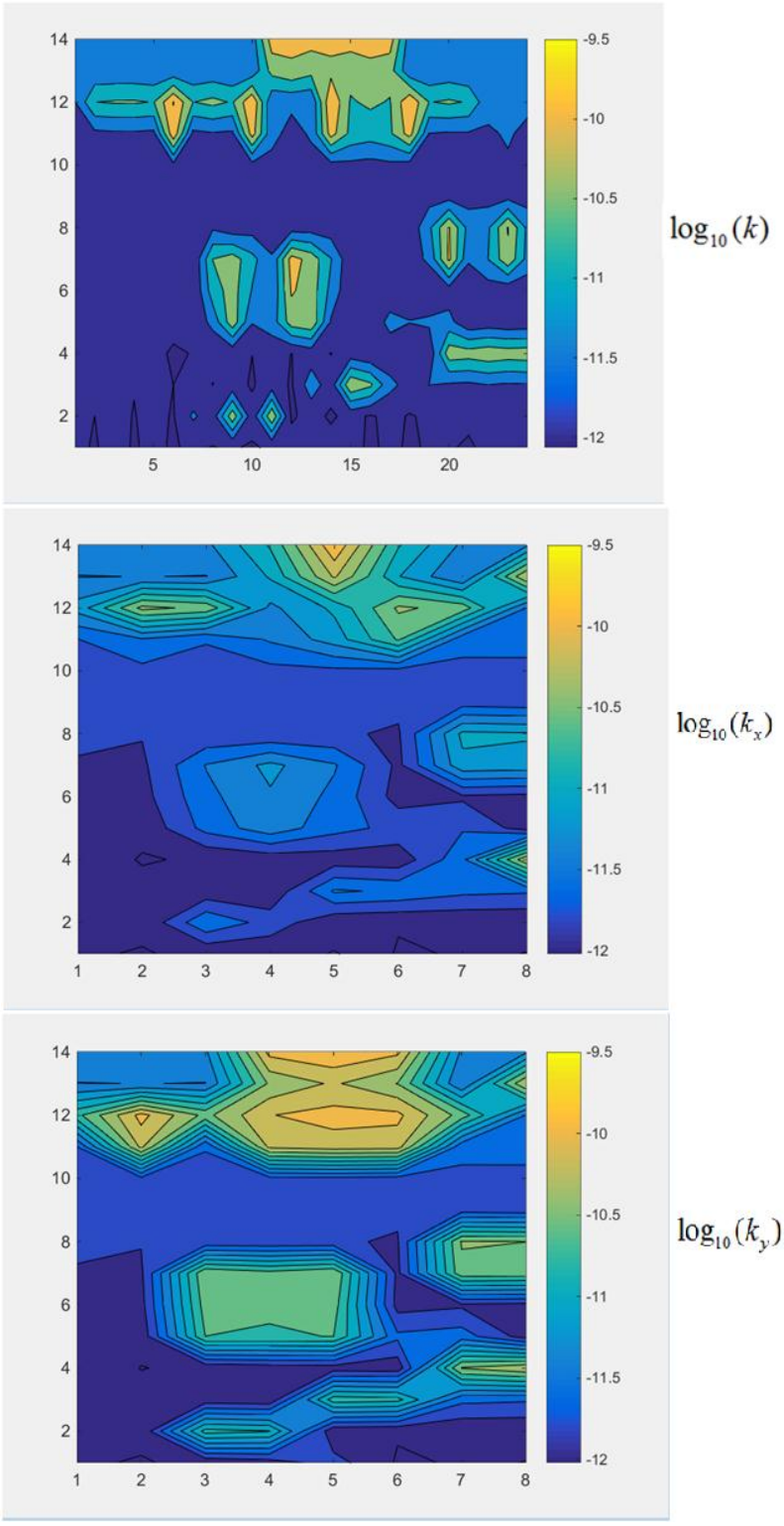

Figure 5.19 $\log_{10}(k)$ distribution (m^2), fine-scale modelling (upper), coarse-scale modelling (middle - x direction, $\log_{10}(k_x)$), coarse-scale modelling (bottom - y direction, $\log_{10}(k_y)$). Number on the left and bottom coordinate is mesh number.

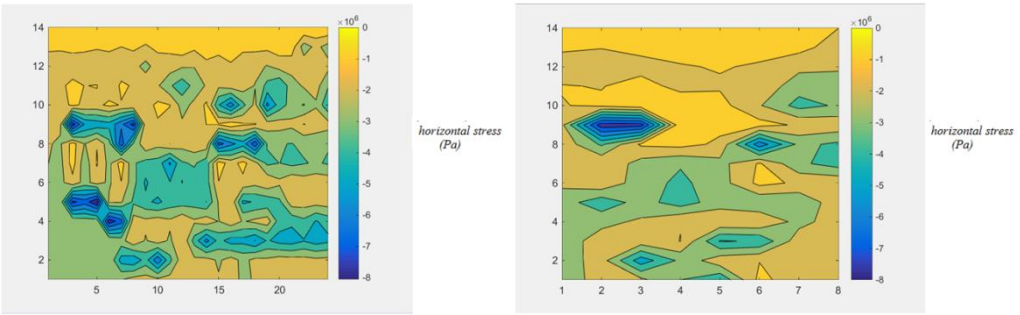

Figure 5.20 Horizontal stress distribution, fine-scale modelling (left), coarse-scale modelling (right). Number on the left and bottom coordinate is mesh number.

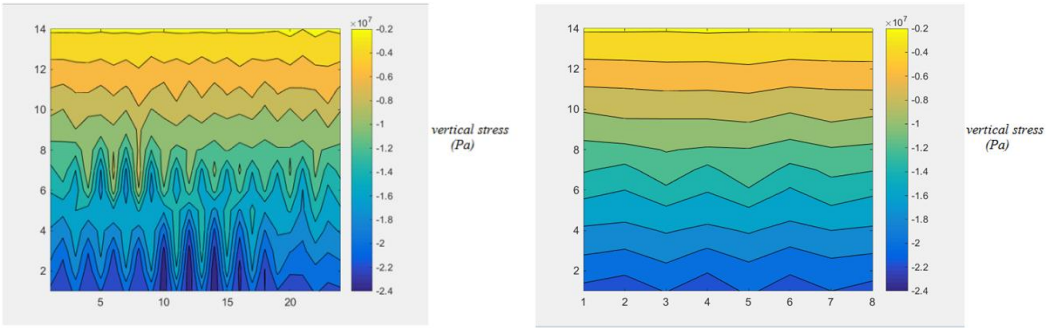

Figure 5.21 Vertical stress distribution, fine-scale modelling (left), coarse-scale modelling (right). Number on the left and bottom coordinate is mesh number.

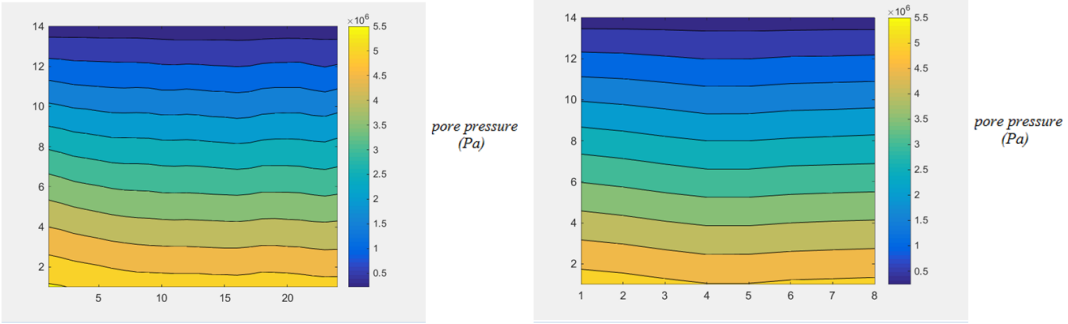

Figure 5.22 Pore pressure distribution, fine-scale modelling (left), coarse-scale modelling (right). Number on the left and bottom coordinate is mesh number.

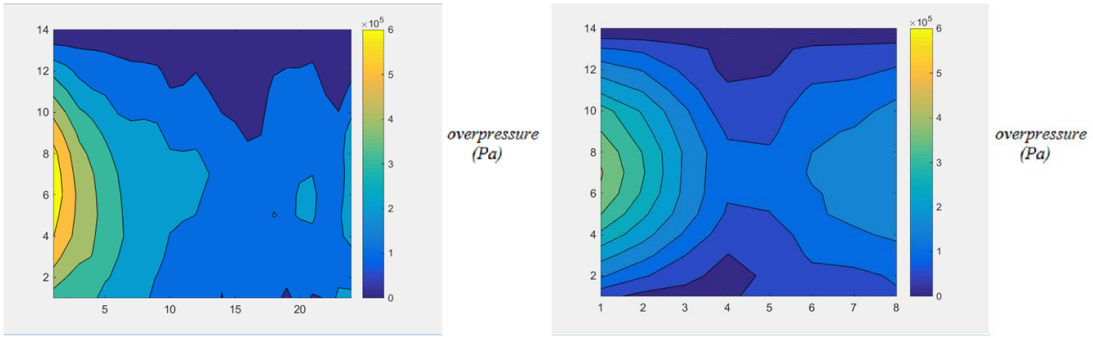

Figure 5.23 Overpressure distribution, fine-scale modelling (left), coarse-scale modelling (right), Number on the left and bottom coordinate is mesh number.

There are 9 nodes on the top surface of upscaled model, final heights of upscaled and fine-scale models (average adjacent nodes into one) are utilized for comparison. After upscaling,

relative errors for each node (1 - 9, from left to right) on the top surface between fine-scale and upscaled models are shown in **Table 5.11**.

Node	1	2	3	4	5	6	7	8	9
Error (%)	0.99%	0.29%	1.36%	1.52%	1.71%	1.62%	1.54%	1.88%	1.34%

Table 5.11 Final height error of coarse-scale model compared with fine-scale model

The results demonstrate that this updating upscaling method captures the evolution of pore pressure and height of fine-scale model. Upscaled conductivities are different in x direction and y direction, but both are functions of effective stress, conductivity of grid diagram results are shown in **Figure 5.19**. Corresponding upscaling effective stresses in x and y directions meet the fine-scale results as shown in **Figure 5.20** - **Figure 5.22**.

It needs to point out that the amplitude of each pressure pulse is a function of the discretization as shown in **Figure 4.6**. The results presented are optimized under the limitation of FLAC academic version, however finer discretization model will generate different results. Actually the simulation is more 'separate mass deposits' (depth of 50m for each mass deposit） than continuous sedimentation. After each separate mass is deposited, greater overpressure generates in the lower adjacent area. The overpressure will dissipate through two directions, flow out through the top surface and flow towards the low-pore pressure deeper part. This effect is also shown in **Figure 4.10**. Moreover, it is not easy for the overpressure in bottom layer to generate and enlarge considering the impermeable bottom boundary condition and more compressed properties (low porosity and permeability). Hence, the higher overpressure region is not located in the deepest part.

Figure 5.23 indicates that the main overpressure area is located in the left part of the basin due to the arrangement of high permeability levees and boundary effect. However, overpressure dissipation of coarse-scale model is faster than the fine-scale model as a result of the permeability upscaling method. In a word, the updating upscaling technology captures the evolution of this basin sedimentation in conductivity, stress and pore pressure distribution.

5.5 Discussion and Conclusion

In this chapter, a numerical upscaling technique for Modified Cam Clay model is proposed. Heterogeneous Modified Cam Clay materials can be upscaled to a homogenous anisotropic elastic material in elastic deformation and a homogenous Modified Cam Clay material in

elastic-plastic deformation. Complex facies, property distributions and anisotropic deformation have been considered in this upscaling technique.

Elastic and elastic-plastic properties for each cell vary with stress, and hence the related upscaled properties also vary with the stress condition. Therefore the developed technology is only suitable for a short time step or a small effective stress variation. The piecewise linear approximation combined with this technology can be used for the large-strain non-linear consolidation. More efforts are required for further research in order to fully capture the evolution of multi-dimensional consolidation.

A three-dimensional mechanical constitutive model based on the theory of critical state is necessary for modelling three-dimensional deformations in sedimentary basins. This chapter simulate the evolution of a basin from North Africa using a real multidimensional mechanical constitutive model - Modified Cam Clay model. Simulation results show heterogeneity and its effect on conductivity, stress and overpressure. The corresponding numerical-updating upscaling captures the evolution of coarse-scale model in stress, permeability, overpressure and final thickness.

There are constraints for applying upscaling techniques:

(1) Regions for upscaling must be selected with care. If the characteristics' difference is too large between grids in the region, average displacement may not capture deformation character of the whole region.

(2) Coarse blocks must be chosen to be so that their sizes are not too big to induce large 'errors'. As shown in Khajeh's research (Khajeh, 2012), upscaling error increases with the increase of upscaling ratios. In terms of a given problem, the acceptable error in the response should be quantified by the practitioner and an appropriate block size selected.

(3) Mesh-updating technology is required. Shallow compaction will induce large-strain deformation. Moreover the heterogeneity between meshes will make meshes deform in entirely different way and tightly twisted, and hence fail to compute.

(4) A sudden loading mechanism is not well simulated. The continuous sedimentation process is divided into multistep sudden loading of sediment. When new cells are added, great unbalanced force will be generated. Normally, in soil engineering, this sudden loading

is modelled in two stages - 1) mechanical equilibrium occurs without flow; and 2) fluid flow. In this work fluid-structure interaction is always utilized.

Chapter 6 Conclusions and recommendations for future work

Shallow overpressure can pose significant risks to economics and safety of hydrocarbon production and will impact on hydrocarbon generation deep in a basin and hydrocarbon migration to traps during basin evolution. Heterogeneous fine-grained sediments at shallow burial below the seafloor can often experience large strain of mechanical compaction and variable degrees of overpressure in their pore space as a result of disequilibrium dissipation of pore fluid. However, when basin modelling ignores the heterogeneity of sediments, large strain deformation and fluid flow conditions at smaller length- and/or time-scales than those at basin scales, it can lead to incorrect prediction of sediment compaction, the magnitude of pore pressure and its distribution at shallow burials and consequently basin evolution.

To be specific:

(1) In 1D and 2D, large-strain shallow basin compaction simulators are necessary for addressing the specific issues at shallow depth. It should not only represent the properties of shallow compaction, but also do so with high computational efficiency.

(2) In basin-scale modelling, the basin domain is discretised into blocks, and the evolutionary processes are divided into time steps. High precision simulation results require small enough time steps and mesh sizes which add cost and complexity. The effects of intra-block and time-interval heterogeneity must be taken into account by upscaling in view of simulation cost.

(3) Basins exhibit time and space variations that demand multi-dimensional analysis. Multiple dimensions are considered in current basin modelling tools for fluid flow and thermal modelling, but the existing commercial basin modelling tools still are based on 1D consolidation methods for the mechanical aspects of basin development. Multi-dimensional models are necessary to better describe basin evolution when considering heterogeneous, multi-dimensional fluid flow and deformation.

Facing these problems as described in the introduction, this research focuses on modelling and upscaling of shallow compaction in basins both in 1D and 2D. Research contents follow the research work flow of **Figure 1.2**, accordingly the key findings and conclusions will be summarized.

6.1 Key findings and Conclusions

(1) Firstly, model selection is carried out for shallow compaction in 1 D in order to find the most fitting model.

Consolidation models used in basin modelling can be divided into two categories depending on whether deformation is approximated by small-strain and large-strain deformations. The bigger the compressibility is, the bigger is the difference between small-strain and large-strain results for both self-consolidation and consolidation under surcharge. Hence, it is not reasonable to apply small-strain theory directly into large-strain shallow compaction.

Different from small-strain model, self-weight consolidation is taken into consideration in Gibson's equation, which plays an important role in basin evolution. Influence of self-weight consolidation increases with the increase of initial thickness and unit weight of the soil, but decreases with the increase of effective stress. This provides the fundamental guidance for model selection between small-strain and large-strain model.

By combining of piecewise linear approximation of soil properties, meshes updating, time and space step control technology, the small-strain model has been successfully applied in large-strain consolidation problems. Compared with small-strain model, large-strain consolidation model is more effective and accurate in large-strain basin modelling.

There are more complex large-strain models than Gibson large-strain model, which consider fluid compressibility and sedimentation rates. However, comparison results show that Gibson model is reasonable simple for shallow compaction.

These comprehensive comparisons prove the effectiveness and correctness of Gibson large-strain model for shallow compaction simulation. The corresponding conclusions also provide necessary standards for evaluation of other models.

(2) Secondly, one-dimensional large-strain basin modelling simulator development and verification in 1D are subsequently provided.

A one-dimensional large-strain basin modelling simulator based on Gibson consolidation model is developed and verified with both analytical and experimental results. This simulator can simulate various conditions including self consolidation, consolidation with surcharge, sedimentation and multi-layer sedimentation/consolidation. As for different behaviours of

sediments, constitutive models of pre-consolidation, creep compression, layering model, sedimentation-consolidation are considered.

Then with the correctness and verification, it is now safe to use the simulator to analysis real shallow compaction and upscaling.

(3) Thirdly, the large-strain simulator is applied in Ursa Region - Gulf of Mexico and a laterally heterogeneous alluvial rift basin.

The developed model is applied to Ursa Region, Mississippi canyon area, Gulf of Mexico. However, the large-strain model over predicts the pressure of Ursa region estimated from the Integrated Ocean Drilling Program (IODP). These over predictions provide some enlightenment. For one thing, the data utilized in the model may not be fully representative. IODP pressure curves, with many turning points, show the characteristics of a multi-layer system. A more fine-scale simulation or upscaling method is required. For another, Horizontal flow and Mass transport needs to be considered. As noted, the Blue Unit has regional extent, and the flow pathways potentially associated with this higher-perm unit may be serving to remove fluid energy from the local region examined via a Lateral Transfer mechanism. Moreover, the existence of Mass transport deposits, and their sudden loading or unloading effects, is not fully considered in the model presented here. Correspondingly, the following improvements are required to solve the problems. A more fine-scale model or upscaling should be adopted in the 1D model. And multi-dimensional models are required to solve the problems of lateral fluid flow and mechanical-loading heterogeneity.

Similarly, the laterally heterogeneous alluvial rift basin model proves that multi-dimensional models are necessary to better describe basin evolution when considering lateral heterogeneous, multi-dimensional fluid flow and deformation.

It is then concluded that upscaling and multi-dimensional large-strain model are necessary.

(4) Fourthly, 1D large-strain consolidation upscaling methods are developed correspondingly.

An analytical upscaling method for both small-strain and large-strain consolidation is presented based on some simplification. Multi-layer small-strain (Terzaghi) and large-strain (Gibson) consolidation is solved with the transform matrix and Laplace transformation. Based on the method of the transform matrix, which considers the properties of multi-layer consolidation, an upscaling method is put forward. It turns out to be more effective than the

widely-used weighted average method. The integral properties of multi-layer system change with the increase of affected region and hence are changing.

Analytical upscaling can provide intuitive guidance though with some simplification. Numerical upscaling will provide a more comprehensive understanding. Based on the developed numerical large-strain shallow compaction simulator, multi-layer consolidation characteristic is studied. Multi-layer numerical results reveal that the properties of multi-layer systems are changing with surcharge and time. It is impossible to use one constant relationship to describe consolidation characteristics, which proves the insufficiency of most direct upscaling methods.

Initial and final sediment height of heterogeneous sediment can be captured by only taking into account of relationships of 'void ratio - effective stress'. However, the overpressure and height evolution is quite different without considering relationships of 'conductivity - void ratio'. The real consolidation is a coupling of the processes of mechanical consolidation and fluid flow. Only upscaling of these two relationships simultaneously is meaningful.

Sedimentation of semi-infinite layers is common, such as channel levee systems. Large-strain consolidation of layered systems is studied by numerical methods. When the alternating layer reaches a certain value, the whole system will follow a single consolidation curve. A sensitivity analysis shows that layer number has a great effect on consolidation time. In the real sedimentation, compressibility and conductivity change randomly. When the random layer reaches a certain value, the whole system will follow a single consolidation curve. The bigger the variations of compressibility and conductivity are, the more layers will be needed to reach a single consolidation curve. Curve fitting results demonstrate that it is impossible to find a set of fixed relationships to match the multi-layer consolidation, which means the direct upscaling is impossible. These conclusions may provide feasible guidance for upscaling of semi-infinite heterogeneous layers in basin modelling.

Inversion of deposited sediments' petrophysical properties is important for accurate basin modelling. This research proves that soil properties of large-strain consolidation can be obtained through inversion. This inversion technique is extended to multi-layer systems' properties upscaling successfully. However, differences between upscaling and fine-scale simulation increase over time, which coincides with the nature that parameters of multi-layer system are changing with time. Similar to well testing, this study proves the feasibility of getting heterogeneous sediments' properties through pressure simulation.

These researches reveal the essence of heterogeneous multi-layer system, and proposed feasible upscaling technologies.

(5) Fifthly, 2D shallow compaction model selection and verification.

Basins exhibit time and space variations that demand multi-dimensional analysis. This research uses a multi-dimensional approach to assess the hydro-mechanical responses of a basin-like system. Elastic-plasticity is a more general formulation than simple 1D consolidation, which, in principle, allows for the consideration of horizontal deformations and those which vary laterally. The Modified Cam Clay elastic-plastic material model is a general but widely-accepted way of computing coupled hydro-mechanical processes in fine-grained geomaterials. A two dimensional large-strain basin modelling simulator based on Modified Cam Clay model is developed thereafter, which can also be applied to complex geological processes, such as loading, unloading. The model and its numerical implementation – FLAC are verified with experimental data.

Then an elastic-plastic, multi-dimensional and large-strain shallow compaction simulator is ready to use for simulation and upscaling. However, this simulator has its own limitations. In FLAC the constitutive model is only given displacements and velocities from which it produces stress and strains. However, this algorithm shows its limitations when facing sudden loading/ unloading. When sudden unloading happens, negative pore pressure will generate in the simulation which will not happen in reality. When loading happens, zero effective pressure and fracture will generate which cannot be simulated by FLAC. More advanced algorithm is required for these problems.

(6) Sixthly, the developed shallow compaction simulator is applied in simulation and upscaling.

Similarly, a numerical upscaling technique for Modified Cam Clay material is proposed. Heterogeneous Modified Cam Clay materials can be upscaled to a homogenous anisotropic elastic material in elastic deformation and a homogenous Modified Cam Clay material in elastic-plastic deformation. The upscaling method is verified with a classic ‘checkered box’ model and heterogeneous channel levees system. The upscaled properties of Modified Cam Clay material vary with stress condition, upscaling error increases with the variation of stress condition. Hence upscaled properties can only be applied to a small stress range, and updating technology is necessary.

This simulator and upscaling technology is applied in a case study associated with North Africa basin sedimentation thereafter. Modelling results show the effect of 2D heterogeneity on effective stress and overpressure evolution. Upscaling results demonstrate that this updating upscaling method captures the evolution of pore pressure and height of fine-scale model. The upscaling method is proved to be effective in lowering computational requirements of simulation while honouring local heterogeneities in sediment properties.
These simulators and upscaling methods can then be deliverable for modelling and upscaling of shallow compaction in basins both in 1D and 2D.

6.2 Future work

In the 1D model development, this research considers creep compression and layering phenomenon. Different constitutive models should be evaluated and applied in terms of specific problems.

As for 1D upscaling, semi-infinite layer follows a homogeneous consolidation curve. However finite layers' properties require more efforts to obtain optimal constant properties and hence further reduce computation amount.

2D upscaling properties also vary with effective stress, and hence are changing. Further research is needed for optimal constant properties. Consequently, upscaling can be developed into 3D, then fault, fissure and other geologic structure should also be upscaled.

More research is needed for 2D large-strain consolidation model

(1) Though with fundamentality and adaptability, Modified Cam Clay model has its own limitations, some geotechnical properties will not be expressed properly. More constitutive model should be evaluated and applied.

(2) The simulator, which is based on Modified Cam Clay model, can be developed into 3D when considering the actual three-dimensional geological model.

(3) Mesh-updating technology is required in order to prevent meshes tightly twisted induced by low sedimentation initial stress.

(4) Sudden loading/unloading mechanism requires more researches. A continuous sedimentation process is divided into many steps. When new cells are added, great unbalance

force will generate. Loading/unloading may generate fracturing and negative pore pressure, which requires more mechanism study.

(5) Modelling verification with basin-scale actual data is also required.

Appendix A: Source code

Appendix A.1: Self-consolidation code (Townsend's scenario A)

(1) Input data:

14.8

e0=14.8

9.6 100

initial height=9.6;nodes=100;

3600 100

Time=360;time steps=10 (>5)

10.0450 27.6360

rw=1.025*9.8;rs=2.82*9.8;

7.72 -0.22

a1=7.72;b1=-0.22; e=a1*stress^b1

0.2532e-6 4.65

c1=0.2532*10^(-6);d1=4.65; k=c1*e^d1

20

record step

(2) Input instruction:

14.8

Initial void ratio: e0=14.8

9.6 100

Initial height=9.6; Even distribution nodes in the calculation , number of nodes=100;

3600 100

Appendix

Consolidation time=360(day) ; calculation time steps=100

10.0450 27.6360

unit weight of water r_w=1.025×9.8; unit weight of water r_s=2.82×9.8;

7.72 -0.22

Void ratio-effective stress relationship: $e=a1\sigma^{b1}$ a1=7.72;b1=-0.22;

0.2532e-6 4.65

Void ratio-conductivity relationship: $k=c1e^{d1}$ c1=0.2532E-6;d1=4.65;

20

Record steps for output.

(3) Calculation code:

```
clear;clc
%%%%%%%%%%% read file %%%%%%%%%%%%%%%%%%%%%%%
fid=fopen('data.txt','r+');
a=[];
b=[];
while ~feof(fid)
      str=fgetl(fid);
      if numel(str)~=0
        if (double(str(1))>=48&&double(str(1))<=57)
          a=strread(str,'%f','delimiter',',');
          disp(a');
          b=[b;a]
        end
      end
end
e0=b(1);
h0=b(2);n=b(3);
T=b(4);bushu=b(5)
rw=b(6);rs=b(7);
a1=b(8);b1=b(9);
c1=b(10);d1=b(11);
rstep=b(12);
%%%%%%%%%% caculation %%%%%%%%%%%%%%%%%%%%%%%%
rc=rs-rw;
houdu=0;
a0=h0/(1+e0);
da=a0/(n-1);
dt=T/bushu;
```

```
eding=e0;
m=bushu;
e=zeros(n,1);
p=zeros(n,1);
houhou=zeros(n,1);
aaa=zeros(n,1);
f=zeros(n,1);
fdao=zeros(n,n);
for i=1:n
    e(i)=e0;
end
ebefore=e0*ones(n,1);
ebefore(n)=eding
jilujiange=m/rstep;
%%%%%%%%%%%%%%%%%%%%%%%%%%%%%%%%%%%%%%%%%%%%%%%%%%
for j=1:m  %shi jian bushu
      %%%%%%%%%%%%%%%%%%%%%%%%%% %%%%%%%%%
      keci=0.1*ones(n,1);
      ebefore(n)=eding;
      dde=ebefore(n)-ebefore(n-6);
   for i=n-5:n-1
       ebefore(i)=ebefore(i-1)+dde/6;
   end
      e=ebefore;
      while max(abs(keci))>0.001
%%%%%%%%%%%%%%%%%%%%%%%%%%%%%%%%%%%%%%%%%%%%%
                 i=1;
                 li(i)=(e(i)/a1)^(1/b1);
                 lidao(i)=(e(i)/a1)^((1-b1)/b1)/(a1*b1);
                 lidaodao(i)=(1-b1)*(e(i)/a1)^((1-2*b1)/b1)/(a1^2*b1^2)   ;
                 k(i)=c1*e(i)^d1;
                 kdao(i)=c1*d1*e(i)^(d1-1);
                 kdaodao(i)=c1*d1*(d1-1)*e(i)^(d1-2);
                 aaa(i)=(kdao(i)-k(i)/(1+e(i)))/(1+e(i));
                 bbb(i)=k(i)*lidao(i)/(1+e(i));
                 adao(i)=(kdaodao(i)-2*aaa(i))/(1+e(i));
                 bdao(i)=aaa(i)*lidao(i)+k(i)*lidaodao(i)/(1+e(i));
                 exu=e(i+1)+2*da*(rs-rw)/lidao(i);
                 lixu=(exu/a1)^(1/b1);
                 lidaoxu=(exu/a1)^((1-b1)/b1)/(a1*b1);
                 lidaodaoxu=(1-b1)*(exu/a1)^((1-2*b1)/b1)/(a1^2*b1^2)   ;
                 kxu=c1*exu^d1;
                 kdaoxu=c1*d1*exu^(d1-1);
                 kdaodaoxu=c1*d1*(d1-1)*exu^(d1-2);
                 aaaxu=(kdaoxu-kxu/(1+exu))/(1+exu);
                 bbbxu=kxu*lidaoxu/(1+exu);
                 adaoxu=(kdaodaoxu-2*aaaxu)/(1+exu);
                 bdaoxu=aaaxu*lidaoxu+kxu*lidaodaoxu/(1+exu);
```

```
                fdao(i,i)=(dt*rc)/(rw*da)*(adao(i)*(e(i)-
exu)+aaa(i))+dt/(rw*da*da)*(bdao(i)*(e(i)-exu)+bbb(i)-
bbbxu)+dt/(rw*da*da)*(bdao(i)*(e(i+1)-2*e(i)+exu)-2*bbb(i))+1;
                fdao(i,i+1)=dt/(rw*da*da)*bbb(i);
            for i=2:n-1
                li(i)=(e(i)/a1)^(1/b1);
                lidao(i)=(e(i)/a1)^((1-b1)/b1)/(a1*b1);
                lidaodao(i)=(1-b1)*(e(i)/a1)^((1-2*b1)/b1)/(a1^2*b1^2)   ;
                k(i)=c1*e(i)^d1;
                kdao(i)=c1*d1*e(i)^(d1-1);
                kdaodao(i)=c1*d1*(d1-1)*e(i)^(d1-2);
                aaa(i)=(kdao(i)-k(i)/(1+e(i)))/(1+e(i));
                bbb(i)=k(i)*lidao(i)/(1+e(i));
                adao(i)=(kdaodao(i)-2*aaa(i))/(1+e(i));
                bdao(i)=aaa(i)*lidao(i)+k(i)*lidaodao(i)/(1+e(i));
                fdao(i,i)=(dt*rc)/(rw*da)*(adao(i)*(e(i)-e(i-
1))+aaa(i))+dt/(rw*da*da)*(bdao(i)*(e(i)-e(i-1))+bbb(i)-bbb(i-
1))+dt/(rw*da*da)*(bdao(i)*(e(i+1)-2*e(i)+e(i-1))-2*bbb(i))+1;
                fdao(i,i-1)=-(dt*rc)/(rw*da)*aaa(i)+dt/(rw*da*da)*(-bdao(i-1)*(e(i)-e(i-1))-
bbb(i)+bbb(i-1))+dt/(rw*da*da)*bbb(i);
                fdao(i,i+1)=dt/(rw*da*da)*bbb(i);
            end
            i=n;
                li(i)=(e(i)/a1)^(1/b1);
                lidao(i)=(e(i)/a1)^((1-b1)/b1)/(a1*b1);
                lidaodao(i)=(1-b1)*(e(i)/a1)^((1-2*b1)/b1)/(a1^2*b1^2)   ;
                k(i)=c1*e(i)^d1;
                kdao(i)=c1*d1*e(i)^(d1-1);
                kdaodao(i)=c1*d1*(d1-1)*e(i)^(d1-2);
                aaa(i)=(kdao(i)-k(i)/(1+e(i)))/(1+e(i));
                bbb(i)=k(i)*lidao(i)/(1+e(i));
                adao(i)=(kdaodao(i)-2*aaa(i))/(1+e(i));
                bdao(i)=aaa(i)*lidao(i)+k(i)*lidaodao(i)/(1+e(i));
                fdao(i,i)=1;
            %%%%%%%%%%%%%%%%%%%%%%%%%%%%
            i=1;
            f(i)=(dt*rc)/(rw*da)*aaa(i)*(e(i)-exu)+dt/(rw*da*da)*(bbb(i)-bbbxu)*(e(i)-
exu)+dt/(rw*da*da)*bbb(i)*(e(i+1)-2*e(i)+exu)+e(i)-ebefore(i);
            for i=2:n-1
                f(i)=(dt*rc)/(rw*da)*aaa(i)*(e(i)-e(i-1))+dt/(rw*da*da)*(bbb(i)-bbb(i-1))*(e(i)-
e(i-1))+dt/(rw*da*da)*bbb(i)*(e(i+1)-2*e(i)+e(i-1))+e(i)-ebefore(i);
            end
            f(n)=e(n)-eding;
            %%%%%%%%%%%%%%%%%%%%%%%%%%%%
            keci=fdao\(-f);
            e=e+keci;
        end
        %%%%%%%%%%%%%%%%%%%%%%%%%%%%%%%%%%%%%%%%%%%%
        ebefore=e;
    houhou(1)=0;houdu=0;p(n)=0;
```

```
    for i=2:n
          ddaa=((e(i)+e(i-1))/2+1)*da;
          houhou(i)=houhou(i-1)+ddaa;
          houdu=houdu+ddaa;
    end
      for i=n-1:-1:1
           p(i)=p(i+1)-da*(rw-rs-(li(i+1)-li(i))/da);
      end
    %%%%%%%%%%%%%%%%%
    if mod(j,jilujiange)==0
      houdujilu(j/jilujiange)=houdu;
      tt(j/jilujiange)=dt*j;
      pjilu(:,j/jilujiange)=p;
      ejilu(:,j/jilujiange)=e;
      houhoujilu(:,j/jilujiange)=houhou;
    end
    %%%%%%%%%%%%%%%%%
end
%%%%%%%%%%%%%%%%%
figure(1)
plot(ejilu,houhoujilu)
title('e--height')
xlabel('e')
ylabel('height(m)')
figure(2)
plot(pjilu,houhoujilu)
title('overpressure--height')
xlabel('overpressure(kpa)')
ylabel('height(m)')
figure(3)
plot(tt,houdujilu)
title('t--height')
xlabel('t(day)')
ylabel('height(m)')
r1(:,1)=tt';
r1(:,2)=houdujilu';
 xlswrite('time-height',r1)
 xlswrite('overpressure',pjilu)
 xlswrite('void ratio',ejilu)
 xlswrite('height',houhoujilu)
```

(4) Output results:

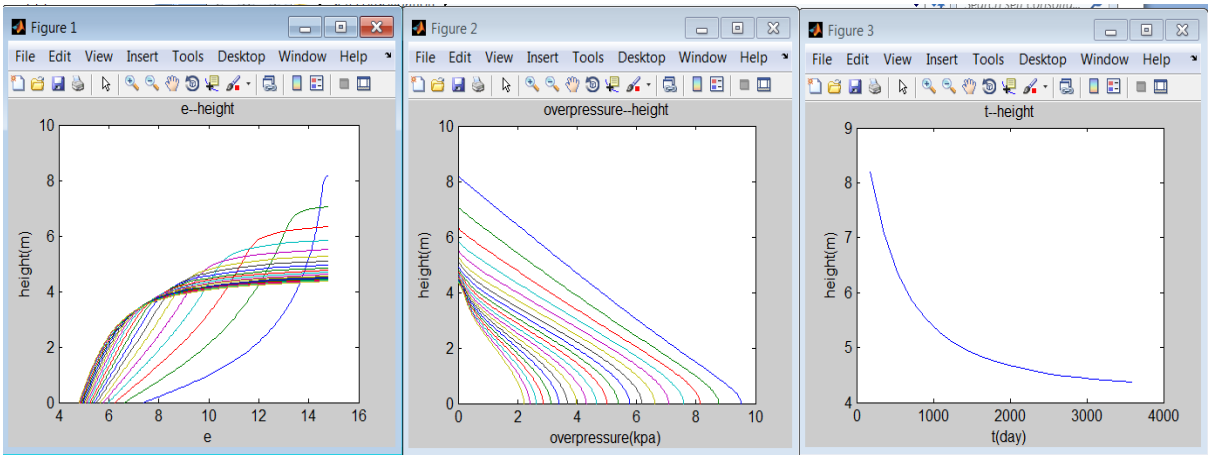

Figure A.1

From left to right 'void ratio-height', 'overpressure-height', 'height-time' profiles change with time.

If the user want get the corresponding data, the data are available in excel file.

'time-height.xls' provides the time and correspond height data.

'overpressure.xls' provides the overpressure data in the corresponding time.

'void ratio.xls' provides the void ratio data in the corresponding time.

'height.xls' provides the height data in the corresponding time.

Appendix A.2: Sedimentation and self-consolidation (Townsend's scenario B)

(1) Input data:

14.8

initial e

10

main steps in the total sediment process

7.2 100

h0=7.2 height increase in each main step ;n=100;

360 10

step time=360; steps in one step=10

10.0450 27.6360

rw=1.025*9.8;rs=2.82*9.8;

7.72 -0.22

a=7.72;b=-0.22;

0.2532e-6 4.65

c=0.2532*10^(-6);d=4.65;

(2) Input instruction:

14.8

Initial void ratio of sedimentation material: e0=14.8

10

Integration is used in sedimentation simulation, sedimentation is divided in many main steps in the total sediment process

7.2 100

Increase height in each main step =7.2; Even distribution nodes in the calculation , number of nodes=100;

360 10

Consolidation time=360(day) ; calculation time steps=100

10.0450 27.6360

unit weight of water rw=1.025×9.8; unit weight of water rs=2.82×9.8;

7.72 -0.22

Void ratio-effective stress relationship: e=a1σb1 a1=7.72;b1=-0.22;

0.2532e-6 4.65

Void ratio-conductivity relationship: $k=c1e^{d1}$ c1=0.2532E-6;d1=4.65;

(3) Calculation code:

```
clear;clc
fid=fopen('data.txt','r+');
a=[];
b=[];
while ~feof(fid)
      str=fgetl(fid);
      if numel(str)~=0
        if (double(str(1))>=48&&double(str(1))<=57)
          a=strread(str,'%f','delimiter',',');
          disp(a');
          b=[b;a]
        end
      end
end

e0=b(1);
duanshu=b(2) ;
h0=b(3);n=b(4);
T=b(5);bushu=b(6)
rw=b(7);rs=b(8);
a1=b(9);b1=b(10);
c1=b(11);d1=b(12);
%%%%%%%%%%%%%%%%%%%%%%%%%%%%%%%%%%%%
a0=h0/(1+e0);
da=a0/(n-1);
dt=T/bushu;
rc=rs-rw;
m=bushu;
e=e0*ones(n,1);
nn=n;
ejilu=zeros(n*duanshu,duanshu)
pjilu=zeros(n*duanshu,duanshu)
houhoujilu=zeros(n*duanshu,duanshu)
%%%%%%%%%%%%%%%%%%%%%%%%%%%%%%%%%%%%
for jj=1:duanshu
  if jj>1
     e=[e;e0*ones(nn,1)];
  end
  n=max(size(e)) ;
  f=zeros(n,1);
  fdao=zeros(n,n);
  ebefore=e;
 %%%%%%%%%%%%%%%%%%%%%%%%%%%%%%%%%%%%
```

```
  for j=1:m  %shi jian bushu
  %%%%%%%%%%%%%%%%%%%%%%%%%%%%%%%%%%%%%%%%%%%%%%%%%%
      keci=0.1*ones(n,1);
      e=ebefore;
      while max(abs(keci))>0.01
            %%%%%%%%%%%%%%%%%%%%%%%%%%%%%%%%%%%%%%%%%%%%%
                 i=1;
                 li(i)=(e(i)/a1)^(1/b1);
                 lidao(i)=(e(i)/a1)^((1-b1)/b1)/(a1*b1);
                 lidaodao(i)=(1-b1)*(e(i)/a1)^((1-2*b1)/b1)/(a1^2*b1^2)   ;

                 k(i)=c1*e(i)^d1;
                 kdao(i)=c1*d1*e(i)^(d1-1);
                 kdaodao(i)=c1*d1*(d1-1)*e(i)^(d1-2);
                 aaa(i)=(kdao(i)-k(i)/(1+e(i)))/(1+e(i));
                 bbb(i)=k(i)*lidao(i)/(1+e(i));
                 adao(i)=(kdaodao(i)-2*aaa(i))/(1+e(i));
                 bdao(i)=aaa(i)*lidao(i)+k(i)*lidaodao(i)/(1+e(i));
                 exu=e(i+1)+2*da*(rs-rw)/lidao(i);
                 lixu=(exu/a1)^(1/b1);
                 lidaoxu=(exu/a1)^((1-b1)/b1)/(a1*b1);
                 lidaodaoxu=(1-b1)*(exu/a1)^((1-2*b1)/b1)/(a1^2*b1^2)   ;
                 kxu=c1*exu^d1;
                 kdaoxu=c1*d1*exu^(d1-1);
                 kdaodaoxu=c1*d1*(d1-1)*exu^(d1-2);
                 aaaxu=(kdaoxu-kxu/(1+exu))/(1+exu);
                 bbbxu=kxu*lidaoxu/(1+exu);
                 adaoxu=(kdaodaoxu-2*aaaxu)/(1+exu);
                 bdaoxu=aaaxu*lidaoxu+kxu*lidaodaoxu/(1+exu);
                 fdao(i,i)=(dt*rc)/(rw*da)*(adao(i)*(e(i)-
exu)+aaa(i))+dt/(rw*da*da)*(bdao(i)*(e(i)-exu)+bbb(i)-
bbbxu)+dt/(rw*da*da)*(bdao(i)*(e(i+1)-2*e(i)+exu)-2*bbb(i))+1;
                fdao(i,i+1)=dt/(rw*da*da)*bbb(i);
            for i=2:n-1
                 li(i)=(e(i)/a1)^(1/b1);
                 lidao(i)=(e(i)/a1)^((1-b1)/b1)/(a1*b1);
                 lidaodao(i)=(1-b1)*(e(i)/a1)^((1-2*b1)/b1)/(a1^2*b1^2)   ;
                 k(i)=c1*e(i)^d1;
                 kdao(i)=c1*d1*e(i)^(d1-1);
                 kdaodao(i)=c1*d1*(d1-1)*e(i)^(d1-2);
                 aaa(i)=(kdao(i)-k(i)/(1+e(i)))/(1+e(i));
                 bbb(i)=k(i)*lidao(i)/(1+e(i));
                 adao(i)=(kdaodao(i)-2*aaa(i))/(1+e(i));
                 bdao(i)=aaa(i)*lidao(i)+k(i)*lidaodao(i)/(1+e(i));
                fdao(i,i)=(dt*rc)/(rw*da)*(adao(i)*(e(i)-e(i-
1))+aaa(i))+dt/(rw*da*da)*(bdao(i)*(e(i)-e(i-1))+bbb(i)-bbb(i-
1))+dt/(rw*da*da)*(bdao(i)*(e(i+1)-2*e(i)+e(i-1))-2*bbb(i))+1;
                fdao(i,i-1)=-(dt*rc)/(rw*da)*aaa(i)+dt/(rw*da*da)*(-bdao(i-1)*(e(i)-e(i-1))-
bbb(i)+bbb(i-1))+dt/(rw*da*da)*bbb(i);
                fdao(i,i+1)=dt/(rw*da*da)*bbb(i);
```

```
            end
            i=n;
                  li(i)=(e(i)/a1)^(1/b1);
                  lidao(i)=(e(i)/a1)^((1-b1)/b1)/(a1*b1);
                  lidaodao(i)=(1-b1)*(e(i)/a1)^((1-2*b1)/b1)/(a1^2*b1^2)   ;
                  k(i)=c1*e(i)^d1;
                  kdao(i)=c1*d1*e(i)^(d1-1);
                  kdaodao(i)=c1*d1*(d1-1)*e(i)^(d1-2);
                  aaa(i)=(kdao(i)-k(i)/(1+e(i)))/(1+e(i));
                  bbb(i)=k(i)*lidao(i)/(1+e(i));
                  adao(i)=(kdaodao(i)-2*aaa(i))/(1+e(i));
                  bdao(i)=aaa(i)*lidao(i)+k(i)*lidaodao(i)/(1+e(i));
                  fdao(i,i)=1;
            %%%%%%%%%%%%%%%%%%%%%%%%%%%%%%%
            i=1;
            f(i)=(dt*rc)/(rw*da)*aaa(i)*(e(i)-exu)+dt/(rw*da*da)*(bbb(i)-bbbxu)*(e(i)-
exu)+dt/(rw*da*da)*bbb(i)*(e(i+1)-2*e(i)+exu)+e(i)-ebefore(i);
            for i=2:n-1
                f(i)=(dt*rc)/(rw*da)*aaa(i)*(e(i)-e(i-1))+dt/(rw*da*da)*(bbb(i)-bbb(i-1))*(e(i)-
e(i-1))+dt/(rw*da*da)*bbb(i)*(e(i+1)-2*e(i)+e(i-1))+e(i)-ebefore(i);
            end
            f(n)=e(n)-e0;
            %%%%%%%%%%%%%%%%%%%%%%%%%%%%%%%
            keci=fdao\(-f);
            e=e+keci;
      end
  %%%%%%%%%%%%%%%%%%%%%%%%%%%%%%%%%%%%%%
      ebefore=e;
  end
   %%%%%%%%%%%%%%%%
   houhou(1)=0;houdu=0;p(n)=0;
   for i=2:n
         ddaa=((e(i)+e(i-1))/2+1)*da;
         houhou(i)=houhou(i-1)+ddaa;
         houdu=houdu+ddaa;
   end
   %%%%%%%%%%%%%%%%%%%%%%%%%%%%%
   li(n)=(e0/a1)^(1/b1);
   for i=n-1:-1:1
       p(i)=p(i+1)-da*(rw-rs-(li(i+1)-li(i))/da);
   end
       %%%%%%%%%%%%%%%%
      houdujilu(jj)=houdu;
      tt(jj)=T*jj;
   for uuu=1:jj*nn
       ejilu(uuu,jj)=e(uuu);
       pjilu(uuu,jj)=p(uuu);
       houhoujilu(uuu,jj)=houhou(uuu);
  end
   %%%%%%%%%%%%%%%%
```

```
end
%%%%%%%%%%%%%%%%%%sh%%%%%%%%%%%%%%%%%%%%%%%%%%%%
figure(1)
plot(ejilu(:,duanshu),houhoujilu(:,duanshu))
title('e--height')
xlabel('e')
ylabel('height(m)')
figure(2)
plot(pjilu,houhoujilu)
title('overpressure--height')
xlabel('pressure(kpa)')
ylabel('height(m)')
figure(3)
plot(tt,houdujilu)
title('time--height')
xlabel('t(day)')
ylabel('height(m)')
  r1(:,1)=tt';
  r1(:,2)=houdujilu';
 xlswrite('time-height',r1)
 xlswrite('overpressure',pjilu)
 xlswrite('void ratio',ejilu)
 xlswrite('height',houhoujilu)
```

(4) Output results:

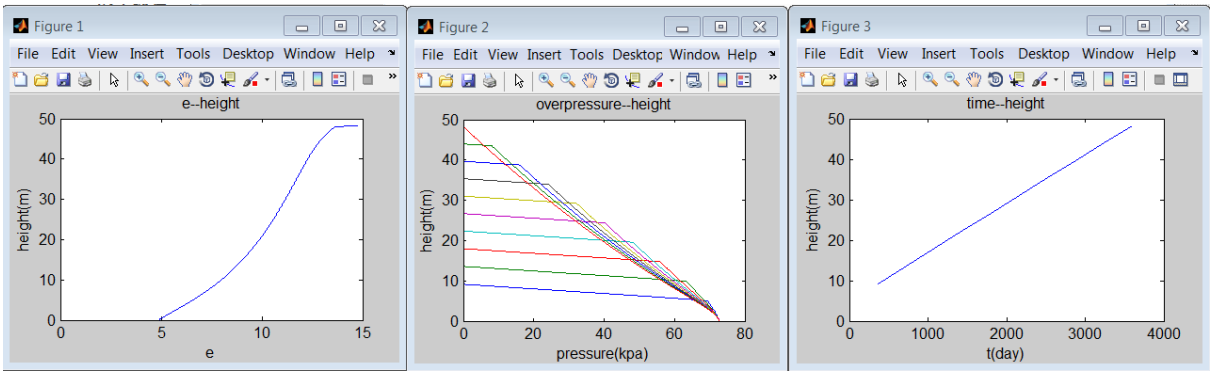

Figure A.2

From left to right 'void ratio-height' at the end, and 'overpressure-height', 'height-time' profiles change with time.

If the user want get the corresponding data, the data are available in excel file.

'time-height.xls' provides the time and correspond height data.

'overpressure.xls' provides the overpressure data in the corresponding time.

'void ratio.xls' provides the void ratio data in the corresponding time.

'height.xls' provides the height data in the corresponding time.

Appendix A.3: Force consolidation (Townsend's scenario C)

(1) Input data:

14.8

e0=14.8

9.4815

up load (kpa)=9.4815

7.2 100

height=7.2;nodes=100;

3600 100

Time=360;time steps=10 (>5)

10.0450 27.6360

rw=1.025*9.8;rs=2.82*9.8;

7.72 -0.22

a1=7.72;b1=-0.22; e=a1*stress^b1

0.2532e-6 4.65

c1=0.2532*10^(-6);d1=4.65; k=c1*e^d1

20

record step

(2) Input instruction:

14.8

Initial void ratio: e0=14.8

9.4815

up load: 9.4815(kpa)

7.2 100

Initial height=7.2; Even distribution nodes in the calculation , number of nodes=100;

3600 100

Consolidation time=360(day) ; calculation time steps=100

10.0450 27.6360

unit weight of water rw=1.025×9.8; unit weight of water rs=2.82×9.8;

7.72 -0.22

Void ratio-effective stress relationship: e=a1σb1 a1=7.72;b1=-0.22;

0.2532e-6 4.65

Void ratio-conductivity relationship: k=c1ed1 c1=0.2532E-6;d1=4.65;

20

Record steps for output.

(3) Calculation code:

```
clear;clc
%%%%%%%%%%% read file %%%%%%%%%%%%%%%%%%%%%%%%
fid=fopen('data.txt','r+');
a=[];
b=[];
while ~feof(fid)
      str=fgetl(fid);
      if numel(str)~=0
        if (double(str(1))>=48&&double(str(1))<=57)
          a=strread(str,'%f','delimiter',',');
          disp(a');
          b=[b;a]
        end
      end
end
e0=b(1);
pding=b(2) ;
```

```
h0=b(3);n=b(4);
T=b(5);bushu=b(6)
rw=b(7);rs=b(8);
a1=b(9);b1=b(10);
c1=b(11);d1=b(12);
rstep=b(13);
%%%%%%%%%%%%%%%%%%%%%%%%%%%%%%%%%%
rc=rs-rw;
houdu=0;
a0=h0/(1+e0);
da=a0/(n-1);
dt=T/bushu;
eding=a1*(pding)^b1
m=bushu;
e=zeros(n,1);
p=zeros(n,1);
houhou=zeros(n,1);
aaa=zeros(n,1);
f=zeros(n,1);
fdao=zeros(n,n);
for i=1:n
     e(i)=e0;
end
ebefore=e0*ones(n,1);
ebefore(n)=eding
jilujiange=m/rstep;
%%%%%%%%%%%%%%%%%%%%%%%%%%%%%%%%%%%%%%%%%%%%%%%
for j=1:m  %shi jian bushu
      %%%%%%%%%%%%%%%%%%%%%%%%%%%%%%%%%%%%%%%%%%%%%
      keci=0.1*ones(n,1);
      ebefore(n)=eding;
      dde=ebefore(n)-ebefore(n-6);
    for i=n-5:n-1
       ebefore(i)=ebefore(i-1)+dde/6;
    end
      e=ebefore;
      while max(abs(keci))>0.001
%%%%%%%%%%%%%%%%%%%%%%%%%%%%%%%%%%%%%%%%
                   i=1;
                   li(i)=(e(i)/a1)^(1/b1);
                   lidao(i)=(e(i)/a1)^((1-b1)/b1)/(a1*b1);
                   lidaodao(i)=(1-b1)*(e(i)/a1)^((1-2*b1)/b1)/(a1^2*b1^2)   ;
                   k(i)=c1*e(i)^d1;
                   kdao(i)=c1*d1*e(i)^(d1-1);
                   kdaodao(i)=c1*d1*(d1-1)*e(i)^(d1-2);
                   aaa(i)=(kdao(i)-k(i)/(1+e(i)))/(1+e(i));
                   bbb(i)=k(i)*lidao(i)/(1+e(i));
                   adao(i)=(kdaodao(i)-2*aaa(i))/(1+e(i));
                   bdao(i)=aaa(i)*lidao(i)+k(i)*lidaodao(i)/(1+e(i));
                   exu=e(i+1)+2*da*(rs-rw)/lidao(i);
```

```
            lixu=(exu/a1)^(1/b1);
            lidaoxu=(exu/a1)^((1-b1)/b1)/(a1*b1);
            lidaodaoxu=(1-b1)*(exu/a1)^((1-2*b1)/b1)/(a1^2*b1^2)   ;
            kxu=c1*exu^d1;
            kdaoxu=c1*d1*exu^(d1-1);
            kdaodaoxu=c1*d1*(d1-1)*exu^(d1-2);
            aaaxu=(kdaoxu-kxu/(1+exu))/(1+exu);
            bbbxu=kxu*lidaoxu/(1+exu);
            adaoxu=(kdaodaoxu-2*aaaxu)/(1+exu);
            bdaoxu=aaaxu*lidaoxu+kxu*lidaodaoxu/(1+exu);
            fdao(i,i)=(dt*rc)/(rw*da)*(adao(i)*(e(i)-
exu)+aaa(i))+dt/(rw*da*da)*(bdao(i)*(e(i)-exu)+bbb(i)-
bbbxu)+dt/(rw*da*da)*(bdao(i)*(e(i+1)-2*e(i)+exu)-2*bbb(i))+1;
           fdao(i,i+1)=dt/(rw*da*da)*bbb(i);
        for i=2:n-1
            li(i)=(e(i)/a1)^(1/b1);
            lidao(i)=(e(i)/a1)^((1-b1)/b1)/(a1*b1);
            lidaodao(i)=(1-b1)*(e(i)/a1)^((1-2*b1)/b1)/(a1^2*b1^2)   ;
            k(i)=c1*e(i)^d1;
            kdao(i)=c1*d1*e(i)^(d1-1);
            kdaodao(i)=c1*d1*(d1-1)*e(i)^(d1-2);
            aaa(i)=(kdao(i)-k(i)/(1+e(i)))/(1+e(i));
            bbb(i)=k(i)*lidao(i)/(1+e(i));
            adao(i)=(kdaodao(i)-2*aaa(i))/(1+e(i));
            bdao(i)=aaa(i)*lidao(i)+k(i)*lidaodao(i)/(1+e(i));
           fdao(i,i)=(dt*rc)/(rw*da)*(adao(i)*(e(i)-e(i-
1))+aaa(i))+dt/(rw*da*da)*(bdao(i)*(e(i)-e(i-1))+bbb(i)-bbb(i-
1))+dt/(rw*da*da)*(bdao(i)*(e(i+1)-2*e(i)+e(i-1))-2*bbb(i))+1;
           fdao(i,i-1)=-(dt*rc)/(rw*da)*aaa(i)+dt/(rw*da*da)*(-bdao(i-1)*(e(i)-e(i-1))-
bbb(i)+bbb(i-1))+dt/(rw*da*da)*bbb(i);
           fdao(i,i+1)=dt/(rw*da*da)*bbb(i);
        end
        i=n;
            li(i)=(e(i)/a1)^(1/b1);
            lidao(i)=(e(i)/a1)^((1-b1)/b1)/(a1*b1);
            lidaodao(i)=(1-b1)*(e(i)/a1)^((1-2*b1)/b1)/(a1^2*b1^2)   ;
            k(i)=c1*e(i)^d1;
            kdao(i)=c1*d1*e(i)^(d1-1);
            kdaodao(i)=c1*d1*(d1-1)*e(i)^(d1-2);
            aaa(i)=(kdao(i)-k(i)/(1+e(i)))/(1+e(i));
            bbb(i)=k(i)*lidao(i)/(1+e(i));
            adao(i)=(kdaodao(i)-2*aaa(i))/(1+e(i));
            bdao(i)=aaa(i)*lidao(i)+k(i)*lidaodao(i)/(1+e(i));
            fdao(i,i)=1;
%%%%%%%%%%%%%%%%%%%%%%%%%%%%%%%%%%%%%%%%%%%%%%%
        i=1;
        f(i)=(dt*rc)/(rw*da)*aaa(i)*(e(i)-exu)+dt/(rw*da*da)*(bbb(i)-bbbxu)*(e(i)-
exu)+dt/(rw*da*da)*bbb(i)*(e(i+1)-2*e(i)+exu)+e(i)-ebefore(i);
        for i=2:n-1
```

```
                f(i)=(dt*rc)/(rw*da)*aaa(i)*(e(i)-e(i-1))+dt/(rw*da*da)*(bbb(i)-bbb(i-1))*(e(i)-
e(i-1))+dt/(rw*da*da)*bbb(i)*(e(i+1)-2*e(i)+e(i-1))+e(i)-ebefore(i);
            end
            f(n)=e(n)-eding;
            %%%%%%%%%%%%%%%%%%%%%%%%%%%%%%%%%%%%%%%%%%%%
            keci=fdao\(-f);
            e=e+keci;
      end
%%%%%%%%%%%%%%%%%%%%%%%%%%%%%%%%%%%%%%%%%%%%%%%%%%%%
      ebefore=e;
   houhou(1)=0;houdu=0;p(n)=0;
   for i=2:n
         ddaa=((e(i)+e(i-1))/2+1)*da;
         houhou(i)=houhou(i-1)+ddaa;
         houdu=houdu+ddaa;
   end
      for i=n-1:-1:1
          p(i)=p(i+1)-da*(rw-rs-(li(i+1)-li(i))/da);
      end
   %%%%%%%%%%%%%%%%%%%%
   if mod(j,jilujiange)==0
      houdujilu(j/jilujiange)=houdu;
      tt(j/jilujiange)=dt*j;
      pjilu(:,j/jilujiange)=p;
      ejilu(:,j/jilujiange)=e;
      houhoujilu(:,j/jilujiange)=houhou;
   end
   %%%%%%%%%%%%%%%%%%%%
end
%%%%%%%%%%%%%%%%%%%%%%%%%%%%%%%%%%%%%%%%%%%%%%%%%%%%
figure(1)
plot(ejilu,houhoujilu)
title('e--height')
xlabel('e')
ylabel('height(m)')
figure(2)
plot(pjilu,houhoujilu)
title('overpressure--height')
xlabel('overpressure(kpa)')
ylabel('height(m)')
figure(3)
plot(tt,houdujilu)
title('t--height')
xlabel('t(day)')
ylabel('height(m)')
r1(:,1)=tt';
r1(:,2)=houdujilu';
 xlswrite('time-height',r1)
 xlswrite('overpressure',pjilu)
 xlswrite('void ratio',ejilu)
```

xlswrite('height',houhoujilu)

(4) Output results:

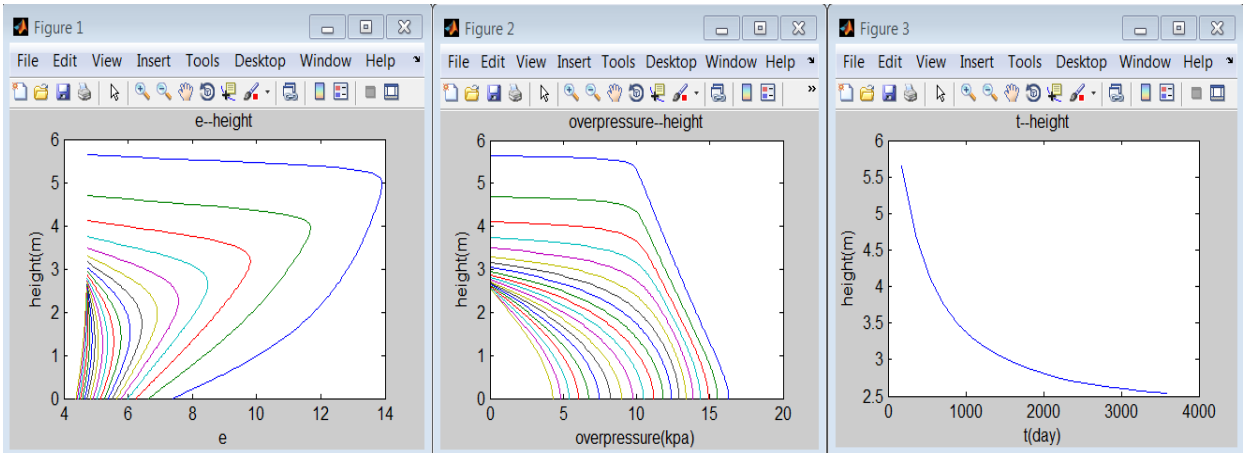

Figure A.3

From left to right 'void ratio-height', 'overpressure-height', 'height-time' profiles change with time.

If the user want get the corresponding data, the data are available in excel file.

'time-height.xls' provides the time and correspond height data.

'overpressure.xls' provides the overpressure data in the corresponding time.

'void ratio.xls' provides the void ratio data in the corresponding time.

'height.xls' provides the height data in the corresponding time.

Appendix A.4: Muti-layer self-consolidation (Townsend's scenario D)

(1) Input data:

4

layer number

9.4815

up load kpa

360 1000

Appendix

Total time=360; time steps=1000

10.0450 27.6360

rw=1.025*9.8;rs=2.82*9.8;

300

nodes numver=100;

2 2 2 2

no1.layer thickness no2.layer thickness.....

7.72 7.72 7.72 7.72

no1.layer a ;no2.layer a.....

-0.22 -0.22 -0.22 -0.22

no1.layer b ;no2.layer b.....

0.2532e-6 0.2532e-6 0.2532e-6 0.2532e-6

no1.layer c ;no2.layer c.....

4.65 4.65 4.65 4.65

no1.layer d ;no2.layer d.....

8 14.8 10 14.8

no1.initial e ;no2.initial e .....

20

record step

(2) Input instruction:

4

layer number

9.4815

Appendix

up load kpa

360 1000

Consolidation time=360(day) ; calculation time steps=100

10.0450 27.6360

unit weight of water rw=1.025×9.8; unit weight of water rs=2.82×9.8;

300

number of nodes=300;

2 2 2 2

no1.layer thickness(m) , no2.layer thickness(m).....

7.72 7.72 7.72 7.72

e=a1σb1 , no1.layer a1 ;no2.layer a1.....

-0.22 -0.22 -0.22 -0.22

e=a1σb1 a1=7.72 no1.layer b1 ;no2.layer b1.....

0.2532e-6 0.2532e-6 0.2532e-6 0.2532e-6

k=c1ed1 no1.layer c1 ;no2.layer c1.....

4.65 4.65 4.65 4.65

k=c1ed1 no1.layer d1 ;no2.layer d1.....

8 14.8 10 14.8

no1.initial void ratio e0 ;no2.initial void ratio e0 .....

20

Record steps for output.

(3) Calculation code:

```
clc;clear
fid=fopen('data.txt','r+');
a=[];
ru=[];
while ~feof(fid)
      str=fgetl(fid);
      if numel(str)~=0
        if (double(str(1))>=48&&double(str(1))<=57)
          a=strread(str,'%f','delimiter',',');
          disp(a');
          ru=[ru;a]
        end
        if double(str(1))==45
          a=strread(str,'%f','delimiter',',');
          disp(a');
          ru=[ru;a]
        end
      end
end
cengshu=ru(1);
liding=ru(2) ;
T=ru(3);bushu=ru(4)
rw=ru(5);rs=ru(6);
n=ru(7);
h=ru(8:7+cengshu);
a=ru(7+cengshu+1:7+2*cengshu);
b=ru(7+2*cengshu+1:7+3*cengshu);
c=ru(7+3*cengshu+1:7+4*cengshu);
d=ru(7+4*cengshu+1:7+5*cengshu);
ee=ru(7+5*cengshu+1:7+6*cengshu);
rstep=ru(8+6*cengshu);
%%%%%%%%%%%%%%%%%%%%%%%%%%%%%%%%%%%%%%%%%%%%
for i=1:cengshu
    guhou(i)=h(i)/ee(i)
end
zongguhou=sum(guhou(1:cengshu))
for i=1:cengshu-1
    pp(i)=round( n*sum(guhou(1:i))/zongguhou )
end
pp=[2,pp,n-1]
eding=a(cengshu)*liding^b(cengshu)
da=zongguhou/(n-1);
dt=T/bushu;
m=bushu;
rc=rs-rw;
e=zeros(n,1);
p=zeros(n,1);
e(1)=ee(1);
```

```
for ii=1:cengshu
    for i=pp(ii):pp(ii+1)
        e(i)=ee(ii);
    end
end
e(n)=eding;
houhou=zeros(n,1);
f=zeros(n,1);
fdao=zeros(n,n);
ebefore=e;
ejilu=zeros(n,m);
pjilu=zeros(n,m);
%%%%%%%%%%%%%%%%%%%%%%%%%%%%%%%%%%%%%%%%%%%%%
for j=1:m+1
%%%%%%%%%%%%%%%%%%%%%%%%%%%%%%%%%%%%%%%%%%%
      keci=0.1*ones(n,1);
      e=ebefore;
      while max(abs(keci))>0.01
            %%%%%%%%%%%%%%%%%%%%%%%%%%%%%%%%%%
                  li(i)=(e(i)/a(1))^(1/b(1));
                  lidao(i)=(e(i)/a(1))^((1-b(1))/b(1))/(a(1)*b(1));
                  lidaodao(i)=(1-b(1))*(e(i)/a(1))^((1-2*b(1))/b(1))/(a(1)^2*b(1)^2)   ;
                  k(i)=c(1)*e(i)^d(1);
                  kdao(i)=c(1)*d(1)*e(i)^(d(1)-1);
                  kdaodao(i)=c(1)*d(1)*(d(1)-1)*e(i)^(d(1)-2);
                  aaa(i)=(kdao(i)-k(i)/(1+e(i)))/(1+e(i));
                  bbb(i)=k(i)*lidao(i)/(1+e(i));
                  adao(i)=(kdaodao(i)-2*aaa(i))/(1+e(i));
                  bdao(i)=aaa(i)*lidao(i)+k(i)*lidaodao(i)/(1+e(i));
                      %%%%%%%%%%%%%%
                  exu=e(2)+2*da*(rs-rw)/lidao(i);
                  lixu=(exu/a(1))^(1/b(1));
                  lidaoxu=(exu/a(1))^((1-b(1))/b(1))/(a(1)*b(1));
                  lidaodaoxu=(1-b(1))*(exu/a(1))^((1-2*b(1))/b(1))/(a(1)^2*b(1)^2)   ;
                  kxu=c(1)*exu^d(1);
                  kdaoxu=c(1)*d(1)*exu^(d(1)-1);
                  kdaodaoxu=c(1)*d(1)*(d(1)-1)*exu^(d(1)-2);
                  aaaxu=(kdaoxu-kxu/(1+exu))/(1+exu);
                  bbbxu=kxu*lidaoxu/(1+exu);
                  adaoxu=(kdaodaoxu-2*aaaxu)/(1+exu);
                  bdaoxu=aaaxu*lidaoxu+kxu*lidaodaoxu/(1+exu);
                 fdao(i,i)=(dt*rc)/(rw*da)*(adao(i)*(e(i)-
exu)+aaa(i))+dt/(rw*da*da)*(bdao(i)*(e(i)-exu)+bbb(i)-
bbbxu)+dt/(rw*da*da)*(bdao(i)*(e(i+1)-2*e(i)+exu)-2*bbb(i))+1;
                 fdao(i,i+1)=dt/(rw*da*da)*bbb(i);
            for ii=1:cengshu
                for i=pp(ii):pp(ii+1)
                  li(i)=(e(i)/a(ii))^(1/b(ii));
                  lidao(i)=(e(i)/a(ii))^((1-b(ii))/b(ii))/(a(ii)*b(ii));
                  lidaodao(i)=(1-b(ii))*(e(i)/a(ii))^((1-2*b(ii))/b(ii))/(a(ii)^2*b(ii)^2)   ;
```

```
                k(i)=c(ii)*e(i)^d(ii);
                kdao(i)=c(ii)*d(ii)*e(i)^(d(ii)-1);
                kdaodao(i)=c(ii)*d(ii)*(d(ii)-1)*e(i)^(d(ii)-2);
                aaa(i)=(kdao(i)-k(i)/(1+e(i)))/(1+e(i));
                bbb(i)=k(i)*lidao(i)/(1+e(i));
                adao(i)=(kdaodao(i)-2*aaa(i))/(1+e(i));
                bdao(i)=aaa(i)*lidao(i)+k(i)*lidaodao(i)/(1+e(i));
               fdao(i,i)=(dt*rc)/(rw*da)*(adao(i)*(e(i)-e(i-
1))+aaa(i))+dt/(rw*da*da)*(bdao(i)*(e(i)-e(i-1))+bbb(i)-bbb(i-
1))+dt/(rw*da*da)*(bdao(i)*(e(i+1)-2*e(i)+e(i-1))-2*bbb(i))+1;
                fdao(i,i-1)=-(dt*rc)/(rw*da)*aaa(i)+dt/(rw*da*da)*(-bdao(i-1)*(e(i)-e(i-1))-
bbb(i)+bbb(i-1))+dt/(rw*da*da)*bbb(i);
                fdao(i,i+1)=dt/(rw*da*da)*bbb(i);
              end
            end
  %%%%%%%%%%%%%%%%%%%%%%%%%%%%%%%%%%%%%%%%%%%%%%%%%%%%%%%%%%%%%%%%
            i=n;
                 fdao(i,i-1)=0;
                 fdao(i,i)=1;
  %%%%%%%%%%%%%%%%%%%%%%%%%%%%%%%%%%%%%%%%%%%%%%%%%%%%%%%%%%%%%%%%
     for ii=1:cengshu-1
            i=pp(ii+1) ;
                 lizhong=((rw-rs)*da*(k(i-1)/(1+e(i-1))-k(i)/(1+e(i)))+k(i-1)/(1+e(i-1))*li(i-
1)+k(i)/(1+e(i))*li(i))/(k(i-1)/(1+e(i-1))+k(i)/(1+e(i)));
                 lizhongcun(ii)=lizhong;
                 ezhongdown=a(ii)*(lizhong)^b(ii);
                 elidaodown=a(ii)*b(ii)*(lizhong)^(b(ii)-1);
                 ezhongup=a(ii+1)*(lizhong)^b(ii+1);
                 elidaoup=a(ii+1)*b(ii+1)*(lizhong)^(b(ii+1)-1);
                 lizhongup=lizhong;
                 lidaozhongup=(ezhongup/a(ii+1))^((1-b(ii+1))/b(ii+1))/(a(ii+1)*b(ii+1));
                 lidaodaozhongup=(1-b(ii+1))*(ezhongup/a(ii+1))^((1-
2*b(ii+1))/b(ii+1))/(a(ii+1)^2*b(ii+1)^2)   ;
                 kzhongup=c(ii+1)*ezhongup^d(ii+1);
                 kdaozhongup=c(ii+1)*d(ii+1)*ezhongup^(d(ii+1)-1);
                 kdaodaozhongup=c(ii+1)*d(ii+1)*(d(ii+1)-1)*ezhongup^(d(ii+1)-2);
                 cc1=k(i-1)/(1+e(i-1))+k(i)/(1+e(i));    % lizhong=cc2/cc1
                 cc2=((rw-rs)*da*(k(i-1)/(1+e(i-1))-k(i)/(1+e(i)))+k(i-1)/(1+e(i-1))*li(i-
1)+k(i)/(1+e(i))*li(i));
                 cc3=(kdao(i-1)*(1+e(i-1))-k(i-1))/((1+e(i-1))^2);
                 cc4=(kdao(i)*(1+e(i))-k(i))/((1+e(i))^2);
                 cc5=cc1*(((rw-rs)*da+li(i-1))*cc3+k(i-1)/(1+e(i-1))*lidao(i-1))-cc3*cc2;
                 cc6=cc1*(cc4*(li(i)-da*(rw-rs))+k(i)/(1+e(i))*lidao(i))-cc2*cc4;
                 lizhongdaodown=cc5*cc1^-2;    %d(lizhong)/d(e(pp-1))
                 lizhongdaoup=cc6*cc1^-2;     %d(lizhong)/d(e(pp))
                 ezhongdowndao=elidaodown*lizhongdaodown;
                 ezhongupdao=elidaoup*lizhongdaoup;     %  d(ezhong)/d(e(pp))
                 aaazhongup=(kdaozhongup-kzhongup/(1+ezhongup))/(1+ezhongup);
                 bbbzhongup=kzhongup*lidaozhongup/(1+ezhongup);
                 adaozhongup=(kdaodaozhongup-2*aaazhongup)/(1+ezhongup);
```

```
bdaozhongup=aaazhongup*lidaozhongup+kzhongup*lidaodaozhongup/(1+ezhongup) ;
%%%%%%%%%%%%%%%%%%%%%%%%%%%%%%%%%%%%%%%%%%%%%%%%%%
        i=pp(ii+1)-1;
            fdao(i,i-1)=-(dt*rc)/(rw*da)*aaa(i)+dt/(rw*da*da)*(-bdao(i-1)*(e(i)-e(i-1))-bbb(i)+bbb(i-1))+dt/(rw*da*da)*bbb(i);
            fdao(i,i)=(dt*rc)/(rw*da)*(adao(i)*(e(i)-e(i-1))+aaa(i))+dt/(rw*da*da)*(bdao(i)*(e(i)-e(i-1))+bbb(i)-bbb(i-1))+dt/(rw*da*da)*(bdao(i)*(ezhongdown-2*e(i)+e(i-1))+(ezhongdowndao-2)*bbb(i))+1;
            fdao(i,i+1)=dt/(rw*da*da)*bbb(i)*ezhongupdao;
        i=pp(ii+1);
            fdao(i,i-1)=(dt*rc)/(rw*da)*aaa(i)*(-ezhongdowndao)+dt/(rw*da*da)*((-bdaozhongup*ezhongdowndao)*(e(i)-ezhongup)+(bbb(i)-bbbzhongup)*(-ezhongdowndao))+dt/(rw*da*da)*bbb(i)*ezhongdowndao;
            fdao(i,i)=(dt*rc)/(rw*da)*(adao(i)*(e(i)-ezhongup)+aaa(i)*(1-ezhongupdao))+dt/(rw*da*da)*((e(i)-ezhongup)*(bdao(i)-bdaozhongup*ezhongupdao)+(bbb(i)-bbbzhongup)*(1-ezhongupdao))+dt/(rw*da*da)*(bdao(i)*(e(i+1)-2*e(i)+ezhongup)+bbb(i)*(ezhongupdao-2))+1;
            fdao(i,i+1)=dt/(rw*da*da)*bbb(i);
        i=pp(ii+1)-1;
            f(i)=(dt*rc)/(rw*da)*aaa(i)*(e(i)-e(i-1))+dt/(rw*da*da)*(bbb(i)-bbb(i-1))*(e(i)-e(i-1))+dt/(rw*da*da)*bbb(i)*(ezhongdown-2*e(i)+e(i-1))+e(i)-ebefore(i);
        i=pp(ii+1);
            f(i)=(dt*rc)/(rw*da)*aaa(i)*(e(i)-ezhongup)+dt/(rw*da*da)*(bbb(i)-bbbzhongup)*(e(i)-ezhongup)+dt/(rw*da*da)*bbb(i)*(e(i+1)-2*e(i)+ezhongup)+e(i)-ebefore(i);
    end
 %%%%%%%%%%%%%%%%%%%%%%%%%%%%%%%%%%%%%%%%%%%%%%%%%%
        i=1;
          f(i)=(dt*rc)/(rw*da)*aaa(i)*(e(i)-exu)+dt/(rw*da*da)*(bbb(i)-bbbxu)*(e(i)-exu)+dt/(rw*da*da)*bbb(i)*(e(i+1)-2*e(i)+exu)+e(i)-ebefore(i);
        for i=2:n-1
           fou=0;
           for iii=1:cengshu-1
              if i==pp(iii+1)
                fou=1;
              end
           end
           if fou==0
              f(i)=(dt*rc)/(rw*da)*aaa(i)*(e(i)-e(i-1))+dt/(rw*da*da)*(bbb(i)-bbb(i-1))*(e(i)-e(i-1))+dt/(rw*da*da)*bbb(i)*(e(i+1)-2*e(i)+e(i-1))+e(i)-ebefore(i);
           end
        end
        f(n)=e(n)-eding;
        %%%%%%%%%%%%%%%%%%%%%%%%%%%%%%%%%%%%%%%%%%%%%%%
        keci=fdao\(-f);
        e=e+keci;
    end
    %%%%%%%%%%%%%%%%%%%%%%%%%%%%%%%%%%%%%%%%%%%%%%%
    ebefore=e;
```

```
    ejilu(:,j)=e;
            li(n)=(e(n)/a(cengshu))^(1/b(cengshu));
            for i=n-1:-1:1
                    fou=0;
                    for iii=1:cengshu-1
                      if i==pp(iii+1)
                        fou=1;
                          if fou==1
                             pzhong=p(i+1)-da*(rw-rs-(li(i+1)-lizhongcun(iii))/da);
                             p(i)=pzhong-da*(rw-rs-(lizhongcun(iii)-li(i))/da);
                           end
                      end
                    end
              p(i)=p(i+1)-da*(rw-rs-(li(i+1)-li(i))/da);
            end
     pjilu(:,j)=p;
end
%%%%%%%%%%%%%%%%%%%%%%%%%%%%%%%%%%%%%%%%%%%%%
jilujiange=m/rstep;
for jjj=1:m
  if mod(jjj,jilujiange)==0
    e=ejilu(:,jjj)
    p=pjilu(:,jjj)
          %%%%%%%%%%%%%%%%%%%%%%%%%
          houhou(1)=0;houdu=0;p(n)=0;
            for i=2:n
                    fou=0;
                    for iii=1:cengshu-1
                      if i==pp(iii+1)
                        fou=1;
                      end
                    end
              if fou==1;
                ddaa=((e(i)+e(i-1))/2+1)*2*da;
                houhou(i)=houhou(i-1)+ddaa;
                houdu=houdu+ddaa;
              end
                ddaa=((e(i)+e(i-1))/2+1)*da;
                houhou(i)=houhou(i-1)+ddaa;
                houdu=houdu+ddaa;
            end
            %%%%%%%%%%%%%%%%%%
              houdujilu(jjj/jilujiange)=houdu;
              tt(jjj/jilujiange)=dt*jjj;
               pppjilu(:,jjj/jilujiange)=p;
              eee(:,jjj/jilujiange)=e;
              houhoujilu(:,jjj/jilujiange)=houhou;
   end
end
figure(1)
```

```
plot(eee,houhoujilu)
title('e--height')
xlabel('e')
ylabel('height(m)')
figure(2)
plot(pppjilu,houhoujilu)
title('overpressure--height')
xlabel('overpressure(kpa)')
ylabel('height(m)')
figure(3)
plot(tt,houdujilu)
title('t--height')
xlabel('t(day)')
ylabel('height(m)')
r1(:,1)=tt';
r1(:,2)=houdujilu';
 xlswrite('time-height',r1)
 xlswrite('overpressure',pppjilu)
 xlswrite('void ratio',eee)
 xlswrite('height',houhoujilu)
```

(4) Output results:

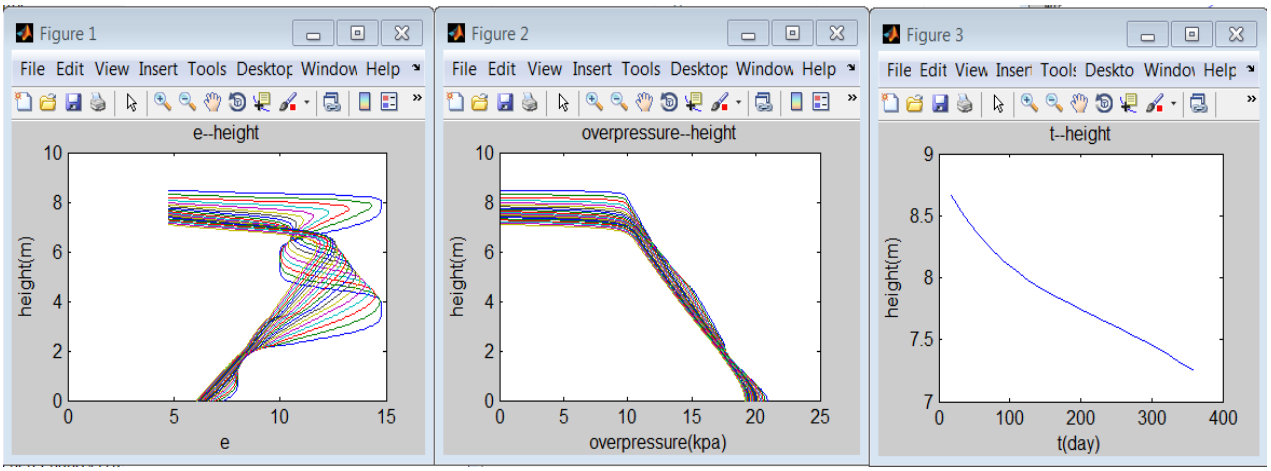

Figure A.4

From left to right 'void ratio-height' at the end, and 'overpressure-height', 'height-time' profiles change with time.

If the user want get the corresponding data, the data are available in excel file.

'time-height.xls' provides the time and correspond height data.

'overpressure.xls' provides the overpressure data in the corresponding time.

'void ratio.xls' provides the void ratio data in the corresponding time.

‘height.xls’ provides the height data in the corresponding time.

References

Abbasi, N., Rahimi, H., Javadi, A.A. and Fakher, A., 2007. Finite difference approach for consolidation with variable compressibility and permeability. Computers and Geotechnics, 34(1): 41-52.

AGRA, 1997. Progress on MFT Modeling. Report to Syncrude Canada Ltd, Engineering report, AGRA Earth & Environmental limited，Edmonton, Alberta.

Ai, Z., Cheng, Y.C. and Zeng, W., 2011. Analytical layer-element solution to axisymmetric consolidation of multilayered soils. Computers and Geotechnics, 38(2): 227-232.

Ai, Z., Wu, C. and Han, J., 2008. Transfer matrix solutions for three-dimensional consolidation of a multi-layered soil with compressible constituents. International Journal of Engineering Science, 46(11): 1111-1119.

Athy, L.F., 1930. Density, porosity and compaction of sedimentary rocks. American Association of Petroleum Geologists Bulletin, 14: 1 - 22.

Audet, D.M., 1996. Compaction and overpressuring in Pleistocene sediments on the Louisiana Shelf, Gulf of Mexico. Marine und Petroleum Geology, 13(5): 414-467.

Backus, G., 1962. Long-wave elastic anisotropy produced by horizontal layering. Journal Geophysical Research, 67(11): 4427 – 4440.

Benson, R.E.J. and Sill, B.J., 1985. Discussion of 'Prediction of consolidation of very soft soil' by K. W. Cargill. Journal of Geotechnical Engineering, 111(11): 1356-1358.

Bethke, C.M., 1985. A numerical model of compaction-driven groundwater flow and heat transfer and its application to the paleohydrology of intracratonic sedimentary basins. Journal of Geophysical Research, 90(B2): 6817-6828.

Bethke, C.M., 1986. Hydrologic constraints on the genesis of the Upper Mississippi Valley mineral district from Illinois basin brines. Economic Geology, 81(2): 233-249.

Bjørlykke, K., 1998. Clay mineral diagenesis in sedimentary basins - a key to the prediction of rock properties. Examples from the North Sea Basin. Clay Minerals, 33: 15-34.

Bjørlykke, K., 1999. Principal aspects of compaction and fluid flow in mudstones. Muds and Mudstones: Physical and Fluid Flow Properties. The Geological Society (London) Special Publications(158): 73-78.

Bjørlykke, K., Ramm, M. and Saigal, G.C., 1989. Sandstone diagenesis and porosity modification during basin evolution. Geologische Rundschau, 78: 243-268.

Booker, J.R. and Rowe, R.K., 1983. 1-D Consolidation of Periodically Layered Soil. Journal of Engineering Mechanics, 109(6): 230 - 244.

Budiansky, B., 1965. On the elastic moduli of some heterogeneous materials. Journal of the Mechanics and Physics of Solids, 13: 223 – 227.

Burst, J.F., 1969. Diagenesis of Gulf Coast clayey sediments and its possible relation to petroleum migration. American Association of Petroleum Geologists Bulletin, 53(73-93).

Cai, Y., Geng, X. and Xu, C., 2007. Solution of one-dimensional finite-strain consolidation of soil with variable compressibility under cyclic loadings. Computers and Geotechnics, 34(1): 31.

Cargill, K.W., 1985. Closure of discussion of 'Prediction of consolidation of very soft soil' by K. W. Cargill. Journal of Geotechnical Engineering, 111(11): 1363-1364.

Chen, R., Zhou, W., Wang, H. and Chen, Y., 2005. One-dimensional nonlinear consolidation of multi-layered soil by differential quadrature method. Computers and Geotechnics, 32(5): 358-369.

Christopher, L.M., 2006. Forward modelling of compaction and fluid flow in the Ursa region, Mississippi canyon area, Gulf of Mexico. The Graduate School College of Earth and Mineral Sciences, The Pennsylvania State University.

Chuhan, F.A., Kjeldstad, A., Bjørlykke, K. and Hoeg, K., 2002. Porosity loss in sand by grain crushing - experimental evidence and relevance to reservoir quality. Marine and Petroleum Geology, 19 (1): 39-53.

Cryer, C.W., 1963. A comparison of the three-dimensional consolidation theories of Biot and Terzaghi. Quarterly Journal of Mechanics and Applied Mathematics, 16: 401–412.

Davis, E.H. and Lee, I.K., 1969. One dimensional consolidation of layered soils. 7th international conference on soil mechanics and foundation engineering 65 - 72.

Djeran Maigre, I. and Gasc Barbier, M., 2000. Hydromechanical Modelling of Experimentally Compacted Saturated Argillaceous Porous Media. Transport in Porous Media, 41(1): 81-103.

Domenico, P.A. and Schwartz, F.W., 1991. Physical and Chemical Hydrogeology.

Eaton, L., 1999. Drilling through deepwater shallow water flow zones at Ursa. Society of Petroleum Engineers/International Association of Drilling Contractors. Amsterdam: 153-164.

Elkateb, T.M., 2003. Quantification of Soil Heterogeneity. PhD dissertation University of Alberta, Edmonton, Canada.

Flemings, P.B., Behrmann, J., Davies, T., John, C. and Team, E.P., 2005. Gulf of Mexico hydrogeology - overpressure and fluid flow processes in the deepwater Gulf of Mexico: slope stability, seeps, and shallow-water flow. IODP Sci. Prosp.308.

Fox, P.J. and Berles, J.D., 1997. CS2: A piecewise-linear model for large strain consolidation. International journal for numerical and analytical methods in geomechanics, 21(7): 453 - 475.

Galloway, W.E., 1984. Hydrogeologic regimes of sandstone diagenesis. American Association of Petroleum Geologists Memoir, 37: 3-14.

Gay, A. and IODP, 2005. Overpressure and fluid flow processes in the deepwater Gulf of Mexico: slope stability, seeps, and shallow-water flow. Integrated Ocean Drilling Program Preliminary Report 308.

Ge, S. and Garven, G., 1992. Hydromechanical modeling of tectonically driven groundwater flow with application to the Arkoma Foreland Basin. Journal of Geophysical Research: Solid Earth (1978–2012), 97(B6): 9119–9144.

Geng, X., 2008. Multi-dimensional Consolidation Theory for Cyclic Loadings, Proceedings of the 2008 International Conference on Advanced Computer Theory and Engineering. IEEE Computer Society, pp. 773-777.

Georgiopoulou, A., Böker, U., Aplin, A.C. and Cartiwright, J., 2008. Characterising regional seal integrity in Case Study B: an integrated approach - 3 Parts Caprocks steering group meeting – Phase II, December 2008 – Sunbury, London

Gibson, R.E., England, G.l. and Hussey, M.J.L., 1967. The theory of one-dimensional consolidation of saturated clays. Geotechnique, 17(2): 261-273.

Gibson, R.E., Schiffman, R.L. and Cargill, K.W., 1981. The theory of one-dimensional consolidation of saturated clays. II. Finite nonlinear consolidation of thick homogeneous layers. Canadian Geotechnical Journal, 18(2): 280-293.

Gibson, R.E., Schiffman, R.L. and Cargill, K.W., 1982. The theory of one-dimensional consolidation of saturated clays: Reply. Canadian Geotechnical Journal, 19(1): 116-116.

Gordon, D. and Flemings, P., 1998. Generation of overpressure and compaction-driven flow in a Plio-Pleistocene growth-faulted basin, Eugene Island 330, offshore Louisiana. Basin Research, 10: 177-196.

Hart, B.S., Fleming, P.B., Disphande, A. and Hedberg, H.D., 1995. Porosity and pressure : role of compaction disequilibrium in the development of geopressures in a Gulf Coast Pleistocene basin. Geology, 23(l): 45.

Hashin, Z., 1955. The moduli of an elastic solid reinforced by rigid particles. Bulletin of the Research Council of Israel, 5c: 46 - 59.

Hedberg, H.D., 1936. gravitational compaction of clays and shales. American journal sciences, 31: 241-297.

Henrich, R. and Hüneke, H., 2011. Chapter 5 - Hemipelagic Advection and Periplatform Sedimentation. In: H. Heiko and M. Thierry (Editors), Developments in Sedimentology. Elsevier, pp. 353-396.

Hill, R., 1965. A self-consistent mechanics of composite materials. Journal of the Mechanics and Physics of Solids, 13: 213 – 222.

Jeeravipoolvarn, S., Chalaturnyk, R.J. and Scott, J.D., 2009. Sedimentation–consolidation modeling with an interaction coefficient. Computers and Geotechnics, 36(5): 751-761.

Jones, M.E. and Addis, M.A., 1985. On changes in porosity and volume during burial of argillaceous sediments. Murine and Petroleum Geology, 2: 247-253.

Kauerauf, A.I. and Hantschel, T., 2009. Fundamentals of Basin and Petroleum Systems Modeling. Springer Berlin Heidelberg, ISBN: 978-3-540-72317-2.

Khajeh, M.M., 2012. A Numerical Local Upscaling Approach for Elastic Rock Mechanical Properties: Dealing with Heterogeneity. American Rock Mechanics Association, 12(654).

Kooi, H., 1997. Insufficiency of compaction disequilibrium as the sole cause of high pore fluid pressures in pre-Cenozoic sediments. Basin Research, 9: 227–241.

Kynch, G., 1952. A theory of sedimentation. Trans Faraday Soc, 1(48): 166–176.

Lee, M.K. and Bethke, C.M., 1994. Groundwater flow, late cementation, and petroleum accumulation in the Permian Lyons sandstone Denver basin. American Association of Petroleum Geologists Bulletin, 78: 217–237.

Lee, M.K. and Williams, D.D., 2000. Paleohydrology of the Delaware basin, western Texas: Overpressure development, hydrocarbon migration, and ore genesis. American Association of Petroleum Geologists Bulletin, 84: 961–974.

Lee, P.K.K., Xie, K. and Cheung, Y., 1992. A study on one-dimensional consolidation of layered systems. Int. J. Numer. Analyt. Meth. Geomech., 16: 815-831.

Leroueil, S., Kabbaj, M., Tavenas, F. and Bouchard, R., 1985. Stress-strain-strain rate relation for the compressibility of sensitive natural clays. Géotechnique, 35(2): 21.

Liu, J. and Lei, G.H., 2013. One-dimensional consolidation of layered soils with exponentially time-growing drainage boundaries. Computers and Geotechnics, 54(0): 202-209.

Long, H., Flemings, P.B., Germaine, J.T., Saffer, D.M. and Dugan, B., 2008. Data report: consolidation characteristics of sediments from IODP Expedition 308, Ursa Basin, Gulf of Mexico. the Expedition 308 Scientists Proceedings of the Integrated Ocean Drilling Program, Volume 308.

Luo, X. and Vasseur, G., 1992. Contributions of compaction and aquathermal pressuring to geopressure and the influence of environmental conditions. American Association of Petroleum Geologists Bulletin, 76: 1550-1559.

Luo, X. and Vasseur, G., 1996. Geopressuring mechanism of organic matter cracking: Numerical modeling. American Association of Petroleum Geologists Bulletin, 80: 856–874.

Luo, X., Vasseur, G., Pouyab, A., Lamoureuxvarb, V. and Poliakov, A., 1998. Elastoplastic deformation of porous media applied to the modelling of compaction at basin scale. Marine and Petroleum Geology, 15: 145 - 162.

Ma, J. and Couples, G., 2008. Caprocks Phase II report. Caprocks Steering Group Meeting.

Mackenzie, J., 1950. The elastic constants of a solid containing spherical holes. Proceedings of the Royal Society London, 63(1): 2 - 11.

Maltman, A., 1994. The geological deformation of sediments: introduction and overview. the geological deformation of sediments:London, Chapman and hall: 1-35.

Marcussen, Ø., 2009. Compaction of siliceous sediments –Implications for basin modeling and seismic interpretation. Dissertation for the degree of Philosophiae Doctor (Ph.D.) Faculty of Mathematics and Natural Sciences Department of Geosciences, University of Oslo Norway.

McVay, M., Townsend, F. and Bloomquist, D., 1986. Quiescent consolidation of phosphatic waste clays. Journal of Geotechnical Engineering, 112(11): 1033-1049.

Mondol, N.H., Bjørlykke, K., Jahren, J. and Hoeg, K., 2007. Experimental mechanical compaction of clay mineral aggregates - Changes in physical properties of mudstones during burial. Marine and Petroleum Geology, 24 (5): 289-311.

Montgomery, J., 2010. An Examination of the FLAC Software: Undrained Triaxial Test on Cam-clay. ECI 280A Term Project.

Morris, P., 2002. Analytical Solutions of Linear Finite-Strain One-Dimensional Consolidation. Journal of Geotechnical and Geoenvironmental Engineering, 128(4): 319-326.

Muir Wood, D., 1990. Soil Behavior and Critical State soil Mechanics.

Murray, F. and Robert, T., 2011. Large-Strain Consolidation Verification Manual.

Pane, V. and Schiffman, R., 1985. Note on sedimentation and consolidation. International Journal of Rock Mechanics and Mining Sciences, 22(4): 116-117.

Pollock, G., 1988. Large Strain Consolidation of Oil Sand Tailings Sludge, MS.c. Thesis, University of Alberta, Edmonton, Canada.

Potter, P.E., Maynard, J.B. and Depetris, P.J., 2005. Mud and Mudstones. Springer, NewYork: 297.

Pouya, A., Djéran-Maigre, I., Lamoureux-Var, V. and Grunberger, D., 1998. Mechanical behaviour of fine grained sediments : experimental compaction and three-dimensional constitutive model. Marine and Petroleum Geology, 15(2): 129 - 143

Praeger, T., 2007. Caprocks Steering Group Meeting report - Characterising Hemipelagites Caprocks Phase II report.

Press, W.H., 2002. Numerical recipes in C++: the art of scientific computing. Cambridge, UK; New York.

Ramm, M. and Bjørlykke, K., 1994. Porosity/depth trends in reservoir sandstones; assessing the quantitative effects of varying pore-pressure, temperature history and mineralogy, Norwegian Shelf data. Clay Minerals, 29(4): 475-490.

Roscoe, K.H. and Burland, J.B., 1968. On the generalized stress strain behaviour of wet clay. Engineering Plasticity: 535 - 609.

Roscoe, K.H. and Schofield, A.N., 1963. Mechanical behaviour of an idealised 'wet' clay. 2nd ECSMFE Wiesbaden, 1: 47 - 54.

Rubey, W.W. and Hubbert, M.K., 1959. Role of fluid pressure in mechanics of overthrust faulting : II. Overthrust belt in geosynclinal area of western Wyoming in light of fluid-pressure hypothesis. 70: 167-206.

Salamon, M., 1968. Elastic moduli of a stratified rock mass. . Journal of Rock Mechanics and Mining Sciences, 5: 519–527.

Santamarina, J.C. and Fratta, D., 2005. Discrete Signals and Inverse Problems: an Introduction for Engineers and Scientists. John Wiley and Sons, Chichester, UK.

Sawyer, D.E., Flemings, P.B., Shipp, R.C. and Winker, C.D., 2007. Seismic geomorphology, lithology, and evolution of the late Pleistocene Mars-Ursa turbidite region, Mississippi Canyon area, northern Gulf of Mexico. American Association of Petroleum Geologists Bulletin, 91(2): 215-234.

Schiffman, R.L., Chen, A.T. and Jordan, J.C., 1969. An analysis of consolidation theories. Journal of the Soil Mechanics and Foundations Division, ASCE, 95: 285 - 312.

Schiffman, R.L. and Stein, J.R., 1970. One-dimensional consolidation of layered systems. J. Soil Mech. and Found. Div., 96 (4): 1499-1504.

Schmid, V. and Mcdonald, D.A., 1979. The role of secondary porosity in the course of sandstone diagenesis. Aspects of Diagenesis (P. A. SchoUe and P. R. Schluger, editors). SEPM Spec. Pub, 26: 175-207.

Schneider, F., Potdevin, J.L., Wolf, S. and Faille, I., 1996. Mechanical and chemical compaction model for sedimentary basin simulators. Tectonophysics, 263: 307-317.

Sclater, J.G. and Christie, P.A.F., 1980. Continental stretching: An explanation of the postmid-Cretaceous subsidence of the central North Sea Basin. Journal of Geophysical Research, 85 (B7)(3711-3739).

Sharp, J.M.J., 1983. Permeability controls on aquathermal pressuring. American Association of Petroleum Geologists Bulletin, 67 2057-2061.

Shi, Y. and Wang, C., 1986. Pore pressure generation in sedimentary basins: overloading versus aquathermal. Journal of Geophysical Research: Solid Earth (1978–2012), 91(B2): 2I53-2162.

Shodja, H. and Feldkamp, J., 1993. Numerical analysis of sedimentation and consolidation by the moving finite element method. Int J Numer Methods Geomech, 17: 53-69.

Smith, J.E., 1971. The dynamics of shale compaction and evolution in pore-fluid pressures. Math. Geol, 3: 239-263.

Somogyi, F., 1980. Large Strain Consolidation of Fine Grained Slurries. Presented at the Canadian Society for Civil Engineering, Winnipeg, Manitoba, May 29-30.

Stehfest, H., 1960. Numerical inverse of laplace transform. Communications of the ACM, 3(3): 171-173.

Suthaker, N.N., 1995. Geotechnics of Oil Sand Fine Tailings, Ph.D. Thesis, University of Alberta, Edmonton, Canada.

Swarbrick, R.E. and Osborne, M.J., 1998. Mechanisms that generate abnormal pressures - an overview. American Association of Petroleum Geologists special volumes: 13-34.

Terzaghi, K.V., 1929. Settlement analysis - the backbone of foundation research. Word Engineering Congress(Tokyo), 8(2).

Terzaghi, K.V., 1943. Theoretical soil mechanics. John Wiley and Sons, New York

Townsend, F.C. and Mcvay, M.C., 1991. SOA: large strain consolidation predictions. Journal of Geotechnical Engineering, 116(2): 222 - 243.

Ulisses, T.M., Garry, D.K. and Roger, N.A., 1994. A physical explanation for the positioning of the depth to the top of overpressures in shale-dominated sequences in the Gulf Coast basin, United States. Journal of Geophysical Research Atmospheres, 99: 2775-2189.

Wangen, M., 1992. Pressure and temperature evolution in sedimentary basins. Geophysical Journal International, 110(3): 601-613.

Wangen, M., 2010. Physical principles of sedimentary basin analysis. Cambridge University Press(isbn: 9780521761253).

Winker, C. and Booth, J., 2000. Sedimentary dynamics of the salt dominated continental slope, Gulf of Mexico; Integration of observations from the seafloor, near-surface and deep subsurface. SEPM Gulf Coast Section 20th Annual research Conference: 1059-1086.

Winker, C. and Shipp, R., 2002. Sequence Stratigraphic Framework for Prediction of Shallow Water Flow in the Greater Mars-Ursa Area, Mississippi Canyon Area, Gulf of Mexico Continental Slope. SEPM Gulf Coast Section 22nd Annual Research Conference.

Wolf, L.W. and Lee, M.K., 2005. Numerical analysis of overpressure development in the New Madrid Seismic Zone. Bulletin of Seismological Society of America, 95: 135–144.

Xie, K. and Leo, C., 2004. Analytical solutions of one-dimensional large strain consolidation of saturated and homogeneous clays. Computers and Geotechnics, 31(4): 301-314.

Xie, K., Xie, X. and Gao, X., 1999. Theory of one dimensional consolidation of two-layered soil with partially drained boundaries. Computers and Geotechnics, 24(4): 265-278.

Xie, K., Xie, X. and Wen, J., 2002. A study on one-dimensional nonlinear consolidation of double-layered soil. Computers and Geotechnics, 29(2): 151-168.

Yang, Y. and Aplin, A.C., 2004. Definition and practical application of mudstone porosity - effective stress relationships. Petroleum Geoscience, 10: 153-162.

Yang, Y. and Aplin, A.C., 2007. Permeability and petrophysical properties of 30 natural mudstones. Journal of Geophysical Research: Solid Earth (1978–2012), 112(B3).

Yang, Y. and Aplin, A.C., 2010. A permeability–porosity relationship for mudstones. Marine and Petroleum Geology, 27(8): 1692-1697.

References

Yang, Y., Aplin, A.C. and Hansen, S., 1995. Assessment of β the compression coefficient of mudstones and its relationship with detailed lithology. Marine and Petroleum Geology, 12(8): 955-963.

Yang, Y., Aplin, A.C. and Larter, S.R., 2004. Quantitative assessment of mudstone lithology using geophysical wireline logs and artificial neural networks. Petroleum Geoscience, 20(2): 141 - 151.

Yardley, G., 2000. An internal report of the GeoPOP project Phase II.

You, Y. and Person, M., 2008. Role of pore pressure generation in sediment transport within half-grabens. Basin Research, 20(3): 419-429.